

Internal-State-Variable Based Constitutive Modelling and its Applicability to Tensile and Creep Deformation of Tempered Martensitic 9% Chromium Steels

By

J. Christopher

(Enrolment No: ENGG02201504003)

**Indira Gandhi Centre for Atomic Research
Kalpakkam - 603102, India**

*A thesis submitted to the
Board of Studies in Engineering Sciences*

*In partial fulfillment of requirements
for the Degree of*

DOCTOR OF PHILOSOPHY

of

**HOMI BHABHA NATIONAL INSTITUTE
Mumbai, India**



November, 2018

Homi Bhabha National Institute

Recommendations of the Viva Voce Committee

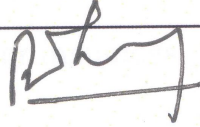
As members of the Viva Voce Committee, we certify that we have read the dissertation prepared by **J. Christopher** entitled "**Internal-State-Variable Based Constitutive Modelling and its Applicability to Tensile and Creep Deformation of Tempered Martensitic 9% Chromium Steels**" and recommend that it may be accepted as fulfilling the thesis requirement for the award of Degree of Doctor of Philosophy.

Chairman - Dr. G. Sasikala



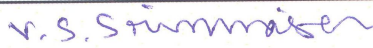
Date: 26.04.2019

Guide- Dr. B.K. Choudhary



Date: 26.4.2019

Co-guide - Dr. V.S. Srinivasan



Date: 26/4/2019

Examiner - Prof. B.P. Kashyap



Date: 26-April-2019

Member 1- Dr. R. Divakar



Date: 26/04/2019

Member 2- Dr. A. Nagesha



Date: 8.5.2019

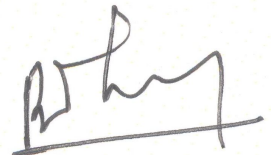
Final approval and acceptance of this thesis is contingent upon the candidate's submission of the final copies of the thesis to HBNI.

I/We hereby certify that I/we have read this thesis prepared under my/our direction and recommend that it may be accepted as fulfilling the thesis requirement.

Date: 26/04/2019

Place: IG CAR, Kalpakkam

V.S. Srinivasan
Co-Guide



Guide

Dr. B.K. Choudhary

STATEMENT BY AUTHOR

This dissertation has been submitted in partial fulfillment of requirements for an advanced degree at Homi Bhabha National Institute (HBNI) and is deposited in the Library to be made available to borrowers under rules of the HBNI.

Brief quotations from this dissertation are allowable without special permission, provided that accurate acknowledgement of source is made. Requests for permission for extended quotation from or reproduction of this manuscript in whole or in part may be granted by the Competent Authority of HBNI when in his or her judgment the proposed use of the material is in the interests of scholarship. In all other instances, however, permission must be obtained from the author.

Date: 26/04/2019

Place: ICAR, Kalpakram


(J. Christopher)

DECLARATION

I, hereby declare that the investigation presented in the thesis has been carried out by me. The work is original and has not been submitted earlier as a whole or in part for a degree / diploma at this or any other Institution / University.

Date: 26/04/2019

Place: ICAR, Kalpakkam


(J. Christopher)

List of Publications arising from the thesis

Journal Publications

1. Prediction of long-term creep behaviour of grade 91 steel at 873 K in the framework of microstructure based creep mechanics approach, **J. Christopher** and B.K. Choudhary, *International Journal of Damage Mechanics*, 2018.
<https://doi.org/10.1177/1056789518796118>
2. On the onset of necking instability in tempered martensitic 9% Cr steels, **J. Christopher** and B.K. Choudhary, *Mechanics Research Communications*, **94** (2018) pp. 114-119.
3. Modeling creep deformation and damage behavior of tempered martensitic steel in the framework of additive creep rate formulation, **J. Christopher** and B.K. Choudhary, *ASME, Journal of Pressure Vessel Technology*, 140 (2018) pp. 051401: 1-8
4. Applicability of improved Dyson-McLean approach to creep deformation behaviour of tempered martensitic P9 steel, **J. Christopher** and B.K. Choudhary, *Materials at High Temperatures*, 35 (2018) pp.387-397.
5. Constitutive modelling of stress-relaxation behaviour of tempered martensitic P91 steel using sine hyperbolic rate law, **J. Christopher** and B.K. Choudhary, *Materials Chemistry and Physics*, 205 (2018) pp. 442-451.
6. Sine hyperbolic models and their applicability towards creep deformation behaviour of 9% chromium steels, **J. Christopher** and B.K. Choudhary, *Transactions of Indian Institute of Metals*, 70 (2017) pp. 519-523.
7. Constitutive description of primary and steady state creep deformation behaviour of tempered martensitic 9Cr-1Mo steel, **J. Christopher** and B.K. Choudhary, *Philosophical Magazine*, 96 (2016) pp. 2256-2279.
8. Constitutive modeling of primary creep behaviour of P9 steel, **J. Christopher** and B.K. Choudhary, *Transactions of Indian Institute of Metals*, 69 (2016) pp. 519-523.
9. Comparative tensile flow and work hardening behaviour of 9 pct chromium ferritic-martensitic steels in the framework of Estrin-Mecking internal-variable approach B.K. Choudhary and **J. Christopher**, *Metallurgical and Materials Transactions A*, 47 (2016) pp. 2642-2655.
10. Comparative evaluation of two physically based models for the description of stress-relaxation behaviour of 9% chromium containing steel, **J. Christopher**, C. Praveen and B.K. Choudhary, accepted in *Frattura ed Integrità Strutturale*, , 48 (2019) pp. 554-562.

Conference Presentations

1. Constitutive modeling of primary creep behaviour of P9 steel, **J. Christopher** and B.K. Choudhary, *7th International Conference on Creep, Fatigue and Creep-Fatigue Interaction (CF-7)*, January 19-22, 2016, IGCAR, Kalpakkam, India.
2. Sine hyperbolic models and their applicability towards creep deformation behaviour of 9% chromium steels, **J. Christopher** and B.K. Choudhary, *International Conference on Emerging Trends in Materials and Manufacturing Engineering (IMME17)*, March 10-12, 2017, NIT Trichy, Tiruchirappalli, India.
3. Applicability of microstructure based damage mechanics approach for 9% Cr tempered martensitic steels, **J. Christopher** and B.K. Choudhary, *Research Scholars Meet on Material Science and Engineering of Nuclear Materials (RSM 2018)*, IGCAR, May 7-9, 2018, Kalpakkam, Tamil Nadu.
4. Comparative evaluation of two physically based models for the description of stress-relaxation behaviour of 9% chromium containing steel, **J. Christopher**, C. Praveen and B.K. Choudhary, *Second International Conference on Structural Integrity (ICONS 2018)*, December 14-17, 2018, IIT Madras, Chennai, India.

Date: 26/04/2019

Place: IGCAR, Kalpakkam


J. Christopher

Dedicated to my family and friends

ACKNOWLEDGEMENTS

Firstly, I would like to express my sincere gratitude to my advisor **Dr. B.K. Choudhary**, Former Head, Deformation and Damage Modelling Section, IGCAR for the continuous support of my Ph.D study and related research, for his patience, motivation, and immense knowledge. His guidance helped me in all the time of research and writing of this thesis.

Besides my advisor, I would like to thank the rest of my thesis committee: **Dr. G. Sasikala**, **Dr. K. Laha**, **Dr. V.S. Srinivasan**, **Dr. R. Divakar** and **Dr. A. Nagesha** for their insightful comments and encouragement. Their precious questions and suggestions at different stages of the work have provided an opportunity to review and reorganise my work appropriately.

I would like to thank **Dr. A.K. Bhaduri**, Director, IGCAR and **Dr. G. Amarendra** Director, Metallurgy and Materials Group, IGCAR for their keen interest, encouragement and giving me an opportunity to pursue my Ph.D. work in computational modelling aspects of mechanical metallurgy.

My special thanks to **Dr. Shaju K. Albert**, AD, MEG/MMG, **Dr. G. Sasikala**, Head, MDTD, **Dr. Anish Kumar**, Dean, Engineering Sciences, and **Dr. G.V. Prasad Reddy**, Head, CSS for their continual encouragement and support.

I sincerely thank **Dr. V.S. Srinivasan**, **Dr. Vani Shankar**, **Dr. E. Isaac Samuel**, **Dr. S. Ravi**, **Dr. G. Sainath** and **Mr. D.P. Rao Palaparti** for their suggestions and motivations. Special thanks to **Dr. V. D. Vijayanand**, **Dr. Surya Deo Yadav**, **Dr. B. Arivazhagan**, **Dr. J. Ganesh Kumar**, **Dr. N.L. Parthasarathi**, **Mr. M. Arvinth Davinci**, **Mr. P. Vasantharaja**, **Mr. V. Ganesan**, **Mrs. J. Vanaja** and **Mrs. M. Divya** for their appreciation, support and good company. I also thank my other colleagues who in each big or small means helped me throughout this entire research period. I would like to acknowledge **Mr. C. Praveen**, Ph.D. student for his technical assistance during this research work and for writing of the thesis. I am grateful to Ph.D. students **Mr. P. Rohith**, **Mr. V. Shiva** and **Mr. K.C. Sahoo** for affording comfortable and joyful laboratory environment. It gives me greatest pleasure to thank all my well-wishers who have contributed in various capacities to this research work.

Finally, I thank wholeheartedly all my family members for their unconditional love, care, support and freedom throughout the period of my Ph.D.

SYNOPSIS

9% chromium containing steels are favoured structural material for high temperature steam generator applications in thermal and nuclear power generating industries. Among 9% Cr steels, 9Cr-1Mo or P9 steel offers a good combination of high creep strength and ductility, good weldability and microstructural stability over long exposures at elevated temperatures. P9 steel modified by the addition of strong carbide/nitride forming elements such as vanadium and niobium along with controlled nitrogen, i.e., 9Cr-1Mo-V-Nb or P91 steel provides significantly higher tensile and creep strength than P9 steel. P9 and P91 steels with close control on trace elements such as sulphur and phosphorous have also emerged as important candidate materials for in-core reactor applications in future sodium cooled fast reactors due to their higher resistance to irradiation creep and void swelling compared to the presently used austenitic stainless steels. Both P9 and P91 steels exhibit an only modest increase in ductile to brittle transition temperature with irradiation compared to other grades of tempered martensitic steels. Constitutive modelling of tensile and creep deformation behaviour of reactor structural and steam generator materials attracts continued scientific and technological interest in view of better understanding of the kinetics of deformation mechanisms and reliable prediction of life and performance of engineering components during service. Models proposed to describe deformation behaviour can be either empirical formulations or linked to the internal microstructural state known as internal-state-variable based models. In the internal-state-variable approach, the kinetic relationships governed by the evolution of dislocation structure with plastic strain to enable the prediction of deformation behaviour of materials. In general, evolution of dislocation structure is determined by two different competing processes such as hardening and dynamic recovery. Hardening results from the storage of forest dislocations due to the interaction of mobile dislocations with various obstacles such as sessile dislocations, grain boundaries, precipitates

and dispersoids, while dynamic recovery deals with a decrease in dislocation density as a result of thermally activated rearrangement and annihilation of dislocations. In the present work, comparative evaluation of tensile flow and work hardening behaviour of P9 steel in two different product forms and P91 steel have been performed for a wide range of temperatures in the framework of dislocation density based models.

In order to model the creep behaviour of materials, apart from strain hardening and dynamic recovery processes, the kinetic aspects related to the evolution of damages with creep strain/time has been considered. Internal-stress based sine hyperbolic creep rate law has been developed for the description of transient creep approaching towards steady state /minimum creep rate in 9% Cr steels. The applicability of the model has been demonstrated for P9 steel in two different heat treated conditions at 793 and 873 K. The tertiary creep behaviour has been examined in the framework of Materials Properties Council (MPC) – Omega methodology and microstructure based continuum creep damage mechanics (CDM) approach by Semba-Dyson-McLean. In addition to the above, internal-stress based sine hyperbolic model has been developed to describe the stress-relaxation behaviour of 9% Cr steel. The validity of the developed model has been demonstrated for P91 steel at 873 K. The thesis comprising of seven chapters dealing with a detailed review of literature, experimental details along with tensile and creep data used for modelling, results and discussion pertaining to the proposed models and its validity, and general conclusions as well as future directions are given briefly in the following;

CHAPTER 1: Introduction

This chapter gives a brief overview of 9% chromium containing tempered martensitic steels along with their tensile and creep properties. A detailed review of literature related to the influence of temperature and strain rate on tensile properties and the development of

dominating damages in these steels have been discussed. In addition to the above, various empirical and physically based constitutive relationships available in the literature describing the tensile and creep deformation behaviour of materials have been presented. Following this, the motivation and scope of the thesis have been brought out.

CHAPTER 2: Material, Initial Microstructure and Experimental Data for Modelling and Parametric Optimisation Methodology

For modelling tensile behaviour of 9% Cr steels, the experimental true stress-true plastic strain data obtained for two different product forms of P9 steel plate and thick-section tubeplate forging and P91 steel have been used. P9 steel plate was tested in normalized and tempered (N+T) condition while P9 steel tubeplate forging was tested in quenched and tempered (Q+T) condition. The tensile data for P91 was obtained in normalized and tempered (N+T) condition. The heat treatment along with microstructure and tensile tests performed at temperatures ranging from 300 to 873 K has been described.

The constant load creep test data obtained on thick section P9 steel tubeplate forging in quenched and tempered (Q+T) and an additional simulated post weld heat treatment (SPWHT) conditions, and used for modelling creep behaviour have been presented. The necessary microstructural details in heat treated and creep tested conditions have been described. In addition to above, creep strain-time data obtained from the literature for normalised and tempered T91 steel have been used to examine long-term creep life prediction. Stress-relaxation data acquired for normalised and tempered P91 steel have been presented and utilised to model stress-relaxation behaviour. In addition, the generalised framework related to the parametric optimisation methodology has also been presented in this chapter.

CHAPTER 3: Dislocation Density Based Model for the Description of Tensile Flow and Work Hardening Behaviour of 9% Cr Steels

Three different variants of Kocks-Mecking-Estrin model have been used to describe the tensile flow and work hardening behaviour. The first variant is known as Kocks-Mecking (K-M) approach, where the dislocation storage rate is dominated only by dislocation structure itself, regardless of the nature of dislocation arrangement. Contrary to Kocks-Mecking approach, Estrin and Mecking proposed a new model for dislocation storage rate controlled by the impenetrable obstacles such as particles/precipitates or, the boundaries when the spacing between these obstacles is much smaller than the obstacles generated due to dislocation structure. This model has been further extended to incorporate the immobilizing effects of both types of obstacles, i.e., the dislocations and the geometrical obstacles. The developed model is known as hybrid model. It is reasonable to assume that the hybrid model can appropriately describe the evolution of dislocation density with plastic strain due to the presence of fine hierarchical boundaries, large amount of precipitates and high initial dislocation density in 9% Cr steels. However, a detailed parametric sensitivity analysis using optimised parameters associated with the hybrid model performed in the present study has demonstrated that dislocation dense martensite lath/cell boundaries and precipitates together act as effective barriers to dislocation motion in 9% Cr steels. These results clearly suggest that the hybrid model reduces to Estrin-Mecking model for the description of the flow behaviour of these steels.

In order to examine the applicability of Estrin-Mecking approach, comparative evaluation of tensile flow and work hardening behaviour of P9 steel plate and thick-section tubeplate forging and P91 steel have been performed for temperatures ranging from 300 to 873 K. Larger gains in dislocation density were predicted for P9 steel tubeplate forging than those obtained for P9 steel plate and P91 steel. This clearly indicates improved work

hardening ability of P9 steel tubeplate forging arises from its softened initial microstructure compared to P9 steel plate and P91 steel. In addition to above, the dynamic recovery model proposed by Bergström and Hallén has been employed for the evaluation of activation energy for cross-slip and climb of dislocations towards the analysis of dynamic recovery parameter obtained from Estrin-Mecking approach. Based on these results, the influence of temperature and initial microstructure on the work-hardening parameters in P9 steel plate and tubeplate forging and P91 steel have been discussed. Finally, a new plastic instability criterion obtained using optimised microstructure related parameters associated with Estrin-Mecking approach and its applicability to 9% Cr tempered martensitic steels have been demonstrated.

CHAPTER 4: Constitutive Modelling of Primary and Steady State Creep Behaviour of 9% Cr Tempered Martensitic Steels

Traditionally, creep modelling and finite element analysis towards engineering creep design are limited to secondary creep and the transient processes such as those occurring during primary creep are generally ignored. Since most of the allowable creep strain is accumulated during the primary stage, it is necessary to incorporate primary creep strain contribution in the analysis for the safe life design of components. It is well known that primary creep of 9% Cr steels is complex in nature due to the synergistic effects of strengthening mechanisms arising from hierarchical boundaries accompanied with dense dislocation population, precipitates and solutes as well as recovery mechanisms. In view of these complexities, an attempt has been made to develop a constitutive model based on internal-variable, i.e., mean internal stress defined as the local internal stress acting against the dislocation motion. A constitutive framework based on sine hyperbolic creep rate relation associated with the concept of stress dependent activation volume and average dislocation segment length related to the Friedel statistics have been derived from the basic Orowan relationship. Following Estrin-Mecking approach, the evolution of mean internal stress from

initial to saturation value during creep deformation has been considered. The sine hyperbolic creep rate relation coupled with the evolution of internal stress as a function of strain provides a better understanding of primary and secondary creep behaviour of 9% Cr steels.

Following the development of primary creep model, its applicability has been demonstrated by comparing the predicted and experimental creep strain-time and creep rate-strain data in P9 steel tubeplate forging in quenched and tempered (Q+T) and simulated post weld heat treatment (SPWHT) conditions at 793 and 873 K. The difference in both the primary and secondary creep characteristics observed between Q+T and SPWHT conditions has been ascribed to the variations in rate constant associated with the model. The lower rate constant values obtained for SPWHT condition than for Q+T condition signifies the enhanced dynamic recovery effects in the additional heat treated SPWHT condition due to the presence of relatively coarse initial microstructure. At all test conditions, good agreement observed between predicted and experimental steady state creep rates demonstrated further applicability of the model. The predicted variations in activation volume at steady state with applied stress have been found to be in accordance with the experimentally reported observations in metals and alloys.

CHAPTER 5: Modelling Totality of Creep Deformation and Development of Damage in 9% Cr Tempered Martensitic Steels

For the assessment of the remaining life of components, it becomes necessary to model the development and damage during tertiary creep in addition to primary and secondary creep. In order to examine the totality of creep deformation, two different approaches have been employed. The first is based on the additive creep rate formulation where the developed sine hyperbolic creep rate formulation for primary creep has been added to tertiary creep rate as a function of tertiary creep strain obtained using MPC-Omega methodology with necessary modification. The applicability of this approach has been

demonstrated for P9 tubeplate steel in quenched and tempered condition for different applied stresses at 873 K.

In the second, the improved Semba-Dyson-McLean model has been used for the description of creep deformation and damage behaviour of 9% Cr steels. Though the developed additive creep rate model describes the creep behaviour accurately, the variable i.e., tertiary creep strain involved in the model cannot be considered as an internal-state-variable. Moreover, microstructural degradation in terms of coarsening of dislocation substructure accompanied with the decrease in dislocation density, coarsening of precipitates, conversion of MX precipitates into Z-phase particularly in the modified grades and depletion of solute Mo from the matrix with subsequent formation of Laves phase and its coarsening contribute dominantly during tertiary creep in 9% Cr steels. These observations suggest a need for internal-state-variables based model for the description of tertiary creep behaviour. In this context, improved Semba-Dyson-McLean model can be considered as a specific case of the internal-state-variables approach where the kinetic creep law has been coupled with differential relationships for various dominating microstructural damages. It is important to mention that the strain-induced subgrain coarsening, which usually occurs in 9-12 % Cr steels, has not been included in the original Dyson-McLean approach. Further, the applicability of the improved model has been demonstrated only for the prediction of single creep strain trajectories each at 773 K and 873 K and a single value of dislocation density at saturation irrespective of initial applied stresses and temperatures were used by Semba-Dyson-McLean. In view of this, two important modifications in terms of the procedure have been incorporated in the present analysis. The first has been related to applied stress dependence of dislocation density at saturation and the other deals with optimisation methodology. Applicability of improved Semba-Dyson-McLean approach has been shown for P9 steel in Q+T and SPWHT conditions for a wide range of stresses at 873 K. It has been

observed that influence of different heat treatments on creep characteristics is reflected in the optimised material constants associated with the model. In case of T91 steel at 873 K, Semba-Dyson-McLean model has been further modified to account for coarsening of $M_{23}C_6$ and conversion of useful MX precipitates into deleterious Z-phase in the long-term creep regime.

CHAPTER 6: Internal-stress Based Sine Hyperbolic Creep Rate Model for Stress-Relaxation Behaviour of 9% Cr Steels

Based on experimental observations in P91 steel, it has been shown that the subgrain coarsening remains dominant during deformation under stress-relaxation conditions at high temperatures. The variation in subgrain size with time during stress-relaxation in turn is related to the variations in obstacle spacing with time. These observations clearly indicate that the activation volume and internal stress vary with time or relaxation stress in 9% Cr steels. In general, the model proposed by Feltham based on dislocation-obstacle interaction has been widely used for describing the stress-relaxation behaviour of metals and alloys. It has been reported that the predicted relaxation stress vs. time data derived by Feltham model exhibit significant deviations from the experimental data particularly at longer durations. Further, the assumptions of constancy in activation volume and internal stress in Feltham model directly imply constancy in the obstacle or inter-barrier spacing. In view of above, the newly developed sine hyperbolic kinetic creep model accounting for the variations in activation volume and internal stress with time with suitable modification has been successfully used to describe the stress-relaxation behaviour of P91 steel. Good correlation has been shown between the predicted and experimental relaxation stress-time data for the steel. The observed increase in values of predicted activation volume and inter-barrier spacing with increase in hold time implies continual microstructural coarsening during stress-relaxation in P91 steel.

CHAPTER 7: General Conclusions and Future Directions

The final chapter of the thesis outlines the important findings in relation to the developed internal-state-variable models and their applicability towards tensile and creep deformation behaviour of 9% Cr steels. For further improvements and numerical implementation into finite element platform, a few recommendations have been suggested for future directions.

Contents

Synopsis	vii
List of Symbols	xix
List of Figures	xxvi
List of Tables	xxxiii
Chapter 1: Introduction	1
1.1 9% Chromium Containing Tempered Martensitic Steels and their Applications	1
1.2 Microstructural Features of Tempered Martensitic Steels	3
1.3 Influence of Temperature and Strain rate on the Tensile Properties of 9% Cr Steels	5
1.4 Creep Behaviour of 9% Cr Steels	9
1.4.1 Creep Deformation and Rupture Behaviour	9
1.4.2 Creep Ductility and Failure Behaviour	12
1.4.3 Creep Damage Tolerance Factor for 9% Cr Steels	14
1.4.4 Strengthening Mechanisms and Loss of Strength during Creep in 9% Cr Steels	16
1.5 Stress Relaxation Behaviour of 9% Cr Steels	20
1.6 Constitutive for the Inelastic Deformation Behaviour	22
1.6.1 Empirical Formulations	22
1.6.2 Internal-State-Variable Models	29
1.7 Motivation and Thesis Outline	35
1.8 Significance of the Performed Research	38
Chapter 2: Material, Initial Microstructure and Experimental Data for Modelling and Parametric Optimisation Methodology	39
2.1 Experimental Details Related to Modelling of Tensile Work Hardening Behaviour	39
2.2 Experimental Data Related to Modelling of Creep Behaviour	41
2.3 Initial Microstructure of Tempered Martensitic Steels Used for Modelling Tensile and Creep Behaviour	44
2.4 Experimental Data for Modelling of Stress-Relaxation Behaviour	49
2.5 ODE Parametric Optimisation Methodology and its Implementation	50
Chapter 3: Dislocation Density Based Model for the Description of Tensile Flow and Work Hardening Behaviour of 9% Cr Steels	57
3.1 Introduction	57
3.2 Modelling Framework and Numerical Implementation	60

3.3	Parametric Sensitivity Analysis	64
3.4	Influence of Temperature on Flow Behaviour of P9 Plate, P9 Tubeplate and P91 Steels	67
3.5	Variations in Work Hardening Parameters with Temperature for P9 Steel Plate and Tubeplate Forging, and P91 Steel	71
3.6	Applicability of Estrin-Mecking One-Internal-Variable Approach to 9% Cr Steels	77
3.7	Influence of Temperature and Initial Microstructure on Flow and Work hardening Behaviour of 9% Cr Steels	78
3.8	Revisiting Considère Necking Instability Criterion and the Predictability of the Model towards Tensile Properties of 9% Cr Steels	85
3.9	Conclusions	94
Chapter 4:	Constitutive Modelling of Primary and Steady State Creep Behaviour of 9% Cr Tempered Martensitic Steels	97
4.1	Introduction	97
4.2	Framework of the Proposed Sine Hyperbolic based Creep Rate Model	98
4.3	Numerical Implementation and Optimisation	102
4.4	Applicability of the Proposed Model	105
4.5	Conclusions	117
Chapter 5:	Modelling Totality of Creep Deformation and Development of Damage in 9% Cr Tempered Martensitic Steels	119
5.1	Introduction	119
5.2	Framework of Additive Creep Rate Formulation	120
5.2.1	Tertiary creep behaviour: MPC-Omega Methodology and its modification	120
5.2.2	Formulation for the totality of Creep Behaviour	123
5.3	Predictability of Additive Creep Rate Formulation	123
5.4	Microstructure Based Dyson-McLean Approach	132
5.5	Semba-Dyson-McLean Approach for P9 steel	136
5.6	Numerical Implementation of Semba-Dyson-McLean Model	139
5.7	Applicability of the Semba-Dyson-McLean model	143
5.8	Further Modification in Semba-Dyson-McLean Model for Simulating Long-Term Creep Behaviour of T91 Steel	148
5.9	Formulation for the Prediction of Long-term Creep Behaviour of T91 Steel	150
5.10	Material Constants Associated with the Developed Model	153
5.11	Applicability of the Modified Semba-Dyson-McLean Approach	156
5.12	Conclusions	161

Chapter 6:	Internal-Stress Based Sine Hyperbolic Creep Rate Model for Stress-Relaxation Behaviour of 9% Cr Steels	163
6.1	Introduction	163
6.2	Internal-Stress Based Model and its Numerical Implementation	165
6.3	Implications of the Internal-Stress Based Model	168
6.4	Conclusions	174
Chapter 7:	General Conclusions and Future Directions	177
7.1	Tensile Flow and Work Hardening Behaviour of 9% Cr Steels	177
7.2	Transient Creep Behaviour of 9% Cr Tempered Martensitic Steels	178
7.3	Totality of Creep Deformation and Development of Damage in 9% Cr Tempered Martensitic Steels	179
7.4	Stress-Relaxation Behaviour of 9% Cr Steels	181
7.5	Future Directions	182
References		185

List of Symbols

The following list provides that the list of symbols used in this thesis. The symbols are also explained in the text, appropriately.

$\dot{\varepsilon}_s$	Steady state creep rate
$\dot{\varepsilon}_{\min}$	Minimum creep rate
A and n	Norton's power law coefficient and exponent
σ_a	Applied stress at constant creep load tests
t_r	Creep rupture life
A' and n'	Power law coefficient and exponent
λ	Creep damage tolerance factor
ε_f	Creep strain to failure
$\dot{\varepsilon}$ or $\dot{\varepsilon}_{in}$	Inelastic strain rate
$\dot{\varepsilon}_{p+s}$	Primary plus secondary creep rate
$\dot{\varepsilon}_t$	Tertiary creep rate
ε_t	Tertiary creep strain
$\dot{\varepsilon}_e$	Elastic strain rate
ε	Inelastic strain
ε_u	Uniform plastic strain
σ_r	Relaxation stress
σ	True stress
K_H and n_H	Strain hardening coefficient and exponent associated with Hollomon relationship
σ_{0L}	Additional stress term in Ludwik relationship
K_L and n_L	Strain hardening coefficient and exponent associated with Ludwik relationship

ε_0	Pre-strain term in Swift relationship
K_S and n_S	Strain hardening coefficient and exponent associated with Swift relationship
K_1 and n_1	Strain hardening coefficient and exponent associated with Ludwigson relationship
K_2 and n_2	Additional constants in Ludwigson relationship
σ_1 and σ_s	Initial stress and saturation stress associated with the Voce relationship
n_V	Rate constant in Voce relationship
A_p	Strain hardening coefficient associated with strain and strain rate dependent power law relationship
n_p and m_p	Strain hardening and strain rate hardening exponents
A_1, A_2 and n_j	Constants related to strain hardening in Johnson-Cook model
B	Strain rate hardening in Johnson-Cook model
$\dot{\varepsilon}_{ref}$	Reference strain rate
T, T_0 and T_m	Working temperature, room temperature and melting temperature
LMP	Larson-Miller parameter
C_1	Constant associated with the Larson-Miller approach
α_A	Constant associated with the Andrade relationship
β_g	Amplitude of the transient creep strain
γ	Decay time
K_1	Constant associated with the Li-Akulov relationship
$\dot{\varepsilon}_i$	Initial creep rate
A_{KR} and n_{KR}	Power law coefficient and exponent in Kachanov-Robotnov model
ω	Empirical damage variable
B_{KR}, χ and ϕ	Material constants in Kachanov-Robotnov model

θ_1 and θ_3	Strain-like scaling parameters in theta-projection
θ_2 and θ_4	Strain rate-like parameters affecting the curvature of primary and tertiary creep in theta-projection
ρ	Dislocation density inside the lath
ρ_i	Initial dislocation density inside the lath
ρ_f	Forest dislocation density
ρ_m	Mobile dislocation density
ρ_{dip}	Dipole dislocation density
ρ_w	Dislocation density in subgrain wall
$\rho_{m, interior}$	Cell-interior mobile dislocation density
$\rho_{i, interior}$	Cell-interior immobile dislocation density
ρ_{sat}	Dislocation density at saturation in Estrin-Mecking model
ρ_c	Critical dislocation density at which necking instability sets-in
f_i and f_w	Volume fraction of cell interior and cell wall
θ	Instantaneous work hardening rate
σ_0	Flow stress contribution other than dislocations
σ_l	Initial flow stress
σ_d	Flow stress contribution from dislocations
σ_{sat}	Flow stress at saturation in Estrin-Mecking model
m	Strain rate sensitivity
M	Taylor factor
α	Constant
μ	Shear modulus

b	Burger's vector
L	Mean free path for dislocations
L_i and L_s	Initial and saturation mean free paths for dislocations
k_L	Rate constant associated with the evolution of mean free path
k_2	Dynamic recovery parameter
k_1 and k	Dislocation accumulation parameters
C_c and A_m	Constants associated with the Bergstorm and Hallen model
Q	Activation energy for self-diffusion
Q_c	Activation energy for cross slip mechanism
Q_m	Activation energy for vacancy diffusion
ψ	Constant in necking instability-criterion
σ_i	Internal stress
σ_e	Effective stress
σ_{es}	Effective stress at saturation
σ_{i0} and σ_{is}	Initial and saturation internal stresses
m_i and q	Constants in Shaker and El-Magd model
β_V	Dislocation velocity exponent
ε_0	Rate constant in Esposito and Bonora model
ΔV and \bar{V}	Activation volume and scaled activation volume
$\dot{\gamma}$	Shear strain rate
τ	Shear stress
τ_s	Shear stress at saturation

τ_i and τ_e	Internal and effective shear stresses
v	Average velocity of dislocation segments
ν_D	Debye frequency
l_s	Average segment length of the dislocation
A_s	Average area swept out by the dislocation segments
Γ_{net}	Net activation frequency
Γ_f and Γ_b	Forward and back ward activation frequencies
Δd	Activation distance
R	Gas constant
k	Boltzmann constant
Z	Pre-sine hyperbolic factor
Ω	Creep rate accelerating factor in MPC-Omega method
β and η	Tertiary creep constants associated with the additive creep rate law
$\dot{\epsilon}_0$	Characteristic strain rate
D_d	Damage parameter related to the kinetics of evolution of dislocation density
C_d	Rate constant for dislocation multiplication
ρ_t	Dislocation density at time t
D_s	Damage defining solute depletion
\bar{c}_t	Mean concentration of solute in the matrix at time t
c_0	Initial concentration of solute in the matrix
K_s	Rate constant associated with the solute depletion
H	Normalised kinematic back stress

h	Effective modulus
H_{\max}	Maximum attainable normalised kinematic back stress
$H_{\max,0}$	Initial value of H_{\max}
$\sigma_{i,\max}$	Maximum attainable kinematic back stress
σ_{Orowan}	Orowan stress
$\sigma_{0,N}$	Normalizing stress
$\sigma_{0,i}$	Initial normalizing stress
$\sigma_{or,i}$	Initial Orowan stress
D_p	Damage associated with the precipitate coarsening
K_p	Rate constant associated with the precipitate coarsening
d_i and d_t	Precipitate size at time $t = 0$ and at time t
D_C	Damage parameter associated with the cavitation
$A_{C,i}$ and $A_{C,t}$	Area fraction of cavitated boundary facets at $t = 0$ and at time t
ϕ_{sg}	Volume fraction of subgrain boundaries
d_{sg}	Subgrain size
k_{sg}	Constant associated with the variations in subgrain size
K_d	Rate constant associated with dislocation storage
r_0 and r_t	Outer and inner cut-off radii
N_i and N_t	Number density of precipitate at time $t = 0$ and at time t
D_N	Damage associated with the variation in number density of precipitate
$\chi_{0,i}$	Constant in modified Semba-Dyson-McLean model
$f^{M_{23}C_6}$	Volume fraction of $M_{23}C_6$ precipitate

k_f	Rate constant associated with the variations in number density of MX with time
t_{MX}	Time beyond which appreciable change in number density of MX
C_0	Constant in Orowan relationship
C_m	Effective modulus of the sample-machine system
h_r	Power law coefficient
m_r and k_r	Power law exponents

List of Figures

Figure 1.1	Schematic of the lath martensitic structure with hierarchical boundaries [12, 13].	4
Figure 1.2	Schematic of tempered lath martensitic hierarchical substructure with $M_{23}C_6$ and MX precipitates [15].	5
Figure 1.3	Variations in normalised yield strength with temperature for P92 steel with different strain rates [19].	6
Figure 1.4	Variations in normalised ultimate tensile strength with temperature for P92 steel with different strain rates [19].	6
Figure 1.5	Variations in elongation in fracture with temperature for P92 steel with different strain rates [19].	7
Figure 1.6	Variations in reduction in area with temperature for P92 steel with different strain rates [19].	8
Figure 1.7	SEM fractographs showing transgranular fracture in P92 steel tested at (a) 300 K, (b) 573 K and (c) 873 K for the strain rate of $1.26 \times 10^{-3} \text{ s}^{-1}$. The presence of chisel tip appearance along with dimples can be seen at 300 K in (a). At intermediate and high temperatures, the dominance of ductile dimples can be seen in (b) and (c) [19].	9
Figure 1.8	Variations in creep strain with time displaying three stages of creep behaviour in P9 steel [22].	10
Figure 1.9	Variations in secondary creep rate with applied stress for P9 steel exhibiting two-slope behaviour with high and low stress exponent values at high and low stress regimes, respectively [22].	10
Figure 1.10	Variations in rupture life (t_r) with applied stress (σ_a) for P9 steel exhibiting two-slope behaviour with high and low stress exponent values at high and low stress regimes, respectively [23].	11
Figure 1.11	Variations in reduction in area (RA) with rupture life (t_r) for P9 and P92 steels at 873 K [32].	12
Figure 1.12	SEM fractographs showing transgranular fracture in creep tested specimens of P9 steel tubeplate forging at 873 K. Typical cup and cone fracture in (a) and increase in the size of the dimples with decreasing stress and increasing rupture life can be seen in (b) 150 MPa for 12 h, (c) 100 MPa for 412 h and (d) 60 MPa for 12575 h [22, 32].	13
Figure 1.13	SEM fractographs showing (a) transgranular fracture in P92 steel tested at 132 MPa for 57,421 h, (b) Secondary cracks are shown by arrows and (c) formation of creep cavities (shown by arrows) due to decohesion at Fe2(W, Mo)-boundary interface [32].	14

- Figure 1.14** Average creep rate ($\frac{\epsilon_f}{t_r}$) vs. secondary creep rate ($\dot{\epsilon}_s$) showing a constant value of creep damage tolerance factor $\lambda = 5$ for T91 steel at three different temperatures [24]. 15
- Figure 1.15** Change of dislocation structure during creep at 873 K for the stress level of 70 MPa. (a) As received (b) 9992 h, (c) 30030 h, (d) 50064 h, (e) 70000 h and (f) 80736.8 h [45]. 19
- Figure 1.16** Precipitates distributions based on the results of elemental maps of Cr, V and Nb. (a) As received (b) 9992 h, (c) 30030 h, (d) 50064 h, (e) 70000 h and (f) 80736.8 h { Red: $M_{23}C_6$, blue: V-rich MX, green: Nb-rich MX, white: Z-phase} [45]. 19
- Figure 1.17** Variations in relaxation stress (σ_r) with hold time (t) [55]. 20
- Figure 1.18** Variations in strain rate ($\dot{\epsilon}$) with relaxation stress (σ_r) [55]. 21
- Figure 1.19** TEM microstructure of P91 steel (a) as received and (b) after stress relaxation testing at 873 K for 20 h [57]. 21
- Figure 1.20** Variations in experimental true stress with true plastic strain for P9 steel at 300 K. The fitted curves related to the different flow relationships are superimposed. 25
- Figure 1.21** Schematic representation of rupture life vs. $1/T$ plot for the estimation of slope i.e. LMP and intercept ($-C_1$) value for Larson-Miller parametric approach. Here, $\sigma_1 > \sigma_2 > \sigma_3$. 26
- Figure 1.22** Variations in applied stress (σ_a) vs. Larson-Miller parameter (LMP) at 793 and 873 K for P9 steel. The average creep-rupture strength values obtained using optimised material constant $C_1 = 26$ for P9 steel have been superimposed [70]. 26
- Figure 1.23** Variations in experimental and predicted creep strain-time data shows the applicability of the θ -projection model towards 9% Cr steels [79]. 28
- Figure 2.1** Microstructure of normalized and tempered plate material of P9 steel showing (a) tempered lath martensite and (b) precipitates on grain and lath boundaries and in the matrix region. Presence of $M_{23}C_6$ carbides and Cr_2N precipitates are shown by arrows in (c). 46
- Figure 2.2** Microstructure of thick section tube plate forging of P9 steel showing (a) tempered lath martensite and pro-eutectoid ferrite as stringers at prior austenite grain boundaries and (b) coarse precipitates on grain and lath boundaries and in the matrix region. Presence of $M_{23}C_6$ carbides and Cr_2N precipitate in tempered lath martensite is shown in (c). 47
- Figure 2.3** Microstructure of 9Cr–1Mo steel tube plate forging in SPWHT condition showing tempered lath martensite and precipitates at the boundaries and in the matrix region. 48

Figure 2.4	SEM micrograph showing tempered lath martensite and fine precipitates on the grain and lath boundaries and in the matrix region in normalized and tempered P91 steel.	48
Figure 2.5	Microstructure of P91 steel in normalised and tempered condition.	50
Figure 2.6	Schematic flow diagram describing the numerical algorithm for optimisation of Parameters/material constants associated with the internal-state-variable approaches.	51
Figure 3.1	Schematic illustration of variations of instantaneous work hardening rate (θ) vs. normalised shear stress (τ/τ_s) exhibiting different stages of work hardening in single crystals deformed in single slip and polyslip. However, work hardening stages in polyslip can also be considered as a representative plot for deformation in polycrystalline materials. I, II, III, IV refer to the short form of stage-I, stage-II, stage-III and stage-IV, respectively and TS refers transient stage.	58
Figure 3.2	Typical example for the variations in $\theta\sigma_d$ with σ_d and θ with σ for P91 steel at 300 K depicts the dominance of stage-III work hardening in tempered martensitic steels. Note that stage-II work hardening behaviour does not appear either in $\theta\sigma_d$ vs. σ_d or in θ with σ plots.	60
Figure 3.3	Variations in least-square error with dislocation accumulation parameter (k_1) at 300, 598 and 773 K for P9 steel tubeplate forging and plate, and P91 steel.	64
Figure 3.4	Variations in least-square error with hardening parameter (k) at 300, 598 and 773 K for P9 steel tubeplate forging and plate, and P91 steel.	66
Figure 3.5	Influence of temperature on true stress (σ)-true plastic strain (ϵ) behaviour of thick section tubeplate forging of P9 steel.	68
Figure 3.6	Averaging scheme for load-elongation curves showing type A, A+B and C serrations at intermediate temperatures in P9 steel tubeplate forging. Average load-elongation values considered for evaluating true stress-true plastic strain are shown by broken lines.	69
Figure 3.7	True stress (σ)-true plastic strain (ϵ) data of P9 steel plate and tubeplate forging and P91 steel at (a) 300 K, (b) 623 K and (c) 773 K. Respective best fit data predicted by Estrin-Mecking approach are superimposed as full lines.	70
Figure 3.8	Variations of shear modulus compensated (a) initial stress (σ_I/μ) and (b) σ_0/μ with temperature for P9 steel plate and tubeplate forging and P91 steel.	72
Figure 3.9	Variations of hardening parameter (k) with temperature for P9 steel plate and tubeplate forging and P91 steel.	72
Figure 3.10	Variations of recovery parameter (k_2) with temperature for P9 steel plate and tubeplate forging and P91 steel.	73

Figure 3.11	Variations of dislocation density at saturation (ρ_{sat}) with temperature for P9 steel plate and tubeplate forging and P91 steel.	75
Figure 3.12	Variations of normalized saturation stress (σ_{sat}/μ) with temperature for P9 steel plate and tubeplate forging and P91 steel.	76
Figure 3.13	Evolution of dislocation density (ρ) with true plastic strain (ϵ) at different temperatures for P9 steel tubeplate forging.	80
Figure 3.14	Evolution of dislocation density (ρ) with true plastic strain (ϵ) at (a) 300 K, (b) 623 K and (c) 773 K for P9 steel plate and tubeplate forging and P91 steel.	81
Figure 3.15	Variations of the ratio of saturation dislocation density (ρ_{sat}) and initial dislocation density (ρ_i) with temperature for P9 steel plate and tubeplate forging and P91 steel.	85
Figure 3.16	Schematic representation of the variations in instantaneous work hardening rate evaluated by $\theta = d\sigma/d\epsilon$ and $\theta_d = d\sigma_d/d\epsilon$ as well as the different stress values with the plastic strain (ϵ). Considered instability criterion has been marked as $d\sigma/d\epsilon = \sigma$.	87
Figure 3.17	Variations in the values of scaling factor (ψ) with temperature for 9% Cr steels.	88
Figure 3.18	Variations in (a) $\sqrt{\rho_c/\rho_i}$ and (b) true uniform plastic strain (ϵ_u) with temperature for P9 plate and tubeplate forging and P91 steel.	90
Figure 3.19	Comparison between experimental ($\epsilon_{u, Exp}$) and predicted ($\epsilon_{u, Pred}$) true uniform plastic strain values for P9 and P91 steels showing $\epsilon_{u, Pred} = \epsilon_{u, Exp}$ for different temperatures in the range 300-873 K.	91
Figure 3.20	Comparison between experimental ($\epsilon_{u, Exp}$) and predicted ($\epsilon_{u, Pred}$) true uniform plastic strain values using the simplified formulation for P9 and P91 steels at different test temperatures.	92
Figure 3.21	Variations of (a) predicted initial stress (σ_I) with experimental true yield stress ($\sigma_{Exp,YS}$) and (b) predicted ultimate tensile strength ($\sigma_{Pre,UTS}$) with experimental true ultimate tensile strength ($\sigma_{Exp,UTS}$) for P9 steel plate and tubeplate forging and P91 steel over temperatures ranging from 300 to 873 K. Theoretical $\sigma_I = \sigma_{Exo,YS}$ and $\sigma_{Pre,UTS} = \sigma_{Exp,UTS}$ are superimposed as full lines.	93
Figure 4.1	Creep strain-time data of P9 steel in Q+T and SPWHT conditions for (a) 60 MPa and (b) 100 MPa at 873 K.	102
Figure 4.2	Schematic flow diagram for optimisation of parameters associated with the developed sine hyperbolic creep rate model.	103
Figure 4.3	Experimental and predicted creep strain-time data in Q+T and SPWHT conditions for (a) 60 and (b) 100 MPa at 873 K and (c) 225 MPa at 793 K.	106

Figure 4.4	Experimental and predicted (a) creep rate-creep strain and (b) creep rate-time data for P9 steel in SPWHT condition for different applied stresses at 873 K.	107
Figure 4.5	Variations in the deviation of strain values as $\Delta\varepsilon = \varepsilon_{\text{exp}} - \varepsilon_{\text{pred}}$ with time for P9 steel in SPWHT condition at 873 K for the stress level of 50 MPa.	108
Figure 4.6	Variations of normalised initial internal stress with normalised applied stress at 793 and 873 K for Q+T and SPWHT conditions.	108
Figure 4.7	Variations of normalised internal stress at saturation with normalised applied stress at 793 and 873 K for Q+T and SPWHT conditions.	109
Figure 4.8	Variations in the ratio of (a) σ_{i0}/σ_a and (b) σ_{is}/σ_a with normalised applied stress at 793 and 873 K for Q+T and SPWHT conditions.	111
Figure 4.9	A representative plot of the evolution of internal stress and effective stress with time for 80 MPa at 873 K in Q+T condition.	111
Figure 4.10	Predicted vs. experimental steady state creep rate at 793 and 873 K for Q+T and SPWHT conditions.	113
Figure 4.11	Evolution of internal stress with strain for (a) high stresses at 793 K and (b) low stresses at 873 K in SPWHT condition.	114
Figure 4.12	Predicted vs. experimental steady state creep rate for Q+T and SPWHT conditions at 793 and 873 K. The prediction is based on the approximation in internal stress as $0.98\sigma_{is}$ at steady state strain.	115
Figure 4.13	Predicted steady state creep rate with effective stress obeying power law function for Q+T and SPWHT conditions at 793 and 873 K.	116
Figure 4.14	Variations in pre sine hyperbolic factor, parameter Z with normalised applied stress at 793 and 873 K.	117
Figure 4.15	Variations in predicted activation volume with the normalised applied stress at 793 and 873 K.	117
Figure 5.1	Typical creep rate ($\dot{\varepsilon}$) - creep strain (ε) data for 9% chromium containing steels at high temperatures.	121
Figure 5.2	Theoretical plots depicting the influence of tertiary fitting constants (a) β with $\eta = 0.5$ or Ω with $\eta = 1$ and (b) η with $\beta = 25$ on the ratio between tertiary creep rate with steady state creep rate	122
Figure 5.3	Experimental creep strain (ε) - time (t) data for P9 steel tubeplate forging at 873 K for 60 MPa. The respective best-fit data obtained for Model-A and Model-B are superimposed as broken and full lines, respectively.	124
Figure 5.4	Experimental creep strain ($\dot{\varepsilon}$) - time (ε) data for P9 steel tubeplate forging at 873 K for 60 MPa. The respective best-fit data obtained for Model-A and Model-B are superimposed as broken and full lines, respectively.	124

Figure 5.5	The predicted variations in primary plus secondary and tertiary strain contributions with time for Model-A and Model-B are depicted as broken and full lines, respectively.	125
Figure 5.6	Experimental creep rate ($\dot{\epsilon}$) - creep strain (ϵ) for P9 steel tubeplate forging at 873 K for different stress levels. The best-fit data of Model-B are superimposed as solid lines for different stresses.	126
Figure 5.7	The variations in tertiary fitting constants such as β and η with applied stress for 9Cr-1Mo steel tubeplate forging at 873 K.	127
Figure 5.8	The variations in $\beta\epsilon_{tr}^n$ with life fraction for P9 steel tubeplate forging at 873 K for different stress levels.	128
Figure 5.9	Experimental (a) creep stain (ϵ) vs. time (t) and (b) creep rate ($\dot{\epsilon}$) vs. strain (t) for 9Cr-1Mo steel with different conditions of tubeplate forging in quenched and tempered (Q+T), tubeplate forging in simulated post-weld heat treatment (SPWHT) and plate material in normalized and tempered (N+T) at 873 K for 60 MPa. The best-fit creep data predicted using Model-B are superimposed as full lines.	129
Figure 5.10	Variations in $\beta\epsilon_{tr}^n$ with life fraction (t/t_r) for P9 steel with different conditions of tubeplate forging in quenched and tempered (Q+T), tubeplate forging in simulated post-weld heat treatment (SPWHT) and plate material in normalized and tempered (N+T) at 873 K for 60 MPa.	131
Figure 5.11	Comparison between experimental ($t_{r,exp}$) and predicted ($t_{r,pre}$) rupture lives for P9 steel in different conditions. $t_{r,exp} = t_{r,pre}$ relation is shown by full line.	131
Figure 5.12	Schematic flow diagram describing numerical algorithm for optimisation of material constants associated with the Semba-Dyson-McLean model [108].	142
Figure 5.13	Representative plots describing the evolution of strain dependent (normalised kinematic back stress (H), normalised maximum attainable kinematic back stress (H_{max}) and damage associated with dislocation density (D_d)) and time dependent damage arising from precipitate coarsening (D_p) and solute depletion (D_s) during creep deformation for Q+T condition at 60 MPa.	142
Figure 5.14	Experimental and predicted creep strain-time data for P9 steel in (a) Q+T and (b) SPWHT conditions for different stress levels at 873 K.	145
Figure 5.15	Experimental and predicted creep rate-time data for P9 steel in (a) Q+T and (b) SPWHT conditions for different stress levels at 873 K.	146
Figure 5.16	Comparison between experimental and predicted steady state creep rates at 873 K for P9 steel in Q+T and SPWHT conditions.	147
Figure 5.17	Comparison between experimental and predicted time to reach specified strain levels at 873 K for P9 steel in (a) Q+T and (b) SPWHT conditions.	147

- Figure 5.18** Variations of (a) dislocation density with strain fitted by the integral form of Kocks-Mecking-Estrin relationship given in Equation (5.29) and (b) normalised number density of MX with time described by exponential function i.e. Equation (5.40). Experimental data are extracted from the Ref. [45]. 154
- Figure 5.19** Comparison between predicted and experimental (a) creep strain-time and (b) creep rate-time data for different stress levels at 873 K. Experimental data are extracted from the Refs. [26, 45, 192]. 157
- Figure 5.20** Comparison of predicted and experimental data for (a) minimum creep rate vs. applied stress and (b) applied stress vs. rupture life at 873 K for T91 steel. Experimental data are extracted from the Refs. [26, 45, 192]. 158
- Figure 5.21** The variations in predicted minimum creep rate with the applied stress at 873 K for T91 steel. Experimental data obtained for very low stress levels depicting diffusion creep regime [200] are superimposed. 159
- Figure 5.22** Comparison between predicted and experimental creep rate-time data for 80 MPa at 873 K for MGA and MGC heats of T91 steel containing 0.12 and 0.28% Ni [192], respectively. Dash and Dash-dotted lines represent predicted creep curves with the constant number density of MX precipitate and a significant decrease in the number density of MX precipitate, respectively. 159
- Figure 5.23** Comparison between predicted and extrapolated creep-rupture strength values for 10^5 h for the three heats MGA, MGB and MGC containing 0.12, 0.20 and 0.28% Ni [192], respectively. 160
- Figure 6.1** Variations of relaxation stress (σ_r) with hold time (t) for two different strain holds of 1.3 and 2.5% for P91 steel at 873 K. The best-fit σ_r -t is shown by solid lines for both the strain holds. 169
- Figure 6.2** Variations of relaxation stress (σ_r) with hold time (t) for two different strain holds of 1.3 and 2.5% for P91 steel at 873 K. The best-fit σ_r -t is shown by solid lines for both the strain holds. 169
- Figure 6.3** Variations of minimum creep rate ($\dot{\epsilon}_{min}$) with applied stress (σ_a) for P91 steel at 873 K. The prediction based on sine hyperbolic model is given by solid line. 170
- Figure 6.4** Variations in relaxation stress (σ_r), internal stress (σ_i) and effective stress (σ_e) with hold time (t) for two different strain holds of 1.3 and 2.5% for P91 steel at 873 K. 171
- Figure 6.5** Variations of predicted mean free path (L) with hold time (t) for two different strain holds of 1.3 and 2.5% for P91 steel at 873 K. 172
- Figure 6.6** Variations of activation volume (ΔV)/ b^3 with (a) hold time (t) and (b) effective stress (σ_e) for two different strain holds of 1.3 and 2.5% for P91 steel at 873 K. 172
- Figure 6.7** Variations of pre-sinh factor (Z) with relaxation stress (σ_r) for two different strain holds of 1.3 and 2.5% for P91 steel at 873 K. 173

List of Tables

Table 1.1-	Chemical composition of 9% chromium containing steels according to EN10216-2 [5] and 10^5 creep rupture strength for a given service temperature.	2
Table 2.1-	Chemical composition (Wt. %) of P9 plate and tubeplate forging and P91 steels.	39
Table 2.2-	Details of product form and heat treatment conditions employed for tensile tests in 9% Cr steels.	40
Table 2.3-	Details of product form, heat treatment and creep tested conditions of 9% Cr steels employed for creep constitutive modelling.	43
Table 2.4-	The Weight Percent of Different Precipitates Calculated using Thermo-Calc Software TCFE6 Steels/Fe-alloys Database [112] in P9 steel Plate and Tubeplate Forging and P91 steel. The Respective Volume Fractions of the Precipitates are given in Brackets.	45
Table 3.1-	The Calculated Values of Constants and Activation Energy for Dynamic Recovery Model Proposed by Hallén and Bergström [117, 118].	75
Table 4.1-	Material constants used for the prediction of primary and secondary creep strain-time data.	105
Table 5.1-	The optimised parameters associated with the model for depicting creep data of P9 steel for 60 MPa at 873 K.	130
Table 5.2-	Material constants associated with improved Dyson-McLean model.	140
Table 5.3-	Approximate or equivalent guiding values* reported in the literature [100, 108, 183-188] for fixing the lower and upper bounds for the optimisation.	141
Table 5.4-	Optimised values of material constants for P9 steel in Q+T and SPWHT conditions.	143
Table 5.5-	Material constants with fixed values for numerical integration.	154
Table 5.6-	Values of optimised material constants obtained for T91 steel in the framework of the modified Semba-Dyson-McLean approach.	155
Table 6.1-	Optimised material constants for two different strain holds at 1.3 and 2.5% at 873 K.	167

Chapter 1: Introduction

1.1 9% Chromium Containing Tempered Martensitic Steels and their Applications

Creep resistant steels that can be used for long durations at elevated temperatures are essential for the construction of power plants, and chemical and petroleum industries. Among the creep resistant steels, 9Cr-1Mo (P9) tempered martensitic steel and its modified version such as 9Cr-1Mo-V-Nb (P91) are favoured structural materials for steam generator applications in power plants. Modified version, P91 steel is developed by adding strong carbide/nitride forming elements such as vanadium and niobium along with the controlled addition of nitrogen in P9 steel. In general, P91 steel exhibits significantly higher tensile and creep strengths than P9 steel. The choice of 9% chromium containing steels for steam generator applications is mainly due to its better high temperature mechanical properties compared to the alternative 2.25Cr-1Mo steel in addition to low thermal expansion coefficient and high resistance to stress corrosion cracking in water-steam systems compared to austenitic stainless steels [1]. Progress in recent years has led to further improvement in P91 steel in order to achieve better creep strength and weld characteristics at elevated temperatures by modifying its chemical composition [2, 3]. It was reported that an increase in aluminium content from 0.0015 to 0.017 wt. % or a decrease in the ratio of nitrogen to aluminium (N:Al) from 7.2 to 2.8 resulted in the increasing volume fraction of aluminium nitrides, in place of the beneficial carbonitrides. Therefore, it was recommended to have a high N:Al ratio in P91 steel for achieving better creep resistance and improved type-IV crack resistance of the weldments [2]. It was well established that the controlled addition of boron to 9% Cr steels improves type-IV cracking resistance of weldments by suppressing the fine grain microstructure in the heat affected zone and thereby reducing the mechanical constraint [3]. The continual improvement in thermal efficiency by increasing the operating temperature and pressure of the boilers in the next generation of coal-fired ultra-supercritical (USC) and

advanced USC power plants resulted in the development of commercially available new 9% Cr steels such as 9Cr-1Mo-1W-V-Nb (E911), and 9Cr-0.5Mo-1.8W-V-Nb (P92). Both E911 and P92 steels exhibit higher creep rupture strength compared to P91 steel [4]. The chemical composition (wt.%) of 9% Cr tempered martensitic steels [5] along with 10^5 h creep rupture strength [6] for a given service temperature are presented in Table 1.1.

Table 1.1- Chemical composition of 9% chromium containing steels according to EN10216-2 [5] and 10^5 h creep rupture strength for a given service temperature.

Chemical composition (wt.%)	P9	P91	E911	P92
C	Max. 0.15	0.08 - 0.12	0.09 - 0.13	0.07 - 0.13
Si	0.25 - 1.00	0.20 - 0.50	0.10 - 0.50	Max. 0.50
Mn	0.30 - 0.60	0.30 - 0.60	0.30 - 0.60	0.30 - 0.60
P	Max. 0.025	Max. 0.02	Max. 0.02	Max. 0.02
S	Max. 0.02	Max. 0.01	Max. 0.01	Max. 0.01
Al	Max. 0.04	Max. 0.04	Max. 0.04	Max. 0.04
Cr	8.00 - 10.00	8.00 - 9.50	8.50 - 9.50	8.50 - 9.50
Ni	-	Max. 0.04	0.10 - 0.40	Max. 0.04
Mo	0.90 - 1.10	0.85 - 1.05	0.90 - 1.10	0.30 - 0.60
W	-	-	0.90 - 1.10	1.50 - 2.00
V	-	0.18 - 0.25	0.18 - 0.25	0.15 - 0.25
Nb	-	0.06 - 0.10	0.06 - 0.10	0.04 - 0.09
B	-	-*	0.0005 - 0.005	0.001 - 0.006
N	-	0.03 - 0.07	0.05 - 0.09	0.03 - 0.07
Cu	Max. 0.30	Max. 0.30	-	-
T_{service} , K	823	873	873	873
$\sigma_{10^5/T_{\text{service}}}$, MPa [6]	92	94	98	113

*In boron added P91 steel, wt. % of B is in the range of 0.009 to 0.013 [3].

Tempered martensitic P9 and P91 steels have also emerged as favoured candidate materials for in-core (wrapper and fuel clad) applications in the fuel subassemblies for future fast reactors. Hexagonal wrapper tubes in fast reactors are designed to operate in the temperature range 673–873 K under high neutron flux of $\sim 10^{15}$ neutrons $\text{cm}^{-2}\text{s}^{-1}$ [1, 7, 8]. Austenitic stainless steel presently used for wrapper tubes suffers significant dimensional changes in terms of bowing of fuel subassemblies due to differential void swelling

originating from the uneven distribution of neutron flux and temperature in the reactor core [7]. These dimensional changes result in severe fuel handling problems, thereby restricting the fuel burn-up. In order to achieve high fuel burn-up (~200 GWd/t) for economical nuclear energy, tempered martensitic steels with inherent void swelling resistance are under active consideration for wrapper applications [7]. However, irradiation induced degradation in fracture properties in terms of increase in ductile to brittle transition temperature (DBTT) and decrease in upper shelf energy are a matter of major concern for tempered martensitic/ferritic steels. It is known that the presence of trace elements affects the fracture properties adversely, and DBTT increases rapidly with increase in sulphur and phosphorous contents in tempered martensitic/ferritic steels [9,10]. Among the various grades of tempered martensitic/ferritic steels, P9 steel with close control over sulphur and phosphorous content exhibits the modest increase in DBTT with irradiation compared to its stabilised grade counterparts [1]. In view of this, P9 steel is being considered for hexagonal wrapper tubes for future fast reactors. For in-core clad applications, P91 steel has been chosen as a candidate material due to its superior creep strength than P9 steel in addition to its higher swelling resistance. Tempered martensitic 9% Cr steels with suitable compositional modifications are under consideration for blanket module of fusion reactors. The chemical composition of conventional P91 steel has been tailored by substituting the elements having long half-life transmutants like Mo, Nb, Ni, Cu, Co, Al, and N with comparatively lower activation counterparts such as W, Ta, Mn, V, and C to develop Low Activation Ferritic–Martensitic steels [11]. These modifications improve the handling and disposal issues of fusion reactor structural components.

1.2 Microstructural Features of Tempered Martensitic 9% Cr Steels

In normalised and tempered condition, the microstructure of 9% Cr steels consists of hierarchical boundaries which are formed during normalizing treatment by the transformation

of parent austenite to lath martensitic structure. The typical lath martensitic structure with different hierarchical boundaries is shown in Figure 1.1. The small lath-like crystals are

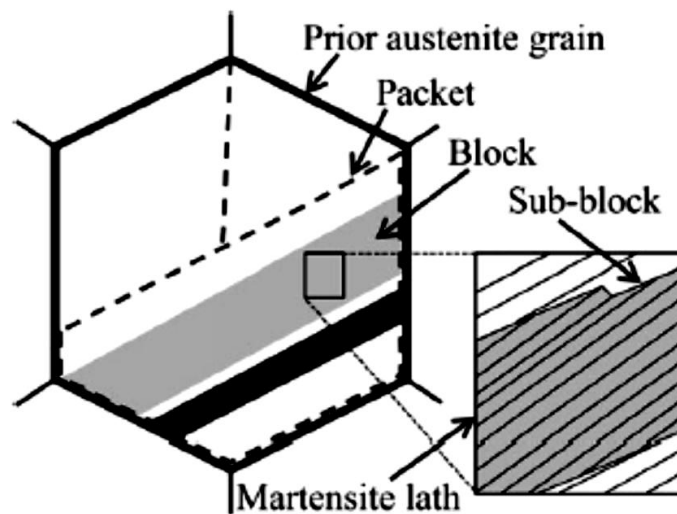


Figure 1.1 Schematic of the lath martensitic structure with hierarchical boundaries [12, 13].

known as the basic unit for the development of hierarchical substructure in 9% Cr steels. The flat boundary i.e. habit plane of lath is nearly parallel to the closed packed planes of both martensite (α') and austenite (γ) crystals. The prior austenite grain is subdivided by lath groups with similar habit planes, referred to as packets. These packets are further subdivided by lath groups with similar crystal orientations, referred to as blocks. A block contains sub-blocks, which are lath groups of the same orientation relationship variant with austenite. The works of Morito et al. [12, 13] and Kitahara et al. [14] introduced the crystallographic hierarchy of lath martensite based on the orientation relationship between martensite and parent prior austenite. The crystallographic orientation relationships are derived as $\{110\}\alpha' // \{111\}\gamma$ and $\langle 111\rangle\alpha' // \langle 110\rangle\gamma$. The 24 possible variants are grouped into four packets, including six variants sharing the same $\{110\}$ habit plane, and are further subdivided into blocks separated by high-angle boundaries, sub-blocks and low-misoriented laths. The shear deformation involved in martensitic transformation causes a severely dislocated lath structure, which is initially supersaturated with interstitial carbon. Relaxation processes occur

during tempering which results in the precipitation of $M_{23}C_6$ ($M = Cr, Fe$) carbides and MX ($M = Cr, Fe$ and $X = V, N$) carbonitrides along with a decrease in dislocation density as compared to as-quenched lath martensitic microstructure. Figure 1.2 schematically depicts the tempered lath martensitic microstructure.

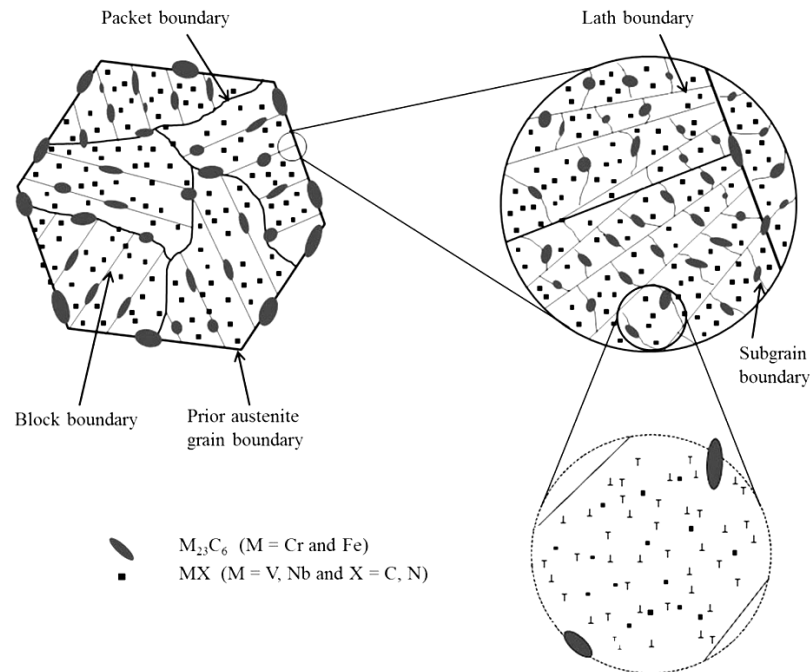


Figure 1.2 Schematic of tempered lath martensitic hierarchical microstructures with $M_{23}C_6$ and MX precipitates [15].

1.3 Influence of Temperature and Strain rate on the Tensile Properties of 9% Cr Steels

Evaluation of elevated temperature tensile properties is a preliminary step toward characterisation of the materials' performance for high temperature applications. In view of above, detail investigations related to the influence of strain rate and temperature on tensile properties of various grades of 9% Cr steels had been reported elsewhere [16-21]. For all the 9% Cr steels, the reported variations in modulus compensated yield and ultimate tensile strengths with temperature and strain rate exhibited three distinct temperature regimes. This is shown in Figure 1.3 and Figure 1.4 for P92 steel as an example [19]. At all the strain rates,

the variations in strength values with temperature displayed a gradual decrease with increasing temperature from 300 to 473 K in Regime-I followed by distinct plateaus/peaks at

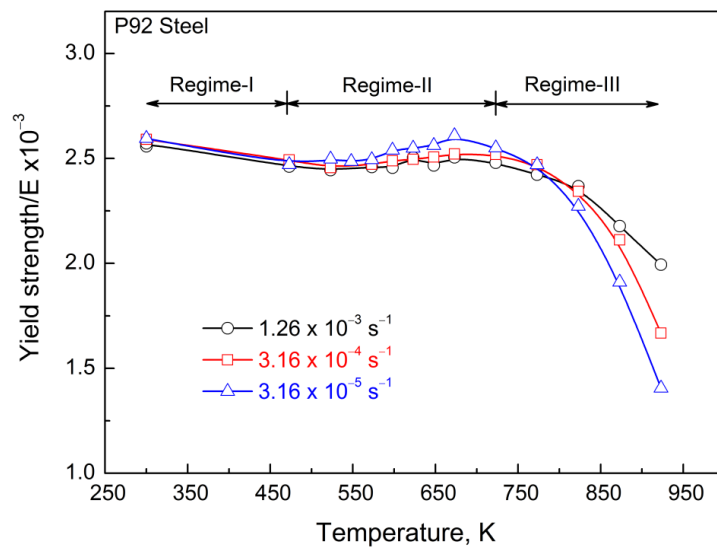


Figure 1.3 Variations in modulus compensated yield strength with temperature for P92 steel with different strain rates [19].

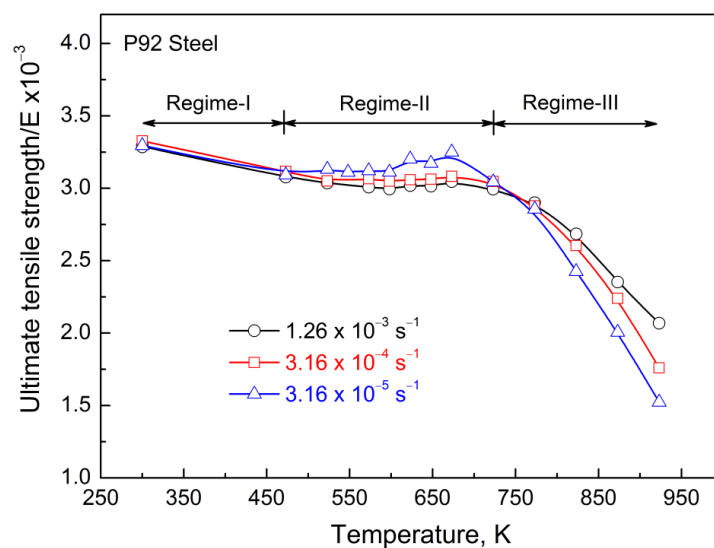


Figure 1.4 Variations in modulus compensated ultimate tensile strength with temperature for P92 steel with different strain rates [19].

intermediate temperatures in Regime-II and a rapid decrease at high temperatures in Regime-III. The influence of negative strain rate sensitivity is displayed as the increase in both the yield and ultimate tensile strength values with decrease in strain rate at intermediate temperatures. In Regime-III, at high temperatures, the strength values decreased rapidly with

an increase in temperature and decrease in strain rate. Similar to strength values, the reported variations in ductility in terms of elongation to fracture and reduction in area exhibited three distinct temperature regimes for various grades of 9% Cr steels. Figure 1.5 and Figure 1.6 typically depict the variations in elongation to fracture and reduction in area with temperature, respectively for P92 steel. At all the strain rates, elongation to fracture exhibited three distinct temperature regimes as a rapid decrease in values from 300 to 473 K followed by ductility minima at intermediate temperatures and an increase at high temperatures (Figure 1.5). The variations in reduction in area with temperature displayed a marginal influence with an increase in temperature from 300 K to 473 K followed by a decrease in the values to a minimum at intermediate temperatures and a rapid increase at high temperatures (Figure 1.6). At high temperatures, reduction in area exhibited a systematic increase with decreasing strain rate. The temperature for the occurrence of minimum in reduction in area decreased with decreased in strain rate. In common, 9% Cr steels generally exhibit serrated flow, one of the most important manifestations of dynamic strain aging (DSA) at intermediate temperatures in the range of 523 to 673 K. It has been suggested that the locking of mobile dislocations by

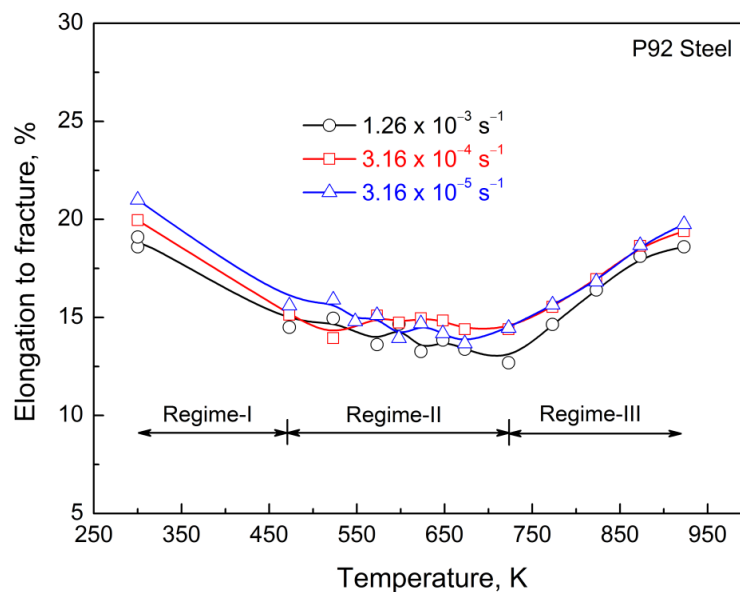


Figure 1.5 Variations in elongation in fracture with temperature for P92 steel with different strain rates [19].

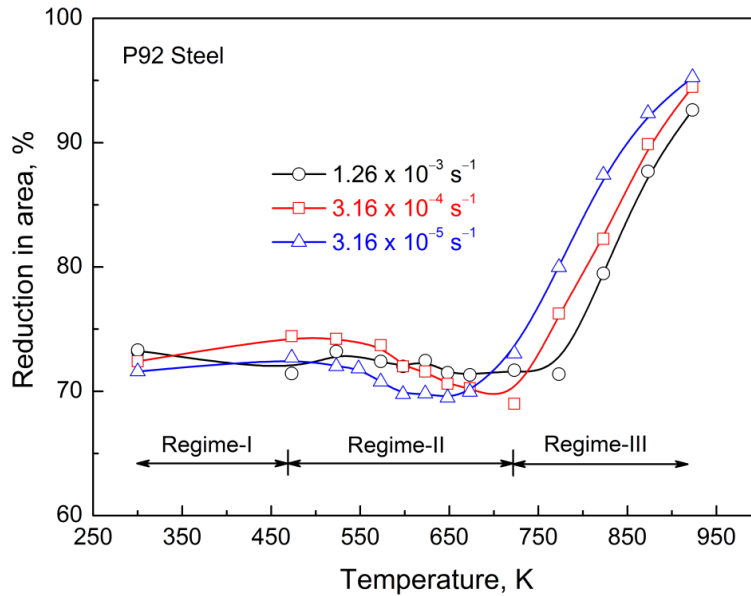


Figure 1.6 Variations in reduction in area with temperature for P92 steel with different strain rates [19].

diffusing interstitial atoms such as carbon to be the source of serrations in 9% Cr steels [16, 18, 20, 21]. The other manifestations of dynamic strain aging have been demonstrated in terms of the occurrence of plateaus/peaks in the modulus compensated yield and ultimate tensile strength, and average work hardening rate and ductility minima at intermediate temperatures in these steels. Scanning electron microscopic studies on the tensile fracture surface revealed that the fracture mode remains transgranular ductile for 9%Cr steels as shown in Figure 1.7. It has been reported that the fracture mode was characterised by dimples resulting from coalescence of microvoids at all the temperatures and strain rates. The large amount of chisel tip appearance resulting from decohesion and split in the martensite lath boundaries along with ductile dimples was observed at 300 K for 9% Cr steels as shown in Figure 1.7 (a). With increase in temperature, significant reduction in the regions having chisel tip appearance was noticed and the fracture was mainly dominated by the presence of equiaxed dimples (Figure 1.7 (b) and (c)). The size of equiaxed dimples increases with increase in temperature, indicating dominance of growth process at high temperatures as shown for 873 K in Figure 1.7 (c).

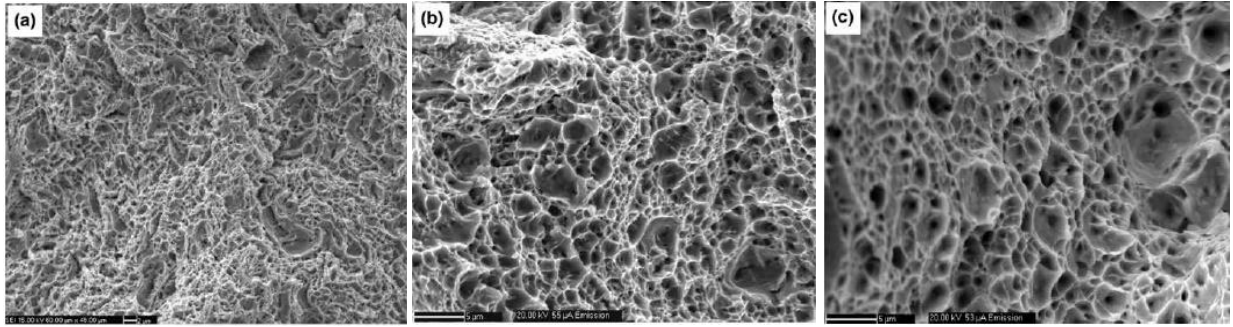


Figure 1.7 SEM fractographs showing transgranular fracture in P92 steel tested at (a) 300 K, (b) 573 K and (c) 873 K for the strain rate of $1.26 \times 10^{-3} \text{ s}^{-1}$. The presence of chisel tip appearance along with dimples can be seen at 300 K in (a). At intermediate and high temperatures, the dominance of ductile dimples can be seen in (b) and (c) [19].

1.4 Creep Behaviour of 9% Cr Steels

1.4.1 Creep Deformation and Rupture Behaviour

The creep deformation of 9% Cr steels has been characterised by negligibly small instantaneous or loading strain followed by well-defined primary, secondary and tertiary creep as shown in Figure 1.8. The secondary creep has been identified by a constant creep rate for a significant duration i.e. steady state creep ($\dot{\epsilon}_s$) in P9 steel [22]. For other grades, the secondary creep rate is characterised as minimum creep rate ($\dot{\epsilon}_{\min}$). The occurrence of minimum creep rate results from a balance between hardening and recovery/damage processes dominant in the transient and tertiary creep regimes, respectively. In common, the stress dependence of secondary creep rate obeyed power law relationship in 9% Cr steels and the relationship is expressed as

$$\dot{\epsilon}_s \text{ or } \dot{\epsilon}_{\min} = A\sigma_a^n, \quad \text{Equation (1.1)}$$

where A and n are the stress coefficient and stress exponent, respectively. The variations in secondary creep rate with applied stress in double logarithmic plots exhibited two-slope behaviour characterised by distinct values of stress exponent in the low and high stress regime, respectively. Figure 1.9 depicts the two-slope behaviour associated with high value

of $n = 10.2$ in the high stress regime and $n = 5.8$ in the low stress regime for P9 steel at 873 K [23]. For modified 9Cr–1Mo steel in the high stress regime, Choudhary and Isaac Samuel [24] reported the values of stress exponent n in the range 12–12.9 for the temperatures

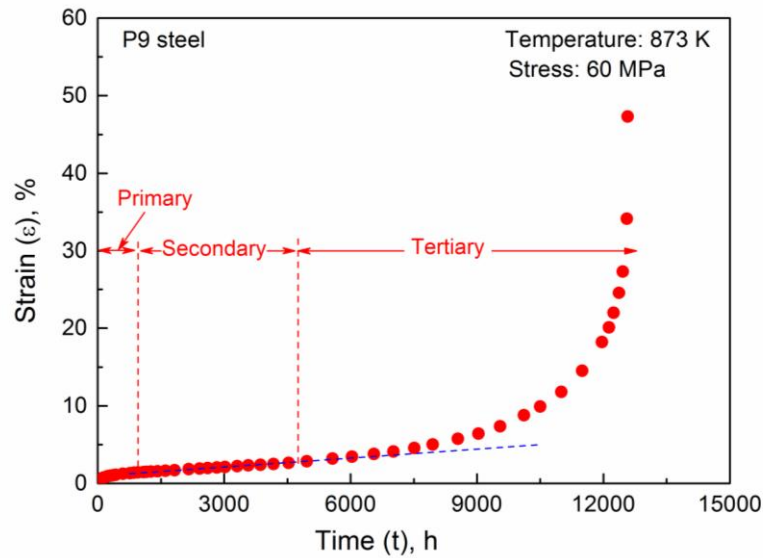


Figure 1.8 Variations in creep strain with time displaying three stages of creep behaviour in P9 steel [22].

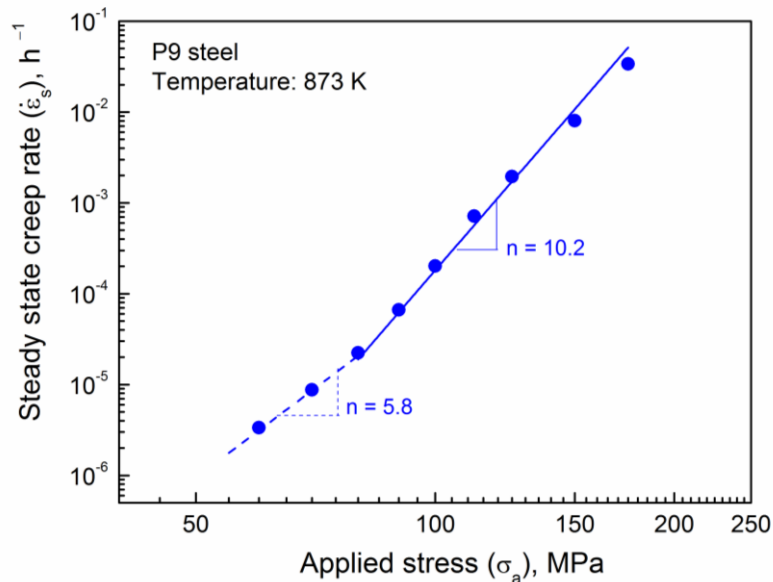


Figure 1.9 Variations in secondary creep rate with applied stress for P9 steel exhibiting two-slope behaviour with high and low stress exponent values at high and low stress regimes, respectively [23].

ranging from 823 – 873 K. A stress exponent of 15 at 873 K has been observed by Spigarelli and Quadrini [25] for the steel. Kimura et al. [26] reported high values of stress exponent $n =$

16 at 823 K and 12 at 873 K at high stresses for modified 9Cr–1Mo steel. In P92 steel, Ennis et al. [27] and Sklenicka et al. [28] reported high values of stress exponent i.e., $n = 16$ and 18 , respectively, in the high stress regime at 873 K. Apart from high n values, high activation energy value in the range of $468\text{--}719 \text{ kJ mol}^{-1}$ has been reported in the high stress regime for 9% Cr steels [24, 29]. All these investigations indicate that the 9% Cr ferritic steels exhibit high values of stress exponent and apparent activation energy in the high stress regime. It has been shown [29, 30] that the high values of n and activation energy can be rationalized by invoking the concept of resisting stress/back stress into the power law relationship. Similar to applied stress dependence of secondary creep rate, the variations in rupture life (t_r) with applied stress followed the power-law relationship for 9% Cr steels and the relationship is given as

$$t_r = A' \sigma_a^{n'} \quad , \quad \text{Equation (1.2)}$$

where A' and n' are the power-law coefficient and exponent, respectively.

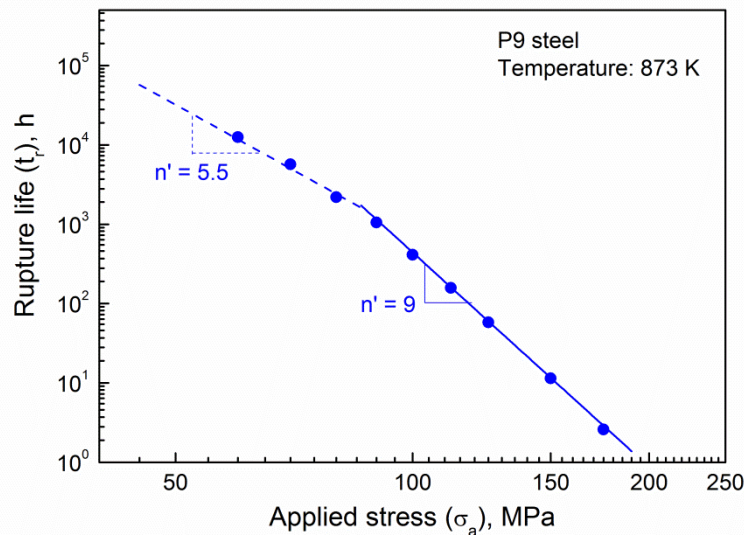


Figure 1.10 Variations in rupture life (t_r) with applied stress (σ_a) for P9 steel exhibiting two-slope behaviour with high and low stress exponent values at high and low stress regimes, respectively [22].

Like stress exponent values in the stress dependence of creep rate, stress dependence of rupture life also exhibited high stress exponent value i.e. $n' = 9$ and low value i.e. $n' = 5.5$ in the high stress and low stress regimes, respectively for P9 steel at 873 K as shown in Figure 1.10 [22]. Choudhary and Isaac Samuel [24] reported that stress exponent values (n') associated with the stress dependence of rupture life exhibited high in the range 13.0–10.7 for temperature range 823–873 K for P91 steel in the high stress regime. High value of n' of 9.7 is reported for P92 steel at 923 K in the high stress regime [31]. Choudhary reported that P92 steel exhibited $n' = 7.2$ and 17.1 in the low and high stress regimes at 873 K, respectively [32]. Different values of stress exponents (n') obtained in the low and high stress regimes are in agreement with the stress dependence of minimum creep rate in 9% Cr steels.

1.4.2 Creep Ductility and Failure Behaviour

The reported variations in reduction in area with rupture life for P9 and P92 steels at 873 K are shown in Figure 1.11, respectively. P9 steel displayed significantly higher creep ductility at longer durations than P92 steel [22, 32]. On the contrary, P92 steel exhibited

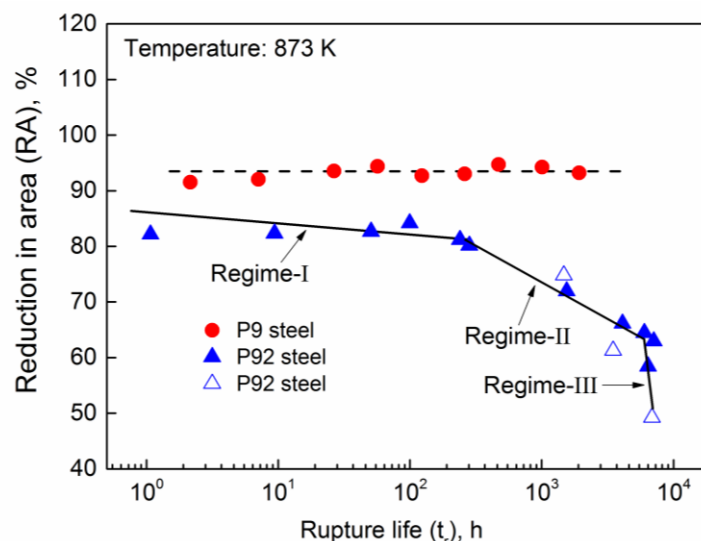


Figure 1.11 Variations in reduction in area (RA) with rupture life (t_r) for P9 and P92 steels at 873 K [32].

significant decrease in creep ductility at intermediate (Regime-II) and longer (Regime-III) rupture lives as shown in Figure 1.11. Hald [4] reported the ductility window for different rupture lifetimes for P91, P92 and E911 steels using numerous literature data. It was pointed out that there is a considerable decrease in creep ductility with increase in rupture life for P91, P92 and E911 steels over the temperature range 823 K to 923 K. In P9 steel, the reported higher creep ductility resulted in the occurrence of transgranular ductile fracture showing cup and cone fracture (Figure 1.12 (a)) and presence of ductile dimples as a consequence of micro-void coalescence (Figure 1.12 (b)-(d)). Increase in the size of the dimples with decreasing stress and increasing rupture life can be seen in Figure 1.12 (b) to 1.12 (d). These observations suggested that nucleation of voids at high applied stresses and growth processes at low stresses dominate fracture behaviour in 9% Cr steels.

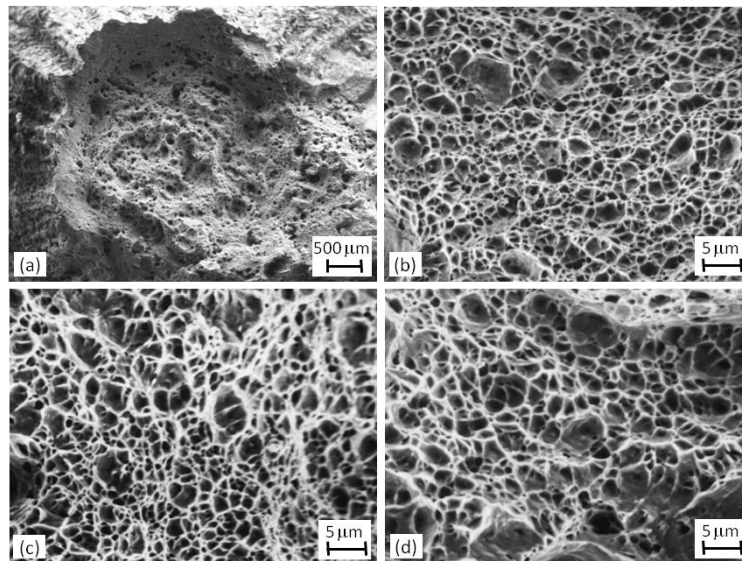


Figure 1.12 SEM fractographs showing transgranular fracture in creep tested specimens of P9 steel tubeplate forging at 873 K. Typical cup and cone fracture in (a) and increase in the size of the dimples with decreasing stress and increasing rupture life can be seen in (b) 150 MPa for 12 h, (c) 100 MPa for 412 h and (d) 60 MPa for 12575 h [22, 32].

Similar to P9 steel, all other grades of 9% Cr steel also exhibited transgranular fracture as shown in Figure 1.13 (a) for P92 as a typical example [22, 32]. However, reduced ductile

features and a few intergranular cracks appearing on the fracture surface (shown by arrows in Figure 1.13 (b)) confirmed that the presence of large number of secondary cracks (Figure 1.13 (c)) originating mainly from decohesion of Laves phase $[\text{Fe}_2(\text{W},\text{Mo})]$ at the grain and lath boundaries [32].

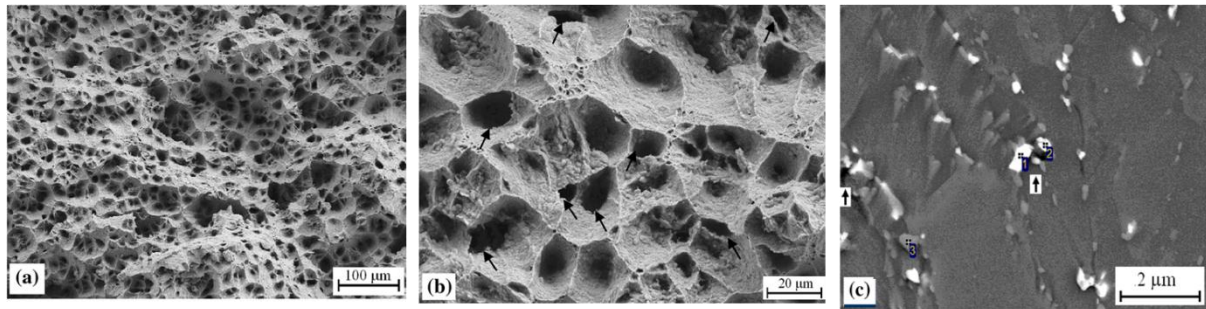


Figure 1.13 SEM fractographs showing (a) transgranular fracture in P92 steel tested at 132 MPa for 57,421 h, (b) Secondary cracks are shown by arrows and (c) formation of creep cavities (shown by arrows) due to decohesion at $\text{Fe}_2(\text{W}, \text{Mo})$ -boundary interface [32].

1.4.3 Creep Damage Tolerance Factor for 9% Cr Steels

Creep deformation and damage processes have been treated appropriately in the framework of continuum creep damage mechanics (CDM) approach [33, 34]. An important outcome of the CDM approach is the creep damage tolerance factor λ defined as the ratio of strain to failure ε_f to Monkman-Grant strain $\dot{\varepsilon}_s \cdot t_r$ [35] as

$$\lambda = \frac{\varepsilon_f}{\dot{\varepsilon}_s \cdot t_r} . \quad \text{Equation (1.3)}$$

It has been suggested that the creep damage tolerance factor λ assesses the susceptibility of material to localized cracking and therefore, λ is a better measure of creep ductility [36-38]. Ashby and Dyson [37] demonstrated that each damage micromechanism, when acting alone, results in a characteristic value of λ and a characteristic shape of creep curve. Creep damage due to growth of cavities by coupled diffusion and power-law creep results in λ values in the range 1.5-2.5. When damage is dominated by thermal-coarsening of particles and dislocation

substructure softening, λ can be as high as 5 or more. The typical evaluation of creep damage tolerance factor λ by using double logarithmic plots of average creep rate ($\frac{\epsilon_f}{t_r}$) vs. steady state creep rate ($\dot{\epsilon}_s$) is shown in Figure 1.14 for T91 steel for 823, 873 and 923 [24]. Here, T refers to tube product of modified 9Cr-1Mo steel.

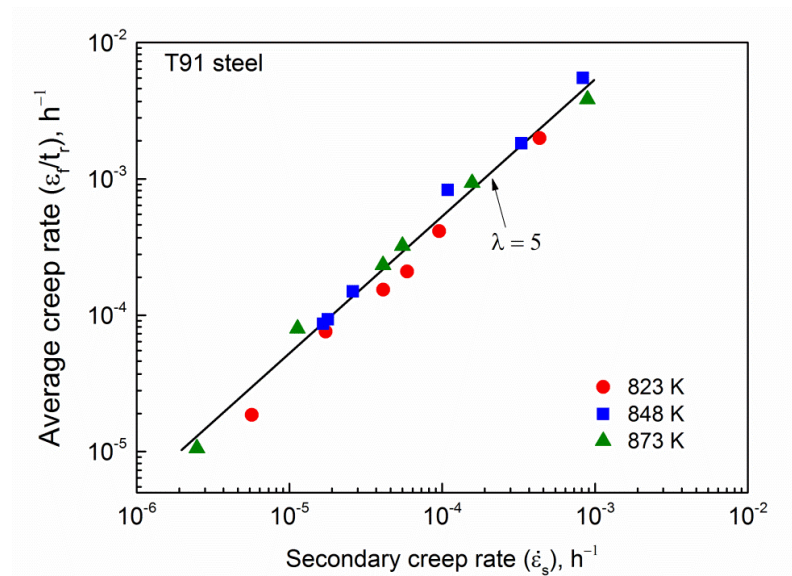


Figure 1.14 Average creep rate ($\frac{\epsilon_f}{t_r}$) vs. secondary creep rate ($\dot{\epsilon}_s$) showing a constant value of creep damage tolerance factor $\lambda = 5$ for T91 steel at three different temperatures [24].

Choudhary [22] used the constant load creep test data obtained on 9Cr-1Mo ferritic steel for the analysis, and reported values of $\lambda = 10$ and 5 for low and high stress regimes, respectively. Shrestha et al. [29] reported the values of λ between 4–5 for P91 steel crept in the temperature range of 873-973 K and at stresses of 35–350 MPa. Sakhivel et al. [39] determined the value of $\lambda = 6$ for P92 steel creep tested at 873, 923 and 973 K over a stress range of 80–220 MPa. The high values of λ reported for 9% Cr steels essentially indicated the microstructural degradation as dominant creep damage mechanism [22, 38, 39].

1.4.4 Strengthening Mechanisms and Loss of Strength during Creep in 9% Cr Steels

The creep strength of 9% Cr tempered martensitic is derived from the (i) solid solution strengthening due to the presence of molybdenum/tungsten in matrix, (ii) precipitation hardening from finely distributed carbide/carbonitride precipitates, (iii) dislocation strengthening arising from the initial high dislocation density and (iv) boundary hardening from fine hierarchical lath/sub-block/block/packet/prior-austenitic-grain boundaries. It is generally possible to combine several strengthening mechanisms contributing towards creep strength, but it is often difficult to quantify each of these contributions to the overall creep strength in 9% Cr steels.

Substitutional solute atoms, such as Mo and W, which have much larger atomic sizes than that of solvent iron, have been favoured as solid solution hardeners for 9% tempered martensitic creep-resistant steels. Precipitation hardening is one of the important creep strengthening mechanisms in tempered martensitic 9% Cr steels at elevated temperatures. To achieve enough strengthening using this effect, 9% Cr steels usually contain several kinds of precipitates in the matrix and at boundaries. Some of the important precipitates are carbides/carbonitrides such as $M_{23}C_6$, MX and M_2N (where M denotes the metallic elements, C are the carbon atoms and X are the carbon and nitrogen atoms) and intermetallic compound such as the $Fe_2(Mo,W)$ Laves phase. In P9 steel, precipitation hardening results mainly from the chromium rich $M_{23}C_6$ carbides at the boundaries and needle shaped chromium rich Cr_2N precipitates in the matrix region [22]. In other grades of 9% Cr steels, the strength contribution from precipitation arise by the presence of $M_{23}C_6$ carbides at the hierarchical boundaries and fine distribution of MX type Nb-rich carbonitride and V-rich carbonitride/nitride in the matrix regions [40]. A dispersion of fine precipitates stabilises dislocations in the matrix and sub-grain structure, which enhances dislocation hardening and sub-boundary hardening. Several mechanisms have been proposed for the threshold stress,

i.e. stress needed for a dislocation to pass through precipitates such as the Orowan mechanism, local climb mechanism, general climb mechanism, and Srolovitz mechanism [41]. Quantitatively, irrespective of specific mechanisms, the threshold stress is indirectly proportional to the inter-precipitate spacing (L). Martensitic steels in the normalised condition are characterised by high dislocation density within the laths (10^{16} - 10^{18} m^{-2}). During tempering, a more thermodynamically stable microstructure with still high dislocation density (10^{12} - 10^{14} m^{-2}) within the subgrains formed. The dislocation substructure in 9%Cr steels is characterised by small elongated subgrain (200–400 nm in width) and low-angle boundaries [42, 43]. Fine hierarchical boundaries accompanied with high dislocation density have a very intensive impact on the 9%Cr steel hardening with the boundary and dislocation strengthening mechanisms. An increase in subgrain size and a decrease in dislocation density take place during creep/service exposure in 9% Cr steels due to dynamic/static recovery mechanism [44, 45]. Figure 1.15 shows the dislocation structure of the interrupted samples and that of the virgin material. The virgin material had fine subgrains and high dislocation density. The continual increase in subgrain size and a decrease in dislocation density with interrupted time are noticed. The matrix recovery and polygonization process results in the disappearance of martensite lath microstructure and the formation of polygonized ferrite microstructure [46]. The lath microstructure stability depends on the stability of $M_{23}C_6$ carbides precipitated on the tempered martensite lath boundaries and on the subgrain boundaries preventing their growth due to the matrix polygonization and repolygonization processes [47, 48]. MX precipitates are characterised by nanometric dimensions of about 10–50 nm, and in spite of their low volume fraction of 0.020–0.025, they ensure very strong hardening of creep-resistant steels [42, 47]. The hardening with MX precipitates is ensured by anchoring and hindering the motion of dislocations [42, 47]. The coarsening of fine precipitates during creep causes an increase in inter-precipitate spacing (L) and hence a

decrease in threshold stress over long exposures. This results in decrease in creep rupture strength of the 9% Cr steels. In general, $M_{23}C_6$ precipitates exhibit higher coarsening rate than MX precipitates. In steel with micro-addition of boron, the carbon atoms in $M_{23}C_6$ carbides are partially replaced by boron during the tempering, which results in the formation of $M_{23}(C,B)_6$ precipitates. Like $M_{23}C_6$ carbides, these precipitates occur at the grain boundaries and at the martensite lath boundaries. However, these precipitates are more finely dispersed and characterised by higher thermodynamic stability compared to $M_{23}C_6$ carbides [3]. This results in a slower increase in the size of these precipitates, which has a positive effect on the stability of tempered martensite lath microstructure and results in higher creep resistance. Though the coarsening rate of MX precipitates is insignificant in 9% Cr steels, the conversion of MX into deleterious Z-phase Cr(V, Nb)N precipitates influences the long-term creep rupture strength of P91 and 12 Cr steels [45, 49]. Coarsening of $M_{23}C_6$ precipitates and conversion of MX into Z-phase are depicted in Figure 1.16 for modified 9Cr-1Mo steel at 873 K for the low stress level of 70 MPa [45]. Many viewpoints exist in the literature about the strengthening or weakening effect of the Laves phase. Hald [50] and Yamamoto et al. [51] proposed that the Laves phase has a strengthening effect, much like the $M_{23}C_6$ precipitates, in pinning the subgrain boundaries. The role of large Laves phase particles in causing embrittlement by nucleating cavities at the particle–matrix boundaries has also been explored [52]. Another view is that the Laves phase depletes the matrix of solute strengthening elements and leads to weakening [53]. Oruganti et al., [54] considered that by taking above viewpoints into account, Laves phase would act as a strengthening or stabilising agent for the subgrain boundaries at least in the initial stages of precipitation. Upon coarsening beyond a certain size, the strengthening mechanism could shift to matrix constraint much like a composite material. This can subsequently lead to fracture initiation if strain incompatibility develops at the particle–matrix boundary. Hence, it was pointed out

that the Laves phase would play a role in determining the long-term creep ductility rather than rupture strength [54] as shown in Figure 1.13.

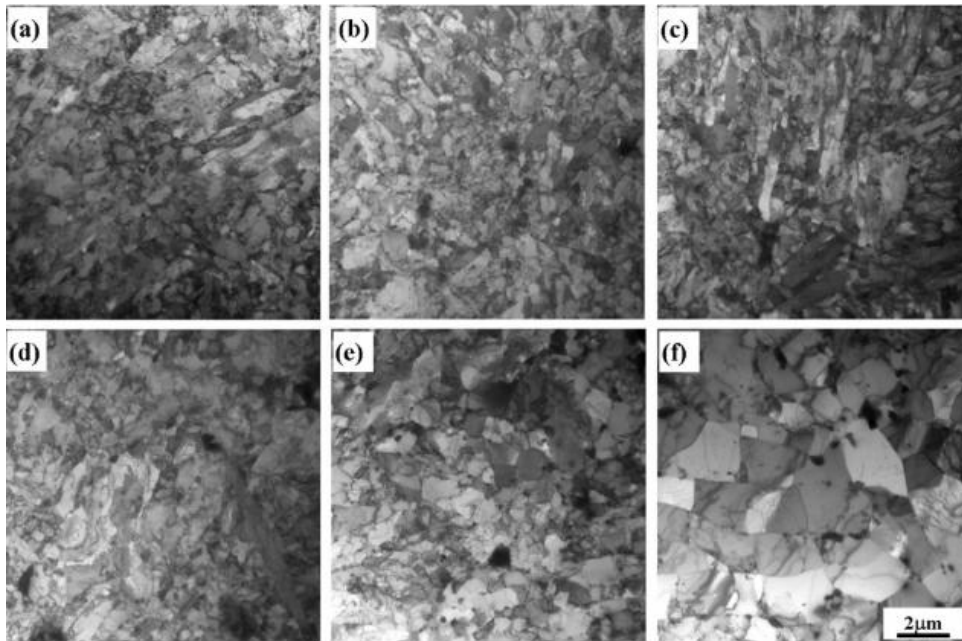


Figure 1.15 Change of dislocation structure during creep at 873 K for the stress level of 70 MPa. (a) As received (b) 9992 h, (c) 30030 h, (d) 50064 h, (e) 70000 h and (f) 80736.8 h [45].

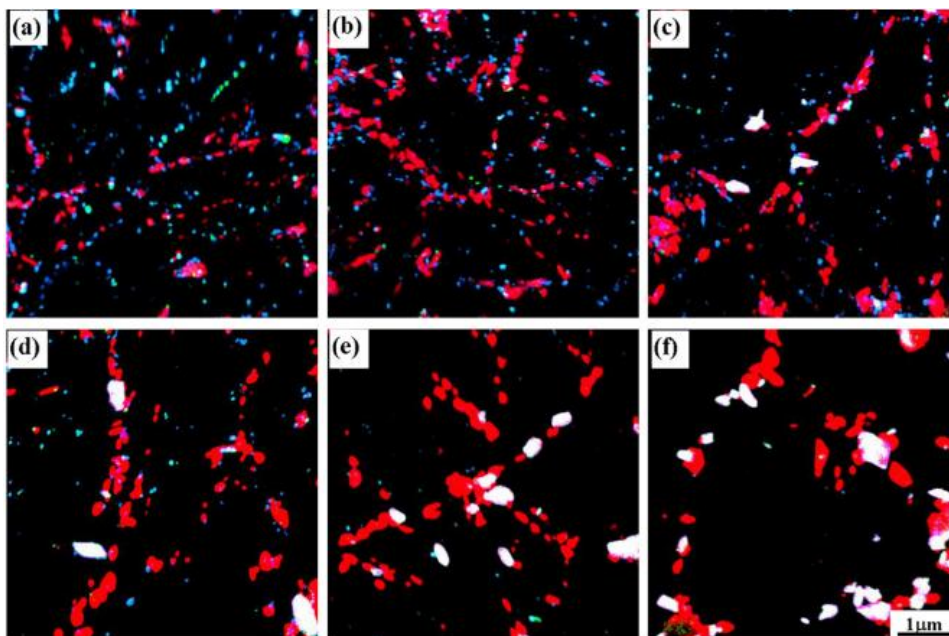


Figure 1.16 Precipitates distributions based on the results of elemental maps of Cr, V and Nb. (a) As received (b) 9992 h, (c) 30030 h, (d) 50064 h, (e) 70000 h and (f) 80736.8 h { Red: $M_{23}C_6$, blue: V-rich MX, green: Nb-rich MX, white: Z-phase} [45].

1.5 Stress Relaxation Behaviour of 9% Cr Steels

In the case of creep test, the load/stress remains constant but creep strain increases with time whereas, during stress relaxation test, the total strain remains constant but the stress decreases with hold time. The variations in relaxation stress with time for 9% Cr steel is typically shown in Figure 1.17 for P91 steel for the strain hold level of 1.3 % at 873 K [55]. It has been observed that the stress decreases rapidly during the initial hold time followed by only marginal decrease in the stress values at longer hold duration. According to Woodford [56], stress relaxation data (i.e., relaxation stress vs. hold time) can generate a stress vs. inelastic strain rate curve at nearly constant steady state at high temperatures within a few hours as compared to long-term creep tests. Praveen et al. [55] reported that the calculated

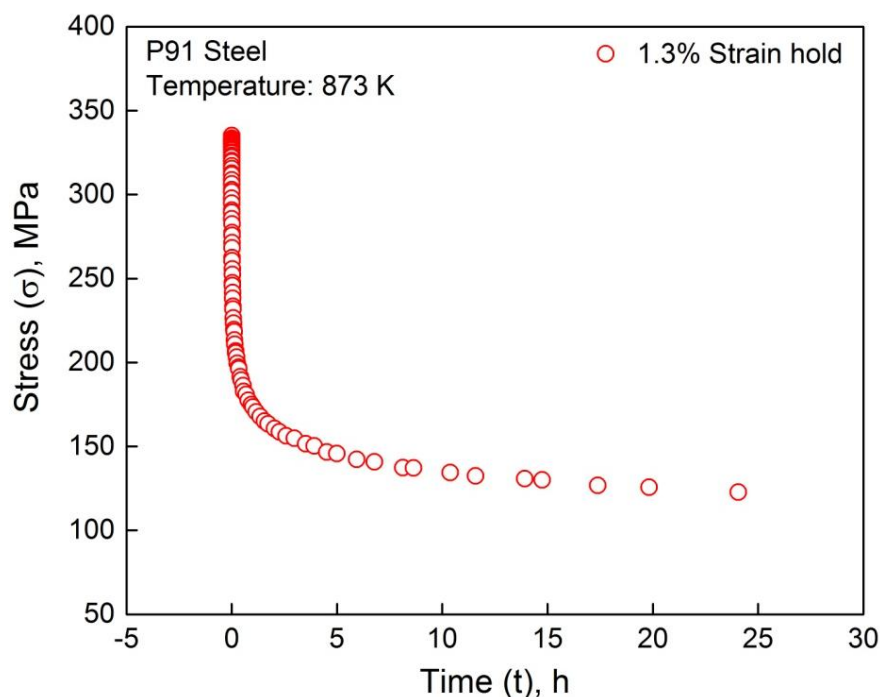


Figure 1.17 Variations in relaxation stress (σ_r) with hold time (t) [55].

inelastic strain rate by differentiating the relaxation stress vs. time data can be considered as minimum creep rate. Like monotonic creep, the relaxation stress dependence of creep rate obeyed power law i.e. $\dot{\epsilon}_s = A\sigma_r^n$ and the high value of stress exponent (n) close to 10 was

reported as shown in Figure 1.18. Guguloth et al. [57] also reported the high value of stress exponent close to 8 for P91 steel based on the minimum creep rate vs. stress data generated from the stress relaxation test. It was pointed out that subgrain coarsening remains the predominant microstructural degradation mechanism during stress relaxation of 9% Cr steels as shown in Figure 1.19 [57].

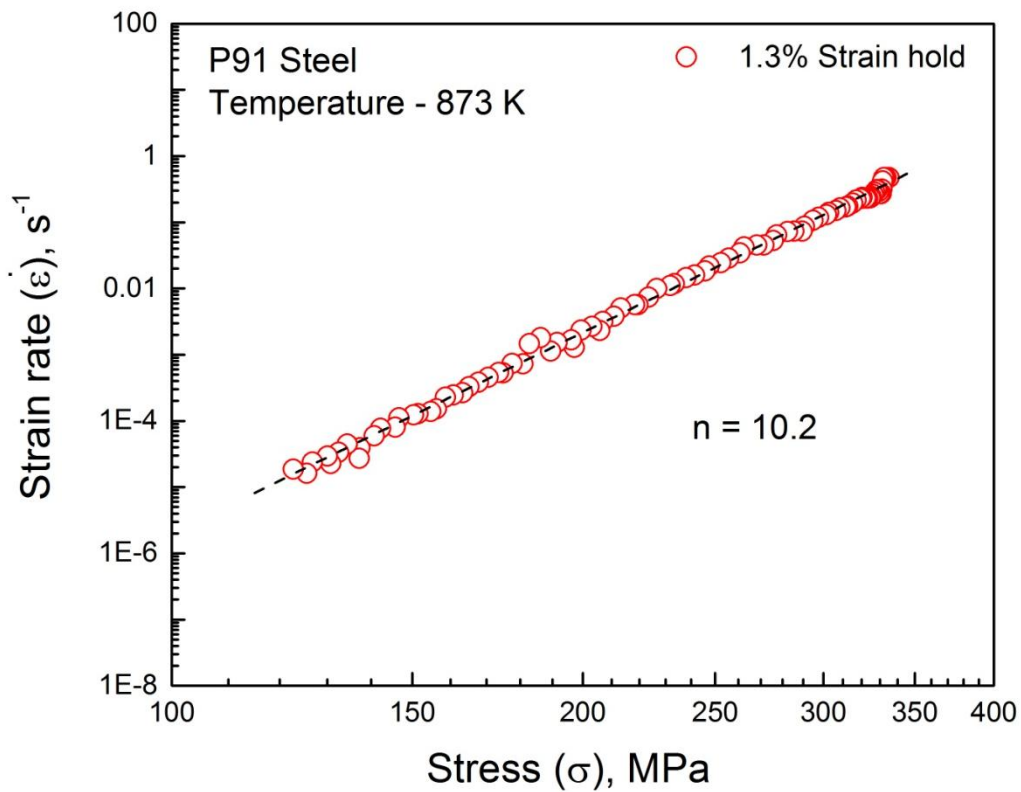


Figure 1.18 Variations in strain rate ($\dot{\epsilon}$) with relaxation stress (σ_r) [55].

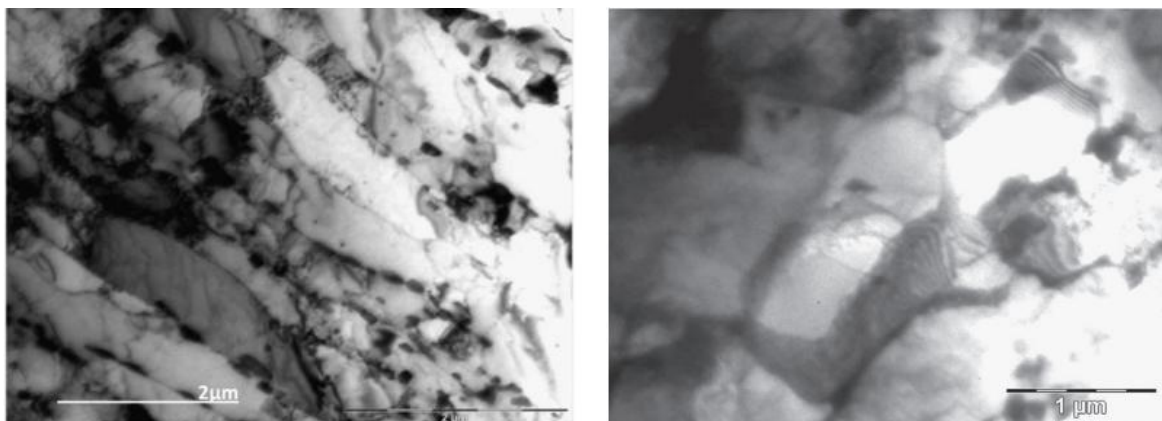


Figure 1.19 TEM microstructure of P91 steel (a) as received and (b) after stress relaxation testing at 873 K for 20 h [57].

1.6 Constitutive Models for the Inelastic Deformation Behaviour

Constitutive modelling of tensile and creep behaviour of materials attract continued scientific interest for understanding the physical phenomena controlling the deformation in metals and alloys. It also attracts technological importance for improved material processing as well as the safe performance of the components during service. Moreover, modelling can be used as a research tool for the development of new or improved alloy design concepts. An appropriate description of deformation and damage behaviour of materials becomes necessary for determining the stress-strain field distribution for damage tolerant design of structural components using finite element analysis. Extensive numerical simulations of inelastic deformation behaviour of structural materials with the aid of the finite element method play a significant role in the contemporary engineering practice. These simulations require constitutive model i.e. mathematical description of a material behaviour under different loading conditions. Models can be either empirical or internal-state-variable based formulations. Large number of relationships has been widely used to describe the tensile and creep deformation behaviour of materials. Some of them relevant to the present study have been discussed in the following subsections.

1.6.1 Empirical Formulations

For the description of tensile flow behaviour of materials, the simplest mathematical description proposed by Hollomon [58] is given as

$$\sigma = K_H \varepsilon^{n_H}, \quad \text{Equation (1.4)}$$

where σ is the true stress, $\varepsilon^{\#}$ is the true plastic strain, n_H is the strain hardening exponent and K_H is the strain hardening co-efficient. Equation (1.4) implies that true stress value is zero at

[#] *In the present thesis, ε denotes the inelastic strain. However, based on the context, inelastic strain (ε) can be either referred as a plastic or creep strain in the present thesis.*

the initial zero plastic strain. In view of this discrepancy in the Hollomon relationship, modification in Equation (1.4) has been proposed by Ludwik [59] and Swift [60], separately. Ludwik [59] introduced a new additional stress term i.e. σ_{0L} into the Hollomon relationship and it is given as

$$\sigma = \sigma_{0L} + K_L \varepsilon^{n_L}, \quad \text{Equation (1.5)}$$

where n_L is the strain hardening exponent and K_L is the strain hardening co-efficient. Swift [60] introduced a strain term ε_0 for accounting the pre-strain left in the material as

$$\sigma = K_S (\varepsilon + \varepsilon_0)^{n_S}, \quad \text{Equation (1.6)}$$

where n_S is the strain hardening exponent and K_S is the strain hardening co-efficient. It has been observed that, in many face centered cubic metals and alloys having low stacking fault energy, σ - ε data could not be described by Holloman relationship at all strains due to large positive stress deviation at low strains [61]. In order to account for the large positive stress deviation at low strains, Ludwigson [61] proposed an additional terms in Equation (1.4) as

$$\sigma = K_1 \varepsilon^{n_1} + \exp(K_2 + n_2 \varepsilon), \quad \text{Equation (1.7)}$$

where K_1 and n_1 are the same as K_H and n_H in the Holloman relation, respectively, and K_2 and n_2 are additional constants. Ludwigson [61] reported that the second term on the right hand side corresponds to deformation mode dominated by planar slip at low strains, whereas the first term relates to the extensive cross slip and consequent cell formation at high strains. In order to describe σ - ε behaviour of materials exhibiting saturation stress at high stress/strain levels, Voce [62] proposed an interesting relationship and it is written as

$$\sigma = \sigma_S - (\sigma_S - \sigma_I) \exp(-n_V \varepsilon), \quad \text{Equation (1.8)}$$

where σ_S and σ_I are the saturation and initial stresses, respectively. The constant n_V is used to determine the rate with which the stress tends to reach steady state value. In this approach, the flow curve is viewed as a transient of the flow stress from some initial value to the

saturation value where equilibrium structure prevails at a given strain rate and temperature. The applicability of the flow relationships proposed by Hollomon [58], Ludwik [59], Swift [60], Ludwigson [61], and Voce [62] were demonstrated for 9% Cr steels and it is presented in Figure 1.20 as an example [63]. Analysis in the framework of different flow relationships suggested that the tensile flow behaviour of 9% Cr steels is described by Ludwigson equation most appropriately in the temperature range 300–793 K. At high temperatures (823–873 K), Ludwigson equation reduces to Hollomon equation [63]. However, Voce equation as a single flow relationship can describe σ – ε_p data adequately in the entire temperature range of interest [64]. Voce relationship is also employed to predict the tensile properties of the steel for the wide range of temperature and strain rate conditions [64]. However, the above proposed relationships do not include the simultaneous dependence of strain and strain rate on the flow behaviour of materials. The power law relationship accounting for both strain hardening and strain rate hardening [65] is given as

$$\sigma = A_p \varepsilon^{n_p} \dot{\varepsilon}^{m_p}, \quad \text{Equation (1.9)}$$

where A_p is the constant, n_p and m_p are the strain hardening and strain rate hardening exponents, respectively. The influence of strain hardening, strain rate hardening, and varying temperature on flow behaviour of materials can be taken into consideration by the Johnson-Cook model [66] and it is represented as

$$\sigma = \left(A_1 + A_2 \varepsilon^{n_j} \right) \left(1 + B \ln \left[\frac{\dot{\varepsilon}}{\dot{\varepsilon}_{ref}} \right] \right) \left(1 - \left[\frac{T - T_0}{T_m - T_0} \right]^{m_T} \right), \quad \text{Equation (1.10)}$$

where A_1 , A_2 and n_j are the constants related to strain hardening. The constant B is related to strain rate hardening and the constant m_T is related to thermal softening. $\dot{\varepsilon}_0$ is the reference strain rate and T , T_0 and T_m are the working temperature, room temperature and melting temperature, respectively.

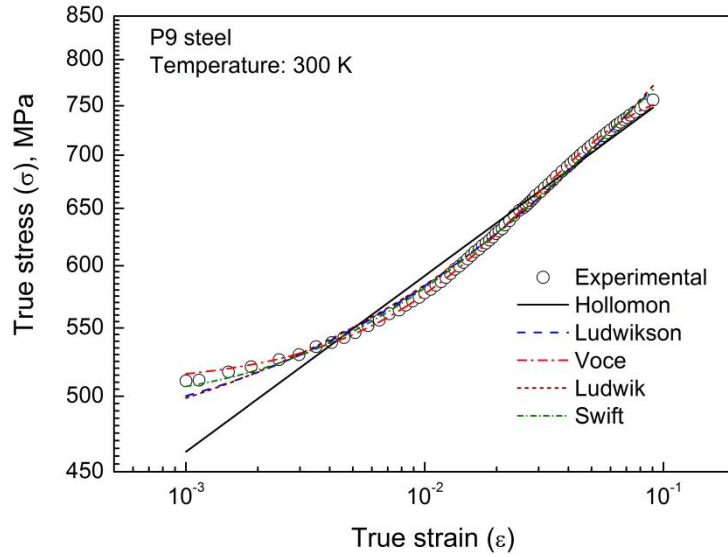


Figure 1.20 Variations in experimental true stress with true plastic strain for P9 steel at 300 K. The fitted curves related to the different flow relationships are superimposed [63].

For describing the creep behaviour of materials, various empirical models were proposed. Some of the developed relationships were used to describe the specific creep property either secondary creep rate or rupture life as given in Equations (1.11) and (1.12). In order to predict and extrapolate the long-term creep rupture lives, several time-temperature parametric approaches have also been developed. In general, three different methodologies such as Larson-Miller approach [67], Orr-Sherby-Dorn approach [68], and Manson-Haferd approach [69] have been employed in literature. Among the developed methodologies, Larson-Miller approach [67] is the most widely used one for the prediction of stress vs. rupture life behaviour in metals and alloys. Larson and Miller [67] proposed a method that correlates the temperature (T) with rupture life (t_r) at a constant engineering stress σ and the proposed equation is represented as,

$$LMP = T(\log t_r + C_1), \quad \text{Equation (1.11)}$$

where C_1 is a constant. The term LMP is known as Larson-Miller parameter. According to Equation (1.11), the plot of \log (rupture life) vs. $1/T$ displayed a straight line with slope i.e. LMP and intercept $-C_1$ at $1/T = 0$ as shown in Figure 1.21. Family of lines

representing $\log t_r$ vs. $1/T$ for different levels of stress ($\sigma_1 > \sigma_2 > \sigma_3$) are also shown in the figure. For a given stress, the value of LMP can be calculated by substituting rupture life and temperature in Equation (1.11) for the known value of constant C_1 .

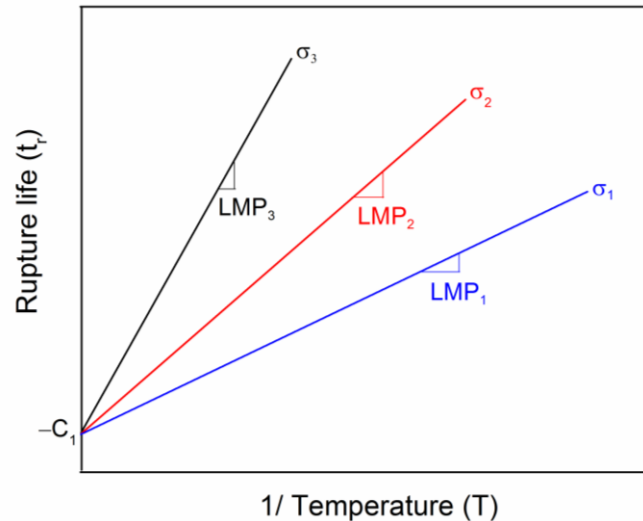


Figure 1.21 Schematic representation of rupture life vs. $1/T$ plot for the estimation of slope i.e. LMP and intercept ($-C_1$) value for Larson-Miller parametric approach. Here, $\sigma_1 > \sigma_2 > \sigma_3$.

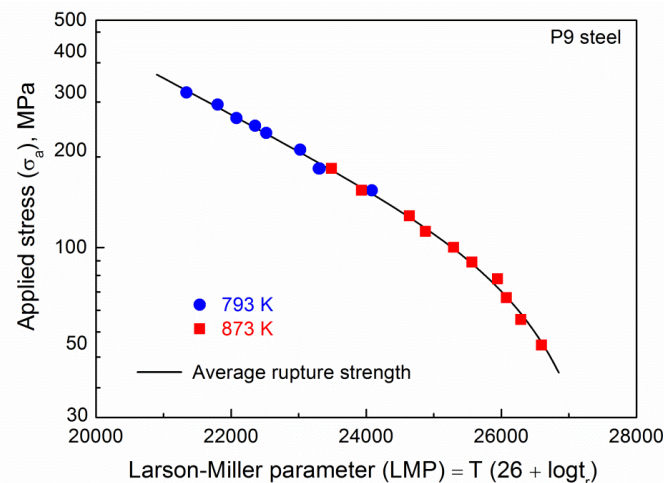


Figure 1.22 Variations in applied stress (σ_a) vs. Larson-Miller parameter (LMP) at 793 and 873 K for P9 steel. The average creep-rupture strength values obtained using optimised material constant $C_1 = 26$ for P9 steel have been superimposed [70].

A single master curve can be constructed by plotting LMP vs. stress for various temperatures. Representative plot of applied stress vs. LMP for P9 steel is shown in Figure 1.22 [70]. In common, polynomial curve fitting has been performed on the master curve to obtain a best-fit

equation which is further used to estimate and extrapolate rupture lives for a specific combination of stress and temperature. However, as the metallurgical complexity of engineering alloys has increased, the adoption of a single function to represent the rupture behaviour throughout the entire ranges of temperature and stress has become increasingly challenging [71]. This is one of the major limitations of the Larson-Miller parametric approach.

Some of the proposed models can be used to describe either primary and secondary creep deformation or tertiary creep behaviour. The formulations proposed to describe primary and secondary creep deformation are given as [72-75]

$$\varepsilon = \alpha_A t^{\frac{1}{3}} + \dot{\varepsilon}_{\min} t, \quad \text{Equation (1.12)}$$

$$\varepsilon = \beta_g [1 - \exp(-\gamma t)] + \dot{\varepsilon}_{\min} t, \quad \text{Equation (1.13)}$$

$$\varepsilon = \frac{\dot{\varepsilon}_{\min}}{K_1} \ln \left[1 + \frac{\dot{\varepsilon}_i - \dot{\varepsilon}_{\min}}{\dot{\varepsilon}_{\min}} (1 - \exp(-K_1 t)) \right] + \dot{\varepsilon}_{\min} t. \quad \text{Equation (1.14)}$$

The constants α_A , β_g , γ and K_1 associated with the above equations depend on temperature and applied stress. The term $\dot{\varepsilon}_i$ is the initial creep rate. For an approximate description of the primary creep strain versus time relationship, these equations are equivalent and a choice must be made only when accurate description is necessary. Equation (1.13) is very popular because of its simplicity. In Equation (1.13), β_g is the amplitude of the transient creep strain and γ is the decay time. Damage mechanics based empirical approach proposed by Kachanov and Rabotnov [76, 77] has been widely used to describe the tertiary creep behaviour. Accordingly, the creep rate is defined as

$$\dot{\varepsilon} = A_{KR} \left(\frac{\sigma}{1 - \omega} \right)^{n_{KR}}, \quad \text{Equation (1.15)}$$

where ω is an empirical damage-variable. The material constants A_{KR} and n_{KR} are Norton's law constants describing secondary creep behaviour. The damage variable ω varies from 0 to 1 corresponding to undamaged state (i.e., $t = 0$) and failure ($t = t_r$) of materials, respectively.

In Kachnov-Rabotnov model, the damage rate is described as

$$\dot{\omega} = B_{KR} \frac{\sigma^\chi}{(1-\omega)^\phi}, \quad \text{Equation (1.16)}$$

where B_{KR} , χ and ϕ are material constants, which controls the tertiary creep behaviour. Some empirical-analytical models can provide the complete creep description towards deformation and damage behaviour of engineering materials. One of the popular models for complete description of creep behaviour of materials is theta-projection methodology [78].

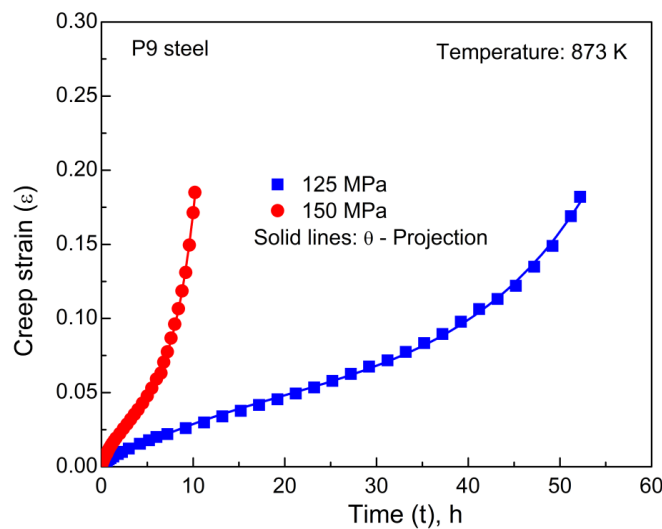


Figure 1.23 Variations in experimental and predicted creep strain-time data shows the applicability of the θ -projection model towards 9% Cr steels [79].

In the theta-projection concept [78], a typical creep curve is visualised as a combination of decaying primary and accelerating tertiary stages [78, 79]. The creep strain-time relationship is represented as,

$$\varepsilon = \theta_1 (1 - \exp[-\theta_2 t]) + \theta_3 (\exp[\theta_4 t] - 1), \quad \text{Equation (1.17)}$$

Where $\theta = \{\theta_1 \theta_2 \theta_3 \theta_4\}$ is a set of quantities which determines the shape of the creep curve. θ_1 and θ_3 act as strain-like scaling parameters for the primary and tertiary stages, respectively. θ_2 and θ_4 are strain rate like parameters affecting the curvature of the primary and the tertiary. The applicability of theta-projection has been presented for P9 steel in Figure 1.23. Though empirical models are very popular for the description of tensile and creep behaviour of materials, their extrapolation capabilities are usually poor outside the range of experiments [80,81]. Since the parameters associated with these models are easy to optimise, the applicability of empirical models are demonstrated more frequently than internal-state-variable based models. In addition, empirical-analytical models can be easily implemented into the finite element codes for the simulations.

1.6.2 Internal-state-variable models

Internal-state variable defines the current average microscopic state of the system. In general, the evolution of any microstructural features such as dislocation density, precipitate or dispersoid size/volume fraction/number density, internal stress, solute concentration, grain size, subgrain size, volume fraction of different phases, vacancy concentration, texture, misorientation, etc. can be considered as internal-state variables. The continual improvement in understanding of underlying microstructure variables in engineering materials has led to the development of new constitutive models or modification in existing models. Internal-state-variable models have been applied mostly to simulate simple uniaxial tests where the specimen geometry plays no significant role, typically at constant strain rate/stress/strain, but their potential as constitutive laws for finite element simulations begins to be exploited as well. Admittedly, these microstructure-based models must be fitted to experimental data as well. The most prominent microstructural state variable to define the deformation behaviour of the material is the dislocation density (ρ). In common, the evolution of dislocation density

has been coupled to kinetic rate relationship to define the work hardening or creep behaviour of materials. For instance, the kinetic law defining the flow stress in functional form is represented as

$$\sigma = \sigma(\rho, \dot{\varepsilon}, T) . \quad \text{Equation (1.18)}$$

To describe creep, at a constant applied stress σ , the kinetic Equation (1.18) is considered in the inverted form as

$$\dot{\varepsilon} = \dot{\varepsilon}(\rho, \sigma, T) . \quad \text{Equation (1.19)}$$

In both cases, the appropriate evolution relationship for dislocation density with strain must be provided for the complete description. For instance, in the one-internal-variable models of Kocks [82], Kocks and Mecking [83] and Estrin and Mecking [84], the rate dependent flow stress is generally written as

$$\sigma = \left(\sigma_0 + M \alpha \mu b \sqrt{\rho} \right) \left(\frac{\dot{\varepsilon}}{\dot{\varepsilon}_0} \right)^{\frac{1}{m}} , \quad \text{Equation (1.20)}$$

where σ is the flow stress at the strain rate ($\dot{\varepsilon}$), $\dot{\varepsilon}_0$ is the reference strain rate, σ_0 is the flow stress contribution other than dislocation, ρ is the dislocation density and m is the strain rate sensitivity. Equation (1.20) can also be rewritten as

$$\dot{\varepsilon} = \dot{\varepsilon}_0 \left(\frac{\sigma}{\sigma_0 + M \alpha \mu b \sqrt{\rho}} \right)^m . \quad \text{Equation (1.21)}$$

As mentioned earlier, both Equations (1.20) and (1.21) should be coupled with the evolution of dislocation density for quantifying the flow stress or inelastic strain values for given strain/time. The generalised formulation for the evolution of dislocation density with strain in the Kocks-Mecking-Estrin approach is given as

$$\frac{d\rho}{d\varepsilon} = M \left(\frac{1}{bL} - k_2 \rho \right) , \quad \text{Equation (1.22)}$$

where storage rate i.e. $\frac{d\rho^+}{d\varepsilon}$ is defined by the term $\frac{M}{bL}$ and recovery rate $\frac{d\rho^-}{d\varepsilon}$ is defined as

$-k_2\rho$. In Equation (1.22), L is the mean free path and k_2 is the dynamic recovery parameter.

The specific definition for mean free path L depends on the nature of obstacle. However, continual improvements in dislocation-density based modelling for the description of deformation behaviour of materials have been found. One such model is two-internal-variable approach proposed by Barlat et al. [85]. In the two-internal-variable approach, the flow stress in terms of forest dislocation density is represented as

$$\sigma = \left(\sigma_0 + M \alpha \mu b \sqrt{\rho_f} \right) \left(\frac{\dot{\varepsilon}}{\dot{\varepsilon}_0} \right)^{\frac{1}{m}}. \quad \text{Equation (1.23)}$$

According to Barlat et al. [85], the evolution of forest dislocation density is given as

$$\frac{d\rho_f}{d\varepsilon} = M \left(\frac{1}{bL} - k_2 \rho_f \right). \quad \text{Equation (1.24)}$$

Equation (1.24) describing the evolution of forest dislocation density with strain is the same as the generalised Equation (1.22) proposed by Kocks-Mecking [82, 83]. Barlat et al. [85] introduced the two new relationships for the evolution of mean free path and mobile dislocation density for the description of work hardening behaviour of aluminium alloys. The proposed relationships are given as

$$\frac{dL}{d\varepsilon} = -k_L (L - L_S). \quad \text{Equation (1.25)}$$

$$\frac{d\rho_m}{d\varepsilon} = \frac{M}{b} \left(\frac{1}{L_S} - \frac{1}{L} \right). \quad \text{Equation (1.26)}$$

The constant k_L in Equation (1.25) defines the rate at which mean free path approaches to the final value L_S at saturation. Since the evolution of mean free path of dislocations and the mobile dislocation density are interdependent through Equation (1.25), the evolution of three internal variables, i.e., the forest dislocation density, mean free path and mobile dislocation

density with plastic strain (Equation (1.26)) reduces to two-internal-variable approach. Christopher and Choudhary [86, 87] demonstrated the applicability of two-internal-variable approach for the description of three-stage (Transient stage, Stage-II and Stage-III) work hardening behaviour of type 316L(N) SS for the wide range of temperature and strain rate conditions. Similar to Barlat et al. [85] approach, the model proposed by Kubin-Estrin [88,89] model describes the deformation behaviour of materials using the evolution of mobile and forest dislocation densities. In case of deformation exhibiting large strains with stage-IV and stage-V behaviour, a split of the total dislocation density into the densities of cell interior (ρ_{interior}) and cell wall (ρ_w) dislocations appears to be more appropriate than separation into mobile and immobile dislocation densities [90]. Roters et al. [81] reported the three-internal-variable models based on the evolution of cell-interior mobile dislocation density ($\rho_{m, \text{interior}}$) and two kinds of the immobile dislocation densities. In immobile dislocation population, cell interior ($\rho_{i, \text{interior}}$) and cell wall (ρ_w) dislocation densities were treated separately. Since hyperbolic based rate equation has been used to describe the strain rate relation. By weighting the stress in the cell interiors and cell walls using the corresponding volume fractions of the cell walls (f_w) and cell interiors (f_i) in Roters et al. [81] model, the flow stress was calculated and it is given as

$$\sigma = M (f_i \tau_i + f_w \tau_w). \quad \text{Equation (1.27)}$$

Among the above models, the one-internal-variable approach proposed by Kocks-Mecking-Estrin is most widely used for the description of tensile, creep and stress-relaxation behaviour of engineering materials. All other specified (multi-variable) models are mostly employed only for the description of work hardening behaviour of materials.

Apart from dislocation density based models, in the past, great emphasis has been given to describe high-temperature creep by considering internal stress (σ_i) as a single internal variable representing resistance to creep deformation of materials [91, 92]. Internal

stress resulting from the contributions of strain hardening and dynamic recovery appears to be an appropriate internal variable during primary creep. Saxl and Kroupa [93] considered internal stress as a measure of the effects of internal long-range stresses on glide motion of dislocations. On the basis of stochastic concept of deformation, Dobes [94] demonstrated that the macroscopic value of effective stress, σ_e (where $\sigma_e = \sigma_a - \sigma_i$) is an adequate measure of local effective stresses determined by a level of local internal stresses in micro-volumes. In general, the macroscopic mean value of the internal variable can be obtained experimentally [95]. When the influence of materials structure is described by internal stress as a single internal variable, only two equations are required for constitutive description: a kinetic equation relating the creep rate ($\dot{\varepsilon}$) to the internal stress and an evolution equation of the internal stress. Shaker and El-Magd [96] proposed the creep rate relation for describing primary and steady state creep behaviour of austenitic steel and aluminium as

$$\dot{\varepsilon} = \dot{\varepsilon}_s \left(\frac{\sigma_a^2 - \sigma_i^2(t)}{\sigma_a^2 - \sigma_{is}^2} \right) \frac{\sinh \left[\frac{\Delta V (\sigma_a - \sigma_i(t))}{kT} \right]}{\sinh \left[\frac{\Delta V (\sigma_a - \sigma_{is})}{kT} \right]}, \quad \text{Equation (1.28)}$$

where ΔV is the activation volume, σ_{is} is the internal stress at steady state and k is the Boltzmann constant. The time dependence of internal stress evolution relation is given as

$$\sigma_i(t) = \sigma_{i0} + (\sigma_{is} - \sigma_{i0}) \left[1 - \exp(-m_i t^q) \right], \quad \text{Equation (1.29)}$$

where σ_{i0} is the initial internal stress, m_i and q are constants. Coupled Equations (1.28) and (1.29) can be successfully used to describe the primary and steady state creep behaviour. In addition to above, Esposito and Bonora [97] developed a mechanism based model for primary creep by assuming that the creep rate in transient regime can be given as a function of steady state creep rate and internal stress. This is expressed as

$$\dot{\varepsilon} = \dot{\varepsilon}_s \exp \left[\frac{\beta_V + 1}{RT} \Delta V \sigma_{is} \exp \left(-\frac{\varepsilon}{\varepsilon_0} \right) \right]. \quad \text{Equation (1.30)}$$

where β_v is the dislocation velocity exponent and ε_0 is the rate constant. As a matter of convenience, Equation (1.30) has been reformulated in terms of applied stress as

$$\dot{\varepsilon} = \dot{\varepsilon}_s \exp \left[\frac{\bar{V} \sigma_a}{RT} \exp \left(-\frac{\varepsilon}{\varepsilon_0} \right) \right], \quad \text{Equation (1.31)}$$

where \bar{V} is the scaled activation volume. The successful application of the model has been demonstrated by describing primary creep behaviour of class M materials including P91 steel and Rene 80 nickel based superalloy [97]. In common, models based on either dislocation density or internal stress provides better description towards primary and steady-state creep deformation behaviour of materials. Since damage evolution relationships are not considered into these models, they cannot predict the tertiary creep behaviour of materials. In this regard, a critical review of microstructure based model in the framework of continuum creep damage mechanics approach has been reported by Dyson and McLean [53, 98, 99]. A set of linear differential equations is represented in Dyson-McLean model as

$$\begin{aligned} \dot{\varepsilon} &= \dot{\varepsilon}(\sigma, T, H, D_i) \\ \dot{H} &= \dot{H}(\sigma, T, H, D_i) . \\ \dot{D}_i &= \dot{D}_i(\sigma, T, H, D_i) \end{aligned} \quad \text{Equation (1.32)}$$

The first equation in the above set describes strain accumulation as function of stress (σ), temperature (T), extent of stress redistribution between the matrix and the precipitate (H), and the damage due to the structural changes occurring in the material (D_i). The subsequent equations represent evolution of stress redistribution and damages. In case of three dominant damage mechanisms operate during creep, five equations are required to simulate its behaviour. The successful implementation of Dyson-McLean approach [53] has been demonstrated for describing the creep behaviour of nickel-based alloys and tempered martensitic steels [53, 54, 98-101]. Similar to Dyson-McLean approach, Basirat et al. [102] developed the new internal-state-variable model with damage parameters for the complete

description of creep strain-time trajectories in 9% Cr steels. In Basirat et al. [102] model, the strain rate was represented as

$$\dot{\epsilon} = \dot{\epsilon}(\rho_m, \rho_{dip}, \sigma, T, D_i), \quad \text{Equation (1.33)}$$

where ρ_{dip} is the dipole dislocation density. Surya et al [103] also demonstrated the applicability of internal-state-variable based model for the description of creep deformation and damage behaviour of P92 steel and the creep strain rate was formulated as

$$\dot{\epsilon} = \dot{\epsilon}(\rho_m, \rho_{dip}, \rho_w, \sigma, T, D_i), \quad \text{Equation (1.34)}$$

where ρ_w is the dislocation density in subgrain boundaries. In general, formulations related to internal-variable model appear to be complex but they provide a better understanding of deformation kinetics than empirical-analytical models.

1.7 Motivation and thesis outline

In the present thesis, internal-state-variable approaches have been employed to understand the tensile, creep and stress-relaxation behaviour of 9% Cr steels. Since the involved models are data-driven formulations, large volume of experimental data obtained on 9% Cr steels have been used in the present investigation. The details of experimental data are presented in **Chapter 2**. The objectives of the present thesis mainly focus on modelling of tensile and creep behaviour listed as

- (i) Establishment of interrelationship between microstructural features of 9% Cr steels and its mechanics of deformation in the framework of internal-state-variable based models
- (ii) Critical assessment of existing models or development of new relationships for modelling deformation and damage behaviour
- (iii) Demonstration of the applicability of model by accurate prediction

- (iv) Evaluation of creep rupture lives by using newly developed model formulations.

With these objectives, the present research work has been formulated. Accordingly, the chapters in this thesis have been designed. In **Chapter 3**, the outcome of the comparative evaluation of tensile work hardening behaviour P9 steel plate and thick-section tubeplate forging and P91 steel in the framework of dislocation-density based strain rate independent Kocks-Mecking-Estrin formulation [82-84] have been discussed. It is well known that three different variants of Kocks-Mecking-Estrin model [82-84] have been used to describe the tensile flow and work hardening behaviour of materials. The appropriate variant was chosen by parametric sensitivity analysis. Using the chosen variant, the reason for the difference in work hardening ability among 9% steels has been studied. In addition, instability criterion [104] has been revisited in terms of dislocation density based approach for 9% Cr steels. The new interrelationship between uniform plastic strain and dynamic recovery parameter has been developed. In **Chapter 4**, the development of a new constitutive model based on single internal-variable, i.e., internal stress for the description of primary and secondary deformation behaviour of 9% Cr steels has been presented. In this constitutive framework, sine hyperbolic creep rate relation associated with the concept of stress dependent activation volume and average dislocation segment length related to the Friedel statistics [105] has been derived from the basic Orowan relationship [106]. Following Estrin-Mecking approach [84], the evolution of mean internal stress from initial to saturation value during creep deformation has been considered. The sine hyperbolic creep rate relation coupled with the evolution of internal stress as a function of strain provides a better understanding of primary and secondary creep behaviour of 9% Cr steels. Following the development of primary creep model, its applicability has been demonstrated by comparing the predicted and experimental creep strain-time and creep rate strain data in P9 steel tubeplate forging in quenched and tempered (Q+T) and simulated post weld heat treatment

(SPWHT) conditions at 793 and 873 K. The validity of the model has been shown by comparing the experimental as well as predicted creep data in two different heat treatment conditions. In **Chapter 5**, two different approaches have been discussed for the description of the totality of creep deformation and damage behaviour of 9% Cr steels. The first is based on the additive creep rate formulation where the developed sine hyperbolic creep rate formulation for primary creep has been added to tertiary creep rate as a function of tertiary creep strain obtained using MPC-Omega methodology [107] with necessary modification. The applicability of this approach has been demonstrated for P9 tubeplate steel in quenched and tempered condition for different applied stresses at 873 K. Though the developed additive creep rate model describes the creep behaviour accurately, the variable i.e., tertiary creep strain involved in the model cannot be considered as an internal-state-variable. It is well known that microstructural degradation (Section 1.4.4) in terms of coarsening of dislocation substructure accompanied by the decrease in dislocation density, coarsening of precipitates, conversion of MX precipitates into Z-phase particularly in the modified grades and depletion of solute Mo from the matrix with subsequent formation of Laves phase and its coarsening dominates during tertiary creep in 9% Cr steels [40, 45, 49]. The above observations suggested the need for internal-state-variable based model for the description of tertiary creep behaviour. In this context, the second approach i.e. microstructure based Semba-Dyson-McLean model [108] has been employed for the description of creep deformation and damage behaviour of P9 and Grade 91 steels. In order to account for the influence of microstructural damages arising from the coarsening of $M_{23}C_6$ and conversion of useful MX precipitates into deleterious Z-phase on creep behaviour of the steel, original kinetic creep law proposed by Dyson and McLean [99] has been modified in the present investigation. Applicability of the developed model has been demonstrated for the prediction of long-term creep behaviour of Grade 91 steel. The role of Z-phase on creep rupture life has

also been discussed. **Chapter 6** deals about the description of stress-relaxation behaviour of P91 steel using the newly developed sine hyperbolic kinetic creep model with suitable modification. Applicability of that model has been demonstrated for the prediction of experimental data. The final **Chapter 7** outlines the important findings in relation to the developed internal-state-variable models and their applicability towards tensile and creep deformation behaviour of 9% Cr steels. In addition, a few recommendations have been suggested for future directions.

1.8 Significance of the performed research

- Considered criterion has been revisited for tempered martensitic steels in the framework of dislocation density based approach.
- New sine hyperbolic model has been developed for the description of primary and secondary creep deformation behaviour of 9% Cr steels. The applicability of the model has also been demonstrated for the description of stress-relaxation behaviour of the steels.
- Omega-methodology has been empirically modified for the better prediction of tertiary creep behaviour of tempered martensitic steels and new additive creep rate formulation has been developed to describe the totality of creep deformation and damage behaviour of the steels.
- Improvement has been made in the continuum damage mechanics based Dyson-McLean approach for the prediction of long-term creep behaviour of Grade 91 steels at 873 K.

Chapter 2: Material, Initial Microstructure and Experimental Data for Modelling and Parametric Optimisation Methodology

2.1 Experimental Details Related to Modelling of Tensile Work Hardening Behaviour

The experimental true stress-true plastic strain data obtained on two different product forms of P9 steel, i.e., thin-section plate and thick-section tubeplate forging and P91 steel are used in this study. The chemical composition of the P9 and P91 steels is given in Table 2.1.

Table 2.1- Chemical composition (Wt. %) of P9 plate and tubeplate forging and P91 steels.

Product form	C	Si	Mn	S	P	Cr	Mo	Nb	V	N	Fe
P9 steel: Plate	0.100	0.48	0.45	0.002	0.008	8.44	0.95	-	-	140 ppm	Bal.
P9 steel: Tubeplate forging	0.100	0.75	0.63	0.001	0.020	9.27	1.05	-	-	190 ppm	Bal.
P91 steel	0.097	0.31	0.37	0.005	0.018	9.29	0.92	0.08	0.26	0.057	Bal.

P9 steel with 20-mm plate thickness was tested in normalized and tempered (N+T) condition. The hot-rolled plate was normalized at 1223 K for 15 minutes followed by air cooling and tempered at 1053 K for 2 hours followed by air cooling. P9 steel tubeplate forging of 1000-mm diameter and 300-mm thickness was tested in quenched and tempered (Q+T) condition. The hot forged tubeplate was austenitized with controlled heating (heating time: 8 hours) to 1223 K and soaking at 1223 K for 5 hours followed by quenching in water. Tempering treatment involved controlled heating (heating time: 8 hours) to 1023 K and soaking at 1023 K for 8 hours followed by air cooling. P91 steel of 12-mm plate thickness was normalized at 1333 K for 25 minutes followed by air cooling and tempered at 1023 K for 1 hour followed

by air cooling. The details of product form and heat treatment conditions employed for tensile tests have been summarized in Table 2.2.

Table 2.2- Details of product form and heat treatment conditions employed for tensile tests in 9% Cr steels.

Steel and product form	Heat treatment
P9 steel: Plate (N+T)*	Austenitizing: 1223 K/15 minute, Air cooled Tempering: 1053 K/2 h, Air cooled
P9 steel: Tubeplate forging (Q+T)*	Austenitizing: 1223 K/5 h, Water quenched Tempering: 1023 K/8 h, Air cooled
P91 steel (N+T)	Austenitizing: 1333 K/25 min, Air cooled Tempering: 1023 K/1 h, Air cooled

*N+T: Normalized and tempered; Q+T: Quenched and tempered

Specimen blanks of 12-mm diameter and 60-mm length were machined with stress axis in rolling direction from plate materials of P9 and P91 steels. In P9 steel tubeplate forging, 12-mm diameter and 60-mm long specimen blanks were machined with stress axis in the thickness direction from the outer annulus of 300-mm width of the forging. Cylindrical button head specimens with 4 mm gauge diameter and 26 mm gauge length were machined. Tensile tests were performed in air using a floor model Instron 1195 universal testing machine equipped with a three-zone temperature control furnace and a stepped-load suppression unit. Tests were performed on P9 and P91 steels employing a nominal strain rate of $1.26 \times 10^{-3} \text{ s}^{-1}$ at temperatures ranging from 300 to 873 K. The temperatures for all tests were controlled within ± 2 K. Load-elongation curves were recorded using the Instron autographic recorder for all the tests. Use of suitable chart speed provided strain resolution of 7.5×10^{-4} and stepped zero load suppression gave stress resolution of 0.8 MPa. True stress–true plastic strain data were evaluated using a computer program from load-elongation curves

up to the maximum load values. Since strain gauge was not employed, the cross head displacement was taken as the sum of the deformation in the specimen and extension due to the machine frame and load-train assembly. The initial linear portion of load-elongation curves was contributed by the displacement due to elastic deformation in the specimen, machine frame and load-train assembly. The combination of these elastic strains was subtracted from the total strain by appropriately using the slope of the initial linear portion for the calculation of plastic strain. Stress and plastic strain data were used to determine the true stress (σ)-true plastic strain (ϵ).

2.2 Experimental Data Related to Modelling of Creep Behaviour

The creep strain-time data obtained on P9 and T91 steels were used to demonstrate the applicability of the proposed creep models. Since the model development is the prime focus in the present research, the validation of the model has been performed for the specific data set and the details related to this aspect are summarized in Table 2.3.

For the evaluation of the applicability of sine hyperbolic based primary and secondary creep model, the constant load creep test data obtained on thick section P9 steel tubeplate forging in quenched and tempered (Q+T) and simulated post weld heat treatment (SPWHT) conditions are used. The chemical composition of the steel is given in Table 2.1 in a second row. The details related to quenched and tempered (Q+T) heat treatment condition is presented in Table 2.2. An additional heat treatment involving slow heating to 998 K and soaking at 998 K for 3 h followed by slow cooling was given on the Q+T specimen blanks. The heating and cooling rates of 50 K/h above 673 K were used in this heat treatment. The additional heat treatment was intended to simulate post weld heat treatment (SPWHT) on Q+T specimen blanks. Cylindrical creep specimens with 10 mm gauge diameter and 50 mm gauge length were machined from Q+T and SPWHT specimen blanks. Monotonic creep tests

793 and 873 K were conducted in air environment in ATS make creep machines on Q+T and SPWHT specimens. The test temperatures were controlled within ± 2 K. Elongation values at regular intervals were obtained using LVDT transducer with strain resolution 4×10^{-4} and attached to the bottom of the high temperature extensometer at room temperature. The time-intervals for data acquisition were judiciously selected between 1 min and 1 h depending upon the different stages of deformation as well as the overall duration of creep tests.

In order to demonstrate the applicability of the additive creep rate model, the experimental creep strain-time data obtained at stresses ranging from 60 to 125 MPa on P9 steel tubeplate forging in quenched and tempered (Q+T) condition at 873 K have been used. The applicability of the proposed model has also been examined for different initial microstructures particularly at low applied stress of 60 MPa at 873 K. In view of that, the creep strain (ϵ)-time (t) data obtained for P9 steel tubeplate forging in simulated post-weld heat treatment (SPWHT) condition and for P9 steel plate material in normalized and tempered (N+T) condition was used. The chemical composition and heat treatment condition of P9 steel plate were given in Table 2.1 and Table 2.2, respectively.

For the evaluation of the applicability of Semba-Dyson-McLean creep model [108], in addition to creep strain-time data obtained on P9 steel tubeplate forging in Q+T and additional SPWHT condition at 873 K, the data obtained for MGC heat of T91 steel has also been used. Since the quantitative microstructural details were available for creep tested T91 steel at 873 K for the lowest stress level of 70 MPa in MGC heat, the data obtained for that heat was chosen to model the long-term creep behaviour of the steel. The details heat treatment condition corresponding to MGC is also included in the Table 2.3. The chemical composition (in wt. %) of T91 steel was as follows: Fe-0.09C-8.70Cr-0.90Mo-0.35Mn-0.29Si-0.002S-0.009P-0.28Ni-0.032Cu-0.22V-0.072Nb-0.001Al-0.044N.

Table 2.3- Details of product form, heat treatment and creep tested conditions of 9% Cr steels employed for creep constitutive modelling.

Product form with nomenclature	Heat treatment	Creep test conditions	
		Temperature	Applied stress levels
<i>Sine Hyperbolic Based Model: Prediction of Primary and Secondary Creep</i>			
P9 steel: Tubeplate forging (Q+T)	Austenitizing: 1223 K/5 h, Water quenched Tempering: 1023 K/8 h, Air cooled	793 K	150-250 MPa
		873 K	60-150 MPa
P9 steel: Tubeplate forging (SPWHT) *	Q+T plus simulated post weld heat treatment: 998 K/3 h with heating and cooling rates of 50 K h ⁻¹ above 673 K	793 K	175-237 MPa
		873 K	50-100 MPa
<i>Additive Creep Model : Prediction of Complete Creep Strain-Time Data</i>			
P9 steel: Tubeplate forging (Q+T)	Austenitizing: 1223 K/5 h, Water quenched Tempering: 1023 K/8 h, Air cooled	873 K	60-125 MPa
P9 steel: Tubeplate forging (SPWHT)	Q+T plus simulated post weld heat treatment: 998 K/3 h with heating and cooling rates of 50 K h ⁻¹ above 673 K		60 MPa
P9 steel: Plate (N+T)	Austenitizing: 1223 K/15 minute, Air cooled Tempering: 1053 K/2 h, Air cooled		60 MPa
<i>Semba-Dyson-McLean : Prediction of Complete Creep Strain-Time Data</i>			
P9 steel: Tubeplate forging (Q+T)	Austenitizing: 1223 K/5 h, Water quenched Tempering: 1023 K/8 h, Air cooled	873 K	60-112 MPa
P9 steel: Tubeplate forging (SPWHT)	Q+T plus simulated post weld heat treatment: 998 K/3 h with heating and cooling rates of 50 K h ⁻¹ above 673 K		50-100 MPa
T91 steel: N+T [26]	Austenitizing: 1323 K/10 min, Air cooled Tempering: 1038 K/30 min, Air cooled		70-160 MPa

* SPWHT: Simulated post weld heat treatment

2.3 Initial Microstructure of Tempered Martensitic Steels Used for Modelling Tensile and Creep Behaviour

Optical metallographic examinations were performed on P9 steel plate (N+T) and tube plate forging (Q+T and SPWHT) specimens prepared using standard metallographic techniques and by immersion etching in 1 gram picric acid + 5 ml HCl +100 ml ethyl alcohol. Scanning electron microscopic (SEM) examinations were performed on N+T P9 and P91 steels. Transmission electron microscopic (TEM) examination was conducted on the carbon replica extracted from P9 steel tubeplate forging.

The microstructure of P9 steel in normalized and tempered condition was composed of fine tempered lath martensite and precipitates as shown in Figure 2.1. Average prior austenite grain size measured by the linear intercept method was $\sim 25 \mu\text{m}$ for the plate material of P9 steel. The boundaries of prior austenite grains and martensite laths were decorated with precipitates and the intralath matrix regions contained a large number of fine precipitates (Figure 2.1(b)). The precipitates present at lath and prior austenite grain boundaries have been observed to be M_{23}C_6 carbides rich in chromium, whereas intralath matrix regions contain fine M_2X , i.e., Cr_2N precipitates shown in Figure 2.1(c) [22, 109, 110]. The microstructure of P9 steel tubeplate forging in Q + T condition composed of tempered lath martensite along with a few stringers of pro-eutectoid ferrite at prior austenite grain boundaries (Figure 2.2(a)). Pro-eutectoid ferrite in the tubeplate forging has been measured as 2% using point count method and no significant difference in pro-eutectoid ferrite was observed between the surface and along the thickness within 300 mm outer annulus of the forging. Tubeplate forging displayed coarse prior austenite grain size of $120 \mu\text{m}$. Tubeplate forging displayed coarser austenite grains, martensite packets, and lath martensite and coarse precipitates than those shown by plate material of P9 steel (Figure 2.2(b)). Transmission electron microscopic investigation on the carbon extraction replica revealed the presence of M_{23}C_6 and M_2X precipitates (Figure 2.2(c)). Among the heat treated conditions, P9 steel in

SPWHT condition displayed relatively coarser microstructure (Figure 2.3) than those in Q+T condition (Figure 2.2 (a) and (b)). The microstructure of P91 steel in N+T condition was composed of tempered lath martensite with fine $M_{23}C_6$ carbides decorated along prior austenite grain and martensite lath boundaries (Figure 2.4). The matrix regions contain fine MX type V(C,N) and Nb(C,N) precipitates (Figure 2.4) [45, 111]. The prior austenite grain size of 19 μm was obtained for P91 steel. The calculated weight percentage of equilibrium precipitates using Thermo-Calc Software TCFE6 steels/Fe-alloys database [112] in P9 steel plate and tubeplate forging and P91 steel are presented in Table 2.3. The respective volume fractions of the precipitates in the steels are given in brackets. The precipitates observed in metallographic examinations in P9 and P91 steels (Figures 2.1-2.4) are in agreement with those predicted by thermodynamic analysis (Table 2.4). Further, the higher weight percentage of MX precipitates present in P91 steel than the M_2X in P9 plate and tubeplate forging indicates hardened microstructure comprising of finer precipitate distribution in P91 steel (Table 2.4).

Table 2.4- The Weight Percent of Different Precipitates Calculated using Thermo-Calc Software TCFE6 Steels/Fe-alloys Database [112] in P9 steel Plate and Tubeplate Forging and P91 steel. The Respective Volume Fractions of the Precipitates are given in Brackets.

Steel and product form	$M_{23}C_6$	MX	M_2X
P91 steel	1.73 (1.8×10^{-2})	0.35 (4.0×10^{-3})	-
P9 steel: Plate	1.88 (1.9×10^{-2})	-	0.13 (1.7×10^{-3})
P9 steel: Tubeplate forging	1.90 (1.9×10^{-2})	-	0.17 (2.3×10^{-3})

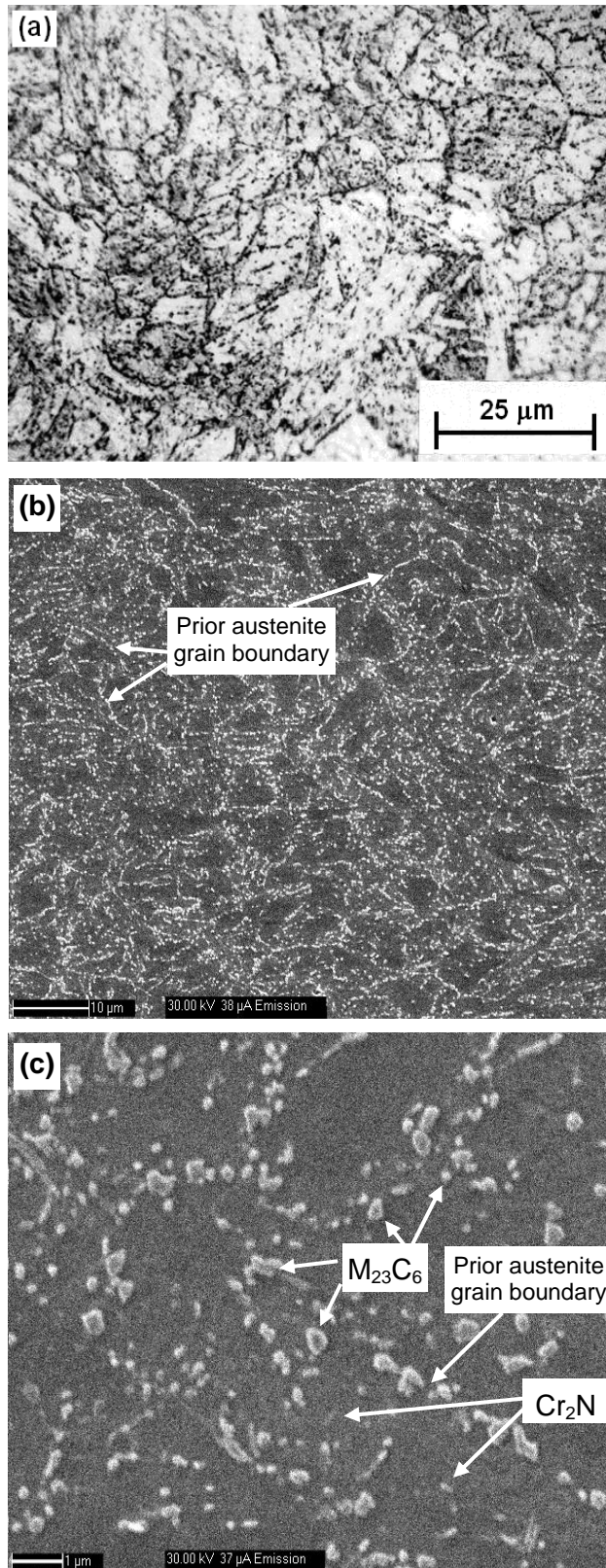


Figure 2.1 Microstructure of normalized and tempered plate material of P9 steel showing (a) tempered lath martensite and (b) precipitates on grain and lath boundaries and in the matrix region. Presence of $M_{23}C_6$ carbides and Cr_2N precipitates are shown by arrows in (c).

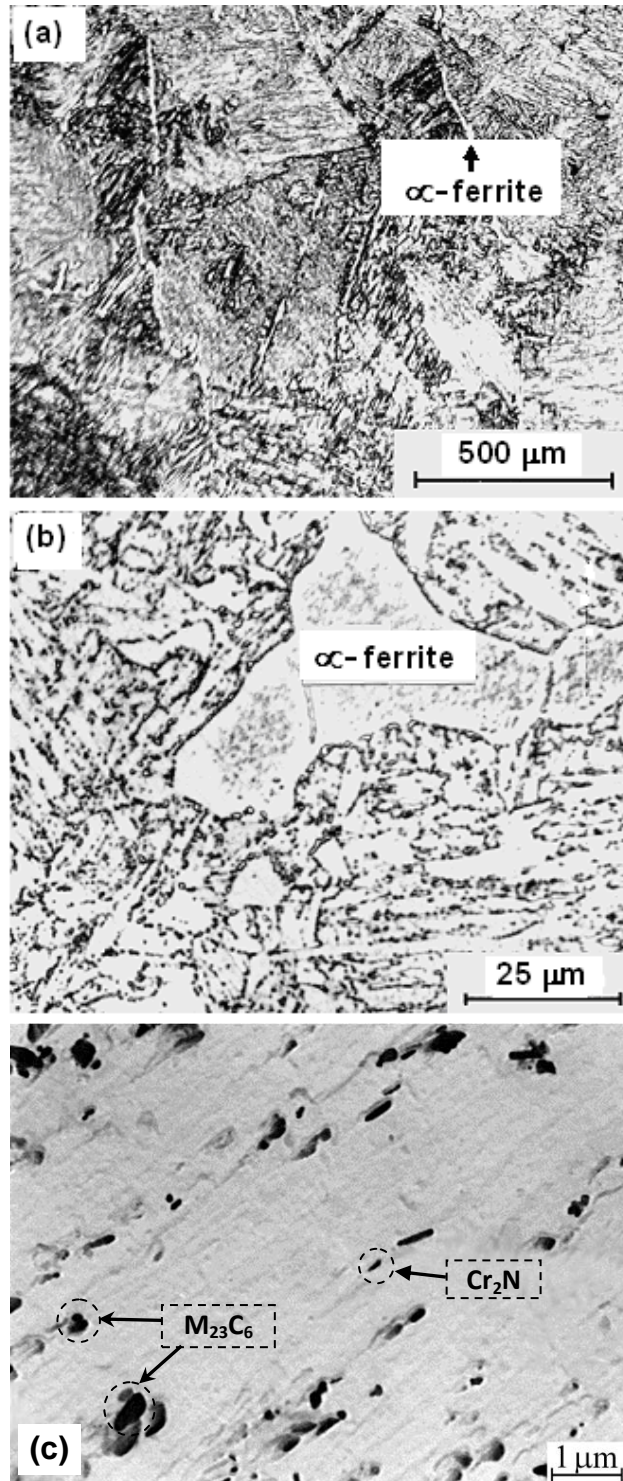


Figure 2.2 Microstructure of thick section tube plate forging of P9 steel showing (a) tempered lath martensite and pro-eutectoid ferrite as stringers at prior austenite grain boundaries and (b) coarse precipitates on grain and lath boundaries and in the matrix region. Presence of M_{23}C_6 carbides and Cr_2N precipitate in tempered lath martensite is shown in (c).

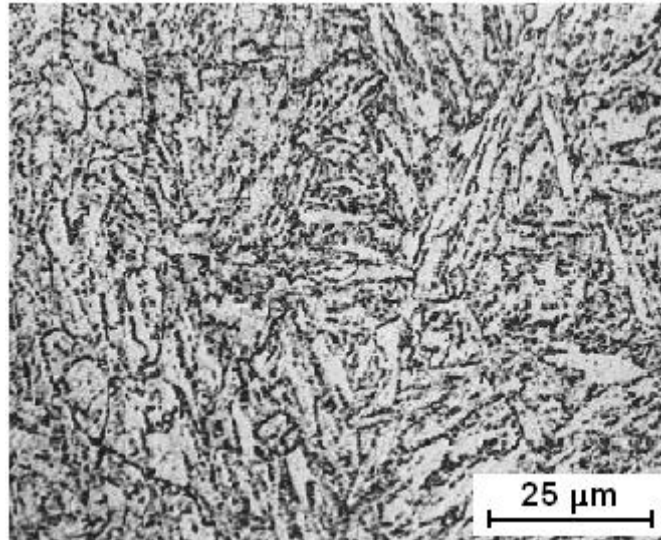


Figure 2.3 Microstructure of 9Cr-1Mo steel tube plate forging in SPWHT condition showing tempered lath martensite and precipitates at the boundaries and in the matrix region.

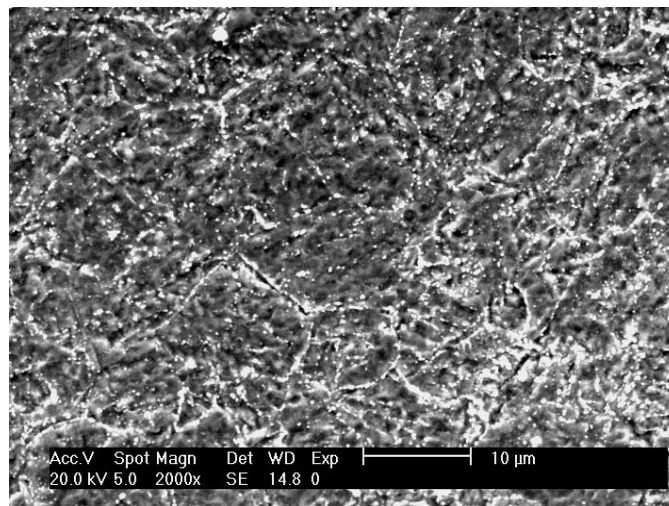


Figure 2.4 SEM micrograph showing tempered lath martensite and fine precipitates on the grain and lath boundaries and in the matrix region in normalized and tempered P91 steel.

2.4 Experimental Data for Modelling of Stress-Relaxation Behaviour

Stress-relaxation data acquired for P91 steel in normalised and tempered condition has been used in the present investigation. The chemical composition (in term of wt. %) of the steel was as follow: Fe-0.10C-8.10Cr-0.92Mo-0.33Ni-0.38Si-0.46Mn-0.18V-0.073Nb-0.020P-0.002S-0.034Al-0.049N. P91 steel was austenitised at 1323 K for 30 minutes followed by air cooling and tempered at 1023 K for 1 hour followed by air cooling. The microstructure in normalised and tempered condition displayed high dislocation density along with elongated dislocation cells and subgrains (Figure. 2.5). The boundaries were decorated with $M_{23}C_6$ carbides and the matrix regions contained fine MX type carbides/carbonitrides of vanadium and niobium [45, 111].

Following heat treatments, cylindrical specimens having dimensions of 32.5 mm gauge length and 6.4 mm gauge diameter were machined. Stress-relaxation tests at 873 K were conducted in air environment under total strain controlled mode at 1.3 and 2.5% strain holds in a servo-hydraulic universal testing system equipped with a data acquisition system. Test temperature was controlled within ± 2 K. Stress-relaxation tests were performed by employing nominal loading strain rate of $1 \times 10^{-4} \text{ s}^{-1}$ to the desired total strains of 1.3 and 2.5% followed by strain holds for 24 hours. The desired total strain levels were maintained using LVDT transducers with strain resolution $4 \times 10^{-4} \text{ s}^{-1}$ for the entire hold duration followed by unloading using strain rate $4 \times 10^{-4} \text{ s}^{-1}$. The stress-relaxation data was acquired by judiciously selecting small time intervals in terms of relaxation stress (σ_r) vs. hold time (t).

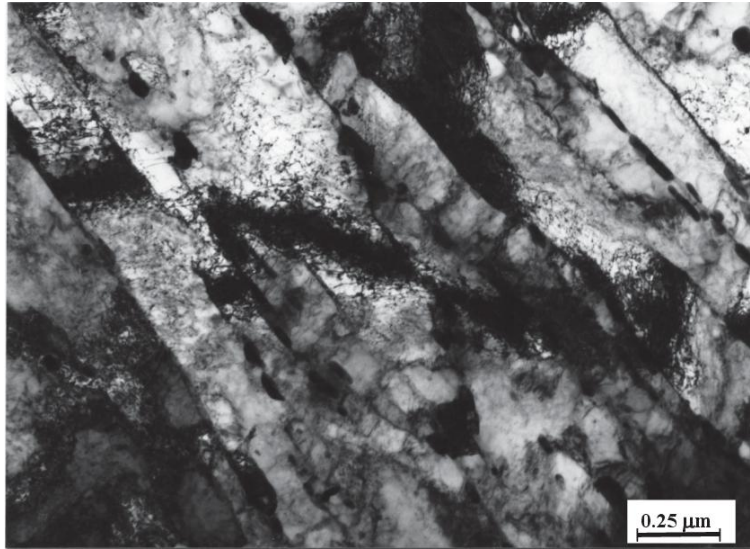


Figure 2.5 Microstructure of P91 steel in normalised and tempered condition.

2.5 ODE Parametric Optimisation Methodology and its Implementation

The employed internal-state-variable models in this thesis are having two or more first-order coupled ordinary differential equations (ODE) depending on their complexity of formulation. The optimum parameters or material constants associated with the models are needed to be identified for the better description of inelastic deformation behaviour of materials. In view of this, ODE parametric optimisation algorithm has been developed. The schematic representation of the algorithm in terms of flow chart has been presented in Figure 2.6. An iterative methodology has been invoked. Experimental data (true stress vs. true plastic strain or creep strain vs. time) and the initial guess values with their upper and lower bounds have been provided to initialize the iteration procedure. Using the initial guess values, the numerical integration of differential equations was performed. In the present investigation, irrespective of complexity of equations, 4th order Runge-Kutta method has been employed for the numerical integration of simultaneous first-order coupled ordinary differential equations.

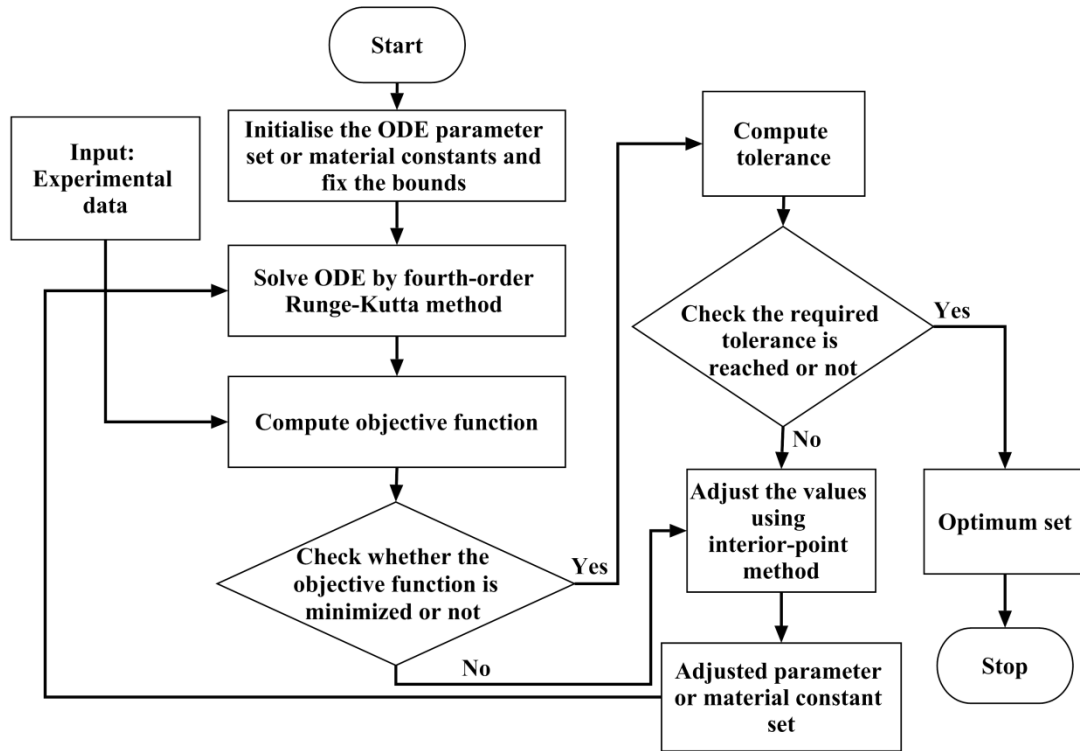


Figure 2.6 Schematic flow diagram describing the numerical algorithm for optimisation of Parameters/material constants associated with the internal-state-variable approaches.

Consider the differential equations for 'n' number of variables and it is represented as

$$\begin{aligned}
 \frac{dV_1}{dX} &= f_1(X, V_1, V_2, \dots, V_n) \\
 \frac{dV_2}{dX} &= f_2(X, V_1, V_2, \dots, V_n) \\
 &\cdot \\
 &\cdot \\
 &\cdot \\
 \frac{dV_3}{dX} &= f_3(X, V_1, V_2, \dots, V_n)
 \end{aligned}
 \tag{2.1}$$

For modelling tensile deformation behaviour, V_1 refers to stress and X refers to plastic strain. In case of modelling creep behaviour, V_1 is for creep strain and X defines the time, whereas for modelling the stress relaxation behaviour, V_1 and X indicate the relaxation stress and hold time, respectively. Other variables such as $V_2 \dots V_n$ represent the internal-state-variables associated with the particular model. In the 4th order Runge-Kutta numerical integration, four

different slope values (i.e. κ_1 – first slope; κ_2 – second slope; κ_3 – third slope and κ_4 – fourth slope) were calculated. The first slope was evaluated as

$$\begin{aligned} \kappa_{1,V_1^i}^i &= f_1\left(X^i, V_1^i, V_2^i, \dots, V_n^i\right) \\ \kappa_{1,V_2^i}^i &= f_2\left(X^i, V_1^i, V_2^i, \dots, V_n^i\right) \\ &\cdot \\ &\cdot \\ &\cdot \\ \kappa_{1,V_n^i}^i &= f_n\left(X^i, V_1^i, V_2^i, \dots, V_n^i\right) \end{aligned} \quad \text{Equation (2.2)}$$

where i refers to the iteration number inside the Runge-Kutta scheme. The second slope value was computed as

$$\begin{aligned} \kappa_{2,V_1^i}^i &= f_1\left(X^i + \frac{h}{2}, V_1^i + \frac{h}{2}\kappa_{1,V_1^i}^i, V_2^i + \frac{h}{2}\kappa_{1,V_2^i}^i, \dots, V_n^i + \frac{h}{2}\kappa_{1,V_n^i}^i\right) \\ \kappa_{2,V_2^i}^i &= f_2\left(X^i + \frac{h}{2}, V_1^i + \frac{h}{2}\kappa_{1,V_1^i}^i, V_2^i + \frac{h}{2}\kappa_{1,V_2^i}^i, \dots, V_n^i + \frac{h}{2}\kappa_{1,V_n^i}^i\right) \\ &\cdot \\ &\cdot \\ &\cdot \\ \kappa_{2,V_n^i}^i &= f_n\left(X^i + \frac{h}{2}, V_1^i + \frac{h}{2}\kappa_{1,V_1^i}^i, V_2^i + \frac{h}{2}\kappa_{1,V_2^i}^i, \dots, V_n^i + \frac{h}{2}\kappa_{1,V_n^i}^i\right) \end{aligned} \quad \text{Equation (2.3)}$$

where h indicates step size either in terms of incremental plastic strain ($\Delta\varepsilon$) or incremental time (Δt). The third slope (κ_3) value was computed as

$$\begin{aligned} \kappa_{3,V_1^i}^i &= f_1\left(X^i + \frac{h}{2}, V_1^i + \frac{h}{2}\kappa_{2,V_1^i}^i, V_2^i + \frac{h}{2}\kappa_{2,V_2^i}^i, \dots, V_n^i + \frac{h}{2}\kappa_{2,V_n^i}^i\right) \\ \kappa_{3,V_2^i}^i &= f_2\left(X^i + \frac{h}{2}, V_1^i + \frac{h}{2}\kappa_{2,V_1^i}^i, V_2^i + \frac{h}{2}\kappa_{2,V_2^i}^i, \dots, V_n^i + \frac{h}{2}\kappa_{2,V_n^i}^i\right) \\ &\cdot \\ &\cdot \\ &\cdot \\ \kappa_{3,V_n^i}^i &= f_n\left(X^i + \frac{h}{2}, V_1^i + \frac{h}{2}\kappa_{2,V_1^i}^i, V_2^i + \frac{h}{2}\kappa_{2,V_2^i}^i, \dots, V_n^i + \frac{h}{2}\kappa_{2,V_n^i}^i\right) \end{aligned} \quad \text{Equation (2.4)}$$

The last slope value was evaluated as

$$\begin{aligned}
\kappa_{4,V_1^i}^i &= f_1 \left(X^i + h, V_1^i + h\kappa_{3,V_1^i}^i, V_2^i + h\kappa_{3,V_2^i}^i, \dots, V_n^i + h\kappa_{3,V_n^i}^i \right) \\
\kappa_{4,V_2^i}^i &= f_2 \left(X^i + h, V_1^i + h\kappa_{3,V_1^i}^i, V_2^i + h\kappa_{3,V_2^i}^i, \dots, V_n^i + h\kappa_{3,V_n^i}^i \right) \\
&\cdot \\
&\cdot \\
&\cdot \\
\kappa_{4,V_n^i}^i &= f_n \left(X^i + h, V_1^i + h\kappa_{3,V_1^i}^i, V_2^i + h\kappa_{3,V_2^i}^i, \dots, V_n^i + h\kappa_{3,V_n^i}^i \right)
\end{aligned}$$

Equation (2.5)

The individual variable for the next time or strain step i.e. X+h was estimated as

$$\begin{aligned}
V_1^{i+1} &= V_1^i + h \left(\frac{\kappa_{1,V_1^i}^i}{3} + \frac{\kappa_{2,V_1^i}^i}{3} + \frac{\kappa_{3,V_1^i}^i}{3} + \frac{\kappa_{4,V_1^i}^i}{3} \right) \\
V_2^{i+1} &= V_2^i + h \left(\frac{\kappa_{1,V_2^i}^i}{3} + \frac{\kappa_{2,V_2^i}^i}{6} + \frac{\kappa_{3,V_2^i}^i}{6} + \frac{\kappa_{4,V_2^i}^i}{3} \right) \\
&\cdot \\
&\cdot \\
&\cdot \\
V_n^{i+1} &= V_n^i + h \left(\frac{\kappa_{1,V_n^i}^i}{3} + \frac{\kappa_{2,V_n^i}^i}{6} + \frac{\kappa_{3,V_n^i}^i}{6} + \frac{\kappa_{4,V_n^i}^i}{3} \right)
\end{aligned}$$

Equation (2.6)

Till the end of plastic strain or time value, the numerical integration was performed. Following numerical integration, the objective function was evaluated. Based on the modelling framework, the objective function differs. For example, the objective function for modelling tensile work hardening behaviour is simple least-square error (LSE) formulation and it is given as

$$LSE = \frac{\sum_{j=1}^n (\sigma_j^{pred} - \sigma_j^{exp})^2}{n - p},$$

Equation (2.7)

where n is the total number of experimental points and p is the number of fitting parameters.

The superscript ‘Pred’ and ‘Exp’ denote numerically predicted strain value and experimental

value, respectively. σ_j^{Exp} and σ_j^{Pred} are the experimental and predicted true stress data for a given plastic strain, respectively. In the case of modelling stress-relaxation behaviour, the σ in Equation (2.7) is replaced by σ_r . For primary and secondary, and additive creep rate models, the objective function in terms of relative least-square error (*RLSE*) is defined as

$$RLSE = \sum_{j=1}^n \left(\frac{\varepsilon_j^{pred} - \varepsilon_j^{exp}}{\varepsilon_j^{exp}} \right)^2, \quad \text{Equation (2.8)}$$

where n refers to the number of creep strain-time data points. ε_j^{Exp} and ε_j^{Pred} are the experimental and predicted creep strain data for a given time, respectively. For the description of creep behaviour using Semba-Dyson-McLean model [108], relative least-square error (*RLSE*) value was evaluated by

$$RLSE = \sum_{i=1}^I \left(\sum_{j=1}^{n_i} \left(\frac{\varepsilon_j^{Pred} - \varepsilon_j^{Exp}}{\varepsilon_j^{Pred}} \right)^2 \right), \quad \text{Equation (2.9)}$$

where I corresponds to the number of creep experiments and n_i is the number of creep strain-time data in the i^{th} experiment. Low values in objective function signify the minimum difference between the predicted and experimental data values. In order to achieve the minima in the objective function, parameter/material constant set associated with the model should be adjusted to the improved values using gradient based interior-point method. This method starts with initial guess parameters inside the feasible region and then uses the projected steepest direction to get the next improved parameters [113]. In the present analysis, barrier function formulation in the interior-point method has been used. This formulation converts a constrained optimisation problem into a series of unconstrained ones. The optimal solutions to these unconstrained sub-problems are in the interior of the feasible region and they converge to the constrained solutions as a positive barrier parameter in the logarithmic barrier function approaching to zero. The fitting procedure was considered as a

converged one when the objective function values computed in two successive iterations are smaller enough than the tolerance value of 1×10^{-6} . When the tolerance value greater than 1×10^{-6} was obtained, the material constant values were readjusted using interior-point algorithm [113] followed by numerical integration to evaluate the least-square error value. These iterations were continued until the tolerance value lower than 1×10^{-6} was obtained. The derived values at the end of iterations were treated as the optimised parameter/material constant set. For different initial guess values, the present iterative strategy has been repeated in order to assure that the derived set of material constants converge towards a global or local minimum.

Chapter 3: Dislocation Density Based Model for the Description of Tensile Flow and Work Hardening Behaviour of 9% Cr Steels

3.1 Introduction

Work hardening of metals and alloys is associated with the evolution of dislocation substructure which in turn is determined by two different competing processes [82-84]. Among the two, the hardening results from the storage of forest dislocations due to the interaction of mobile dislocations with various obstacles such as sessile dislocations, grain and twin boundaries, precipitates and dispersoids. The other is dynamic recovery, which determines the decrease in dislocation density as a result of thermally activated rearrangement and annihilation of dislocations. Several models have been proposed to describe the evolution of dislocation density with plastic strain for the description of deformation behaviour of materials under different loading conditions [81-90, 114]. These models have been categorized based on the number of internal-variables involved to define the deformation characteristics of materials. The selection of a specific model to describe the work hardening behaviour depends on the existence of different stages of work hardening behaviour of metals and alloys. It is known that the instantaneous work hardening rate ($\theta = d\sigma/d\varepsilon$) as a function of flow stress (σ) reveals different stages of microstructure evolution during tensile deformation [83, 115]. Figure 3.1 shows a simplified and generalised version of θ i.e. $d\tau/d\gamma$ versus τ/τ_s plots (where τ is the shear stress, γ is the shear strain and τ_s is the saturation shear stress) exhibiting various stages of work hardening in single crystals deformed in single slip and polyslip. In the case of single crystals deformed in the single slip, stage-I or the easy glide region at low stresses is characterised by a low work hardening rate. Stage-I depends strongly on crystal orientation and does not occur when deformation takes place by multiple-slip from the beginning. A rapid increase in work hardening rate results in a transition from stage-I to athermal stage-II hardening which is weakly sensitive or insensitive

to temperature and strain rate. Following stage-II, typical stage-III results in a continuous and linear decrease in the work hardening rate that depends on applied strain rate and temperature. As stage-III approaches to a saturation level, stage-IV appears at large strains.

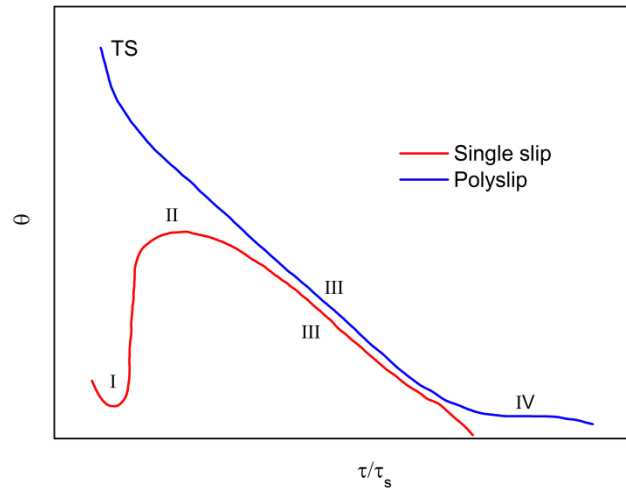


Figure 3.1 Schematic illustration of variations of instantaneous work hardening rate (θ) vs. normalised shear stress (τ/τ_s) exhibiting different stages of work hardening in single crystals deformed in single slip and polyslip [83]. However, work hardening stages in polyslip can also be considered as a representative plot for deformation in polycrystalline materials. I, II, III, IV refer to the short form of stage-I, stage-II, stage-III and stage-IV, respectively and TS refers transient stage.

Stage-IV is characterised by the low and nearly constant work hardening rate. Contrary to the deformation of single crystal with single slip, polyslip in single crystal or polycrystal exhibit a rapid decrease in θ at low stresses (Transient stage) followed by stage-III and stage-IV. In polycrystals, the appearance of stage-II work hardening depends on material and test variable. It has been suggested that stage-II can be better realised by $\theta\sigma$ versus σ plot rather than θ versus σ plot [84, 116]. Christopher and Choudhary [116] further suggested that rather than $\theta\sigma$ versus σ plots, $\theta\sigma_d$ (where, σ_d is the flow stress contribution from dislocation and it is evaluated as $\sigma_d = M\alpha\mu b\rho^{0.5}$) versus σ_d plots provides better visualisation on all the three-stages of work hardening behaviour (transient stage, stage-II and stage-III) in austenitic stainless steel. It is well known that two-internal-variable models provide better description

for true stress-true plastic strain data for the materials showing three-stage (transient stage, stage-II and stage-III) or four-stage (transient stage, stage-II and stage-III and stage-IV) work hardening behaviour [85-90]. Contrary to this, the description for the true stress-true plastic strain data obtained for the materials exhibiting the dominance of stage-III work hardening behaviour can be better provided by one-internal-variable approaches [87]. It is common that tempered martensitic 9% Cr steels exhibit dominance of stage-III work hardening behaviour, irrespective of test conditions [64]. Both $\theta\sigma_d$ vs. σ_d and θ vs. σ plots exhibit two-stage work hardening behaviour characterised by a rapid decrease in work hardening rate at transient stage followed by the linear decrease in stage-III as shown in Figure 3.2 for P91 steel at 300 K as an example. The dominance of stage-III over TS is more discernible from Figure 3.2. Therefore, in the present study, tensile flow and work-hardening behaviour of P9 steel in the two different product forms of thin-section plate and thick-section tubeplate forging and P91 steel have been examined in the framework of dislocation dynamics based one-internal-variable Kocks-Mecking-Estrin [82-84] approach at temperatures ranging from 300 to 873 K. In addition, the dynamic recovery model proposed by Bergström and Hallén [117-118] has also been employed for the evaluation of activation energy for cross-slip and climb of dislocations towards the analysis of dynamic recovery parameter obtained from the one-internal-variable approach. The influence of temperature and initial microstructure on the work-hardening parameters associated with the one-internal-variable approach in P9 and P91 steels have been presented in this chapter. Finally, the interrelationship between uniform plastic strain and dynamic recovery parameter has been established by revisiting the Considère instability criterion [104] for 9% chromium containing tempered martensitic steels.

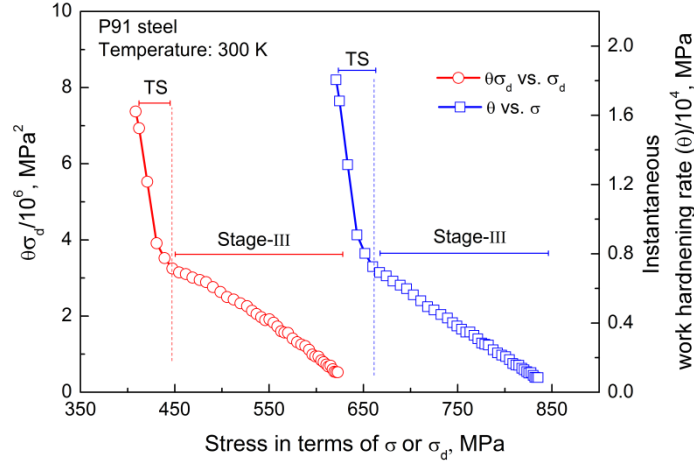


Figure 3.2 Typical example for the variations in $\theta\sigma_d$ with σ_d and θ with σ for P91 steel at 300 K depicts the dominance of stage-III work hardening in tempered martensitic steels. Note that stage-II work hardening behaviour does not appear either in $\theta\sigma_d$ vs. σ_d or in θ with σ plots.

3.2 Modelling Framework and Numerical Implementation

Three different variants of Kocks-Mecking-Estrin approach have been proposed in the literature [82-84]. Irrespective of different variants, the rate of evolution of total dislocation density with strain originates from the two competitive processes, i.e., the storage of dislocations (hardening) and annihilation/rearrangement of dislocations (recovery), which is superimposed in an additive manner. The evolution of total dislocation density (ρ) with true plastic strain (ε_p) is expressed as

$$\frac{d\rho}{d\varepsilon} = M \left(\frac{d\rho^+}{d\varepsilon} - \frac{d\rho^-}{d\varepsilon} \right), \quad \text{Equation (3.1)}$$

where dislocation storage rate $d\rho^+/d\varepsilon$ is inversely related to the dislocation mean free path (L). The rate of dynamic recovery i.e. $d\rho^-/d\varepsilon$ is determined either by the cross slip of screw dislocations at low temperatures or by the diffusion controlled climb of edge dislocations at high temperatures. The boundary between the two temperature regimes generally falls between one-half and two-thirds of the melting point temperature. The rate of dynamic

recovery is expressed with dynamic recovery parameter k_2 as $\frac{d\rho^-}{d\varepsilon_p} = k_2\rho$. According to the

Kocks-Mecking one-internal-variable formulation [82, 83], dislocation structure is treated as the only obstacle to the moving dislocation, and regardless of its arrangement, the mean free path (L) is assumed to be directly proportional to $1/\rho^{0.5}$. Therefore, Equation (1.22) can be written as

$$\frac{d\rho}{d\varepsilon} = M \left(\frac{k_1 \rho^{0.5}}{b} - k_2 \rho \right), \quad \text{Equation (3.2)}$$

where k_1 is the dislocation accumulation or hardening parameter. Estrin and Mecking [84] disregarded the assumption that the mean free path of dislocation is proportional to $1/\rho^{0.5}$, when the spacing between impenetrable obstacles such as particles/precipitates or the grain boundaries is much smaller than the obstacles generated due to dislocation structure itself. An appropriate assumption for this condition is the mean free path that is considered to be a constant in the dislocation accumulation term in Equation (1.22), and the dislocation density evolution with strain is written as,

$$\frac{d\rho}{d\varepsilon} = M \left(\frac{k}{b} - k_2 \rho \right), \quad \text{Equation (3.3)}$$

where k is a constant and is equal to $1/L$. This model is popularly known as modified or Estrin-Mecking one-internal-variable model [84]. In order to incorporate the immobilising effects of both the type of obstacles, i.e., the dislocations and the impenetrable geometrical obstacles such as particles and the boundaries, the term $1/L$ is assumed as a linear combination of the inverse spacing of these obstacles and expressed as

$$\frac{1}{L} = (k + k_1 \rho^{0.5}). \quad \text{Equation (3.4)}$$

The resulting evolution equation for dislocation density with strain is given as a hybrid of Equations (3.2) and (3.3) [84] as

$$\frac{d\rho}{d\varepsilon} = M \left(\frac{k + k_1 \rho^{0.5}}{b} - k_2 \rho \right). \quad \text{Equation (3.5)}$$

The macroscopic flow strength of material related to the microscopic internal variable, i.e., dislocation density for strain rate independent formulation of Equation (1.20) is expressed as

$$\sigma = \sigma_0 + M\alpha\mu b\rho^{0.5}. \quad \text{Equation (3.6)}$$

The term σ_0 is arising from the strength contributions other than dislocation density such as solutes, grain boundaries and precipitates. The work hardening rate ($\theta = d\sigma/d\varepsilon_p$) can be derived from the differential form of Equation (3.6) as

$$\frac{d\sigma}{d\varepsilon} = \frac{M\alpha\mu b}{2\rho^{0.5}} \frac{d\rho}{d\varepsilon}. \quad \text{Equation (3.7)}$$

The flow behaviour of materials can be examined from the numerical integration of work hardening rate given in Equation (7) coupled with dislocation density evolution equation along with appropriate initial boundary conditions, i.e., the initial dislocation density (ρ_i) and the initial stress (σ_I). The initial stress for ρ_i as initial dislocation density can be viewed from the generalised flow stress relation given in the Equation (3.6) as $\sigma_I = \sigma_0 + M\alpha\mu b\rho_i^{0.5}$. In the present investigation, it was considered that the initial stress (σ_I) is equivalent to the true yield strength at $\varepsilon = 0.001$.

Among the three variants, the choice of particular variant depends on the initial microstructure of the material. The microstructure of 9% Cr steel consists of initial high dislocation density inside lath, hierarchical boundaries in terms of prior austenite grains and martensite packets, blocks, sub-blocks and laths [12, 13], and a large amount of precipitates [40]. In view of this, the hybrid model for the evolution of total dislocation density with strain has been assumed to be more appropriate and therefore, the hybrid model has been chosen initially for the work hardening analysis.

The coupled first-order differential forms of Equation (3.5) and Equation (3.7) were integrated by the fourth-order Runge-Kutta method, and the evolution of dislocation density

and flow stress with plastic strain was estimated. The unknown constants in the differential equations such as initial stress (σ_i), hardening parameters (k and k_1) and dynamic recovery parameter (k_2) were optimised using interior-point algorithm by fitting predicted true stress-true plastic strain with experimental σ - ε_p data obtained on P9 and P91 steels (Figure 2.6). The multiplication of $M\alpha$ approximately equal to unity and the value of b as 0.268 nm have been considered for numerical integration. Based on the transmission electron microscopic examination, the dislocation density inside lath close to 10^{14} m^{-2} has been observed for P91 steel [119]. In the present study, the initial dislocation density values of 1×10^{14} , 8×10^{13} and $6 \times 10^{13} \text{ m}^{-2}$ inside lath have been chosen for P91 steel, P9 plate and P9 tubeplate forging, respectively. The experimentally observed yield strength values have guided the basis for choosing initial dislocation density values for the three steels. The components of experimental yield strength at a plastic strain of 0.001 have been considered as the sum of strength contribution from the initial dislocations and other than dislocations, i.e., $\sigma_{\text{Exp,YS}} = \sigma_0 + M\alpha\mu b\rho_i^{0.5}$. Since the observed $\sigma_{\text{Exp,YS}}$ of P91 steel $>$ $\sigma_{\text{Exp,YS}}$ of P9 plate $>$ $\sigma_{\text{Exp,YS}}$ of P9 tubeplate, the values of σ_0 and ρ_i have been numerically adjusted to satisfy the following constraints such as σ_0 of P91 steel $>$ σ_0 of P9 plate $>$ σ_0 of P9 tubeplate forging and ρ_i of P91 steel $>$ ρ_i of P9 plate $>$ ρ_i of P9 tubeplate forging along with the initial dislocation density value as $1 \times 10^{14} \text{ m}^{-2}$ reported for 9% chromium steels in the literature [8, 40, 119]. The upper and lower bounds for the initial stress (σ_i) value are based on true yield strength with ± 50 MPa. Since the variations of the dynamic recovery parameter (k_2) are expected to increase exponentially with increase in temperature at high temperatures, the upper and lower bounds were chosen in the range 0 to 500 [84]. The range of k values in the order of 1×10^5 to $1 \times 10^8 \text{ m}^{-1}$ are related to the inverse of subgrain width. The lower and upper bound values were fixed for k_1 as 0 to 1 based on the Ref. [120, 121]. During non-linear optimisation, the

goodness of fit was judged by least-square error value. For a given temperature, low least-square error values signify the minimum difference between the predicted and experimental flow stress values. At all temperatures and strain rates, the values of constants were obtained from the best-fit true stress–true plastic strain data.

3.3 Parametric Sensitivity Analysis

In general, after initialisation of the parameter set for a given test condition, the parameter values were converged to the specific value during optimisation. Except at 300 K, the convergence for the hardening parameter k_1 to a specific value was not noticed during optimisation in this analysis. In order to understand the influence of variation in parameter values on least-square error value, the parameter sensitivity analysis has been performed. In this analysis, the sensitivity of this parameter has been examined by adjusting the value of dislocation accumulation parameter, k_1 in the range from 10^{-6} to 1 and simultaneously evaluating the least-square error value without changing the value of other optimised parameters. Similarly, the sensitivity analysis for other hardening parameter k is also performed to understand the relative influence of these two hardening parameters on work hardening behaviour of 9% Cr steels. Figure 3.3 shows the variations in least-square error value with k_1 parameter towards the parametric sensitivity analysis for P9 steel tubeplate forging and plate, and P91 steel at three different temperatures. At 300 K, the dislocation accumulation parameter (k_1) has been successfully optimised to a specific value for P9 and P91 steels. It can be seen that any deviation in k_1 values from the optimised value results in the sharp increase in least-square error values at 300 K. Contrary to this, the dislocation accumulation parameter, k_1 falls less than 10^{-3} and convergence to a specific value is not observed at intermediate and high temperatures. Irrespective of grades and test conditions, other parameters such as initial stress (σ_I), hardening parameter (k) and dynamic recovery

parameter (k_2) converge to a specific value. Figure 3.4 is shown as an example for the convergence of the hardening parameter k with minimum least-square error value for P9 and P91 steels at three different temperatures.

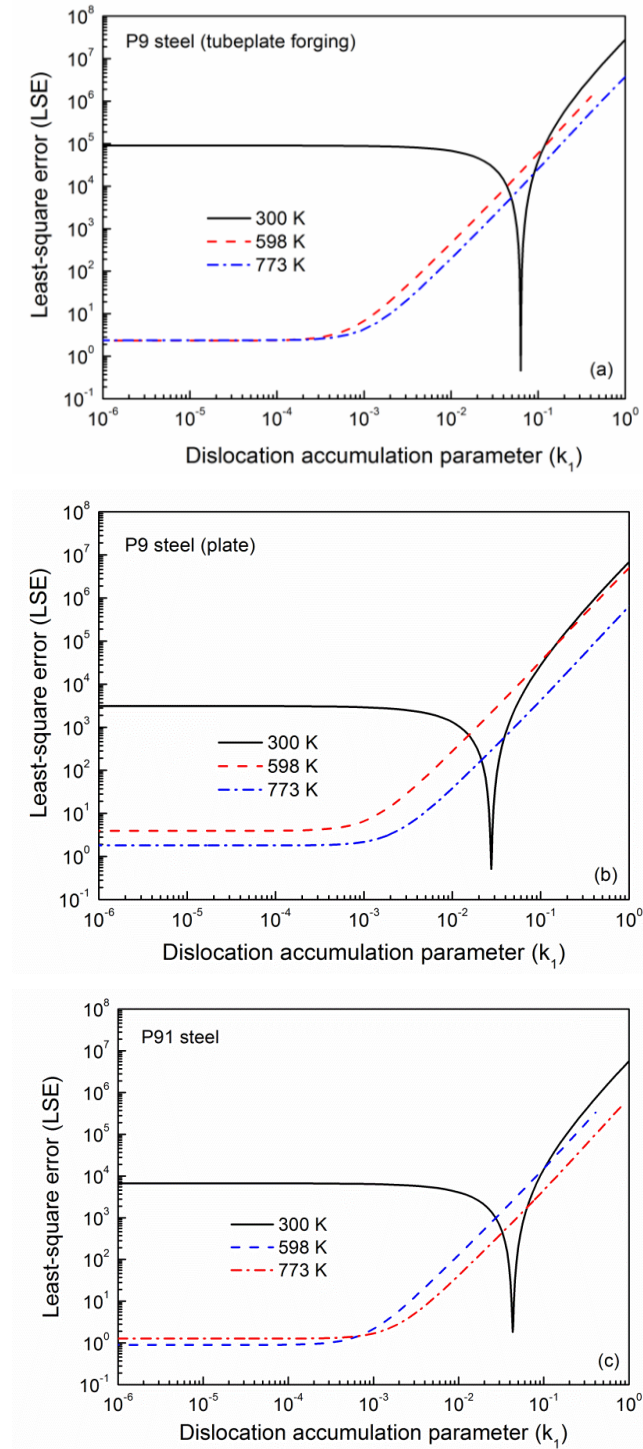


Figure 3.3 Variations in least-square error with dislocation accumulation parameter (k_1) at 300, 598 and 773 K for P9 steel tubeplate forging and plate, and P91 steel.

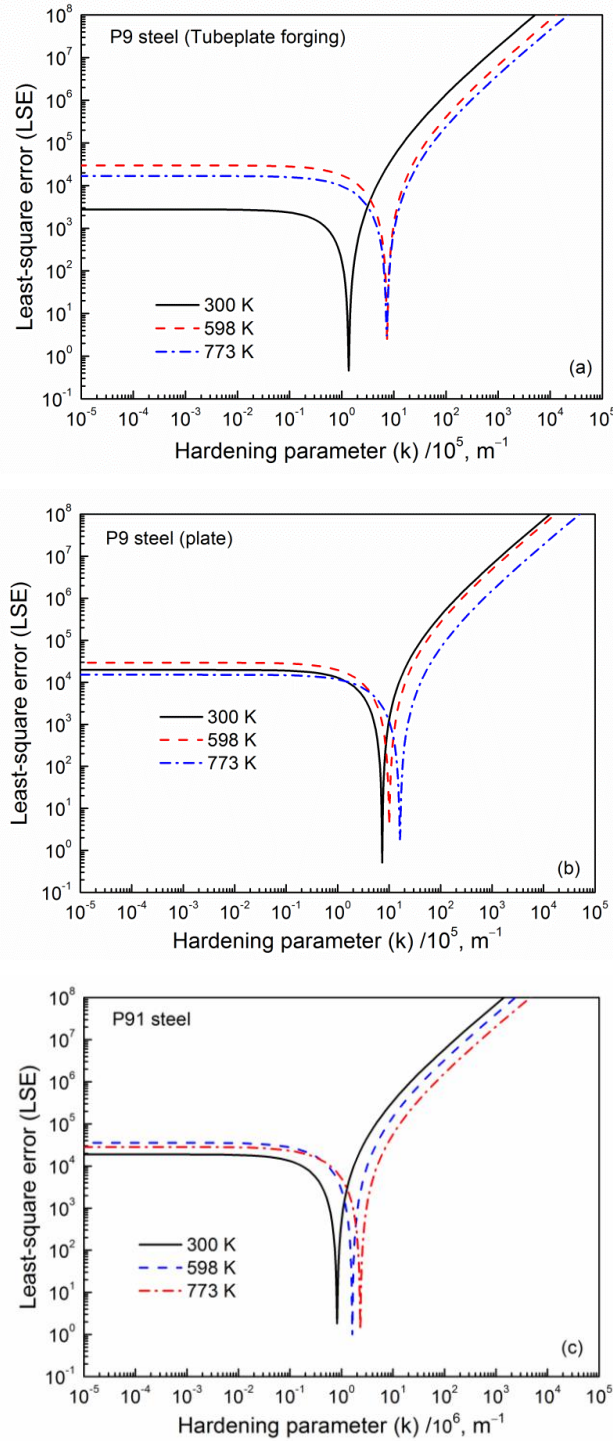


Figure 3.4 Variations in least-square error with hardening parameter (k) at 300, 598 and 773 K for P9 steel tubeplate forging and plate, and P91 steel.

The low values of dislocation accumulation constant, k_1 without convergence in the temperature range 473-873 K clearly provide the evidence of the dominance of k/b over $k_1 \cdot \rho^{0.5}/b$ at intermediate and high temperatures. In view of this, the dislocation storage term $k_1 \cdot \rho^{0.5}/b$ in Equation (3.5) has been disregarded in the present analysis. Accordingly, the

modified or Estrin-Mecking one-internal-variable model for total dislocation density evolution with strain, i.e., Equation (3.3) coupled with Equation (3.7) has been used for describing the macroscopic true stress-true plastic strain behaviour in the entire temperature range 300-873 K for the steels. The analysis using Estrin-Mecking approach resulted in the optimised values of all the parameters, i.e., σ_I , k and k_2 obtained from the convergence to the respective specific values with a low least-square error value.

3.4 Influence of Temperature on Flow Behaviour of P9 Plate, P9 Tubeplate and P91 Steels

True stress (σ)-true plastic strain (ϵ) data obtained at temperatures ranging from 300 K to 873 K for P9 steel tube plate forging is shown as double logarithmic plots of σ vs. ϵ in Figure 3.5. At room and intermediate temperatures in the range 300-723 K, σ - ϵ exhibited curvilinear behaviour with large positive stress deviations at low strains from the extrapolated linear σ - ϵ data at high strains. With increasing temperature, decrease in the positive stress deviations at low strains was observed and σ - ϵ displayed a tendency towards linear behaviour at high temperatures in the range 773–873 K. The increase in temperature on σ - ϵ is reflected in a decrease in flow stress and uniform plastic strain with increasing temperature from 300 to 523 K followed by insignificant variations in the values at intermediate temperatures in the range 523–723 K and a rapid decrease in flow stress and uniform plastic strain at high temperatures above 723 K. Like P9 steel tubeplate forging, P9 steel in plate product form and P91 steel exhibited similar σ - ϵ behaviour in the temperature range 300-873 K and displayed three distinct temperature regimes in the variations of flow stress and uniform plastic strain with temperature.

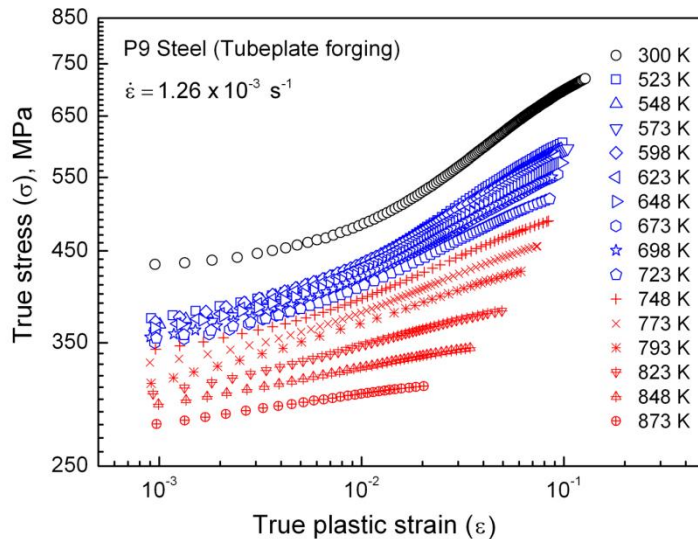


Figure 3.5 Influence of temperature on true stress (σ)-true plastic strain (ϵ) behaviour of thick section tubeplate forging of P9 steel.

It is noteworthy to comment here that during tensile deformation, both the product forms of P9 steel, i.e., plate and tubeplate forging and P91 steel exhibited serrated flow characterised by the occurrence of types A, A+B and C serrations at intermediate temperatures in the range 523-673 K [21, 122]. For measuring average load values from the serrated load-elongation curves, a uniform approach based on the classification of serrations was adopted [123]. Figure 3.6 shows the typical averaging scheme of load-elongation values for types A, A+B and C serrations for tubeplate forging of P9 steel. For type A serrations showing an abrupt rise in the loads followed by discontinuous drops to or below the general level of load-elongation curves, general levels of load values were considered. For type B serrations that oscillate about the general level of load values, mean load values were considered. For type C serrations characterised by load drops always below the general level of load values, envelope load values were taken for stress-strain data. The generated load-elongation data using averaging were considered for the conversion of true stress-true plastic strain data in this analysis.

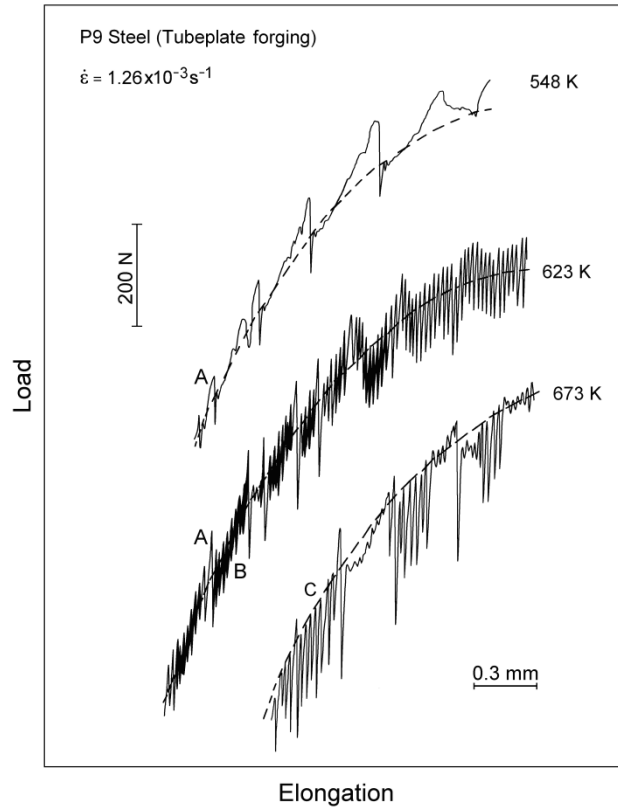


Figure 3.6 Averaging scheme for load-elongation curves showing type A, A+B and C serrations at intermediate temperatures in P9 steel tubeplate forging. Average load-elongation values considered for evaluating true stress-true plastic strain are shown by broken lines.

True stress vs. true plastic strain data at different temperatures have been predicted using the optimised parameters such as σ_I , k and k_2 along with appropriate initial dislocation density in the Estrin–Mecking one-internal-variable model described by the numerical integration of coupled differential Equation (3.3) and Equation (3.7). The comparison of true stress vs. true plastic strain for P9 steel plate and tubeplate forging and P91 steel at 300, 623 and 773 K representing flow behaviour at room, intermediate and high temperatures, respectively, is typically shown in Figure 3.7. The respective best fit σ - ϵ_p data obtained using the Estrin–Mecking approach is superimposed as full lines. At all temperatures, good agreement between the predicted and experimental σ - ϵ data for P9 steel plate and tubeplate forging and P91 steel can be seen in Figure 3.7. P91 steel exhibited consistently higher flow

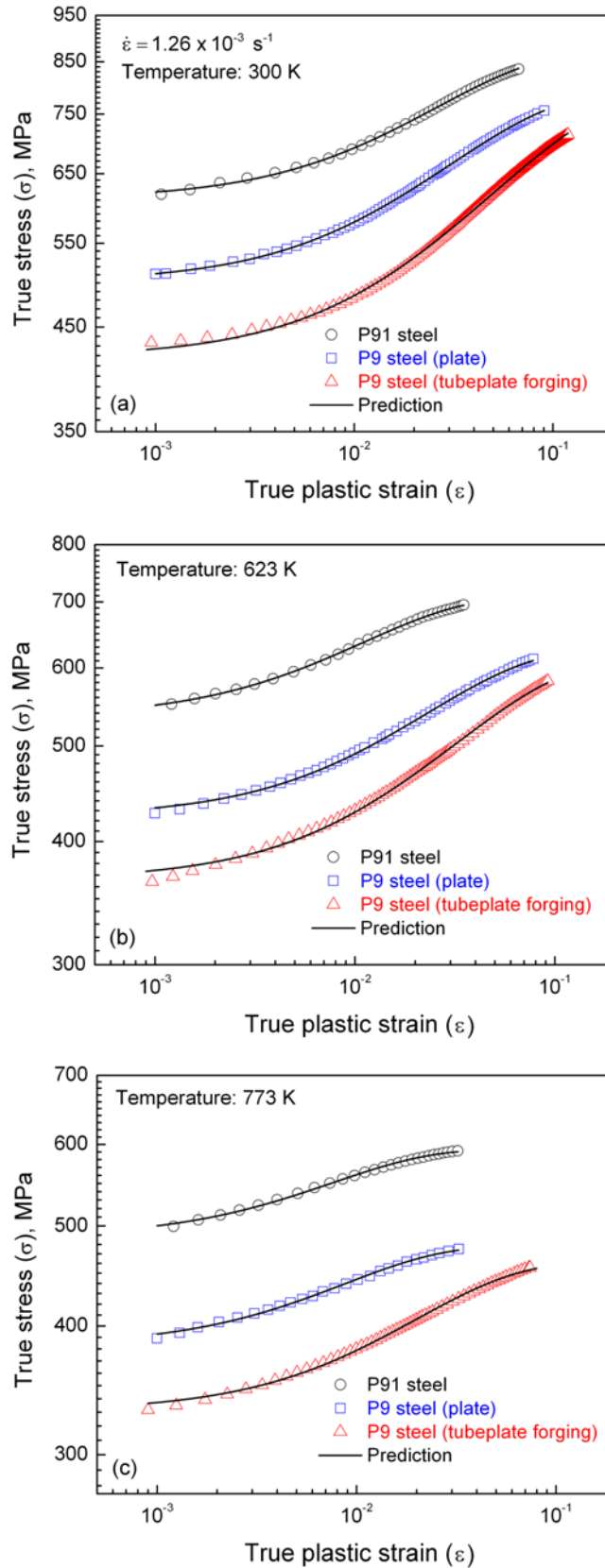


Figure 3.7 True stress (σ)-true plastic strain (ϵ) data of P9 steel plate and tubeplate forging and P91 steel at (a) 300 K, (b) 623 K and (c) 773 K. Respective best fit data predicted by Estrin-Mecking approach are superimposed as full lines.

stresses than those shown by both the plate and tubeplate forging of P9 steel at temperatures ranging from 300 to 873 K. Among the two product forms of P9 steel, the tubeplate forging displayed lower flow stresses than the plate material. Further, P9 steel tubeplate forging exhibited higher average work hardening rate with increasing plastic strain than those observed for P9 steel plate and P91 steel (Figure 3.7).

3.5 Variations in Work Hardening Parameters with Temperature for P9 Steel Plate and Tubeplate Forging, and P91 Steel

The temperature dependence of initial stress (σ_I) and strength contributions arising due to other than dislocations (σ_0) for P9 steel plate and tubeplate forging and P91 steel is shown in Figure 3.8. In order to bring out the influence of temperature alone on σ_I and σ_0 , the shear modulus compensated stress values have been used. The temperature dependence of shear modulus was derived from Young's modulus (E) values taken from French nuclear design code RCC-MR for P91 steel [124]. A marginal decrease in normalized initial stress (σ_I/μ) and strength contributions due to other than dislocations (σ_0/μ) from 300 to 523 K followed by well defined peaks or plateaus at intermediate temperatures and a rapid decrease at high temperatures can be seen in P9 and P91 steels in Figure 3.8. P91 steel exhibited the highest σ_I/μ and σ_0/μ values over temperatures ranging from 300 to 873 K followed by plate and tubeplate forging of P9 steel. The variations in hardening parameter (k) with temperature for P9 and P91 steels are presented in Figure 3.9. Insignificant variations in k have been observed for P9 steel plate and tubeplate forging at room and intermediate temperatures. At high temperatures, an increase in k values with increase in temperature for both plate and tubeplate forging can be seen. P91 steel exhibited a marginal increase in k value at temperatures ranging from 300 to 723 K followed by a rapid increase at high temperatures.

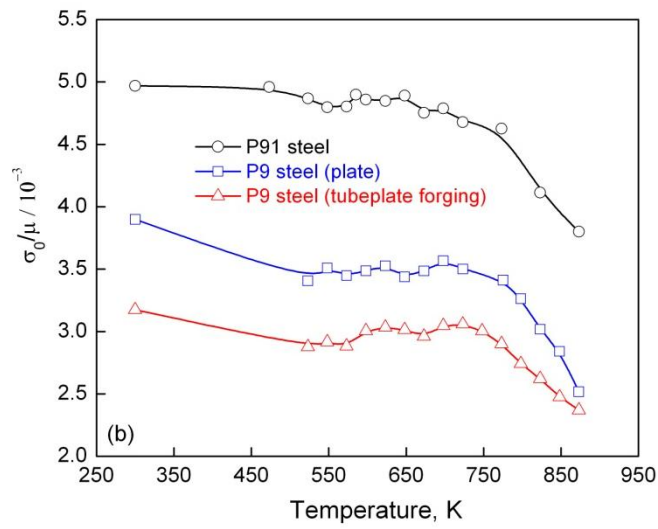
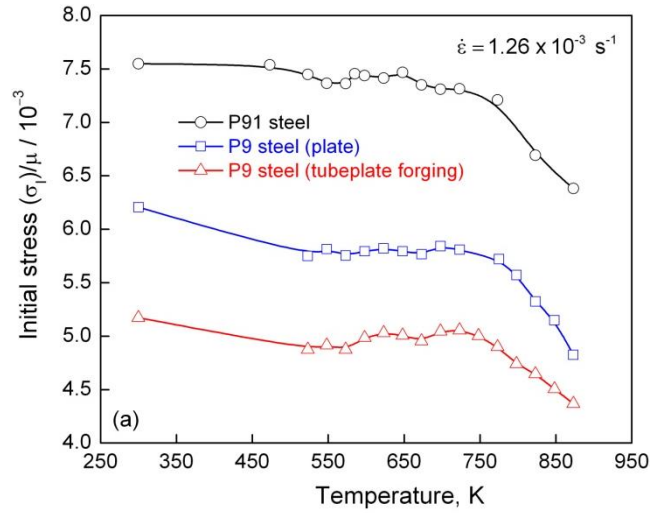


Figure 3.8 Variations of shear modulus compensated (a) initial stress (σ_I/μ) and (b) σ_0/μ with temperature for P9 steel plate and tubeplate forging and P91 steel.

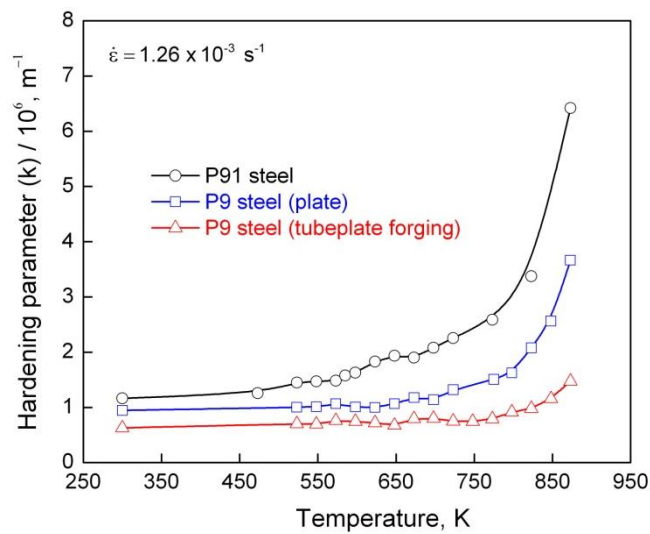


Figure 3.9 Variations of hardening parameter (k) with temperature for P9 steel plate and tubeplate forging and P91 steel.

Further, P91 steel displayed consistently higher k values than those observed for P9 steel plate and tubeplate forging in the temperature range 300-873 K. At all temperatures, tubeplate forging exhibited lower k values than P9 plate material. The variations in dynamic recovery parameter (k_2) with temperature for P9 and P91 steels are shown in Figure 3.10. A marginal increase in k_2 from 300 to 723 K followed by a rapid increase at high temperatures has been observed for P91 steel. Both plate and tubeplate forging of P9 steel exhibited insignificant variations in k_2 at room and intermediate temperatures and rapid increase at high temperatures. Like hardening parameter, a consistently higher k_2 was observed for P91 steel than those for P9 steel plate and tubeplate forging in the temperature range 300-873 K. At all temperatures, tubeplate forging displayed the lowest k_2 values, whereas the k_2 values for P9 steel plate material lay in between those for P9 steel tubeplate forging and P91 steel.

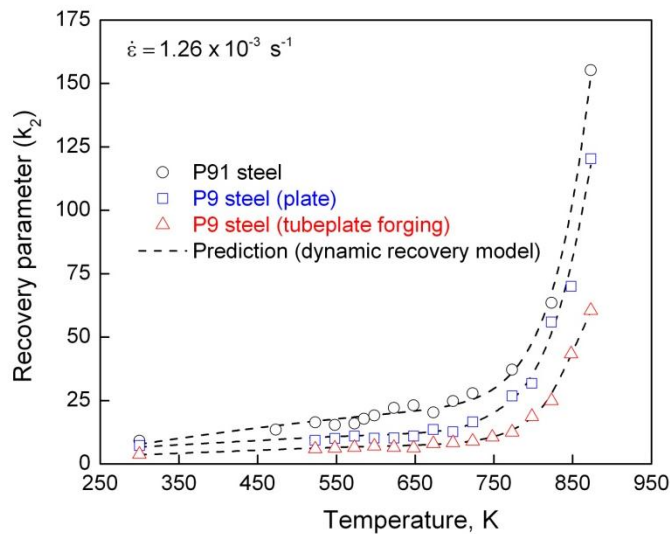


Figure 3.10 Variations of recovery parameter (k_2) with temperature for P9 steel plate and tubeplate forging and P91 steel.

Bergström and Hallén [117, 118] derived the constitutive model for dynamic recovery parameter with an assumption that the dynamic recovery is assisted by cross-slip of screw dislocations at low temperatures, whereas dislocation climb dominates at high temperatures.

Accordingly, the two components of dynamic recovery parameter as cross-slip and climb dominated recovery regimes are expressed in generalized form as

$$k_2 = k_{2,Cross-slip} + k_{2,Climb} \quad \text{Equation (3.8)}$$

The term $k_{2,Cross\ slip}$ is given as

$$k_{2,Cross\ slip} = C_c \exp\left(\frac{-Q_c}{RT}\right), \quad \text{Equation (3.9)}$$

where C_c is a constant, R is the universal gas constant and Q_c is the activation energy for cross slip mechanism. The term $k_{2,Climb}$ in Equation (3.8) is given as

$$k_{2,Climb} = A_m \exp\left(\frac{-Q_m}{3RT}\right), \quad \text{Equation (3.10)}$$

where A_m is a constant and Q_m is the activation energy for vacancy diffusion. Following the assumption that cross-slip dominates at room and intermediate temperatures, k_2 parameter was fitted with Equation (3.9), and the values of C_c and Q_c were evaluated. The values of $k_{2,Climb}$ at high temperatures above 723 K were then computed as $k_{2,Climb} = k_2 - k_{2,Cross\ slip}$ by appropriately using the extrapolated $k_{2,Cross\ slip}$ values for different temperatures. Following this, the values of A_m and Q_m were evaluated from the best fit $k_{2,Climb}$ vs. T using Equation (3.10). The average values of C_c , Q_c , A_m and Q_m for P9 steel plate and tubeplate forging and P91 steel are summarized in Table 3.1. The values of activation energy for cross-slip mechanism Q_c varies closely from 2.7 to 4.5 kJ mol⁻¹, and for climb mechanism, Q_m varies from 297 to 394 kJ mol⁻¹. The predicted values of dynamic recovery parameter using Bergstrom and Hallen [117, 118] approach for P9 steel plate and tubeplate forging and P91 steel at different temperatures are also superimposed as broken lines in Figure 3.10. A good agreement between predicted and experimental k_2 values can be clearly seen in Figure 3.10. The evolution of dislocation density towards steady state or, saturation value (ρ_{sat}) has been obtained for condition $d\rho/d\varepsilon = 0$ in Equation (3.3) and the ρ_{sat} is expressed as

$$\rho_{sat} = \frac{k}{bk_2}$$

Equation (3.11)

Table 3.1- The Calculated Values of Constants and Activation Energy for Dynamic Recovery Model Proposed by Hallén and Bergström [117, 118].

Steel and product form	C_c	$Q_c, \text{kJ mol}^{-1}$	$A_m \times 10^9$	$Q_m, \text{kJ mol}^{-1}$
P91 steel	47.9	4.5	9.27	394
P9 steel: Plate	19.3	2.7	2.88	297
P9 steel: Tubeplate forging	13.3	3.3	3.34	392

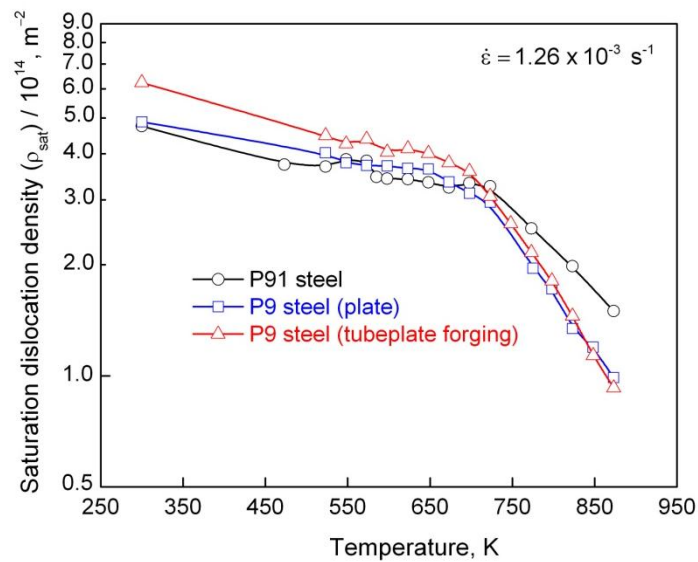


Figure 3.11 Variations of dislocation density at saturation (ρ_{sat}) with temperature for P9 steel plate and tubeplate forging and P91 steel.

The variations in the computed saturation dislocation density with temperature for the three steels are shown in Figure 3.11. A marginal decrease in the dislocation density at saturation in the temperature range 300-723 K followed by a rapid decrease at high temperatures can be seen for P91 steel and the two different product forms of P9 steel. At room and intermediate temperatures, P9 steel tubeplate forging exhibited higher ρ_{sat} values than P9 steel plate and P91 steel. At high temperatures, higher ρ_{sat} values for P91 steel than those for P9 steel plate

and tubeplate forging were obtained. Only a marginal difference in ρ_{sat} values between P91 steel and P9 plate material was noticed at room and intermediate temperatures. At high temperatures, both plate and tubeplate forging of P9 steel displayed similar ρ_{sat} values. Saturation stress (σ_{sat}) has been interpreted as a state of constancy arising due to the equilibrium between dislocation generation and its annihilation and rearrangement to low energy configuration [82-84]. Accordingly, the normalized saturation stress (σ_{sat}/μ) has been evaluated for the condition when dislocation density approaches to its steady state value as

$$\frac{\sigma_{sat}}{\mu} = \frac{\sigma_0}{\mu} + \frac{M\alpha\mu b\rho_{sat}^{0.5}}{\mu}. \quad \text{Equation (3.12)}$$

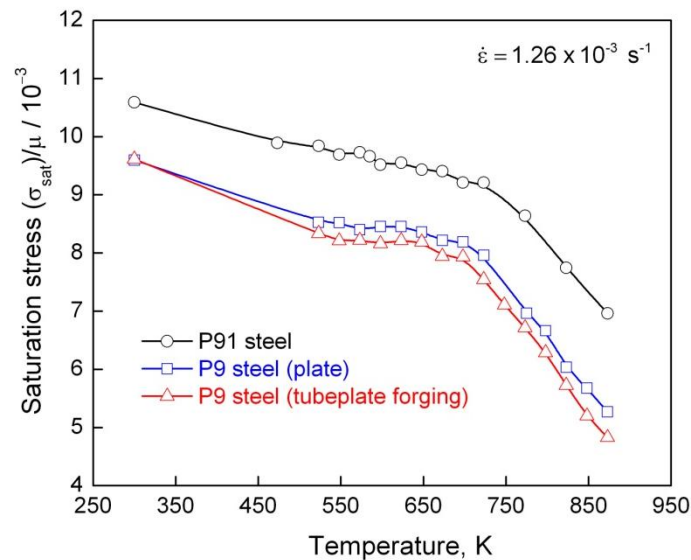


Figure 3.12 Variations of normalized saturation stress (σ_{sat}/μ) with temperature for P91 steel plate and tubeplate forging and P91 steel.

The variations of normalized saturation stress computed using Equation (3.12) with temperature are presented in Figure 3.12. A gradual decrease in σ_{sat}/μ in the temperature range 300-723 K followed by a rapid decrease at high temperatures has been observed for P91 steel. P9 steel in both the product forms displayed three distinct temperature regimes characterised by a marginal decrease with increase in the temperature from 300 to 523 K followed by well-defined plateaus at intermediate temperature and rapid decrease at high temperatures. At all temperatures, P91 steel exhibited significantly higher σ_{sat}/μ values than

those for plate and tubeplate forging of P9 steel. Marginally higher σ_{sat}/μ values were obtained for P9 steel plate than those for tubeplate forging.

3.6 Applicability of Estrin-Mecking One-Internal-Variable Approach to 9% Cr Steels

Accurate prediction and explanation of true stress–true plastic strain behaviour is the key to the applicability of the theory of work hardening to metal and alloys. In the tempered lath martensitic steel consisting of hierarchical boundaries, it has been reported that the plastic flow originates from the preferentially oriented martensitic laths and propagates to the sub-block boundaries [125]. Since sub-block boundaries display a misorientation of about 10° , it has been suggested that the slip would be restricted by the sub-block boundaries at low strains followed by the block boundaries with progress in further deformation. This implies that the size of effective geometrical obstacles unit changes with increase in the plastic deformation [125]. In addition to hierarchical boundaries, the presence of a large amount of fine precipitates such as $M_{23}C_6$ and MX in P91 steel, and $M_{23}C_6$ and M_2X in P9 steel also provide other effective geometrical obstacles for the glide of dislocations along with forest dislocations. The inclusion of the influence of the individual geometrical obstacles such as hierarchical boundaries and precipitates on dislocation accumulation and annihilation processes separately becomes difficult. In view of this, the dislocation accumulation parameter k in Equation (3.5) is assumed to represent the inverse average geometrical obstacle spacing for glide of dislocations. The observed low values of dislocation accumulation constant, k_1 , without convergence in the temperature range 473–873 K (Figure 3.3) clearly indicated the dominance of dislocation storage term k/b over $k_1 \cdot \rho^{0.5}/b$ at intermediate and high temperatures. This also suggested that the hierarchical boundaries and a large amount of precipitates act as effective barriers to the glide of dislocations in tempered martensitic steel. Discounting $k_1 \cdot \rho^{0.5}/b$ term in Equation (3.5), the hybrid model reduces to

the Estrin–Mecking one-internal-variable model, where k represents the global influence of hierarchical boundaries and precipitates on dislocation density evolution with strain. In the present investigation, the analysis in terms of the coupled differential equations, i.e., Equations (3.3) and (3.7) provided an adequate description of the macroscopic true stress-true plastic strain behaviour of P9 and P91 steels at temperatures ranging from 300 to 873 K (Figure 3.7). Good agreement between predicted and experimental true stress-true plastic strain data in P9 and P91 steels is discernible in Figure 3.7. The applicability of one-internal-variable Estrin-Mecking model is also reflected in the low least-square error values obtained for different temperatures in P9 and P91 steels. The average least-square error values of 1.7, 2.6 and 1.1 have been observed over the temperatures ranging from 300 K to 873 K for P9 plate, P9 tubeplate forging and P91 steel, respectively.

3.7 Influence of Temperature and Initial Microstructure on Flow and Work hardening Behaviour of 9% Cr Steels

The variations in the normalized initial stress (σ_I/μ), flow stress contribution from other than dislocations (σ_0/μ) and saturation stress (σ_{sat}/μ) along with dislocation density at saturation ($\rho_{sat} = k/bk_2$) with temperature exhibited three distinct temperature regimes (Figures 3.8, 3.11 and 3.12). The observed grouping of σ - ϵ_p data (e.g., P9 steel tubeplate forging in Figure 3.5) is reflected in the occurrence of plateaus in σ_I/μ , σ_0/μ , σ_{sat}/μ and ρ_{sat} due to dynamic strain ageing (DSA) at intermediate temperatures in P9 and P91 steels. The occurrence of dynamic strain ageing is manifested by serrated flow in the load-elongation curves at intermediate temperatures in P9 and P91 steels [18, 21, 122]. This is typically shown for P9 steel tubeplate forging in Figure 3.6. Based on the measurement of activation energy for the onset of serrated flow, it has been suggested that dynamic interaction between diffusing interstitial solute such as carbon and mobile dislocations to be responsible for DSA

in P9 and P91 steels [18, 21, 122]. In addition to serrated flow, plateaus/peaks in flow stresses represent other manifestations of DSA in 9% Cr steels. Both hardening (k) and dynamic recovery (k_2) parameters display either insignificant variations in P9 steel plate and tubeplate forging or, only marginal increase in values for P91 steel at room and intermediate temperatures (Figures 3.9 and 3.10). Rather than a monotonic increase in k_2 with increasing temperature, the observed insignificant or, marginal variations in k_2 clearly demonstrate reduced dynamic recovery in the DSA temperature regime. It has been reported that DSA causes an increase rate of multiplication of dislocations and delay in recovery of dislocation structure due to reduced mobility of dislocations [16, 126-128]. A significant increase in dislocation density along with an increased work hardening index relative to those at lower and higher temperatures has been observed in the DSA temperature regime [16]. These observations clearly suggest decreased dynamic recovery due to reduced propensity to cross slip in the DSA regime.

The observed sharp decrease in σ_1/μ , σ_0/μ , σ_{sat}/μ and ρ_{sat} , and rapid increase in k_2 with increase in temperature indicate acceleration of recovery processes at high temperatures (Figures 3.8, 3.11 and 3.12). In P9 and P91 steels, the observed low k_2 values indicate the dominance of cross-slip of dislocations at room and intermediate temperatures. A change in recovery mechanism from cross-slip to climb of dislocations results in high k_2 values at high temperatures. It has been reported that the dynamic recovery parameter, k_2 is directly proportional to critical annihilation distance [129, 130]. The critical annihilation distance is defined statistically as the maximum distance between the parallel slip planes of two attractive edge or, screw dislocations that can mutually annihilate each other [129, 130]. An increasing k_2 value with increasing temperature suggests an increase in the probability of annihilation of dislocations. The rapid increase in k_2 at high temperatures is also reflected in the rapid evolution of dislocation density with plastic strain with increase in temperature. The

evolution of dislocation density with plastic strain at room temperature, i.e., 300 K, intermediate temperatures, i.e., 523, 573, 623 and 673 K, and high temperatures, i.e., 773, 823 and 873 K is typically shown for P9 steel tubeplate forging in Figure 3.13. The rapid evolution of dislocation density towards steady state or, saturation value at high temperatures can be seen at 773, 823 and 873 K in Figure 3.13. This is in contrast to the observed variations in the evolution of dislocation density with plastic strain showing only marginal variations at room and intermediate temperatures. A marginal decrease in the dislocation density at high strains with increase in temperature from 300 to 523 K (Figure 3.13) is reflected in the marginal reduction of saturation dislocation density in P9 and P91 steels shown in Figure 3.11. Both P9 steel plate and P91 steel also exhibited nearly similar evolution of dislocation density with plastic strain at different temperatures (Figure 3.14).

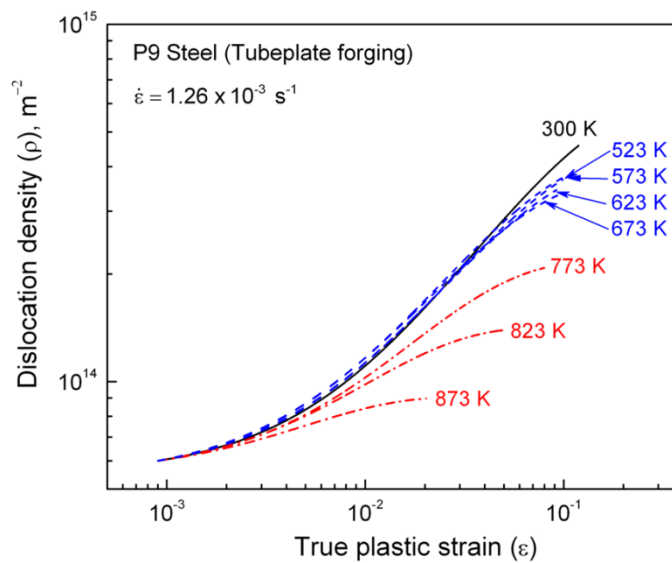


Figure 3.13 Evolution of dislocation density (ρ) with true plastic strain (ϵ) at different temperatures for P9 steel tubeplate forging.

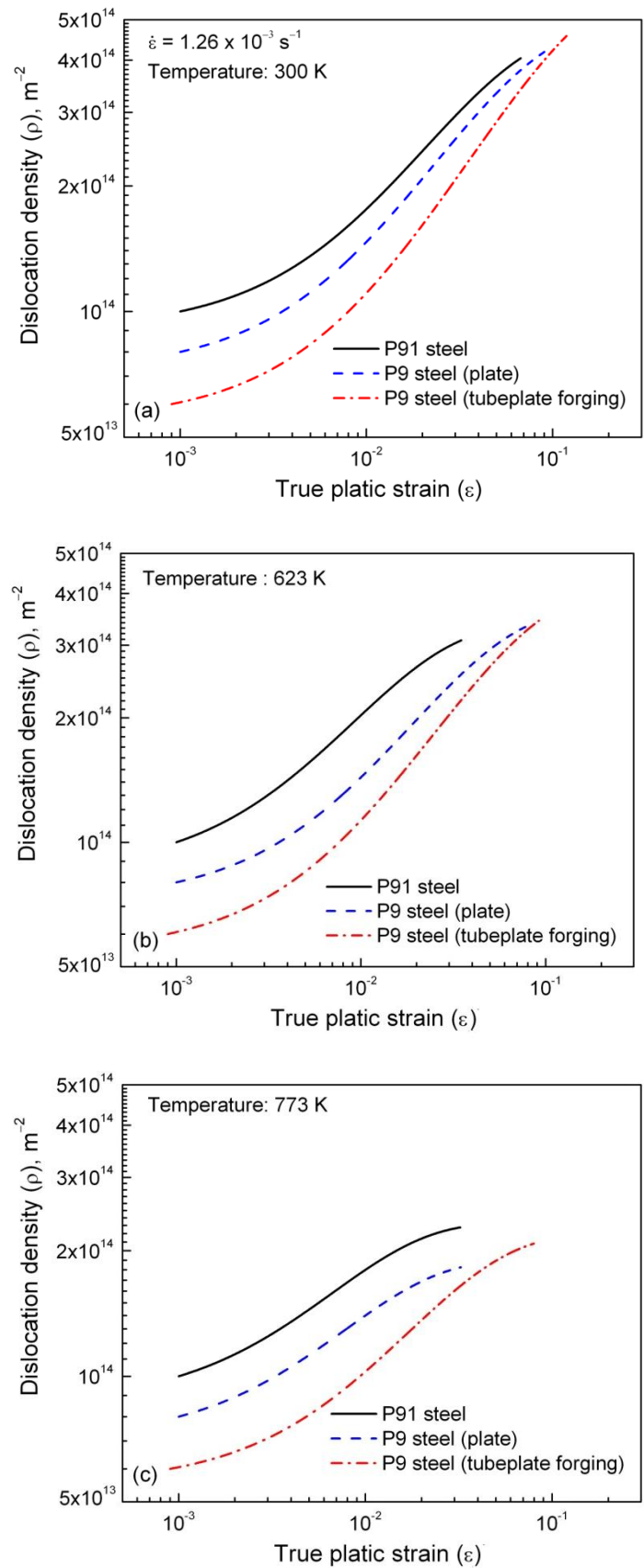


Figure 3.14 Evolution of dislocation density (ρ) with true plastic strain (ϵ) at (a) 300 K, (b) 623 K and (c) 773 K for P9 steel plate and tubeplate forging and P91 steel.

The low values of activation energy in the range 2.7-4.5 kJ mol⁻¹ ($\sim 46.3 \times 10^{-3}$ eV/atom) obtained at room and intermediate temperatures (Table 3.1) is comparable to the reported values of activation energy for cross-slip mechanism in FCC metals having high stacking fault energy and 18-8 stainless steel [118]. Following Bergstrom and Hallen [117-118], activation energy Q values obtained in the range 594-788 kJ mol⁻¹ (i.e., $Q = 2 \times Q_m$) can be assigned for P9 steel plate and tubeplate forging and P91 steel at high temperatures. The activation energy obtained for high temperatures is higher than the activation energy value of 250 kJ mol⁻¹ for self-diffusion in BCC Fe. However, the activation energy values are comparable to the apparent activation energy values in the range 468-719 kJ mol⁻¹ reported for climb-controlled creep deformation in 9% Cr ferritic-martensitic steels in the high stress regime [24, 29, 30]. The high values of activation energy have been rationalised by invoking resisting/back stress concept into power-law creep relationship resulting in the true activation energy close to self diffusion in P9 and P91 steels [29, 30]. Further, the distinct values of activation energy obtained for the temperature range 300-723 K and 773-873 K are consistent with the observed variations in k and k₂ with temperature in the three steels (Figures 3.9 and 3.10).

At all temperatures, significantly higher σ_I/μ and σ_0/μ observed for P91 steel than those for P9 steel plate and tubeplate forging can be attributed to the presence of relatively fine martensite lath structure along with fine M₂₃C₆ carbides decorated on the hierarchical boundaries and the distribution of fine MX type niobium and vanadium carbides/carbonitrides in the matrix (Table 2.4). The large reduction in σ_I/μ and σ_0/μ values obtained for P9 steel tubeplate forging compared to P9 steel plate material arises from the coarseness of microstructure in terms of coarse prior austenitic grain and martensite packet and lath size, relatively low dislocation density and coarse precipitates (Figures 2.1 and 2.2). It is well known that the morphology of tempered martensitic microstructure is greatly influenced by

prior austenitic grain size which in turn is affected by the heating rate, austenitising temperature and soaking duration at austenitising temperature [131, 132]. Increase in prior austenite grain size with increase in the austenitising temperature and/or soaking duration results in the increased size of packets and blocks in the martensitic microstructure [131, 132]. It has been shown that the slow cooling from austenitising temperature leads to the development of coarse packets and blocks size in lath martensitic structure [133]. In the present investigation, the extended austenitising heat treatment (in terms of slow heating and higher soaking duration at austenitising temperature) given on the thick section tubeplate forging resulted in an increase of about 5 times in the prior austenite grain size compared to N+T P9 steel plate material. As a result, P9 steel tubeplate forging also possesses significantly coarser martensitic packets and blocks than those in P9 steel plate material. Further, slow cooling rate experienced by tubeplate forging due to its large section size also add in the coarseness of initial microstructure in terms of coarse packets and blocks size and increased lath width of martensite. The influence of slow cooling rate experienced by tubeplate forging is indicated by the presence of ~2 % pro-eutectoid ferrite in the microstructure [134]. In addition to above, the extended tempering treatment in terms of slow heating to 1023 K and soaking for 8 hours followed by slow cooling employed on the tubeplate forging leads to further softening of lath martensitic microstructure in terms of decrease in dislocation density and coarsening of precipitates [135, 136]. Large inter-particle spacing and reasonably increased precipitate size in P9 steel tubeplate forging can be seen qualitatively in Figure 2.2 compared to P9 steel plate material (Figure 2.1). The coarseness of microstructure in terms of coarse hierarchical boundaries and large inter-particle spacing in the tubeplate forging leads to large inter-barrier distance for moving dislocations. Since hardening parameter, k is inversely related to the mean free path of dislocations, the observed decrease in k values in the order of P91 steel, P9 steel plate and P9 steel tubeplate forging

appears to be appropriate. The dynamic recovery parameters k_2 is treated to be directly proportional to k [137]. Since k and k_2 are interrelated, the decrease in k is reflected in a systematic decrease in k_2 with increase in the degree of microstructural softening in P9 and P91 steels. The improved work hardening in P9 steel tubeplate forging is reflected in the higher saturation dislocation density values compared to P9 steel plate and P91 steel at room and intermediate temperatures (Figure 3.11). The increase in dislocation density from low initial values to higher saturation value at high strains for P9 tube plate forging clearly demonstrate the higher work hardening ability of the steel than P9 plate and P91 steel. The relative gains in dislocation density during plastic deformation in P9 plate and tubeplate forging and P91 steel have been examined from the variations of the ratio of saturation dislocation density (ρ_{sat}) and initial dislocation density (ρ_i) with temperature presented in Figure 3.15. P9 steel tubeplate forging displayed the higher ρ_{sat}/ρ_i ratio indicating larger gains in dislocation density from its initial value than P9 steel plate and P91 steel in the temperature range 300-873 K. P91 exhibited the lowest ρ_{sat}/ρ_i ratio indicating the smallest gain in dislocation density due to deformation. Larger gains in dislocation density indicate improved work hardening ability of P9 steel tubeplate forging over P9 steel plate and P91 steel. Higher work hardening in P9 steel tubeplate forging is also reflected in the larger gains in the flow stress contribution from dislocations ($\rho^{0.5} \propto \sigma_d$) due to its softened microstructure than the plate material of P9 steel. This can be seen as the small difference in saturation stress values between P9 plate and tubeplate forging (Figure 3.12) compared to the observed large differences in the initial flow stress values, σ_I/μ and σ_0/μ (Figure 3.8). Between P9 steel plate and P91 steel, P9 steel plate displayed relatively higher gains in dislocation density indicating improved work hardening characteristics than P91 steel. This resulted in the relatively reduced difference in saturation stress values between P9 steel plate and P91 steel (Figure 3.12) compared to the difference in the respective σ_I/μ and σ_0/μ values (Figure 3.8). The

lower work hardening ability of P91 steel arise from comparatively finer geometrical obstacles such as hierarchical boundaries and fine precipitates than those present in P9 steel plate material. The detailed analysis in the framework of Estrin-Mecking approach suggests that the evolution of internal variable, i.e. the dislocation density with plastic strain and the work hardening parameters depends strongly on the degree of softened microstructure in 9% chromium steels. The comparative examination of flow and work hardening behaviour clearly indicated that the ability to work hardening in 9% chromium containing steels is strongly sensitive to initial microstructure.

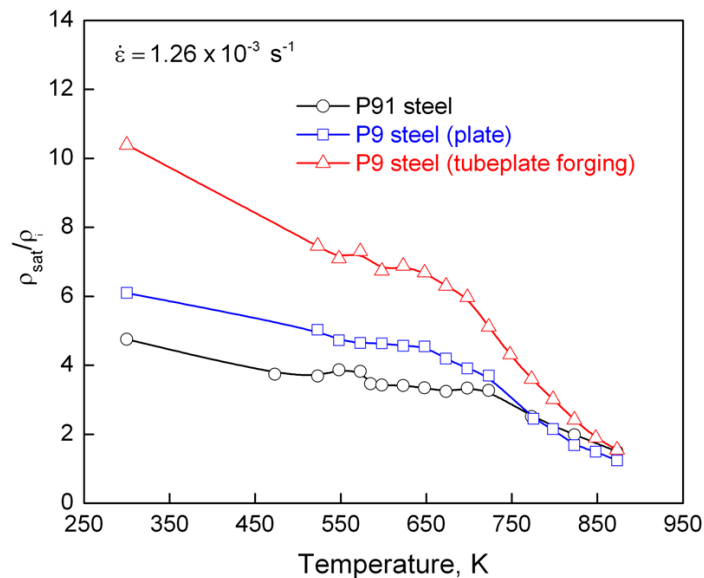


Figure 3.15 Variations of the ratio of saturation dislocation density (ρ_{sat}) and initial dislocation density (ρ_i) with temperature for P9 steel plate and tubeplate forging and P91 steel.

3.8 Revisiting Considère Necking Instability Criterion and the Predictability of the Model towards Tensile Properties of 9% Cr Steels

On the macroscopic scale, plastic deformation is reasonably assumed to be homogenous until necking sets-in at certain critical strain value. According to Considère instability criterion [104], onset of macroscopic localized deformation takes place when the instantaneous strain hardening rate i.e. $d\sigma/d\varepsilon$ (where σ is the true stress and ε is the true plastic strain) is equal to the value of the flow stress and it is represented as

$$\frac{d\sigma}{d\varepsilon} = \sigma.$$

Equation (3.13)

Equation (3.13) is derived from the mechanistic aspect of work hardening behaviour of materials. When the σ - ε data adequately described by the simple Hollomon relationship i.e., $\sigma = K_H \varepsilon^{n_H}$ the interrelationship between the strain hardening exponent and the true uniform plastic strain at the point of necking is given as $n_H = \varepsilon_u$. The true ultimate strength can be predicted as $\sigma = K_H n_H^{n_H}$. It was reported that the tensile work hardening behaviour of tempered martensitic steel for the wide range of strain rates and temperatures can be described adequately by the combination of Ludwigson and Hollomon relationships [63, 138]. The reported strain hardening exponent (n) was greater than that of uniform experimental true plastic strain at all the conditions [138]. Though the parameters associated with the empirical relationships capture the instability point, they do not possess the inherent physical meaning. Contrary to this, the present investigation deals with the Estrin-Mecking approach to capture the instability criterion using physically based parameters.

By using Equation (3.6) and Equation (3.13), Considère criterion had been extensively revisited by Malygin [139] in the framework of dislocation density based model for the theoretical prediction of uniform strain and ultimate tensile strength for fcc materials. From the analytical formulation, it was pointed out that the uniform strain depends on dynamic recovery parameter. Applicability of the developed formulation by Malygin [139] had been expressed for accounting the influence of stacking-fault energy, solid-solution strengthening and grain size on uniform strain and ultimate tensile strength for several fcc alloys. By applying the linear stability analysis to the dislocation density based Kocks-Mecking approach [82, 83], Yasinkov et al. [140] developed the new necking criterion which resembles the Hart instability criterion [141], but not exactly same to it. Validation of the developed criterion had been demonstrated for the prediction of critical strain at which

necking instability sets-in in ultrafine grained steels [142, 143]. However, in this study, relatively simplified formulation has been evolved for prediction of critical dislocation density and critical plastic strain using Estrin-Mecking approach for tempered martensitic steels based on the interrelationship between $\frac{d\sigma}{d\varepsilon}$ and $\frac{d\sigma_d}{d\varepsilon}$. Since the evolution of flow stress with the true plastic strain is directly proportional to the evolution of flow stress contribution from dislocations (σ_d) and $\frac{d\sigma}{d\varepsilon} \equiv \frac{d(\sigma - \sigma_0)}{d\varepsilon} = \frac{d\sigma_d}{d\varepsilon}$ as shown schematically in Figure 3.16, instability criterion for tempered martensitic steels can be viewed based on the evolution of dislocation density rather than flow stress.

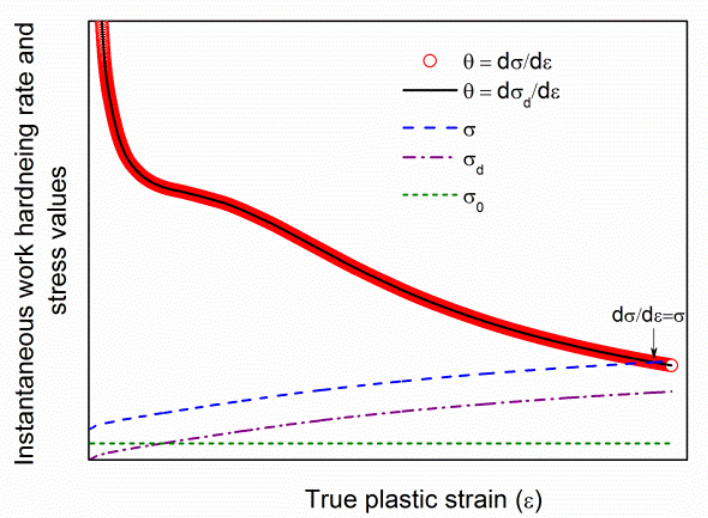


Figure 3.16 Schematic representation of the variations in instantaneous work hardening rate evaluated by $\theta = d\sigma/d\varepsilon$ and $\theta_d = d\sigma_d/d\varepsilon$ as well as the different stress values with the plastic strain (ε). Considered instability criterion has been marked as $d\sigma/d\varepsilon = \sigma$.

In view of this, Equation (3.7) can be written as

$$\frac{d\sigma}{d\varepsilon} = \frac{d\sigma_d}{d\varepsilon} = \frac{d(M\alpha\mu b\sqrt{\rho})}{d\varepsilon} = \sigma = \sigma_0 + M\alpha\mu b\sqrt{\rho}, \quad \text{Equation (3.14)}$$

Equation (3.14) can be used to define the instability condition in terms of dislocation density and the developed relationship is given as

$$\frac{d\sqrt{\rho}}{d\varepsilon} = \frac{\sigma_0}{M\alpha\mu b} + \sqrt{\rho} = \psi\sqrt{\rho}, \quad \text{Equation (3.15)}$$

where ψ can be written as $\frac{\sigma_0}{M\alpha\mu b\sqrt{\rho}} + 1 = \frac{\sigma_{UTS}}{\sigma_{UTS} - \sigma_0}$. In the present analysis, ψ is assumed as a constant over the range of temperatures as shown in Figure 3.17 and it marginally varies with steel grades. This parameter is used to avoid the influence of σ_0 in the formulation. The average values of 1.65, 1.8 and 2.1 were considered for P9 tubeplate forging, P9 plate and P91 steel, respectively.

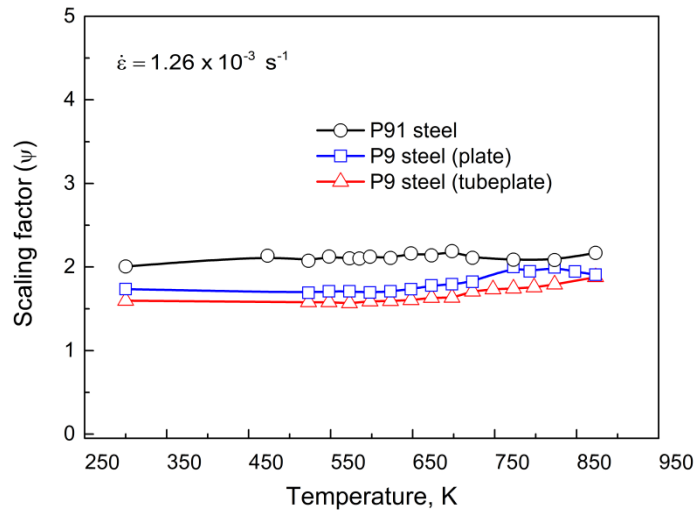


Figure 3.17 Variations in the values of scaling factor (ψ) with temperature for 9% Cr steels.

Integration of Equation (3.3) with the appropriate boundary conditions can be represented as

$$\int_{\rho_i}^{\rho} \frac{d\rho}{\frac{Mk}{b} - Mk_2\rho} = \int_0^{\varepsilon} d\varepsilon. \quad \text{Equation (3.16)}$$

Following integration, Equation (3.16) yields

$$\rho = \rho_{sat} - (\rho_{sat} - \rho_i) \exp(-Mk_2\varepsilon). \quad \text{Equation (3.17)}$$

Using Eq. (7), $\frac{d\sqrt{\rho}}{d\varepsilon}$ can be written as

$$\frac{d\sqrt{\rho}}{d\varepsilon} = \frac{(\rho_{sat} - \rho)}{2\sqrt{\rho}} Mk_2 . \quad \text{Equation (3.18)}$$

By substituting Equation (3.18) into Equation (3.15), the critical dislocation density at which instability sets-in can be expressed as

$$\rho_c = \frac{Mk}{b(2\psi + Mk_2)} . \quad \text{Equation (3.19)}$$

Finally, the proposed new instability criterion can be given in terms of parameters associated with Estrin-Mecking approach [84] as

$$\frac{d\sqrt{\rho}}{d\varepsilon} = \sqrt{\left(\frac{Mk}{b(2\psi + Mk_2)}\right)} = \sqrt{\left(\frac{M}{bL(2\psi + Mk_2)}\right)} . \quad \text{Equation (3.20)}$$

Equation (3.20) suggests that the tensile necking instability in 9% Cr tempered martensitic steels depends on the values of mean free path (L) as well as dynamic recovery parameter (k_2). When ρ approaches critical dislocation density (ρ_c), true plastic strain (ε) approaches true uniform plastic strain (ε_u). Accordingly, Equation (3.17) can be reformulated as

$$\varepsilon_u = \frac{-1}{Mk_2} \ln\left(\frac{\rho_{sat} - \rho_c}{\rho_{sat} - \rho_i}\right) . \quad \text{Equation (3.21)}$$

By substituting the formulations of ρ_{sat} and ρ_c into Equation (3.21), the true uniform plastic strain (ε_u) can be expressed as

$$\varepsilon_u = \left(\frac{-1}{Mk_2}\right) \ln\left(\frac{2\psi k}{Mk_2 k + 2\psi k - 2\psi \rho_i b k_2 - M \rho_i b k_2^2}\right) . \quad \text{Equation (3.22)}$$

The above relationship denotes that the true uniform plastic strain depends on initial dislocation density, mean free path for dislocations and dynamic recovery parameter. In contrast to ε_u , ρ_c does not depend on initial dislocation density as given by Equation (3.19). Similar to the values of the ratio of saturation dislocation density and initial dislocation density (Figure 3.15), higher ratio of the square root of critical density and initial dislocation

densities ($\sqrt{\rho_c/\rho_i}$) obtained for P9 steel clearly suggests comparatively better work hardening ability of P9 steel over P91 steel (Figure 3.18(a)). Among the P9 steels, tubeplate forging exhibits higher ratio than plate material. At all the temperatures, the observed higher true uniform plastic strain values of P9 steel tubeplate forging further confirm the relatively higher work hardening ability of the steel over P9 plate and P91 steel (Figure 3.18 (b)). Using Equation (3.22), true uniform plastic strain values have been predicted at all the temperatures for P9 and P91 steels. Good agreement between the predicted and experimental true uniform plastic strain values has been obtained as shown in Figure 3.19.

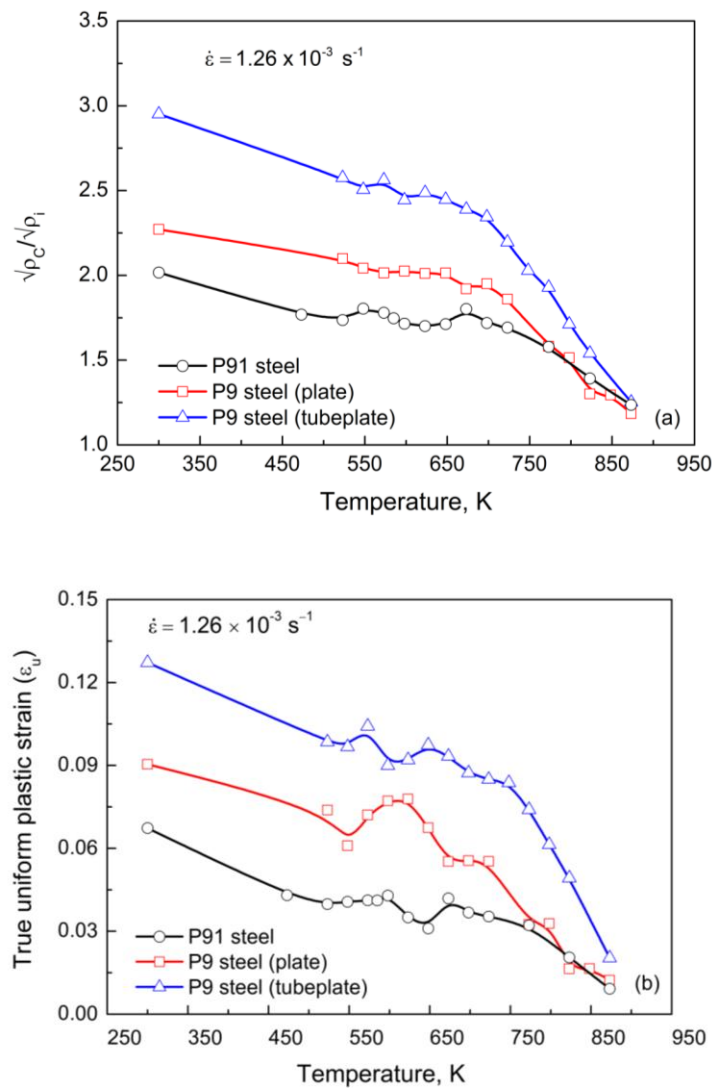


Figure 3.18 Variations in (a) $\sqrt{\rho_c/\rho_i}$ and (b) true uniform plastic strain (ϵ_u) with temperature for P9 plate and tubeplate forging and P91 steel.

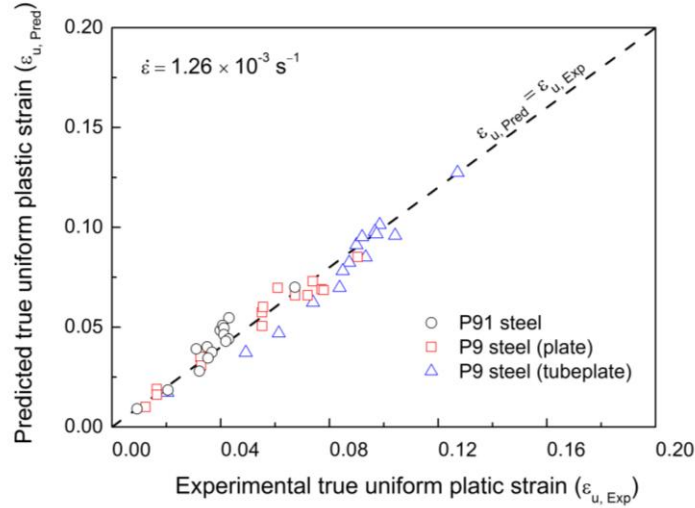


Figure 3.19 Comparison between experimental ($\epsilon_{u, \text{Exp}}$) and predicted ($\epsilon_{u, \text{Pred}}$) true uniform plastic strain values for P9 and P91 steels showing $\epsilon_{u, \text{Pred}} = \epsilon_{u, \text{Exp}}$ for different temperatures in the range 300-873 K.

Equation (3.22) can be further simplified by assuming the dominance of first term Mk_2k over other terms in the denominator inside the natural logarithmic part. After this assumption, the expression for true uniform plastic strain (ϵ_u) in terms of dynamic recovery parameter can be written as

$$\epsilon_u \approx \left(\frac{-1}{Mk_2} \right) \ln \left(\frac{2\psi}{Mk_2} \right). \quad \text{Equation (3.23)}$$

The above simplified relationship was used to estimate the true uniform strain values and these values are comparable with the experimentally observed values as shown in Figure 3.20. This implies that the dynamic recovery primarily governs the work hardening ability of tempered martensitic steels. Though the true uniform plastic strain strongly depends on k_2 , the intrinsic variable i.e. critical dislocation density ρ_c depends on both dynamic recovery and mean free path values. According to Equation (3.19) and Equation (3.23), work hardening behaviour of materials exhibiting lower values of mean free path and dynamic recovery parameter is expected to achieve higher values of critical dislocation density along with uniform plastic strain. On the contrary, in tempered martensitic steels, microstructures having lower mean free path display higher dynamic recovery and vice-versa (Figures 3.9 and 3.10).

This suggests that there is a competition between these two important parameters controlling the work hardening ability of these steels. In spite of lower mean free path with higher critical dislocation density in P91 steel, the strong influence of dynamic recovery restricts its work hardening ability resulting in low values of true uniform plastic strain than those obtained for P9 steel tubeplate forging and plate. It is known that when the mean free path of dislocations limited by the fine boundaries is extremely small, the rate of defect generation and its accumulation inside grains and at boundaries would be very high [144]. The resulting high defect density provides a large driving force for dynamic recovery [144]. In the case of P91 steel, the lower mean free path of dislocations of arising from the geometrical obstacles such as precipitates and hierarchical boundaries with high rates of defect density generation leads to large driving force for higher dynamic recovery than for P9 steel.

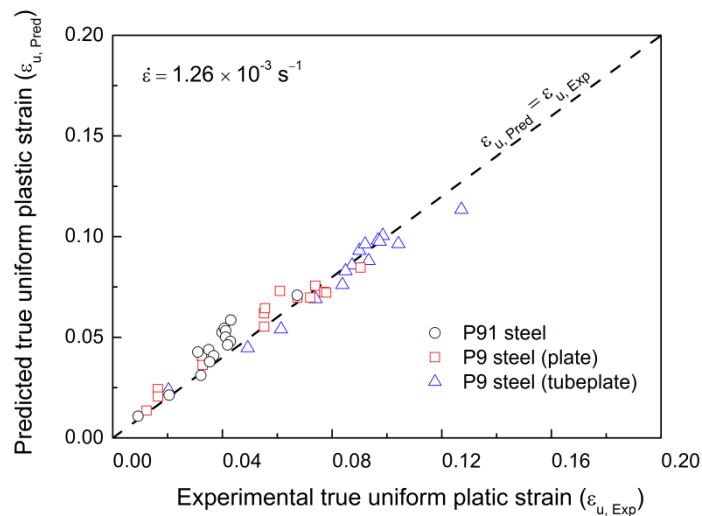


Figure 3.20 Comparison between experimental ($\epsilon_{u, \text{Exp}}$) and predicted ($\epsilon_{u, \text{Pred}}$) true uniform plastic strain values using the simplified formulation for P9 and P91 steels at different test temperatures.

The predictability of Estrin-Mecking one-internal-variable model is further demonstrated by comparing the predicted initial stress (σ_I) with experimental true yield strength ($\sigma_{\text{Exp}, \text{YS}}$) at $\epsilon_p = 0.001$ and the predicted true ultimate tensile strength ($\sigma_{\text{Pre}, \text{UTS}}$) with experimentally measured true ultimate tensile strength ($\sigma_{\text{Exp}, \text{UTS}}$) values in Figures 3.21(a) and 3.21(b),

respectively. The true ultimate tensile stress ($\sigma_{Pre,UTS}$) at different temperatures has been predicted using Equation (3.6) as

$$\sigma_{Pre,UTS} = \sigma_0 + M\alpha\mu b\rho_c^{0.5}. \quad \text{Equation (3.23)}$$

An excellent agreement is observed between the predicted and experimental yield and ultimate tensile strength values as shown in Figure 3.21 for P9 and P91 steels.

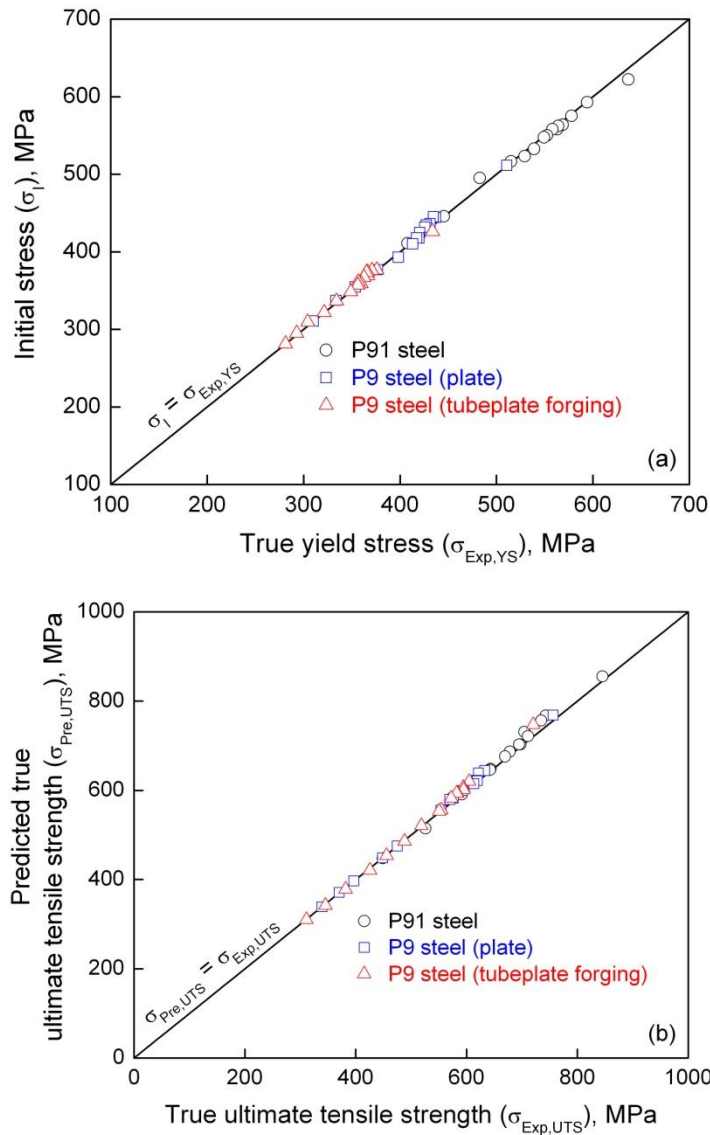


Figure 3.21 Variations of (a) predicted initial stress (σ_I) with experimental true yield stress ($\sigma_{Exp,YS}$) and (b) predicted ultimate tensile strength ($\sigma_{Pre,UTS}$) with experimental true ultimate tensile strength ($\sigma_{Exp,UTS}$) for P9 steel plate and tubeplate forging and P91 steel over temperatures ranging from 300 to 873 K. Theoretical $\sigma_I = \sigma_{Exp,YS}$ and $\sigma_{Pre,UTS} = \sigma_{Exp,UTS}$ are superimposed as full lines.

3.9 Conclusions

Tensile flow and work-hardening behaviour of P9 steel plate and tubeplate forging and P91 steel have been examined successfully in the framework of dislocation dynamics based one-internal-variable approaches for a wide range of temperatures. Detailed analysis towards flow and work-hardening behaviour of 9% Cr steels in the wide range of temperatures indicated that the hybrid model reduced to Estrin–Mecking one-internal-variable model. Parameter sensitivity analysis over optimisation results demonstrated the dominance of dislocation accumulation term k/b over $k_1 \cdot \rho^{0.5}/b$ in the hybrid model at intermediate and high temperatures. This implies that the average mean free path arising from the dislocation dense lath/cell boundaries and precipitates act as effective barriers to glide of dislocations over total dislocation population inside the lath in P9 and P91 steels.

The applicability of Estrin-Mecking one-internal-variable approach to 9% chromium steels is demonstrated in terms of good agreement between predicted and experimental true stress-true plastic strain with low least-square error values over temperatures ranging from 300 to 873 K. At room and intermediate temperatures, insignificant or, marginal variations in the evolution of dislocation density with plastic strain were noticed for P9 and P91 steels. At high temperatures, the dominance of dynamic recovery resulted in rapid evolution of dislocation density towards saturation in all the steels. Similarly, the work hardening parameters associated with the Estrin-Mecking approach exhibited marginal variations in the values at room and intermediate temperatures, and rapid variations at high temperatures. The evaluation of activation energy based on Bergstrom and Hallen model using recovery parameter suggested that the dynamic recovery is controlled by cross-slip of dislocations at room and intermediate temperatures, and climb of dislocations at high temperatures.

At all temperatures, a systematic influence of initial microstructure on the work hardening parameters associated with the Estrin-Mecking approach has been observed. The

P9 steel tubeplate forging exhibited higher work hardening due to its softened microstructure in terms of larger gains in the dislocation density and flow stress contribution from dislocations along with reduced dynamic recovery than the P9 plate and P91 steels in the temperature range 300-873 K. Contrary to this, relatively hardened microstructure in P91 steel displayed lower work hardening ability along with increased dynamic recovery than P9 plate and tubeplate forging.

In addition, Considère criterion has been reexamined based on Estrin-Mecking model for 9% Cr tempered martensitic steels. It has been shown that tensile instability sets-in as the evolution of dislocation density with the plastic strain approaches critical dislocation density which in turn is a function of mean free path and dislocation annihilation parameter. Further, the interrelationship between true uniform plastic strain and dynamic recovery parameter has been established from the present formulation for 9% Cr steels. The observed good agreement between experimental and predicted tensile properties showed a better predictability of the model for 9% chromium containing steels.

Chapter 4: Constitutive Modelling of Primary and Steady State Creep Behaviour of 9% Cr Tempered Martensitic Steels

4.1 Introduction

Modelling creep behaviour becomes essential for safe life design of the high temperature structural components. Traditionally, creep modelling and finite element analysis towards engineering creep design are limited to the secondary creep stage. In this analysis, the integrated form of Norton's power law represents only secondary creep strain contribution to total creep ductility. Several creep strain (ϵ)-time (t) relationships ranging from simple phenomenological to complex constitutive equations have been proposed and used to represent the creep strain accumulation characteristics [145]. The effectiveness of these relationships to model primary, secondary and tertiary creep deformation for specific applications can vary with material characteristics and source data distribution [145]. Often, design engineers require the parameters associated with creep equations for the prediction of long-term creep behaviour in the primary and secondary creep regimes. Since most of the allowable creep strain is accumulated in primary and secondary creep stages, it becomes necessary to incorporate primary creep strain contribution along with secondary creep for the safe-life design of components. In most of the creep relationships [72-75], the terms describing primary and secondary creep strain accumulation are additive in nature. As an alternative to additive models, models based on the internal variables provide better description towards primary and secondary creep deformation behaviour of materials [91-99]. In this regard, the model based on the evolution of internal stress as an internal-variable was considered towards the description of primary and secondary creep deformation behaviour of 9% Cr steels in this investigation. Though a few models were proposed based on the kinetic of evolution of internal-stress for describing the transient behaviour of engineering materials [96, 97], these models do not explicitly include the dependence of steady state ($\dot{\epsilon}_s$) or

minimum creep rate and activation volume (ΔV) or scaled activation volume (\bar{V}) as a function of internal stress (Equations (1.28) and (1.30)). In reality, the parameters such as $\dot{\epsilon}_s$ and ΔV should be considered as a function of internal stress. Another important point in these formulations (Equations (1.28) and (1.30)) is the steady state creep rate used as a parameter for describing primary creep behaviour. In fact, the steady state or minimum creep rate should be derived directly from the governing kinetic creep law. In view of this, a constitutive model without invoking steady state creep rate as a parameter, and by incorporating the stress dependence of activation volume has been developed for the description of primary and steady state creep behaviour of P9 steel in the present study. The concept of stress dependent activation volume and average dislocation segment length based on Friedel statistics [105] has been incorporated into the kinetic creep law. The internal stress formulation proposed by Estrin and Mecking [84] has been coupled with kinetic creep law in order to get a better description of deformation behaviour. The applicability of the model has been demonstrated by describing primary and secondary creep behaviour of P9 steel in two different heat treatment conditions for a wide range of stresses at 793 and 873 K. The parameters associated with the present formulation have been obtained based on error minimisation algorithm using experimental and predicted creep strain-time data. Further, the predictability of the model has been demonstrated by predicting steady state creep rate and their comparison with experimentally measured values in P9 steel.

4.2 Framework of the Proposed Sine Hyperbolic based Creep Rate Model

The model has been originated from the Orowan equation [106]. The shear strain rate produced by the glide motion of mobile dislocations (ρ_m) is described by Orowan's equation [106] as

$$\dot{\gamma} = \rho_m b v. \quad \text{Equation (4.1)}$$

where $\dot{\gamma}$ and v are the shear strain rate and average dislocation velocity, respectively. Equation (4.1) is equivalent to the strain rate relationships derived by Taylor [146] and Seeger [147]. The average velocity v is determined by the rate at which local thermal activation allows the pinned dislocation segments to overcome the energy barriers by climb over individual obstacles when the mobile dislocations are held up by the dispersion of local obstacles. Since the presence of wide distribution of dislocation segment lengths between pinning points and spectrum of obstacle strengths is expected in materials, the probability of thermal activation varies from one pinning point to another. This indicates that the evaluation of velocity of dislocations in terms of the characteristic parameters of individual pinning point is difficult. In view of this, average dislocation velocity (v) in solids containing dispersed obstacles is specified based on average segment length (l_s) and average area (A_s) swept out by dislocation segments released during thermal activation [147] and this is expressed as

$$v = \Gamma_{net} (A_s / l_s), \quad \text{Equation (4.2)}$$

where Γ_{net} is the net activation frequency. The net activation frequency based on forward (Γ_f) and reverse activation frequency (Γ_b) is given by

$$\Gamma_{net} = \Gamma_f - \Gamma_b. \quad \text{Equation (4.3)}$$

The forward frequency with which dislocation segment of length (l_s) attempts the energy barrier (Q) is given as

$$\Gamma_f = \frac{v_D b}{2l_s} \exp\left(\frac{-Q + \tau_e l_s b \Delta d}{kT}\right), \quad \text{Equation (4.4)}$$

where Δd is the activation distance required to thermally overcome the obstacles, Q is the activation energy for self-diffusion of the matrix due to position change of Δd between the normal and activated states and v_D is the Debye frequency. In Equation (4.4), the local effective shear stress (τ_e) is equal to applied shear stress (τ_a) minus internal shear stress (τ_i).

The term $l_s b \Delta d$ has the dimension of volume, i.e., activation volume ΔV . Similarly, the backward frequency with which dislocation segment of length (l_s) attempts the energy barrier is given as

$$\Gamma_b = \frac{v_D b}{2l_s} \exp\left(\frac{-Q - \tau_e l_s b \Delta d}{kT}\right). \quad \text{Equation (4.5)}$$

Substituting Equation (4.4) and Equation (4.5) into Equation (4.3), the net frequency with which dislocation attempts the energy barrier is written as

$$\Gamma_{net} = \frac{v_D b}{2l_s} \exp\left(\frac{-Q}{kT}\right) \left[\exp\left(\frac{\tau_e l_s b \Delta d}{kT}\right) - \exp\left(\frac{-\tau_e l_s b \Delta d}{kT}\right) \right]. \quad \text{Equation (4.6)}$$

The term $l_s b \Delta d$ has the dimension of volume and is thermodynamically termed as activation volume ΔV . Following the substitution of Equation (4.6) into Equation (4.2), the shear strain rate ($\dot{\gamma}$) in Equation (4.1) can be expressed as

$$\dot{\gamma} = \rho_m b^2 \left(\frac{A_s}{2l_s^2} \right) v_D \exp\left(\frac{-Q}{RT}\right) \exp\left[\frac{(\tau_a - \tau_i) \Delta V}{kT}\right]. \quad \text{Equation (4.7)}$$

The stress dependence of the effective obstacle spacing was first considered by Friedel [105, 148] in terms of the glide of dislocation overcoming the obstacles during creep. Friedel pointed out that arithmetic mean value of segment length (l_s) varies with the effective shear stress [105]. Based on the Friedel statistics, the stress dependence of average dislocation segment length, activation area and activation volume swept by the dislocation segment have been considered in the present study as

$$l_s = \frac{\mu b}{((2\pi\tau_i)^2 \tau_e)^{1/3}}, \quad A_s = \frac{l_s^3 (\tau_a - \tau_i)}{\mu b}, \quad \Delta V = b^3 \left[\frac{\mu}{((2\pi\tau_i)^2 \tau_e)^{1/3}} \right]. \quad \text{Equation (4.8)}$$

Substituting Equation (4.8) into Equation (4.7) and by converting shear strain rate ($\dot{\gamma}$) and shear stress fields (τ_a , τ_i and τ_e) to tensile quantities ($\dot{\epsilon}$, σ_a , σ_i and σ_e) using Taylor factor (M), the relationship for macroscopic creep rate $\dot{\epsilon}$ is obtained as

$$\dot{\epsilon} = \frac{\rho_m b^2 v_D \sigma_e (\sigma_i^2 \sigma_e)^{-1/3}}{M^2} \exp\left(\frac{-Q}{RT}\right) \sinh\left(\frac{\sigma_e}{MkT} b^3 \left[\frac{G}{(\sigma_i^2 \sigma_e)^{1/3}}\right]\right). \quad \text{Equation (4.9)}$$

The term internal stress (σ_i) in Equation (4.9) is defined as the resistance characteristic of the structure against deformation. The source of the resistance against dislocation motion consists of the sum of structural phenomena, i.e., long range stresses associated with pile up of dislocations against barriers such as dislocations, dispersed second phase particles, subgrain boundaries and grain boundaries. Total internal stress is a complex superposition of the influences of all the individual phenomena. Though different relationships have been proposed for the evolution of internal stress with strain or time [84, 91], the model based on the accumulation of dislocations against geometrical obstacles such as sub-grain boundaries and precipitates proposed by Estrin-Mecking appears to be more relevant in the present context. Accordingly, the evolution of internal stress with creep strain envisaged in Estrin-Mecking kinetic approach [84] have been used in the present study and this is expressed as

$$\frac{d\sigma_i}{d\epsilon} = \frac{1}{\sigma_i \epsilon_c} (\sigma_{is}^2 - \sigma_i^2), \quad \text{Equation (4.10)}$$

where σ_{is} is the internal stress value at steady state and ϵ_c is the rate constant. Equation (4.10)

in terms of time (t) can be expressed as

$$\frac{d\sigma_i}{dt} = \frac{1}{\sigma_i \epsilon_c} (\sigma_{is}^2 - \sigma_i^2) \dot{\epsilon}. \quad \text{Equation (4.11)}$$

Equations (4.9) and (4.11) are coupled together for describing the primary creep deformation approaching to steady state creep behaviour of materials.

4.3 Numerical Implementation and Optimisation

Creep strain-time data obtained for P9 steel in Q+T and SPWHT conditions were employed to examine the developed model. Typical creep curves for P9 steel in Q+T and SPWHT conditions for 60 and 100 MPa stresses at 873 K are shown in Figure 4.1. SPWHT specimens displayed consistently higher evolution of creep strain with time resulting in higher steady state creep rate and lower rupture life than those obtained for Q+T specimens in all the stress conditions. Creep strain-time data up to steady state creep regime has been considered in the present analysis.

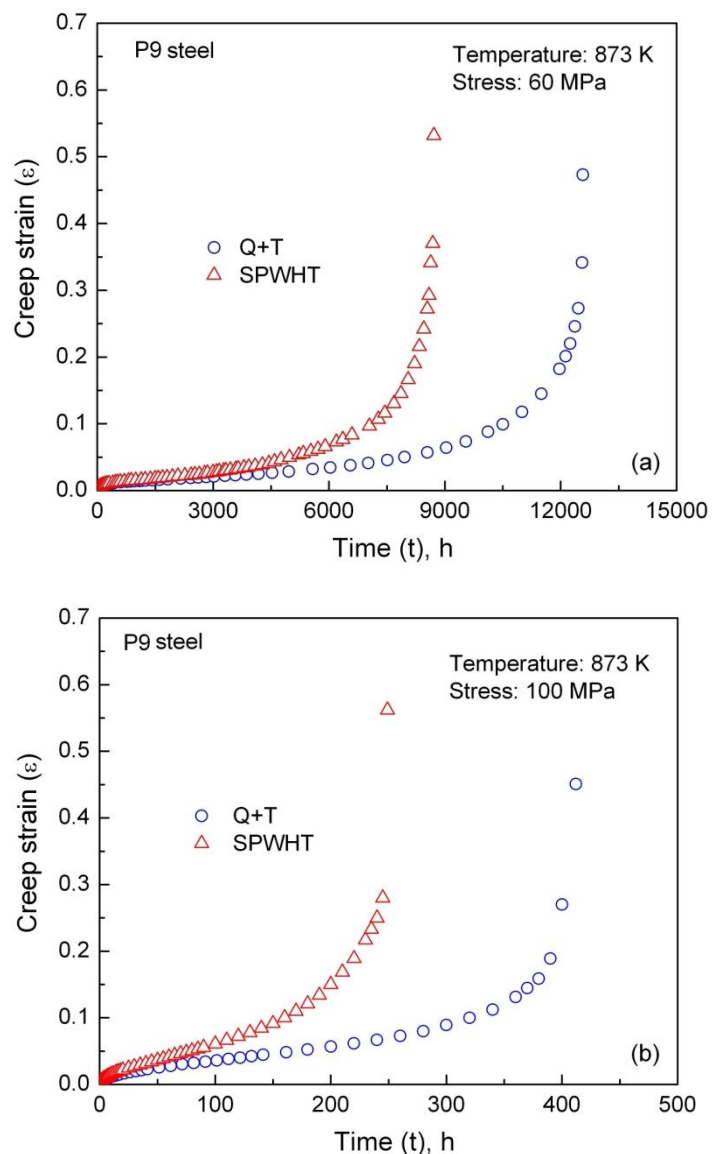


Figure 4.1 Creep strain-time data of P9 steel in Q+T and SPWHT conditions for (a) 60 MPa and (b) 100 MPa at 873 K.

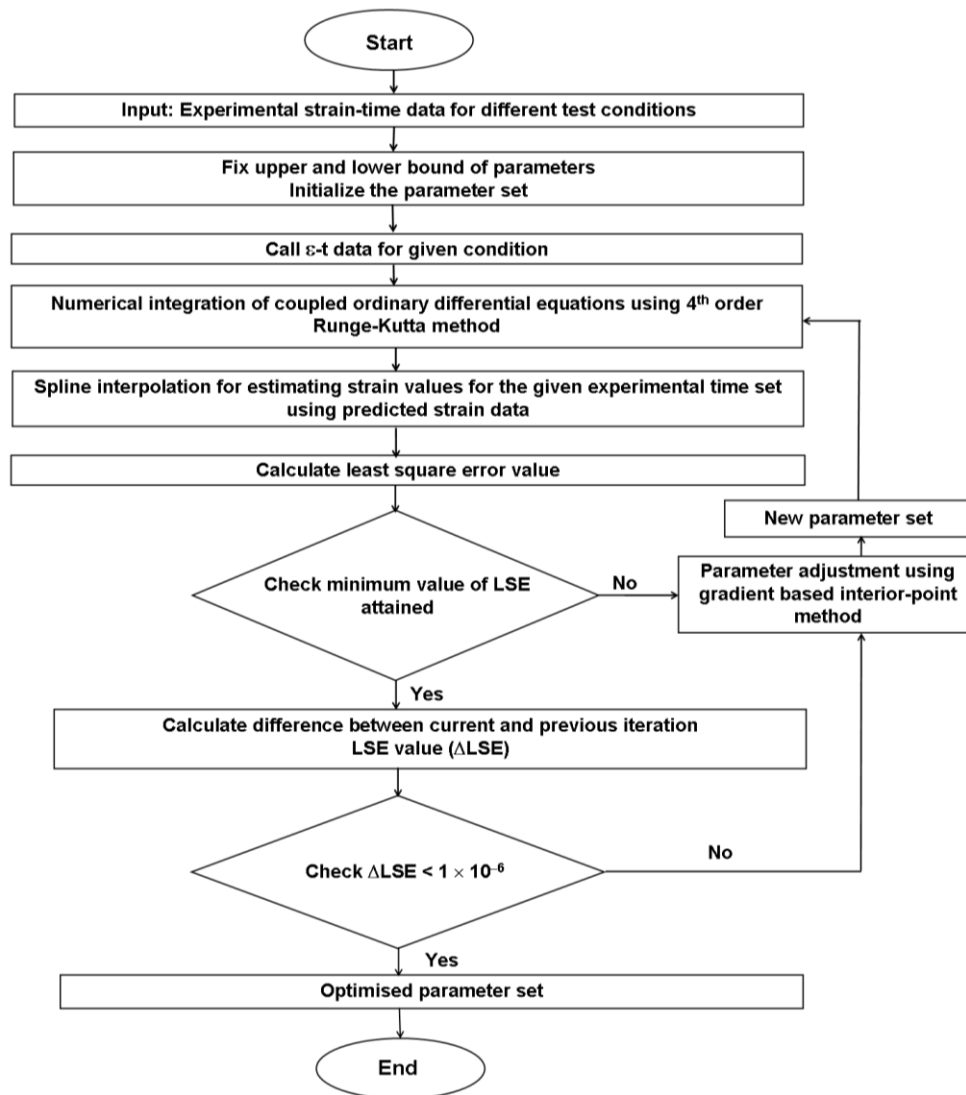


Figure 4.2 Schematic flow diagram for optimisation of parameters associated with the developed sine hyperbolic creep rate model.

The coupled first-order differential equations i.e., Equations (4.9) and (4.11) have been integrated by fourth-order Runge-Kutta method with initial conditions of $\sigma_i = \sigma_{i0}$ and $\varepsilon = 0$ at time $t = 0$. The unknown constants in the differential equations such as initial internal stress (σ_{i0}), steady state internal stress (σ_{is}) and rate constant (ε_c) were optimised using interior point algorithm. The schematic flow diagram for parameter optimisation has been presented in Figure 4.2. The goodness of fit was judged by low values of relative least-square error obtained during optimisation. The iteration process is initialized with some initial guess

within the lower and upper bounds of the parameter set $\{\sigma_{i0}, \sigma_{is}, \varepsilon_c\}$. The upper and lower limits of initial and steady state internal stress values were chosen close to the lower and upper values of applied stress as 50-200 MPa. The lower value of rate constant is kept as zero, while the upper value is chosen as 0.1. The material constants associated with the model are given in Table 4.1. The mobile dislocation density is assumed to be constant [84, 89, 90, 147] and is fixed as one order of magnitude lower than the total dislocation density value of $1.0 \times 10^{14} \text{ m}^{-2}$ for 9% Cr steels [40, 119] as given in Table 4.1. In general, heat treatment conditions influence both the immobile dislocation density (composed of dislocations at hierarchical boundaries and fraction of dislocations in the subgrain interior) and mobile dislocation density in tempered martensitic steels. It is very difficult to measure the exact value of mobile dislocation density for both the heat treatment conditions. In view of this, a typical constant value of mobile dislocation density has been assumed. In common, the uncertainty related to mobile dislocation density has been included in the pre-exponential factor of recovery model [150] and in the power law co-efficient of Kock-Mecking-Estrin one-internal-variable formulation [84, 90]. In these approaches, the weak variation in mobile dislocation density with strain has been accepted. However, it is reasonable to assume a certain definite value of mobile dislocation density as invoked in the present analysis rather than dealing with uncertainty. Lagneborg and coworkers [150, 151] dealt the uncertainty in the evolution of mobile dislocation density with strain based on the formulation of dislocation link distribution. One of the principal advantages in this approach has been the automatic selection of a few mobile dislocation links from the existing dislocation links to derive the creep rate. The applicability of dislocation link distribution model was demonstrated for unidirectional deformation behaviour of austenitic stainless steels [150, 152]. However, a weak variation in mobile dislocation density with strain during creep deformation of AISI 310 stainless steel has been reported [152]. Moreover, it is difficult to derive the network link

distribution and its evolution with time in tempered martensitic steel due to its complex microstructure consisting of hierarchical boundaries along with fine distribution of precipitates. In view of these difficulties, the constancy in mobile dislocation density assumed in present analysis appears to be reasonable. At all test conditions, the values of constants were obtained from the best-fit creep strain-time data.

Table 4.1- Material constants used for the prediction of primary and secondary creep strain-time data.

Material constants	Units	Range	Fixed value
Mobile dislocation density (ρ_m)	m^{-2}	$< 1 \times 10^{13}$	7×10^{12}
Burgers vector (b)	m	-	0.268×10^{-9}
Activation energy (Q)	kJ/mol	244-344	285
Boltzmann constant (k)	J/K	-	1.38×10^{-23}
Taylor factor (M)	-	-	3.0
Shear modulus (μ)	MPa	-	67869 (at 793 K) 64420 (at 873 K)
Gas constant (R)	J/mol-K	-	8.314
Debye frequency (ν_D)	s^{-1}	$5 \times 10^{12} - 1 \times 10^{13}$	1×10^{13}

4.4 Applicability of the Proposed Model

At all test conditions, the present model provided an appropriate description of primary and steady state creep behaviour of P9 steel in Q+T and SPWHT conditions. Representative creep strain-time plots at 873 K for stresses 60 and 100 MPa and at 793 K for 225 MPa are shown in Figures 4.3(a-c) as examples. The symbols correspond to experimental data and the predicted ϵ -t data is represented by full lines. Good agreement between predicted and experimental ϵ -t data can be seen in Figure 4.3.

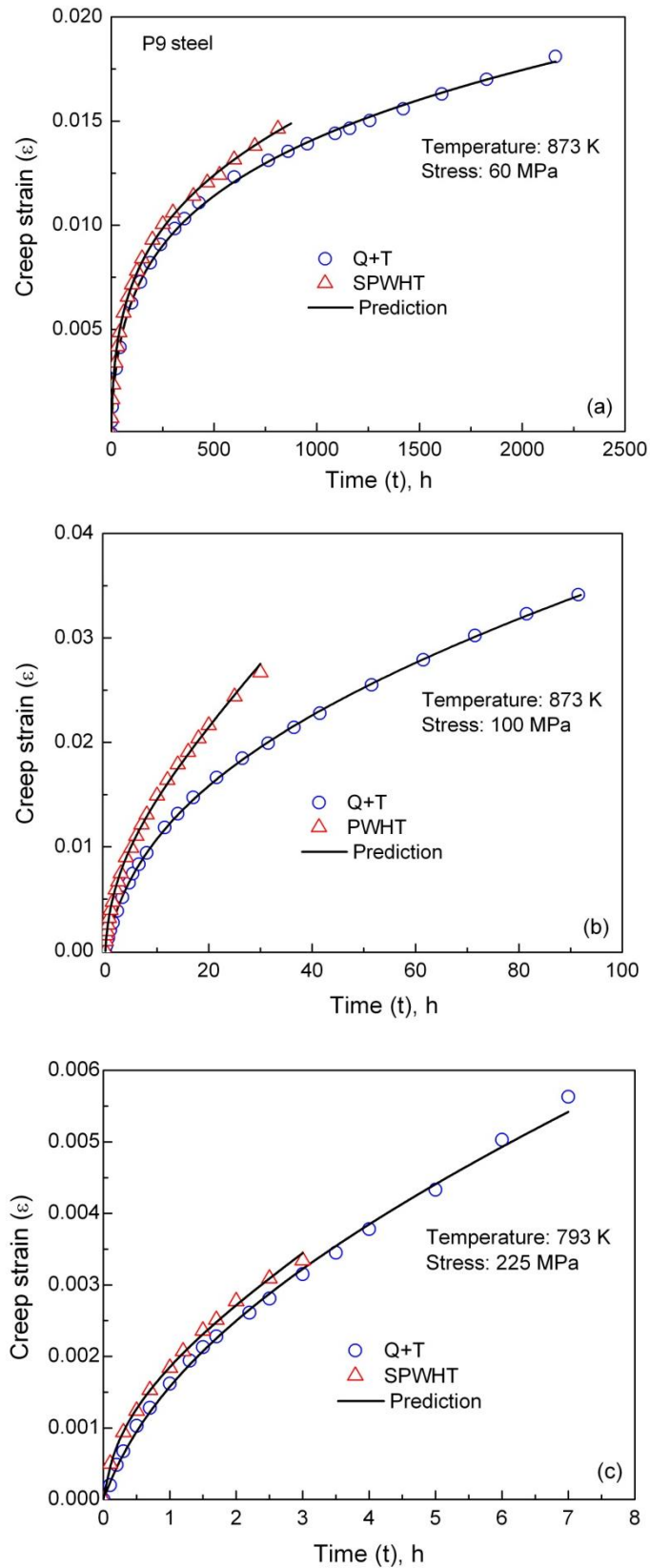


Figure 4.3 Experimental and predicted creep strain-time data in Q+T and SPWHT conditions for (a) 60 and (b) 100 MPa at 873 K and (c) 225 MPa at 793 K.

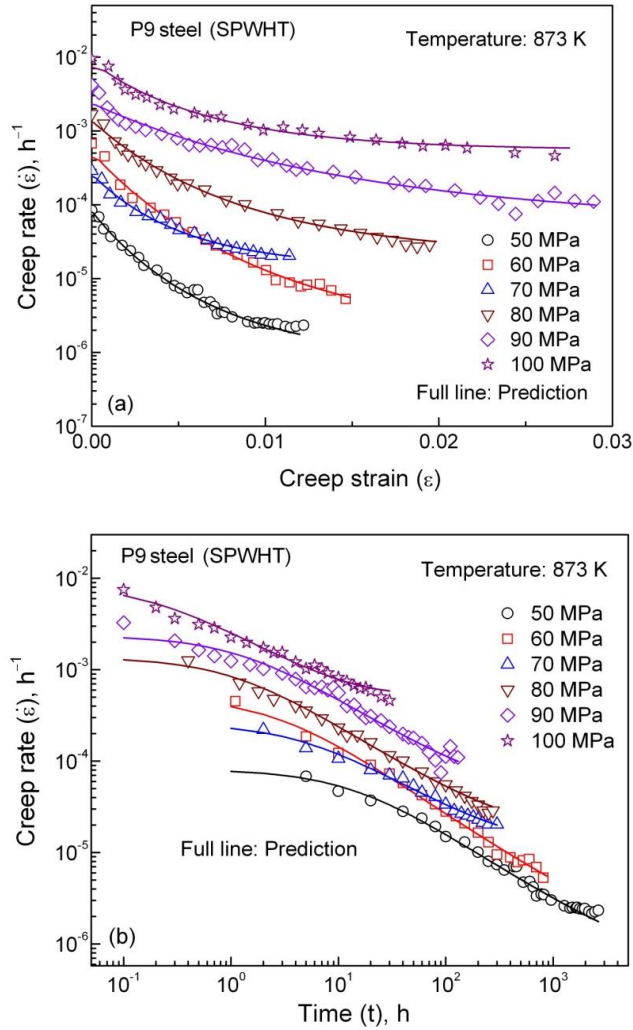


Figure 4.4 Experimental and predicted (a) creep rate-creep strain and (b) creep rate-time data for P9 steel in SPWHT condition for different applied stresses at 873 K.

The accuracy of prediction is also shown in terms of creep rate-strain and creep rate-time at 873 K for SPWHT condition in Figures 4.4(a-b). An excellent agreement between predicted and experimental creep data at different stress levels is discernible in Figure 4.4. The variations in the deviation of strain values as $\Delta\epsilon = \epsilon_{\text{exp}} - \epsilon_{\text{pred}}$ with time exhibiting low values further suggest the statistical suitability of the model for describing creep deformation behaviour of P9 steel. The plot of $\Delta\epsilon$ vs. time is shown in Figure 4.5 as an example for P9 steel in SPWHT condition for 50 MPa. The observed $\Delta\epsilon$ is in the range of ± 0.00025 indicating the appropriateness of the developed model. The variations in the optimised parameters such as initial (σ_{i0}) and saturation (σ_{is}) internal stresses increase with increase in

normalised applied stress irrespective of test conditions (Figures 4.6 and 4.7). Further, the observed initial and saturation internal stresses as a function of applied stress also displayed a marginal difference between Q+T and SPWHT conditions at 793 and 873 K. The variations in rate constant (ϵ_c) with applied stress do not exhibit a clear trend. Irrespective of temperature, the observed average ϵ_c value is lower for P9 steel in SPWHT condition than Q+T condition. The average values of rate constant have been 0.03 and 0.015 for Q+T and SPWHT conditions, respectively below 100 MPa at 873 K. At 793 K, rate constant values of 0.004 for Q+T and 0.0025 for SPWHT above 175 MPa were obtained.

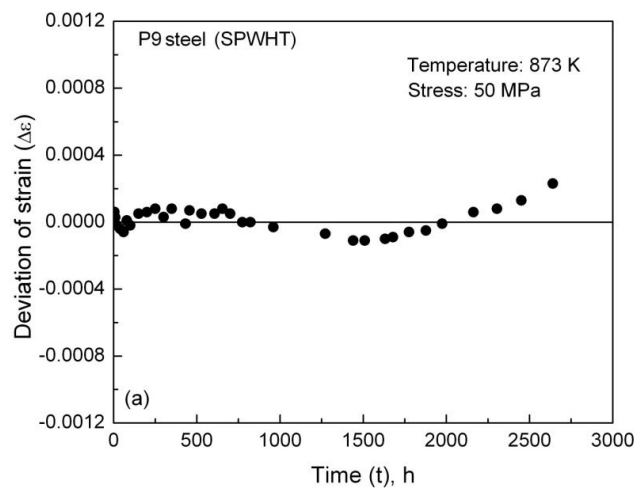


Figure 4.5 Variations in the deviation of strain values as $\Delta\epsilon = \epsilon_{\text{exp}} - \epsilon_{\text{pred}}$ with time for P9 steel in SPWHT condition at 873 K for the stress level of 50 MPa.

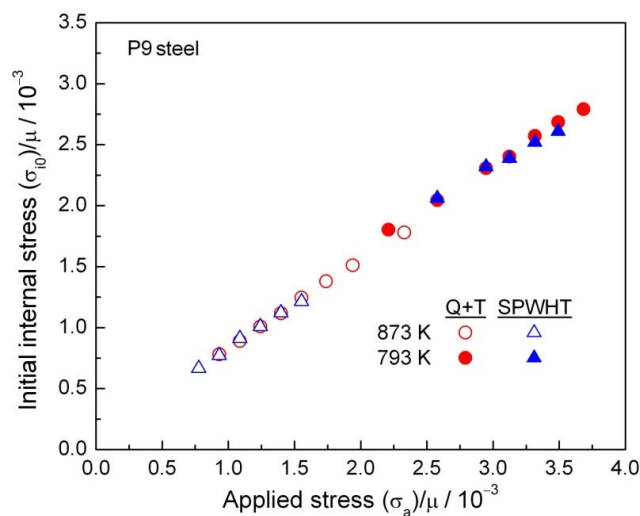


Figure 4.6 Variations of normalised initial internal stress with normalised applied stress at 793 and 873 K for Q+T and SPWHT conditions.

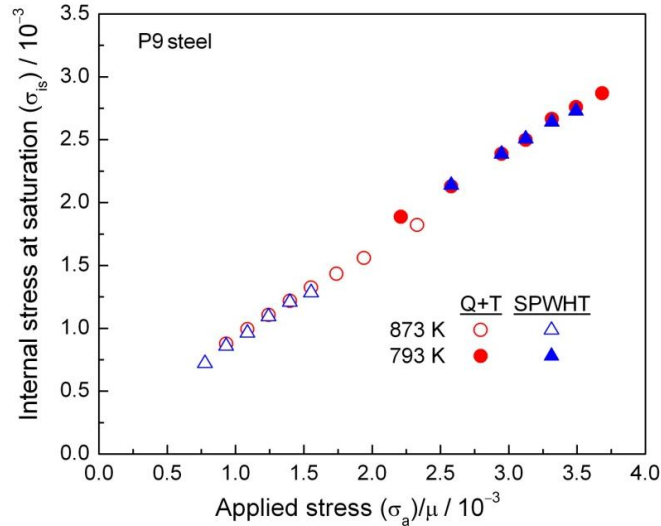


Figure 4.7 Variations of normalised internal stress at saturation with normalised applied stress at 793 and 873 K for Q+T and SPWHT conditions.

As dislocation moves through a solid, it experiences a periodically varying internal stress. Therefore, description of the internal stress requires a three dimensional statistical formulation as the variations of $\sigma_i(x)$ with position x . A number of authors have treated the internal stress as a simple sinusoidal function of position x [153, 154]. In the present study, Estrin-Mecking phenomenological description for internal stress evolution with strain has been used to capture the overall effects of structural changes rather than the local changes of the internal stress. Milicka et al. [91] reported that the constitutive equation describing primary and secondary creep behaviour should show positive initial internal stress along with an increase in values with increase in applied stress. The observed positive values along with an increasing trend in initial internal stress (σ_{i0}) with applied stress confirmed the above requirements. Though the internal stress values increase with increase in applied stress (Figures 4.6 and 4.7), the ratio of σ_{i0}/σ_a and σ_{is}/σ_a decreases with applied stress (Figure 4.8). This suggests that with increase in applied stress, a large fraction of applied stress is utilized for dislocation motion. A similar variations in the ratio of σ_{is}/σ_a with applied stress have been reported for experimentally obtained σ_{is}/σ_a values using stress transient dip test in ferritic

chromium steel [155]. The observed marginally higher ratio of σ_{is}/σ_a at 793 K for a given normalised applied stress than the values obtained at 873 K is on expected lines (Figure 4.8 (b)). This indicates that the effective stress increases with increase in temperature for a given applied stress condition. It has been observed that the variations of ratio of σ_{i0}/σ_a and σ_{is}/σ_a with applied stress (σ_a) obey power law as $\sigma_i \sim (\sigma_a)^k$ as shown in Figure 4.8. The k value in the range of 0.77 to 0.9 was observed for P9 steel. Based on stress change experiments during steady state creep, it has been shown that the increase in internal stress with applied stress obey power law in several metals and alloys [156-159]. The applied stress dependence of internal stress agrees well with the power law ($\sigma_i \sim \sigma_a^{0.87}$) experimentally observed for Al-Li solid solution alloy using stress-dip and stress increment tests during steady state creep conditions [157]. A similar power law dependence of internal stress on applied stress has been reported for many metals and alloys during steady state creep conditions. The reported k value in the range 0.7-1.0 for Cd, Mg, Al-Li and Al-Mg alloys [156-159] is in agreement with those observed in this investigation. The ratio of σ_{is}/σ_a in the range 0.75-0.95 obtained for P9 steel is also in agreement with the reported values for T91 steel [160].

According to the present model, the application of externally applied stress (σ_a) produces plastic flow and consequently the strain hardening during primary creep deformation, thereby causing a continual increase in internal stress with strain. The decrease of creep rate with strain/time results from a decrease in effective stress as shown in Figure 4.9 for Q+T condition at 60 MPa and 873 K as an example. The decrease in effective stress with strain also indicates the concurrent increase in mean internal stress during transient creep in 9% Cr tempered martensitic steels. It is evident that a rapid increase in internal stress or a decrease in effective stress at low strain levels followed by approaching towards saturation during the secondary stage (Figure 4.9).

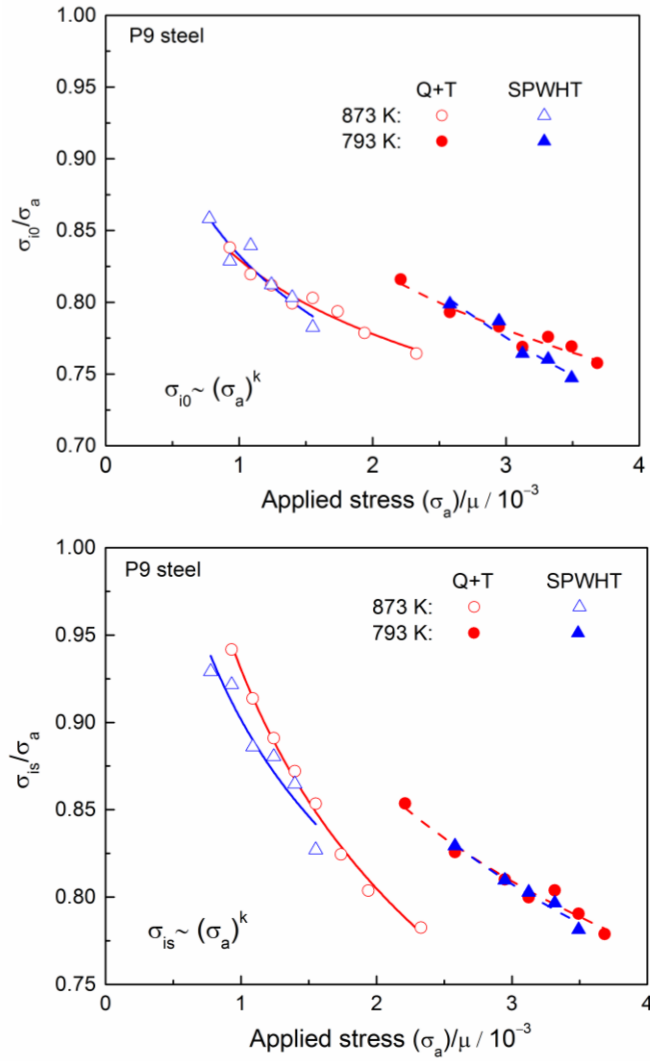


Figure 4.8 Variations in the ratio of (a) σ_{i0}/σ_a and (b) σ_{is}/σ_a with normalised applied stress at 793 and 873 K for Q+T and SPWHT conditions.

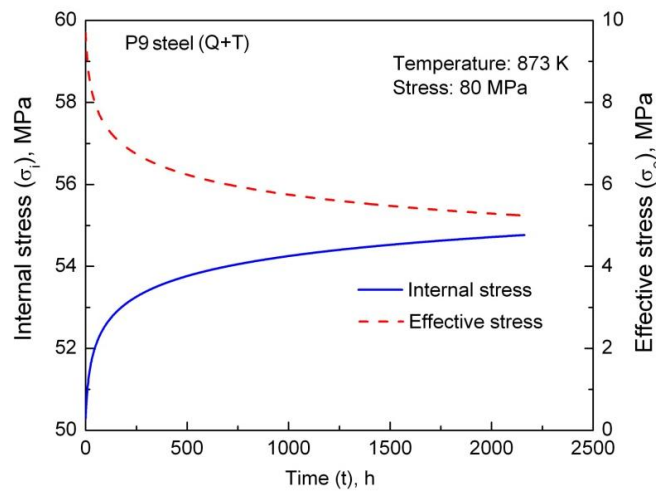


Figure 4.9 A representative plot of the evolution of internal stress and effective stress with time for 80 MPa at 873 K in Q+T condition.

Though there is a reduction in dislocation density inside the lath, the continual accumulation of dislocations in boundaries and formation of new boundaries takes place during primary creep in 9% Cr steels [103, 161, 162]. Orlová and Čadek [163] reported that the internal stress is known to increase during primary creep with the increase in density of dislocations in sub-boundaries. In pure alpha iron, a decrease in strain rate during primary creep was noticed along with the accumulation of dislocation density at subgrain boundaries despite a reduction in the density of dislocation inside the subgrain. It was pointed out that the sub-boundaries must be considered as the main source of internal stress in the primary stage [163]. In the case of 9% Cr steels, the accumulated dislocation in boundaries generates the internal back stress against the dislocation motion which resulted in decrease in strain rate during the transient process as shown in Figure 4.9 [162]. Following Estrin-Mecking [84], the rate constant, ϵ_c is inversely proportional to the dynamic recovery parameter. Though there is only a marginal variations in the initial and saturation internal stress values with respect to heat treatment, the lower ϵ_c values for SPWHT condition relative to those for Q+T condition at both 793 and 873 K suggest enhanced dynamic recovery effects in SPWHT condition. Enhanced dynamic recovery is promoted by the presence of relatively coarse initial microstructure in SPWHT condition than Q+T condition (Figures 2.2 and 2.3). This results in a noticeable difference in the primary and secondary creep characteristics between Q+T and SPWHT conditions (Figures 4.1 and 4.3).

The applicability of the model can be further examined by predicting steady state creep rate in both the heat treatment conditions at 793 and 873 K. When internal stress approaches steady state (σ_{is}) value, the creep rate also approaches to steady state creep rate, $\dot{\epsilon}_s$ and Equation (4.9) can be expressed as

$$\dot{\epsilon}_s = \frac{\rho_m b^2 v_D \sigma_{es} (\sigma_{is}^2 \sigma_{es})^{-1/3}}{M^2} \exp\left(\frac{-Q}{RT}\right) \sinh\left(\frac{\sigma_{es}}{MkT} b^3 \left[\frac{\mu}{(\sigma_{is}^2 \sigma_{es})^{1/3}}\right]\right), \quad \text{Equation (4.12)}$$

where σ_{es} is equal to $\sigma - \sigma_{is}$. A reasonable agreement between the predicted and experimental steady state creep rates has been observed (Figure 4.10). However, at low applied stresses,

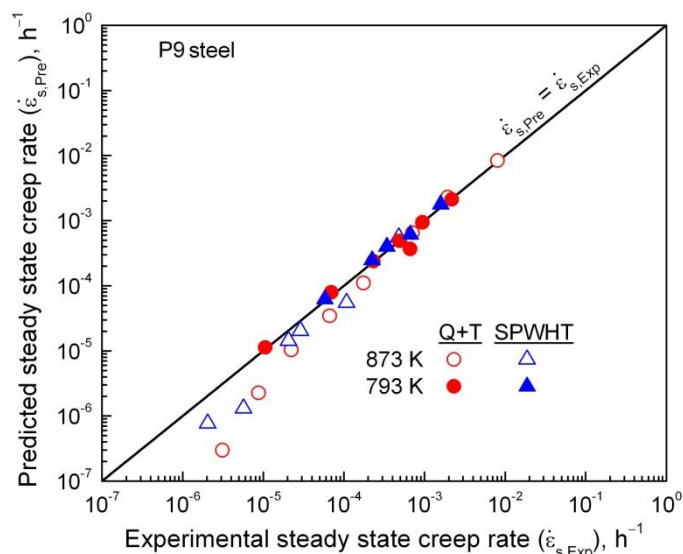


Figure 4.10 Predicted vs. experimental steady state creep rate at 793 and 873 K for Q+T and SPWHT conditions.

the predicted steady state creep rates have been found to be marginally lower than the experimentally measured values as observed in the deviations from the theoretical

$\dot{\epsilon}_{s,Pred} = \dot{\epsilon}_{s,Exp}$ broken line shown in Figure 4.10. The observed lower values of predicted steady state creep rates at low stresses has been examined in terms of the predicted evolution of internal stress with strain. At high stresses, the faster evolution of internal stress approaching towards well defined saturation at the strain equivalent to experimental steady state condition has been observed. Figure 4.11(a) shows the occurrence of well defined saturation in internal stress at high stresses at 793 K as an example. On the contrary, slow evolution of internal stress and absence of well defined saturation at the strain equivalent to experimental steady state condition has been observed at low stresses as shown in Figure 4.11(b). The ratio of internal stress value at the strain equivalent to experimental steady state condition to the predicted σ_{is} value at low applied stresses has been obtained as 0.98. Based on this, the value of internal stress at low stresses has been approximated as 98% of the

predicted steady state value. At applied stresses lower than <100 MPa, $0.98\sigma_{is}$ has been used for evaluating the predicted steady state creep rate in Equation (4.12). Following the modification, a good agreement between the predicted and experimental steady state creep rates has been obtained as shown in Figure 4.12. The theoretical line representing $\dot{\epsilon}_{s,Pred} = \dot{\epsilon}_{s,Exp}$ is also superimposed in Figure 4.12. Based on the present analysis, it can be suggested that the strain to achieve well-defined steady state is slightly away from the experimentally observed strain value at low stresses.

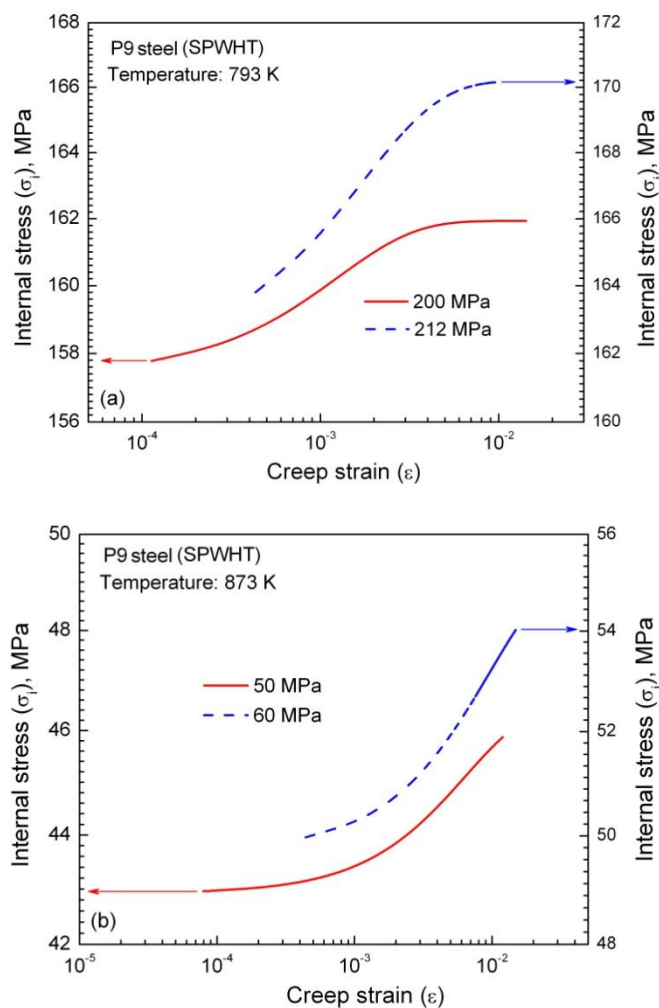


Figure 4.11 Evolution of internal stress with strain for (a) high stresses at 793 K and (b) low stresses at 873 K in SPWHT condition.

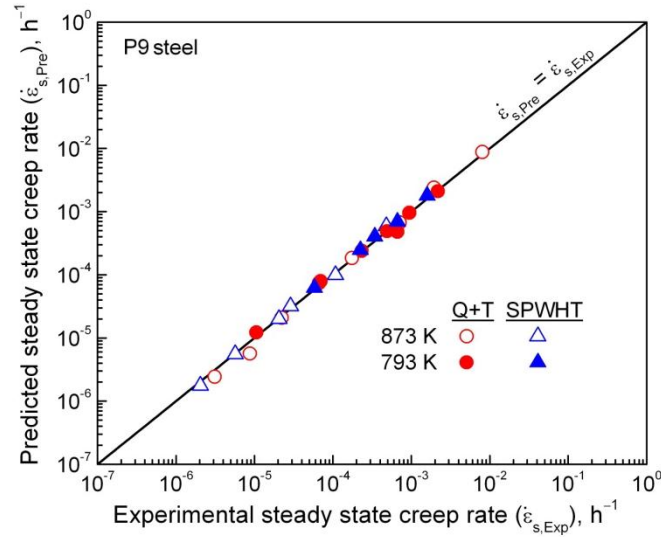


Figure 4.12 Predicted vs. experimental steady state creep rate for Q+T and SPWHT conditions at 793 and 873 K. The prediction is based on the approximation in internal stress as $0.98\sigma_{is}$ at steady state strain.

Statistically, the description of steady state creep rate $\dot{\epsilon}_s = \dot{\epsilon}_s(\sigma_{es})$ by sinh function is equivalent to the description by the power function [91]. The variations in predicted steady state creep rate with effective stress exhibited linear variations in double logarithmic plots at 793 and 873 K as shown in Figure 4.13. This clearly indicates that the effective stress dependence of steady state creep rate obey power law as $\dot{\epsilon}_s = A'\sigma_{es}^n$. The values of stress exponent $n = 5.4$ at 793 K and 4.75 at 873 K, and coefficient $A' = 6.9 \times 10^{-13} \text{ MPa}^{-5.4} \text{ h}^{-1}$ at 793 K and $5.6 \times 10^{-10} \text{ MPa}^{-4.75} \text{ h}^{-1}$ at 873 K have been obtained. Further, invoking the concept of internal stress into creep relationship in the present model, one-slope behaviour in the effective stress dependence of steady state creep rate with n close to 5 has been observed for P9 steel. This is in agreement with the reported observations for the effective stress dependence of steady state creep rate in 9% Cr steels [29, 30]. The two slope behaviour in the applied stress dependence of creep rate with different values of stress exponent and apparent activation energy [26, 29, 30, 164] has been rationalised by incorporating resisting/back stress into creep relationship [29, 164]. In Equation (4.9), the pre sine hyperbolic factor (Z) related to the mean velocity of dislocation motion exhibited applied stress and temperature

dependence as shown in Figure 4.14. Equation (4.9) in terms of Z can be expressed as $\dot{\epsilon}_s = Z \sinh(\Delta V \sigma_{es} / M k T)$. Strong temperature dependence of Z and an increase in Z with applied stress can be seen in Figure 4.14. This is in agreement with the reported variations of Z with respect to temperature and stress in metals and alloys [91, 165]. The variations in activation volume (ΔV) at steady state with normalised applied stress (σ_a / μ) exhibited a non-linear behaviour as shown in Figure 4.15. A rapid decrease in activation volume at low stresses at 873 K followed by a gradual decrease at high stresses at 793 K can be seen in Figure 4.15. The values of activation volume varied from 3300 b^3 at 873 K/50 MPa to 530 b^3 at 793 K/250 MPa. A similar variation in the experimentally measured activation volume with effective stress has been observed for zirconium in the temperature range 898-1098 K with an insignificant influence of temperature [166]. Based on the shear model, Kauzmann [167] reported the value of activation volume as $\Delta V \approx b^3$. Though the values of ΔV depend on the type of alloy and applied stress, ΔV in the range 3300-30 b^3 for creep deformation of 16 different metals and alloys such as lead, tin, Zinc, brass and steel has been reported [167, 168].

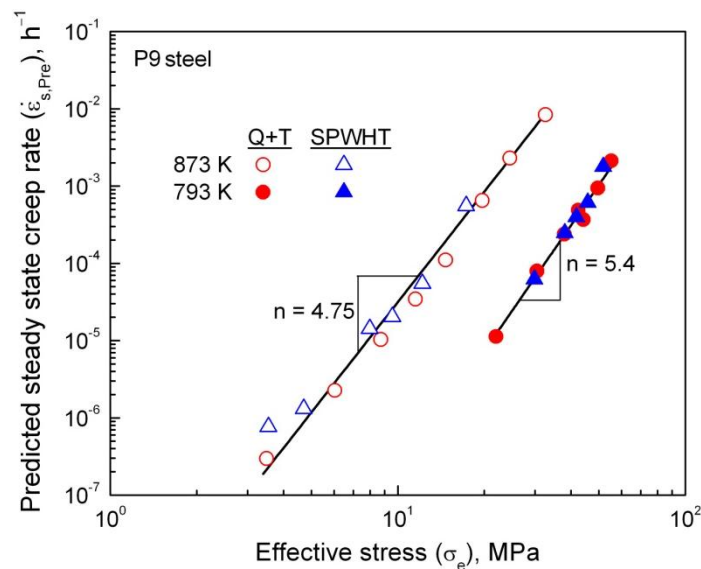


Figure 4.13 Predicted steady state creep rate with effective stress obeying power law function for Q+T and SPWHT conditions at 793 and 873 K.

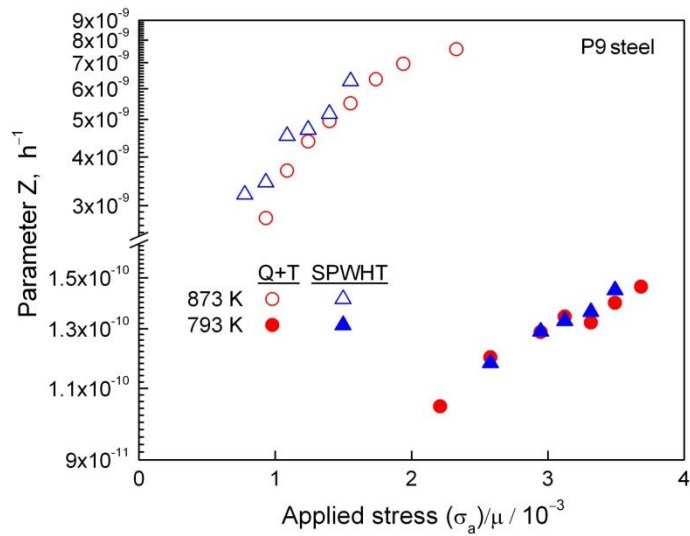


Figure 4.14 Variations in pre sine hyperbolic factor, parameter Z with normalised applied stress at 793 and 873 K.

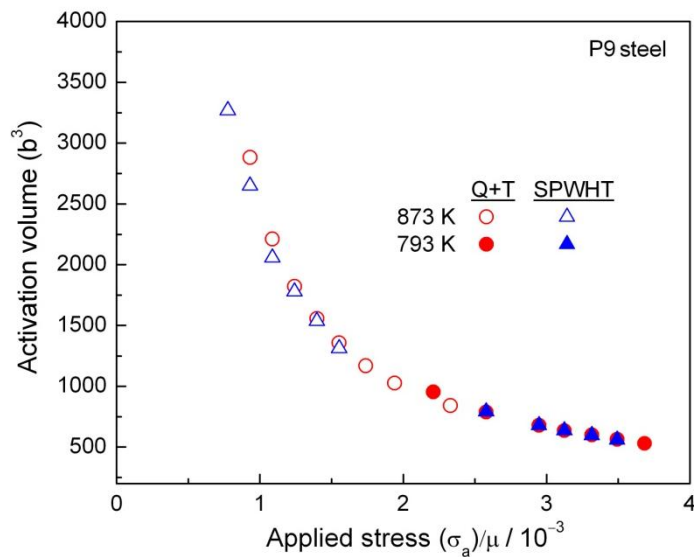


Figure 4.15 Variations in predicted activation volume with the normalised applied stress at 793 and 873 K.

4.5 Conclusions

The constitutive model based on sine hyperbolic creep rate relation associated with the concept of stress dependent activation volume and average dislocation segment length related to the Friedel statistics has been developed. The sine hyperbolic creep rate relation coupled with the evolution of internal stress as a function of strain provides a better understanding of primary and secondary creep behaviour of P9 steel. Following Estrin-

Mecking approach, the evolution of mean internal stress from the initial to saturation value during creep deformation has been considered. The applicability of the model has been demonstrated by comparing the predicted and experimental creep strain-time and creep rate-strain data in P9 steel in quenched and tempered (Q+T) and simulated post weld heat treatment (SPWHT) conditions at 793 and 873 K. The model suggested that the increase in internal stress (or decrease in effective stress) with strain/time results in the observed decrease in creep rate during primary creep in the steel. Irrespective of temperature and heat treatment conditions, the optimised parameters associated with the internal stress values exhibited linear variations with the applied stress. The observed difference in the primary and secondary creep characteristics at 793 and 873 K between Q+T and SPWHT conditions has been ascribed to the variations in rate constant associated with the model. The lower rate constant values for SPWHT condition than for Q+T condition at both 793 and 873 K signifies the enhanced dynamic recovery effects in SPWHT condition due to the presence of relatively coarse initial microstructure. At all test conditions, good agreement observed between predicted and experimental steady state creep rates demonstrated further applicability of the model. The predicted variations in activation volume at steady state with applied stress are in accordance with the experimentally reported observations in metals and alloys.

Chapter 5: Modelling totality of creep deformation and development of damage in 9% Cr tempered martensitic steels

5.1 Introduction

Creep deformation and damage are the most critical issues for determining the structural integrity of the components operating at elevated temperatures in nuclear and other power generating industries. In order to provide reliable design and analysis of high temperature components, it becomes necessary to model the creep deformation and damage behaviour appropriately [169]. Constitutive description for the development of damage during tertiary creep is also required towards the assessment of the remaining life of components during service. In view of above, two different approaches have been employed to examine the totality of creep deformation in 9% Cr containing tempered martensitic steels in the present research. The first is based on the additive creep rate formulation where the developed sine hyperbolic creep rate formulation for transient creep has been added to tertiary creep rate as a function of tertiary creep strain obtained using MPC-Omega methodology [107] with necessary modification. Applicability of the model has been demonstrated for 9% Cr steels. In the second, the microstructure based Semba-Dyson-McLean model [108] has been used for the description of creep deformation and damage behaviour of P9 steels. However, Semba-Dyson-McLean model does not account for the influence of individual precipitates on creep behaviour of 9% Cr steels. In order to account the influence of individual microstructural damages arising from the coarsening of $M_{23}C_6$ and conversion of useful MX precipitates into deleterious Z-phase on long-term creep behaviour [49] of the modified 9Cr-1Mo steel, necessary modifications have been made into the original kinetic creep law proposed by Dyson and McLean. An exponential rate relationship has been introduced for the evolution of number density of MX precipitates with time. It has been shown that the developed model adequately predicts the experimental long-term creep strain-

time as well as creep rate-time data. The role of Z-phase on long-term creep behaviour of T91 steel has also been discussed in this chapter.

5.2 Framework of Additive Creep Rate Formulation

In the additive creep rate formalism, total creep rate ($\dot{\epsilon}$) is defined as

$$\dot{\epsilon} = \dot{\epsilon}_p + \dot{\epsilon}_s + \dot{\epsilon}_{tr}, \quad \text{Equation (5.1)}$$

where $\dot{\epsilon}_p$, $\dot{\epsilon}_s$ and $\dot{\epsilon}_{tr}$ are representative primary, steady state and tertiary creep rate, respectively. For the combined description of primary and secondary creep deformation, the developed sine hyperbolic rate equation has been used (as discussed in Chapter 4). Towards the description of tertiary creep behaviour of tempered martensitic steel as a function of tertiary creep strain, modified MPC-omega method has been proposed. The applicability of the totality of the model has been demonstrated for creep deformation behaviour of tempered martensitic plain P9 steel at 873 K for different stress levels.

5.2.1 Tertiary creep behaviour: MPC-Omega Methodology and its modification

The general functional form of tertiary creep rate as a function of tertiary creep strain i.e., $\frac{d\epsilon_{tr}}{dt} = \dot{\epsilon}_{tr} = \dot{\epsilon}_s f(\epsilon_{tr})$ has been considered to describe the tertiary creep behaviour of P9 steel. Irrespective of the microstructural details of creep damage and its kinetics, the ratio of tertiary and secondary creep rates i.e., $\frac{\dot{\epsilon}_{tr}}{\dot{\epsilon}_s}$ itself can be considered as a measure of the current extent of creep damage. A relation in the generalised form known as MPC-Omega method [107] is expressed as

$$\dot{\epsilon}_{tr} = \dot{\epsilon}_s \exp(\Omega \epsilon_{tr}), \quad \text{Equation (5.2)}$$

where Omega ‘ Ω ’ is the creep rate accelerating factor depends on applied stress and temperature. The increase in creep rate in the tertiary creep region is evaluated from the slope of the semi-logarithmic plot of creep rate vs. creep strain as $\Omega = \frac{d \ln \dot{\epsilon}_{tr}}{d \epsilon_{tr}}$.

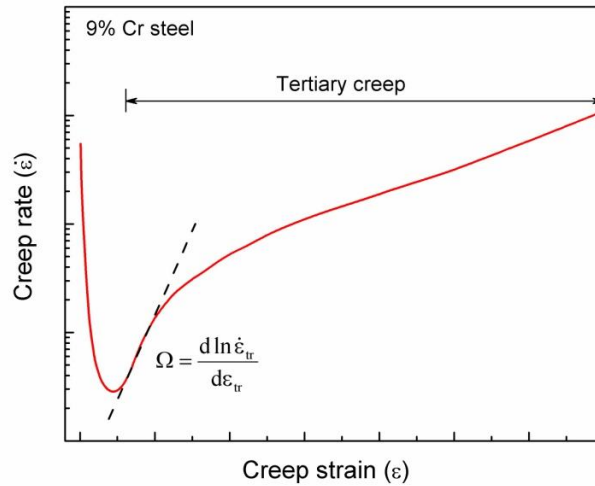


Figure 5.1 Typical creep rate ($\dot{\epsilon}$) - creep strain (ϵ) data for 9% chromium containing steels at high temperatures.

Figure 5.1 shows typical deformation behaviour in the primary, secondary and tertiary creep in 9% chromium tempered martensitic steel. It can be seen that Equation (5.2) represents only the initial linear portion of tertiary creep, where $\Omega = \frac{d \ln \dot{\epsilon}_{tr}}{d \epsilon_{tr}}$ is obeyed. Beyond $\Omega = \frac{d \ln \dot{\epsilon}_{tr}}{d \epsilon_{tr}}$, the accumulation of large tertiary creep strain is not represented by Equation 5.2. The non-linear tertiary creep region is generic to 9% Cr steels [170]. In order to account for the complete tertiary creep trajectory, a modified formulation has been employed in the present analysis as

$$\dot{\epsilon}_{tr} = \dot{\epsilon}_s \exp(\beta \epsilon_{tr}^\eta), \quad \text{Equation (5.3)}$$

where β and η are the tertiary creep constants. According to Eq. 8, the slope of the semi-logarithmic creep rate vs. creep strain data as $\frac{d \ln \dot{\epsilon}_{tr}}{d \epsilon_{tr}} = \beta \eta \epsilon_{tr}^{\eta-1}$ is a function of tertiary creep strain. When η approaches the value of unity, β approaches towards the value of Ω originally

proposed by Prager [107]. In such a condition, the semi-logarithmic plot of creep rate vs. creep strain remains linear during tertiary creep. For 9% Cr steels showing non-linear tertiary creep behaviour (Figure 5.2), the theoretical plots displaying the influence of β and η on the variations of $\ln\left(\frac{\dot{\epsilon}_{tr}}{\dot{\epsilon}_s}\right)$ vs. ϵ_{tr} are shown in Figure 5.2. It can be seen that for a given tertiary creep strain, $\ln\left(\frac{\dot{\epsilon}_{tr}}{\dot{\epsilon}_s}\right)$ increases with increase in β and decrease in η (Figure 5.2). The choice

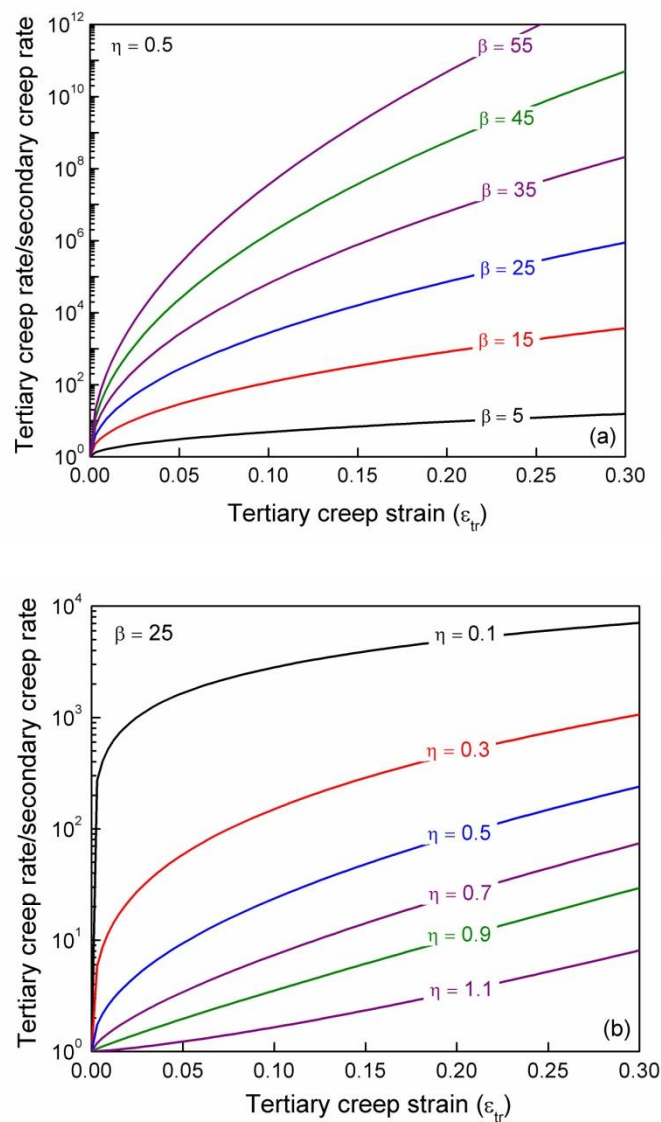


Figure 5.2 Theoretical plots depicting the influence of tertiary fitting constants (a) β with $\eta = 0.5$ or Ω with $\eta = 1$ and (b) η with $\beta = 25$ on the ratio between tertiary creep rate with steady state creep rate

of varying β from 5 to 55 for a fixed value of $\eta = 0.5$ and varying η from 0.1 to 1.1 for a fixed value of $\beta = 25$ have been chosen arbitrarily. The observations in Figure 5.2 clearly suggest that the higher value of β or the lower value of η is directly related to higher creep rate during tertiary creep. In other words, higher β or lower η necessarily indicates low resistance to creep damage.

5.2.2 Formulation for the totality of Creep Behaviour

The complete set of differential equations defining the totality of creep deformation and damage in the primary, secondary and tertiary creep can be given as

$$\dot{\varepsilon} = \dot{\varepsilon}_{p+s} + \varepsilon_{tr}$$

$$\dot{\varepsilon}_{p+s} = \frac{\rho_m b^2 v_D \sigma_e (\sigma_i^2 \sigma_e)^{-1/3}}{M^2} \exp\left(\frac{-Q}{RT}\right) \sinh\left(\frac{\sigma_e}{MkT} b^3 \left[\frac{\mu}{(\sigma_i^2 \sigma_e)^{1/3}}\right]\right) \quad \text{Equation (5.4)}$$

$$\dot{\sigma}_i = \frac{1}{\sigma_i \varepsilon_c} (\sigma_{is}^2 - \sigma_i^2) \dot{\varepsilon}_{p+s}$$

$$\dot{\varepsilon}_{tr} = \frac{\rho_m b^2 v_D \sigma_{es} (\sigma_{is}^2 \sigma_{es})^{-1/3}}{M^2} \exp\left(\frac{-Q}{RT}\right) \sinh\left(\frac{\sigma_{es}}{MkT} b^3 \left[\frac{\mu}{(\sigma_{is}^2 \sigma_{es})^{1/3}}\right]\right) \exp(\beta \varepsilon_{tr}^\eta)$$

In the present analysis, the applicability of the additive creep rate formulation has been demonstrated for P9 steel at 873 K as an example. In addition to initial internal stress (σ_{i0}), internal stress at saturation (σ_{is}), rate constant (ε_c), the additional constants such as β and η associated with the tertiary creep rate model are optimised. For given applied stress, relative least-square optimisation methodology has been adopted for deriving the values of β and η .

5.3 Predictability of Additive Creep Rate Formulation

Typical experimental and predicted creep strain-time data at 60 MPa for P9 steel tubeplate forging in Q+T condition are shown in Figure 5.3. Two different variants of Equation (5.4) have been employed for fitting the experimental creep data. In the first instance, by invoking the original MPC-Omega method, the value of η has been fixed as

unity in Equation (5.4) for the evolution of tertiary creep strain with time. The predicted data for $\eta = 1$ is shown by the full line and designated as ‘Model-A’. In another case, the creep strain-time data has been predicted using optimised parameters without fixing any constants in Equation (5.4), and this is presented by the broken line as ‘Model-B’. It can be clearly seen that compared to Model-A, Model-B accurately predicts the evolution of creep strain with time in the primary, secondary and tertiary creep regimes (Figure (5.3)).

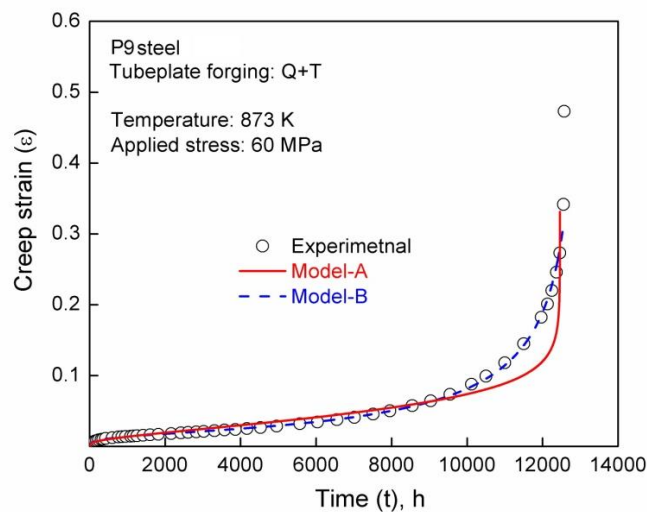


Figure 5.3 Experimental creep strain (ϵ) - time (t) data for P9 steel tubeplate forging at 873 K for 60 MPa. The respective best-fit data obtained for Model-A and Model-B are superimposed as broken and full lines, respectively.

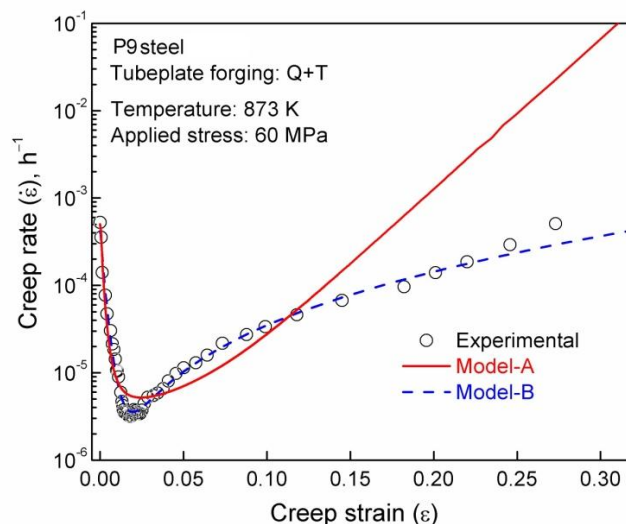


Figure 5.4 Experimental creep strain ($\dot{\epsilon}$) - time (ϵ) data for P9 steel tubeplate forging at 873 K for 60 MPa. The respective best-fit data obtained for Model-A and Model-B are superimposed as broken and full lines, respectively.

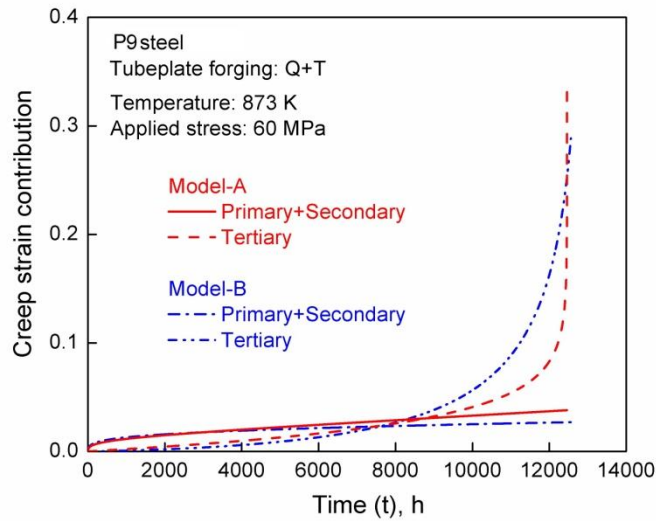


Figure 5.5 The predicted variations in primary plus secondary and tertiary strain contributions with time for Model-A and Model-B are depicted as broken and full lines, respectively.

This is also reflected in the variations of creep rate with creep strain in the semi-logarithmic plot shown in Figure 5.4. The appropriateness of Model-B for the prediction of creep rate vs. creep strain in all the three regimes is discernible in Figure 5.4. On the contrary, a large positive deviation in the predicted creep rate at higher strains using Model-A can be seen in Figure 5.4. The applicability of Model-A and Model-B is further examined from the evolution of primary plus secondary and tertiary creep strain components with time predicted by both the models as shown in Figure 5.5. It can be seen that only a marginal difference in the evolution of primary plus secondary creep strains is observed between the two models. Contrary to this, a significant difference in the evolution of tertiary creep strain between the models can be seen in Figure 5.5. This is similar to that observed for the prediction of total creep strain vs. time data shown in Figure 5.3. All these observations suggest that Model-B consisting of modified MPC-Omega method for tertiary creep (Equation (5.4)) appropriately describes creep deformation behaviour in P9 steel. The applicability of Model-B has been examined over the stresses ranging from 60 to 125 MPa. The variations of experimental as well as predicted creep strain with time and creep rate with creep strain for different stresses

are shown in Figures 5.6. Good agreement between the experimental and predicted creep data suggests the validity of Model-B for P9 steel.

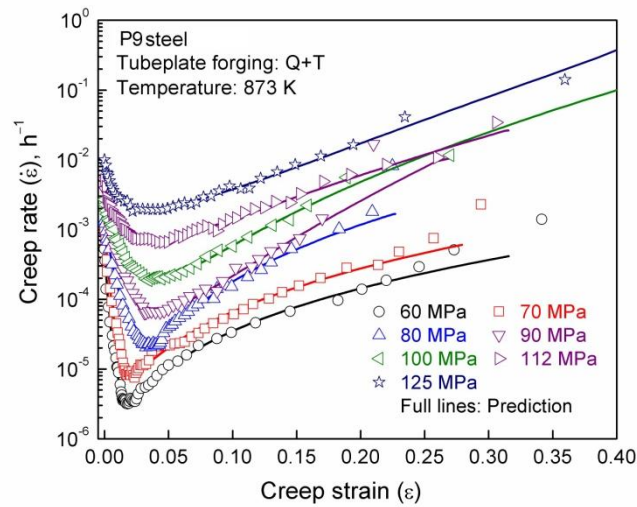


Figure 5.6 Experimental creep rate ($\dot{\epsilon}$) - creep strain (ϵ) for P9 steel tubeplate forging at 873 K for different stress levels. The best-fit data of Model-B are superimposed as solid lines for different stresses.

In the present analysis, a combination of internal stress based approach for primary as well as secondary creep and the modified MPC-Omega method for tertiary creep has been employed for modelling the totality of creep deformation. It was reported that mathematical relationships which provide the best representation of primary, secondary and tertiary creep have been chosen among the different constitutive formalisms [171]. It has been shown that the adopted approach provides an accurate description of experimentally measured creep data in P9 steel (Figures 5.3, 5.4 and 5.6). For fitting experimental creep data with original MPC-Omega method, selection of specific data having linear $\ln \dot{\epsilon}_{tr}$ vs. ϵ_{tr} region becomes necessary as shown in Figure 5.1 [170]. It can be seen that in the present additive creep rate formulation, selection of specific creep data is not required. Moreover, the proposed modified MPC-Omega method effectively accounts for non-linearity in the creep strain-time data generally observed during tertiary creep in 9% chromium tempered martensitic steels.

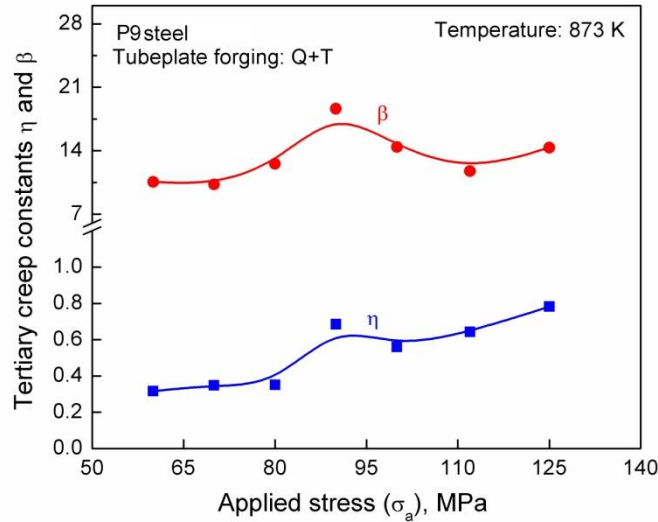


Figure 5.7 The variations in tertiary fitting constants such as β and η with applied stress for 9Cr-1Mo steel tubeplate forging at 873 K.

The variations in tertiary creep constants β and η with applied stress are shown in Figure 5.7. The value of β increases from 10 at 60 MPa to 18 at 90 MPa followed by a marginal decrease to a value around 14 above 100 MPa. A rather low value of $\eta < 1$ for different stresses has been obtained. At low stresses (60-80 MPa), η has the value of about 0.3, while η about 0.66 above 90 MPa has been observed. The low value of η at low stresses necessarily suggests higher evolution of creep rate and lower resistance to deformation during tertiary creep. The dominance of creep damage at low stresses has also been presented as the variations of predicted $\beta \varepsilon_{tr}^{\eta}$ as a function of life fraction (t/t_r) in Figure 5.8. $\beta \varepsilon_{tr}^{\eta}$ vs. t/t_r plots clearly shows two separate groupings of creep data one for high stresses (90-125 MPa) and the other for low stresses (60-80 MPa). Since $\beta \varepsilon_{tr}^{\eta}$ directly correlates with the totality of damage associated with tertiary creep [172], significantly higher values of $\beta \varepsilon_{tr}^{\eta}$ clearly suggest higher dominance of creep damage in the low stress regime (60-80 MPa) than that observed at high stresses. The dominance of microstructural degradation in P9 steel has been ascribed to decrease in dislocation density, coarsening of precipitates and dislocation substructure and depletion of solutes [22]. Based on the detailed analysis in terms of creep

damage tolerance factor (λ) and creep damage criterion, it has been shown that the dominance of microstructural degradation at low stresses is reflected in the high value of $\lambda = 10$ at low stresses compared to $\lambda = 5$ at high stresses [22, 38].

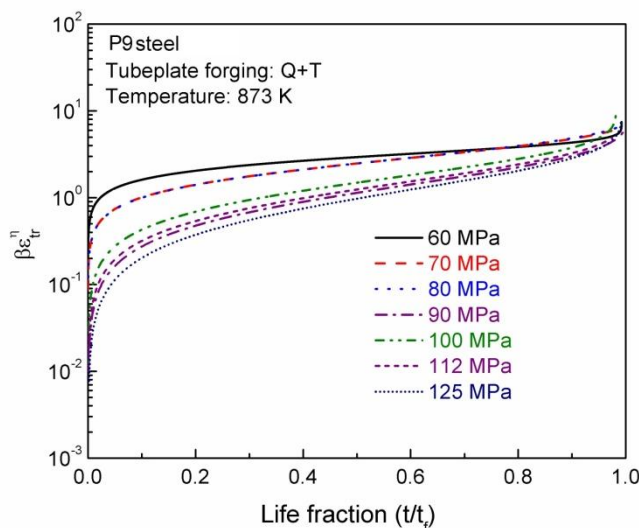


Figure 5.8 The variations in $\beta \epsilon_{tr}^n$ with life fraction for P9 steel tubeplate forging at 873 K for different stress levels.

The applicability of the proposed creep model has been further examined by comparing the creep results for 60 MPa at 873 K for tubeplate forging in Q+T and SPWHT conditions and plate material in N+T condition representing different initial microstructures in P9 steel (Figure 5.9). Tubeplate forging in SPWHT condition representing softened microstructure results in significantly higher evolution of creep strain with time and lower rupture life than those in Q+T condition (Figure 5.9 (a)). Compared to tubeplate forging in Q+T condition, P9 steel plate in N+T condition representing hardened microstructure displayed the lower evolution of creep strain with time and higher rupture life. The respective best-fit creep curves predicted using Model-B for three different microstructures have been superimposed as full lines in Figures 5.9. Good agreement between the experimental and predicted creep strain-time (Figures 5.9 (a)) and creep rate-creep strain (Figures 5.9 (b)) data suggests further applicability of the additive creep rate model for different conditions in P9 steel.

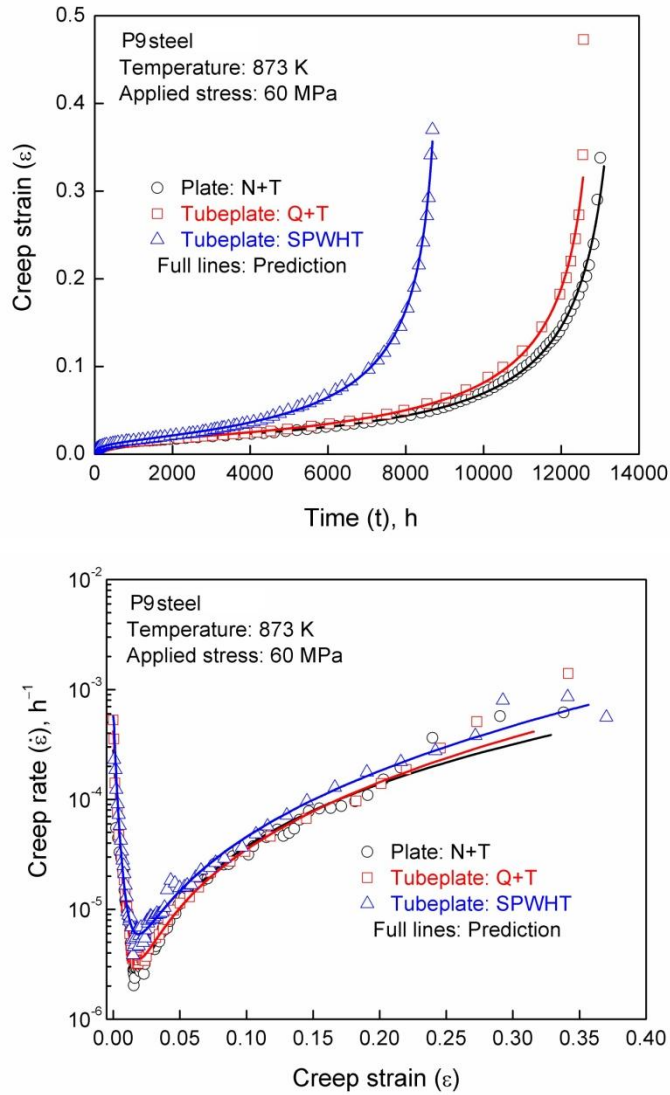


Figure 5.9 Experimental (a) creep strain (ϵ) vs. time (t) and (b) creep rate ($\dot{\epsilon}$) vs. strain (t) for 9Cr-1Mo steel with different conditions of tubeplate forging in quenched and tempered (Q+T), tubeplate forging in simulated post-weld heat treatment (SPWHT) and plate material in normalized and tempered (N+T) at 873 K for 60 MPa. The best-fit creep data predicted using Model-B are superimposed as full lines.

The parameters associated with the proposed creep model for different microstructures are presented in Table 5.1. The observed increased resistance to creep deformation during primary and steady state creep is reflected in the systematic increase in initial internal stress (σ_{i0}) and internal stress at saturation (σ_{is}) in the sequential order as tubeplate forging: SPWHT < tubeplate forging: Q+T < plate: N+T (Table 5.1). However, increased total damage accumulation is replicated in the tertiary creep parameters with a systematic increase

in β and a decrease in η followed the order tubeplate forging: SPWHT < tubeplate forging: Q+T < plate: N+T (Table 5.1). This is consistent with the observed systematic increase in β and decrease in η with decrease in applied stress for P9 steel tubeplate forging in Q+T condition. The predicted evolution of $\beta\varepsilon_r^\eta$ as a function of life fraction (t/t_r) shown in Fig. 5.10 clearly demonstrate marginally higher accumulation of damage for P9 steel plate material in N+T condition than those for tubeplate forging in Q+T and SPWHT conditions. Creep-rupture lives (t_r) has been predicted using the proposed creep Model-B as

$$t_r \approx \frac{\int_0^{\varepsilon_{tr,f}} \exp(-\beta\varepsilon^\eta) d\varepsilon}{\dot{\varepsilon}_s} \approx \frac{\int_0^\infty \exp(-\beta\varepsilon^\eta) d\varepsilon}{\varepsilon_s}, \quad \text{Equation (5.5)}$$

where $\varepsilon_{tr,f}$ is the failure strain. The numerical integration was performed for evaluating the rupture lives for a fixed value of β and η at a given test condition. Figure 5.11 shows comparison between experimental and predicted rupture lives for P9 steel tubeplate forging in Q+T condition for stresses ranging from 60 to 125 MPa, and for tubeplate forging in SPWHT condition and N+T plate material at 60 MPa. Good agreement between experimental and predicted rupture lives is discernible in Figure 5.11.

Table 5.1- The optimised parameters associated with the model for depicting creep data of P9 steel for 60 MPa at 873 K.

Product form	σ_{i0} , MP _a	σ_{is} , MP _a	ε_c	β	η
Tubeplate forging : SPWHT	49.4	55.7	0.016	10.1	0.35
Tubeplate forging : Q + T	49.8	56.4	0.020	10.6	0.31
Plate : N+T	50.2	57.1	0.030	10.8	0.25

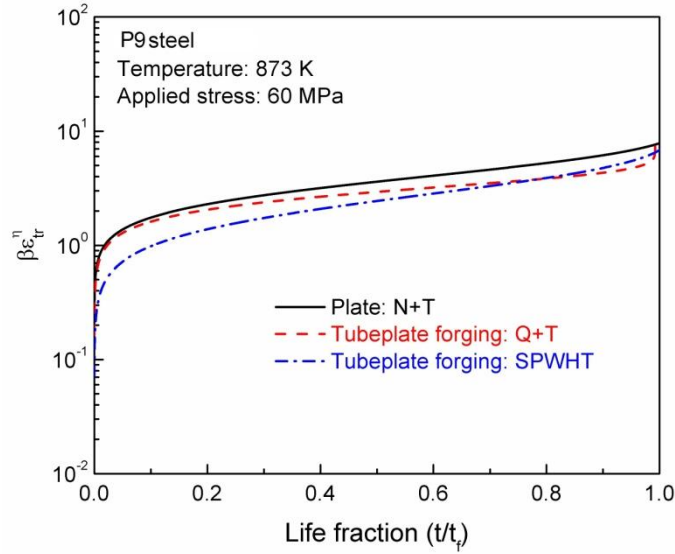


Figure 5.10 Variations in $\beta \epsilon_{tr}^n$ with life fraction (t/t_r) for P9 steel with different conditions of tubeplate forging in quenched and tempered (Q+T), tubeplate forging in simulated post-weld heat treatment (SPWHT) and plate material in normalized and tempered (N+T) at 873 K for 60 MPa.

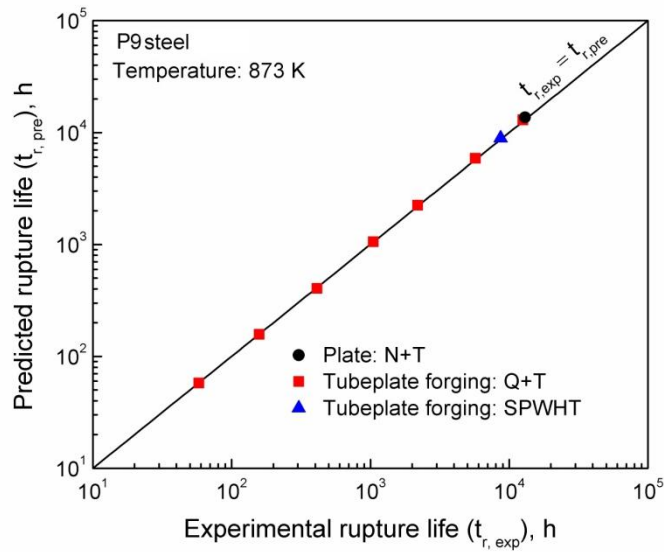


Figure 5.11 Comparison between experimental ($t_{r,exp}$) and predicted ($t_{r,pre}$) rupture lives for P9 steel in different conditions. $t_{r,exp} = t_{r,pre}$ relation is shown by full line.

Though the developed new additive creep rate model accurately predicts the creep strain-time trajectories and rupture lives of 9% Cr steels, the variable i.e., tertiary creep strain involved in the model cannot be considered as an internal-state-variable. Based on the principle of objectivity of constitutive modelling [173], time should not be treated as a state-variable in

creep rate formulations. In that sense, choice of strain rather than time is justified for all realistic conditions for engineering alloys where tertiary creep dominates [174].

5.4 Microstructure Based Dyson-McLean Approach

The kinetic creep law in Dyson-McLean approach is expressed as [53]

$$\dot{\varepsilon} = \dot{\varepsilon}_0 \frac{D_d}{1 - \left(1 - \frac{c_e}{c_0}\right) D_s} \sinh \left[\frac{\sigma(1-H)}{\sigma_{0N}(1-D_C)} \right], \quad \text{Equation (5.6)}$$

where $\dot{\varepsilon}_0$ is the characteristic strain rate, D_d defines the damage parameter related to the variations in dislocation density with time, D_s is damage parameter for the solute depletion from the matrix, c_0 and c_e are solute concentrations at $t = 0$ and at equilibrium in matrix, respectively, D_C is the damage parameter associated with the cavitation damage, H is the normalised kinematic back stress and σ_0 is the normalizing stress related to the dislocation-particle interaction. Damage parameter D_d is defined as

$$D_d = (\rho_t / \rho_i), \quad \text{Equation (5.7)}$$

where ρ_i and ρ_t are the dislocation densities at $t = 0$ (initial) and time t , respectively. The empirical relationship for the evolution of D_d with time has been proposed by Dyson [99] for superalloy as

$$\dot{D}_d = C_d \dot{\varepsilon}, \quad \text{Equation (5.8)}$$

where C_d is the rate constant for dislocation multiplication. The damage defining solute depletion relationship is given as

$$D_s = 1 - (\bar{c}_t / c_0), \quad \text{Equation (5.9)}$$

where \bar{c}_t is the mean concentration of solute in the matrix at time t . The rate of D_s is given as

$$\dot{D}_s = K_s D_s^{1/3} (1 - D_s), \quad \text{Equation (5.10)}$$

where K_s is the rate constant. Ion et al. [175] proposed that the stress redistribution which takes place between the soft phase (matrix) and hard phase (precipitates/dispersoids) during creep deformation leads to the development of kinematic back stress in precipitation strengthened alloys. The rate relationship for kinematic back stress (H) is given by Ion et al., [175] as

$$\dot{H} = \frac{h}{\sigma} \left[1 - \frac{H}{H_{\max}} \right] \dot{\epsilon}, \quad \text{Equation (5.11)}$$

where h and H_{\max} are the effective modulus and maximum attainable normalised kinematic back stress, respectively. In Equation (5.6), the normalizing stress σ_{0N} is given as

$$\sigma_{0N} = \frac{kT}{\alpha\mu b^3} \sigma_{Orowan}, \quad \text{Equation (5.12)}$$

In order to include the influence of coarsening of precipitates on creep damage, the relation for σ_{0N} is modified in terms of dimensionless damage parameter associated with precipitate coarsening (D_p) as $\sigma_{0,i} (1-D_p)$. The term $\sigma_{0,i}$ is the initial normalizing stress and it is equal to

$\frac{kT}{\alpha\mu b^3} \sigma_{or,i}$, where $\sigma_{or,i}$ denotes the initial Orowan stress. The term D_p is defined as

$$D_p = 1 - \frac{d_i}{d_t}, \quad \text{Equation (5.13)}$$

where d_i is the initial size and d_t is the precipitate size at any time t . By using the concept of volume diffusion controlled Ostwald ripening, the evolution rate of D_p is given as

$$\dot{D}_p = \frac{K_p}{3} (1 - D_p)^4, \quad \text{Equation (5.14)}$$

where K_p is the rate constant. The damage parameter for cavitation is defined as [176, 177]

$$D_C = 1 - \frac{A_{C,i}}{A_{C,t}}, \quad \text{Equation (5.15)}$$

where $A_{C,i}$ and $A_{C,t}$ are area fraction of cavitated boundary facets at $t = 0$ and time t , respectively. When cavity nucleates continuously, the evolution of D_C with the time is given as [176, 178]

$$\dot{D}_C = \frac{1}{3\varepsilon_f} \dot{\varepsilon}, \quad \text{Equation (5.16)}$$

where ε_f is the uniaxial creep strain at fracture. Dyson [99] pointed out that continuous nucleation with the constraint cavities growth during creep appears to be the norm in engineering materials. Creep tests are usually carried out either under constant stress or constant load conditions. In case of creep under constant stress condition, the evolution of stress with the time is given as

$$\dot{\sigma} = 0. \quad \text{Equation (5.17)}$$

Alternatively, constant load (P) condition is mathematically defined as

$$dP=0 \text{ i.e. } d(\sigma A)=0, \quad \text{Equation (5.18)}$$

where A is the cross-sectional area of the specimen. Equation (5.18) can be expanded as

$$A d\sigma + \sigma dA = 0. \quad \text{Equation (5.19)}$$

or

$$d \ln(\sigma) = -d \ln(A). \quad \text{Equation (5.20)}$$

Integration of Equation (5.20) with the appropriate boundary conditions can be represented as

$$\int_{\sigma_a}^{\sigma} d \ln(\sigma) = -\int_{A_i}^A d \ln(A), \quad \text{Equation (5.21)}$$

where σ_a and A_i are the initial applied stress and area of the specimen, respectively. Equation (5.21) yields

$$\sigma = \sigma_a \exp(\varepsilon). \quad \text{Equation (5.22)}$$

Differentiation of equation (19) with time resulted in

$$\dot{\sigma} = \sigma \dot{\varepsilon}. \quad \text{Equation (5.23)}$$

For simulating creep curves under constant load conditions, the numerical integration of coupled differential equations has to be performed under the appropriate constraint given by Equation (5.23).

It is important to mention that the strain-induced subgrain coarsening which usually occurs in 9-12 % Cr steels has not been included in the original Dyson-McLean approach and the empirical evolution relationship for dislocation density with strain was considered in the model. In view of above, an improved phenomenological creep damage relationship has been assimilated by Semba et al. (Semba-Dyson-McLean) [108] for the better description of creep deformation behaviour of 9% Cr containing ferritic-martensitic steels. The improved model involving the incorporation of the evolution of subgrain coarsening and its contribution towards normalised kinematic back stress for tempered martensitic steels has been discussed in the following section on “Semba-Dyson-McLean approach for P9 steel”. Since microstructural degradation during creep results from the strain-dependent coarsening of subgrains along with a decrease in dislocation density, Ostwald ripening of precipitates and depletion of Mo from the matrix due to the precipitation of Laves phase [22], creep deformation behaviour of P9 steel based on improved model has been performed in this investigation. The applicability of the improved Dyson-McLean model proposed by Semba et al. [108] was demonstrated only for the prediction of single creep strain trajectories each at 773 K and 873 K and a single value of dislocation density at saturation (ρ_{sat}) irrespective of initial applied stresses and temperatures were reported for P91 steel. In view of this, two simple modifications in terms of the procedure have been incorporated in the present numerical analysis. The first is related to dislocation density at saturation (ρ_{sat}) and the other is related to optimisation methodology. In the analysis, the variations of dislocation density at saturation (ρ_{sat}) with applied stress have been considered, and it has been shown that the dislocation density at saturation (ρ_{sat}) varies with initial applied stress (σ_a) as $\rho_{\text{sat}} =$

$(\sigma_a/M\alpha\mu b)^2$ [179] for the two heat treatment conditions employed in P9 steel at 873 K. The material constants associated with the model have been numerically optimised using error minimization algorithm for different applied stress levels. The predictability of the model has been demonstrated by comparing the predicted and experimental creep strain/strain rate-time data, steady-state creep rate and time to reach different strain levels for P9 steel in two different heat treated conditions.

5.5 Semba-Dyson-McLean Approach for P9 steel

In Equation 5.11, the maximum attainable value of normalised kinematic back stress H , i.e., H_{\max} has been assumed to be constant for conditions, when the volume fraction of the hard phase region remains constant. Semba et al. [108] considered that the majority of load transfer takes place from the subgrain interior to subgrain boundaries during creep deformation in tempered martensitic steels. Based on this, H_{\max} has been viewed as a varying term as a function of volume fraction of subgrain boundaries (ϕ_{sg}) and H_{\max} is expressed as

$$H_{\max} = \frac{\sigma_{i,\max}}{\sigma} = \frac{2\phi_{sg}}{1+2\phi_{sg}}, \quad \text{Equation (5.24)}$$

where $\sigma_{i,\max}$ is the maximum attainable kinematic back stress. Further, it was formulated that the subgrain volume fraction is inversely related to subgrain size (d_{sg}) with the assumption of constant wall thickness. Since the subgrain coarsening is a common phenomenon in 9-12% Cr steels during creep deformation [40], the evolution of H_{\max} with time can be inter-related to the evolution subgrain size with time as

$$\dot{H}_{\max} = (1-H_{\max})H_{\max} \left(-\frac{\dot{d}_{sg}}{d_{sg}} \right). \quad \text{Equation (5.25)}$$

The inter-relationship between the subgrain size and the network dislocation density (ρ) within the subgrain is given as

$$d_{sg} = k_{sg} \sqrt{\rho_t}, \quad \text{Equation (5.26)}$$

where k_{sg} is constant. The relationship for the evolution of H_{max} in terms of the evolution of dislocation density with time can be represented as

$$\dot{H}_{max} = \frac{(1-H_{max})H_{max}}{2} \left(\frac{\dot{\rho}_t}{\rho_t} \right). \quad \text{Equation (5.27)}$$

Since ρ_t is equal to $D_d \cdot \rho_i$ following Equation 5.7, Equation 5.27 can be modified in terms of dislocation multiplication term D_d as

$$\dot{H}_{max} = \frac{(1-H_{max})H_{max}}{2} \left(\frac{\dot{D}_d}{D_d} \right). \quad \text{Equation (5.28)}$$

For precipitation hardened nickel based superalloys, Dyson [99] used an empirical relation for the evolution of D_d with time as given by Equation 5.8. Instead of an empirical formalism, a phenomenological relationship proposed by Kocks-Mecking-Estrin [82-84] has been utilised for the evolution of dislocation density with time in the present study. The evolution of dislocation density with time is given as

$$\dot{\rho}_t = K_d \rho_t^{1/2} \left(1 - \left(\frac{\rho_t}{\rho_{sat}} \right)^{1/2} \right) \varepsilon, \quad \text{Equation (5.29)}$$

where K_d is the rate constant and ρ_{sat} is the dislocation density at steady state. Since dislocation density increases during primary creep and approaches to saturation at steady state in pure metals, the value of H_{max} is expected to increase with accumulating strain. On the contrary, the value of H_{max} is expected to decrease with accumulating strain, since dislocation density decreases continuously with creep strain in tempered martensitic steels.

Accordingly, Equation 5.29 has been modified in terms of damage parameter D_d as

$$\dot{D}_d = K_d \left(\frac{D_d}{\rho_i} \right)^{0.5} \left(1 - \left(\frac{D_d \rho_i}{\rho_{sat}} \right)^{0.5} \right) \dot{\varepsilon}. \quad \text{Equation (5.30)}$$

For P9 steel, following improved Dyson-McLean model, the complete set of first-order differential equations representing the evolution of creep strain, normalised kinematic back stress, maximum attainable normalised kinematic back stress and damage parameters associated with dislocation density, precipitate coarsening and solute depletion, and applied stress (for constant load creep tests) with time has been presented as

$$\begin{aligned}
\dot{\epsilon} &= \dot{\epsilon}_0 \frac{D_d}{1 - \left(1 - \frac{c_e}{c_0}\right) D_s} \sinh \left[\frac{\sigma(1-H)}{\sigma_{0,i}(1-D_p)} \right] \\
\dot{H} &= \frac{h}{\sigma} \left[1 - \frac{H}{H_{\max}} \right] \dot{\epsilon} \\
\dot{H}_{\max} &= \frac{(1-H_{\max})H_{\max}}{2} \left(\frac{\dot{D}_d}{D_d} \right) \\
\dot{D}_d &= K_d \left(\frac{D_d}{\rho_i} \right)^{0.5} \left(1 - \left(\frac{D_d \rho_i}{\rho_{sat}} \right)^{0.5} \right) \dot{\epsilon} \\
\dot{D}_p &= \frac{K_p}{3} (1-D_p)^4 \\
\dot{D}_s &= K_s D_s^{1/3} (1-D_s) \\
\dot{\sigma} &= \sigma \dot{\epsilon}
\end{aligned} \tag{5.31}$$

According to Kadoya et al. [180], the $(1-c_e/c_0)$ term for the solute depletion damage has been included in the creep rate relation in Semba-Dyson-McLean model [108]. In Equation (5.31), the cavitation damage parameter and its rate relationship have not been incorporated. Based on metallographic investigations, it was reported that the absence of typical creep damage in the form of wedge cracks and r-type cavities in the steel [181]. Further, among 9% Cr steels, P9 steel exhibits higher creep ductility in the range 0.4–0.6 irrespective of temperature, stress and heat treatment conditions [22]. Dyson and Gibbons [34] reported that the mechanisms of creep deformation in nickel-base superalloy are ductility dependent. When ductility is low, grain boundary cavitation would lead to accelerated creep, whereas in the case of high ductility, strain softening would be dominant. According to Blum and Chilukuru [182], tertiary creep rate stems from subgrain coarsening accompanied by the global changes in

dislocation density, coarsening of precipitate and solute depletion in tempered martensitic 9-12% Cr steels. Therefore, high creep ductility coupled with the absence of grain boundary cavitation damage and high values of creep damage tolerance factor ($\lambda \geq 5$) reported for P9 steel ruled out the dominance of cavitation damage for extensive tertiary creep [22]. Further, the cut-off creep strain 0.20 has been considered for the numerical analysis against the strain to failure in the range 0.4–0.6 in P9 steel in the present investigation. It is expected that extensive necking even if it is occurring due to coalescence of microvoids (arising from decohesion of matrix-coarse precipitate) towards the extreme end of tertiary creep (i.e., just before failure) would be dominant at strains higher than 0.20. In all the test conditions, the time to reach creep strain of 0.20 has been found to higher than 0.95 times of rupture lives [22]. In view of this, the rate equation related to cavitation damage i.e., Equation (5.16) was not included in the present analysis.

5.6 Numerical Implementation of Semba-Dyson-McLean Model

For numerical simulation, the total number of 11 materials constants similar to those used by Semba et al. [108] has been considered in the present study. Seven material constants i.e., characteristic strain rate ($\dot{\epsilon}_0$), normalising stress ($\sigma_{0,i}$), effective modulus (h), initial value of H_{\max} ($H_{\max,0}$), dislocation storage parameter (K_d), rate constant associated with precipitation coarsening (K_p), and rate constant associated with solute depletion (K_s) were considered for optimisation. The other three constants such as initial concentration of Mo in the matrix (c_0), equilibrium concentration of Mo in the matrix (c_e) and initial dislocation density (ρ_0) have fixed values (Table 5.2). For fixing the initial concentration (c_0) and equilibrium concentration of Mo in matrix (c_e), thermodynamic calculations have been performed using TCFE6 steels/Fe-alloys database for P9 steel [112]. For calculating initial concentration of Mo in matrix, Laves phase (Fe_2Mo) was suspended from the list of

equilibrium phases. For calculating equilibrium concentration of Mo in matrix, Laves phase was allowed to be present along with other equilibrium phases at 873 K. The initial dislocation density (ρ_i) values for P9 steel in Q+T and SPWHT conditions were taken as fixed value of $6 \times 10^{13} \text{ m}^{-2}$ and $4 \times 10^{13} \text{ m}^{-2}$, respectively. In addition to above, material constant related to dislocation density at saturation (ρ_{sat}) has been fixed following Kocks and Mecking [82-84] formulation presented in Equation 23. Since dislocation density at saturation (ρ_{ss}) depends on initial applied stress (σ_a), the value for saturation dislocation density has been obtained using $\rho_{\text{ss}} = (\sigma_a/M\alpha Gb)^2$.

Table 5.2- Material constants associated with improved Dyson-McLean model.

Material constants with fixed value	Units	Value
Initial concentration of Mo in matrix (c_0)	mol	0.33
Equilibrium concentration of Mo in matrix (c_e)	mol	0.19
Initial dislocation density (ρ_i)	m^{-2}	6×10^{13} (Q+T) 4×10^{13} (SPWHT)
Material constants for optimisation	Units	Lower-upper bounds
Characteristic strain rate ($\dot{\epsilon}_0$)	h^{-1}	$1 \times 10^{-11} - 1 \times 10^{-6}$
Normalising stress ($\sigma_{0,i}$)	MPa	2 – 12
Effective modulus (h)	MPa	$1 \times 10^3 - 1 \times 10^5$
Initial value of H_{max} ($H_{\text{max},0}$)	–	0.1 – 1
Rate constant associated with dislocation storage (K_d)	m^{-1}	$1 \times 10^6 - 1 \times 10^9$
Rate constant associated with precipitation coarsening (K_p)	h^{-1}	$1 \times 10^{-6} - 1 \times 10^{-2}$
Rate constant associated with solute depletion (K_s)	h^{-1}	$1 \times 10^{-6} - 1 \times 10^{-2}$

Table 5.3- Approximate or equivalent guiding values* reported in the literature [100, 108, 183-188] for fixing the lower and upper bounds for the optimisation.

Material constants	$\dot{\epsilon}_0, \text{h}^{-1}$	$\sigma_{0,i}, \text{MPa}$	h, MPa	$H_{\max,0}$	K_d, m^{-1}	K_p, h^{-1}	K_s, h^{-1}
0.5Cr-0.5Mo-0.25V steel							
873 K [183]	3.0×10^{-9}	4.75	2.4×10^5	0.59	-	1.2×10^{-4}	-
863 K [184]	1.3×10^{-9}	6.67	5.8×10^4	0.48	-	7.2×10^{-5}	-
913 K [185]	1.7×10^{-8}	4.11	2.4×10^5	0.59	-	4.7×10^{-4}	-
863 K [186]	4.3×10^{-9}	7.93	1.2×10^5	0.41	-	6.8×10^{-5}	-
2.25Cr-1Mo steel							
748 K [187]	8.3×10^{-10}	8.24	1.6×10^5	0.75	-	4.2×10^{-7}	-
9% Cr steels							
873 K [108]	6.0×10^{-11}	7.80	1.0×10^4	0.32	1.9×10^8	8.0×10^{-5}	5.1×10^{-4}
898 K [188]	1.5×10^{-8}	12.50	9.0×10^3	0.20	-	2.7×10^{-4}	-
923 K [188]	6.2×10^{-8}	6.67	1.0×10^4	0.35	-	5.0×10^{-5}	-
873 K [100]	3.0×10^{-11}	5.74	6.0×10^4	0.57	-	-	-

* indicates that the values are rounded off to significant digits

The lower and upper bounds for seven material constant set i.e., $\{\dot{\epsilon}_0, \sigma_{0,i}, h, H_{\max,0}, K_d, K_p, K_s\}$ are presented in Table 5.2. The bounds for seven material constant set i.e., $\{\dot{\epsilon}_0, \sigma_{0,i}, h, H_{\max,0}, K_d, K_p, K_s\}$ were judged based on the information available in the literature for different grades of ferritic steels [100, 108, 183-188]. Since all the reported constitutive equations do not exactly match with present formulation other than Ref. [108], the existing optimised material constants in literature can be viewed as approximately equivalent set based on their physical meaning. They can be considered as guiding values for fixing the bounds for the constant set i.e., $\{\dot{\epsilon}_0, \sigma_{0,i}, h, H_{\max,0}, K_d, K_p, K_s\}$. The guiding values for fixing the lower and upper bounds for different grades of ferritic steels are presented in Table 5.3.

Since interior-point algorithm can be able to track the best possible solution even for the wide bound levels, either upper or lower or both bounds have been widened as shown in Table 5.1 than the values obtained from the literature (Table 5.3). The developed iterative methodology for obtaining the optimum values of material constants $\{\dot{\epsilon}_0, \sigma_{0,i}, h, H_{\max,0}, K_d, K_p, K_s\}$ has been presented in Figure 5.12. The details related to optimisation methodology are already discussed in Chapter 3.

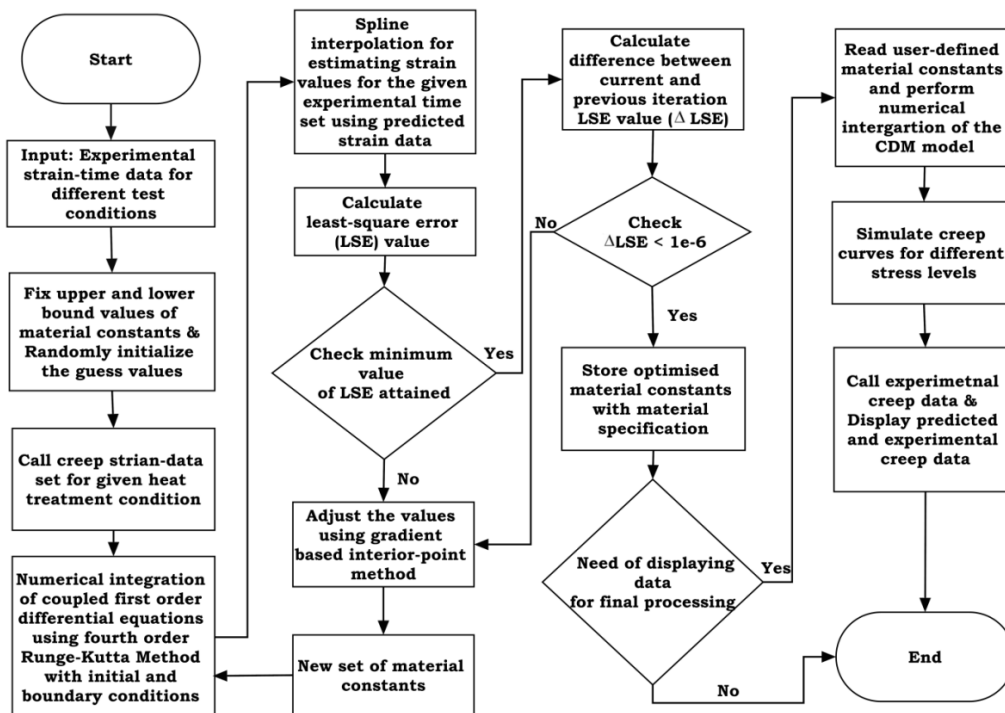


Figure 5.12 Schematic flow diagram describing numerical algorithm for optimisation of material constants associated with the Semba-Dyson-McLean model [108].

The optimised values of material constants have been presented in Table 5.4 for both Q+T and SPWHT conditions. The optimised values for characteristic creep rate ($\dot{\epsilon}_0$), normalising stress ($\sigma_{0,i}$), effective modulus (h), and initial value of H_{\max} ($H_{\max,0}$) show insignificant variations with respect to heat treatment conditions. Contrary to this, the significant influence of prior heat treatments on dislocation storage parameter (K_d), rate constants associated with precipitate coarsening (K_p) and solute depletion (K_s) with heat treatment conditions are explicitly discernible in Table 5.4. For SPWHT condition, three

times lower K_d and about 4.5 times higher K_p and K_s than those in Q+T condition have been obtained (Table 5.4). These values specify that lower dislocation storage rate and higher precipitate coarsening and solute depletion rates prevail in SPWHT condition than in Q+T condition. These observations clearly indicate an enhanced recovery for additionally heat treated SPWHT condition resulting in higher strain accumulation in all the three stages of creep deformation than in Q+T condition (Figure 4.1).

Table 5.4- Optimised values of material constants for P9 steel in Q+T and SPWHT conditions.

Material constants	Units	Optimised material constant set for P9 steel	
		Q+T	SPWHT
Characteristic strain rate ($\dot{\epsilon}_0$)	h^{-1}	1.78×10^{-8}	1.54×10^{-8}
Initial normalising stress ($\sigma_{0,i}$)	MPa	3.2870	3.2402
Effective modulus (h)	MPa	1.15×10^4	1.61×10^4
Initial value of H_{max} ($H_{max,0}$)	–	0.69	0.66
Rate constant associated with dislocation storage (K_d)	m^{-1}	1.34×10^8	3.65×10^7
Rate constant associated with precipitation coarsening (K_p)	h^{-1}	2.3×10^{-5}	1.03×10^{-4}
Rate constant associated with solute depletion (K_s)	h^{-1}	1.02×10^{-5}	4.46×10^{-5}

5.7 Applicability of the Semba-Dyson-McLean model

The optimised constant values can be successfully employed to visualise the way individual damage variables evolve with strain or time. The evolution of strain dependent variables such as normalised kinematic back stress (H), normalised maximum attainable kinematic back stress (H_{max}) and damage parameters associated with dislocation density (D_d) is shown in Figure 5.13 for 60 MPa in Q+T condition as an example. The evolution of time

dependent variables such as damage parameters arising from precipitate coarsening (D_p) and solute depletion (D_s) are also depicted in Figure 5.13. In the improved model, the normalised maximum attainable value of H , i.e., H_{max} is related to current dislocation substructure [108, 175]. A decrease in H_{max} with a continuous decrease in dislocation density (D_d) can be seen in Figure 5.13. Normalised kinematic back stress (H) increases with increase in strain during primary creep followed by a maximum in steady state and a marginal decrease with increase in strain during tertiary creep. The upper bound to stress redistribution is achieved upon H reaching H_{max} for the strain at which creep rate approaches steady state (Figure 5.13). The trend in the evolution of kinematic back stress with primary creep strain followed by approaching saturation is in agreement with those variations observed on single-internal-variable i.e., internal-stress based approach. As expected, the continuous increase in the values of damage parameters associated with the precipitate coarsening (D_p) and solute depletion (D_s) with time can also be seen in Figure 5.13.

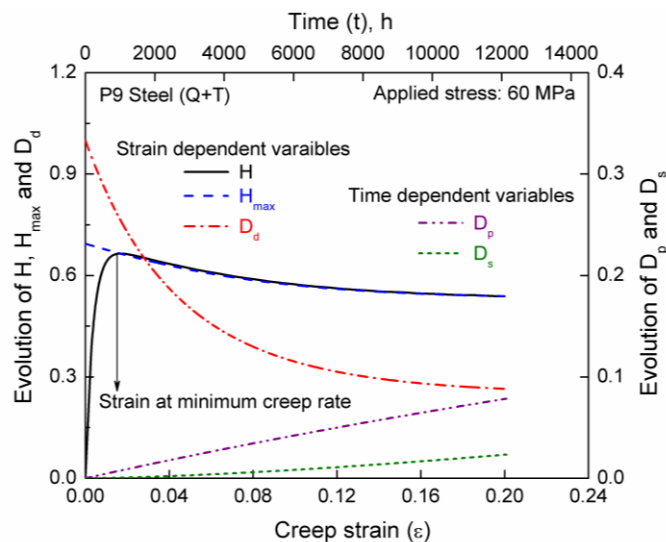


Figure 5.13 Representative plots describing the evolution of strain dependent (normalised kinematic back stress (H), normalised maximum attainable kinematic back stress (H_{max}) and damage associated with dislocation density (D_d)) and time dependent damage arising from precipitate coarsening (D_p) and solute depletion (D_s) during creep deformation for Q+T condition at 60 MPa.

The experimental creep strain-time along with predicted creep strain-time data has been shown in Figure 5.14 (a) and (b) for Q+T and SPWHT conditions, respectively. Symbols

correspond to experimental data and the predicted ϵ - t data is represented by full lines. The accuracy of prediction is also shown by comparing experimental and predicted creep rate–time data in Figure 5.15 (a) and (b) at different stress levels for both the heat treatment conditions. A reasonable agreement between predicted and experimental creep strain–time as well as creep rate–time data at different stress levels is discernible in Figures 14 and 15. The applicability of the model has been further examined by predicting steady state creep rate in both the heat treatment conditions at 873 K. In general, a reasonable agreement between the

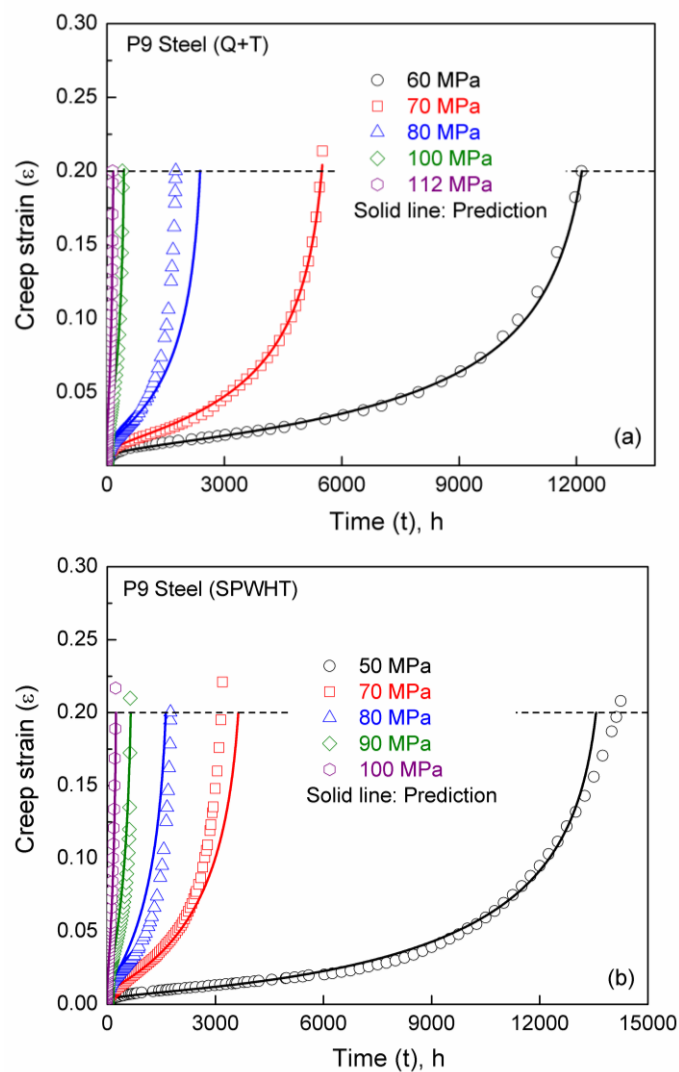


Figure 5.14 Experimental and predicted creep strain–time data for P9 steel in (a) Q+T and (b) SPWHT conditions for different stress levels at 873 K.

predicted and experimental steady state creep rates has been observed for both Q+T and SPWHT conditions as shown in Figure 5.16. In addition to above, the applicability of microstructure based model is also demonstrated by examining the comparison between time to reach specified predicted strains with time to reach the experimental strains for strain levels varying from 1% to 20% for Q+T and SPWHT conditions in Figure 5.17(a) and (b), respectively. It is evident from Figure 5.17 that few data points related to the predicted time to reach 1% strain levels exhibit lower values compared to experimental values obtained for high stress levels of 100 and 112 MPa in Q+T condition and 100 MPa in SPWHT condition.

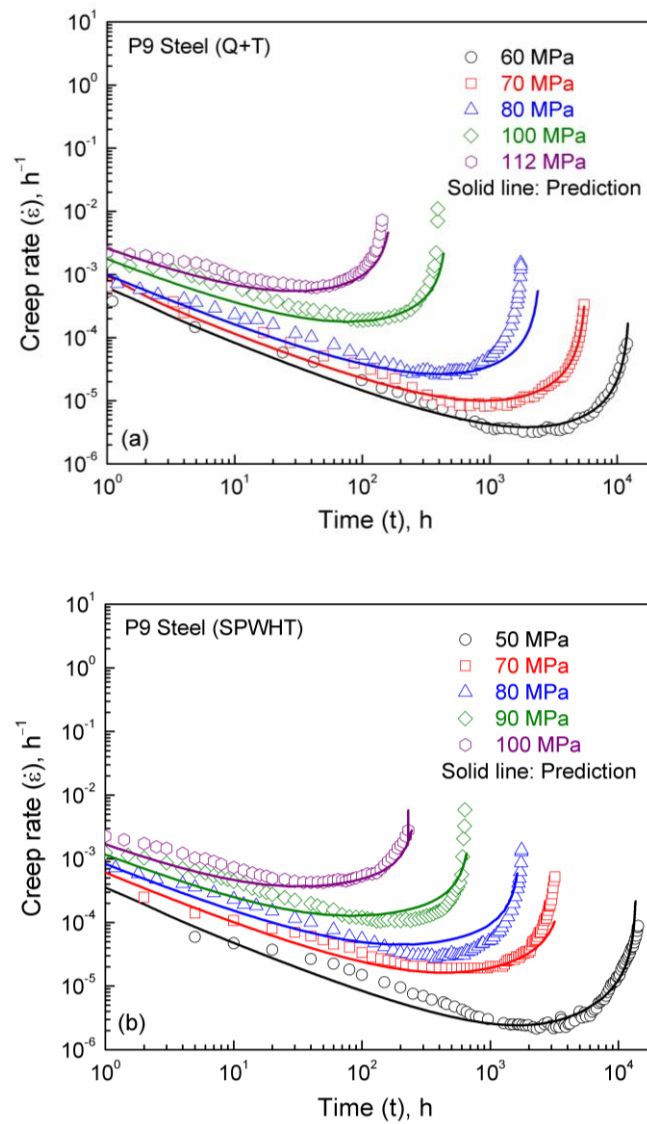


Figure 5.15 Experimental and predicted creep rate-time data for P9 steel in (a) Q+T and (b) SPWHT conditions for different stress levels at 873 K.

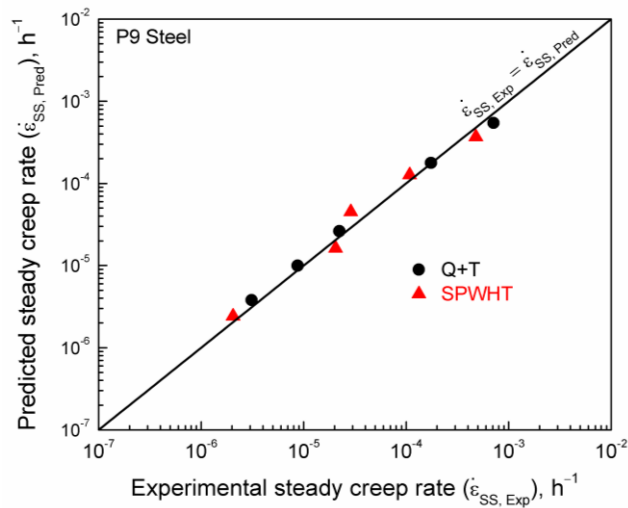


Figure 5.16 Comparison between experimental and predicted steady state creep rates at 873 K for P9 steel in Q+T and SPWHT conditions.

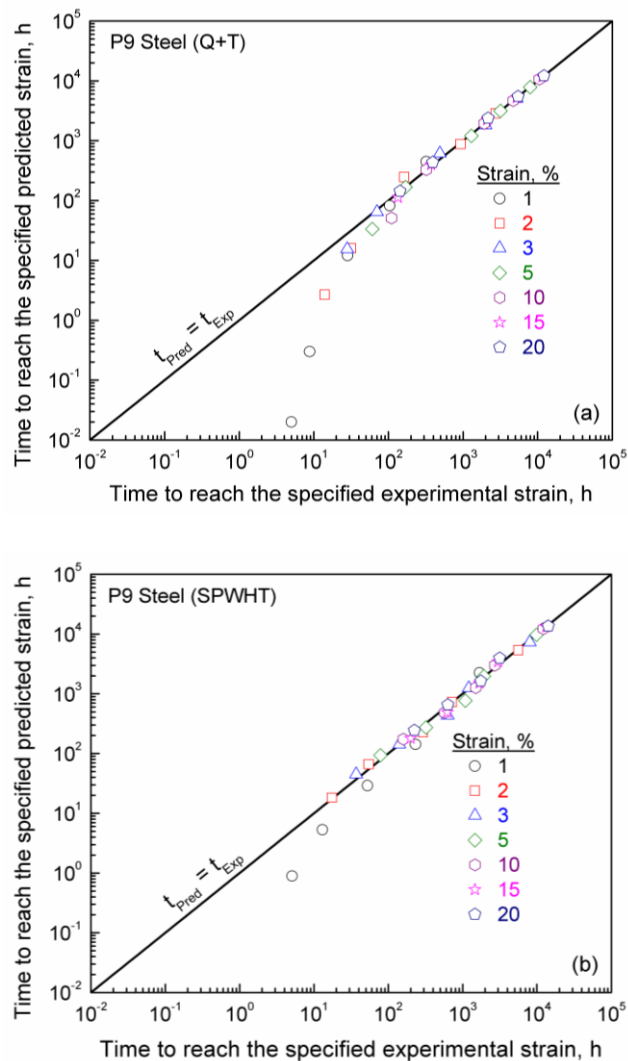


Figure 5.17 Comparison between experimental and predicted time to reach specified strain levels at 873 K for P9 steel in (a) Q+T and (b) SPWHT conditions.

These observations necessarily suggest that the numerical optimisation requires different weighting factors in the least-square function for primary, secondary and tertiary part of creep curves particularly at high stresses. In order to avoid the complex nature of optimisation, different weighting factors have not been used in the present analysis [183, 184]. In view of good correlations obtained for all other strains irrespective of applied stress and heat treatment conditions, the observed deviations in time to reach 1% strain levels at high stresses have been ignored. These observations clearly indicate that the long-term creep-rupture lives can be accurately predicted by the improved microstructure based approach.

5.8 Further Modification in Semba-Dyson-McLean Model for Simulating Long-Term Creep Behaviour of T91 Steel

The normalising stress σ_{0N} related to dislocation-precipitate interaction in Equation (5.6) accounts for the broad variations in inter-particle spacing with strain/time and it does not account for the influence of individual precipitates in both short and long-term creep regimes. For P9 steel, the interaction between dislocation and $M_{23}C_6$ alone dominates the normalising stress σ_{0N} . In other modified versions of 9% Cr steels, apart from $M_{23}C_6$, the finely distributed MX precipitates also influence the dislocation-precipitate interactions. Moreover, it is known that microstructural degradation in 9% Cr steels occurs not only by coarsening of primary precipitates but also by the conversion of MX into secondary precipitate i.e. Z-phase (Cr(V,Nb)N) [49]. Based on the optimised material data obtained on short-term creep data, an effort to predict long-term creep behaviour failed mainly because of non-inclusion of the effects of individual precipitates in T91 steel [189]. In order to account for the influence of individual precipitates on creep damage behaviour of materials, σ_{0N} can be evaluated as described below. According to Ashby [190], Orowan stress is obtained as

$$\sigma_{Orowan} = C_o \frac{M \mu b}{L} \ln \left(\frac{r_o}{r_l} \right), \quad \text{Equation (5.32)}$$

where C_0 is a coefficient equal to $1/2\pi(1-\nu)$ for screw and $1/2\pi$ for edge dislocations, ν is the Poisson's ratio, L is the mean inter-precipitate spacing and r_0 and r_1 are the outer and inner cut-off radius, respectively. The effective inter-particle spacing for material with more than one precipitates [191] is evaluated as

$$\frac{1}{L} = \sum \frac{1}{L^j}, \quad \text{Equation (5.33)}$$

where L^j is the inter-particle spacing of precipitate for j^{th} precipitates. The mean distance in terms of number density per unit volume (N) is equal to $(1/N^j)^{1/3}$. The inner cut-off radius is equal to $2b$ and outer cut-off radius is expressed as $2\left(\frac{\sum N^j r^j}{\sum N^j}\right)$. The precipitate having high number density has the most pronounced effect in determining the outer cut-off radius.

Using these modifications, σ_0 is expressed as

$$\sigma_{0N} = \frac{CMkT}{b^2} \sum (N^j)^{1/3} \ln \left(\frac{\sum 2N^j d^j}{2b \sum N^j} \right), \quad \text{Equation (5.34)}$$

where d^j is the diameter of precipitate. Since the number density and size of precipitates vary with time, the modified equation (23) can be expressed in generalised form as

$$\sigma_{0N} = \chi_{0,i} \sum (1+D_N^j)^{1/3} (N_i^j)^{1/3} \ln \left(\frac{\sum (1+D_N^j) N_i^j (d_i^j / (1-D_p^j))}{2b \sum N_i^j (1+D_N^j)} \right), \quad \text{Equation (5.35)}$$

where $\chi_{0,i}$ is equal to C_0MkT/b^2 . N_i^j and d_i^j are the initial number density and size of precipitates, respectively. The damage parameters D_p^j and D_N^j define damage due to precipitate coarsening and change in number density of precipitates, respectively. The damage parameter D_p^j is given as

$$D_p^j = 1 - (d_i^j / d^j), \quad \text{for } 0 \leq D_p^j \leq 1 \quad \text{Equation (5.36)}$$

The damage parameter D_N^j is written as

$$D_N^j = \left(N_t^j / N_i^j \right) - 1 \text{ for } 0 \geq D_N^j \geq -1 \quad \text{Equation (5.37)}$$

In Equations (5.36) and (5.37), d_t^j and N_t^j are the size and number density of precipitate j at time t, respectively.

5.9 Formulation for the Prediction of Long-term Creep Behaviour of T91 Steel

By incorporating redefined σ_0 (i.e. Equation (5.35)) into rate law in Equation (5.6), the long-term creep behaviour of T91 steel can be predicted. In order to prove the applicability of the modified model, it becomes necessary for finding the relationship for the evolution of number density of MX with time. So, it is highly recommended to perform the long-term interrupted tests for quantitative estimation of the evolution of number density of MX with time. The experimental creep data along with the evolution of dislocation density as well as MX with strain/time has been available for MGC heat of T91 steel for the stress level of 70 MPa at 873 K [26, 45, 192]. In the present analysis, the creep data obtained for MGC heat has been used to examine the prediction of long-term creep behaviour of T91 steel.

For T91 steel, the volume fraction of $M_{23}C_6$ is considered to be fixed as a constant at 873 K. The number density of $M_{23}C_6$ for its fixed volume fraction is defined as

$$N_t^{M_{23}C_6} = \left(6f^{M_{23}C_6} / \pi \right)^{1/3} / \left(d_t^{M_{23}C_6} \right), \quad \text{Equation (5.38)}$$

where $N_t^{M_{23}C_6}$ and $d_t^{M_{23}C_6}$ are the number density and size of $M_{23}C_6$ at time t and $f^{M_{23}C_6}$ is the volume fraction of that precipitate. Since constant volume fraction has been invoked for $M_{23}C_6$, the coarsening of $M_{23}C_6$ carbides determines the variations in the number density of $M_{23}C_6$. For T91 steel, the damage rate \dot{D}_p due to precipitate coarsening can be attributed mainly to the coarsening of $M_{23}C_6$ carbides and accordingly K_p refers to $K_p^{M_{23}C_6}$. Correspondingly, the equation for the kinetics of coarsening of $M_{23}C_6$ carbides has been rewritten as

$$\dot{D}_p = \frac{K_p^{M_{23}C_6}}{3} (1 - D_p)^4. \quad \text{Equation (5.39)}$$

Rate constant $K_p^{M_{23}C_6}$ determines the coarsening kinetics of $M_{23}C_6$. The value of the constant is directly linked to the diffusivity of substitutional elements in the matrix [193]. However, in the present model, the influence of individual diffusivity of the various substitutional elements on the coarsening rate of $M_{23}C_6$ carbides has not been considered. Rather than coarsening kinetics of MX at 873 K, the change in the number density of MX is mainly due to conversion of MX into Z-phase [45]. In the present analysis, the exponential function representing the rapid decrease in the number density of MX has been used and it is represented as

$$\frac{N_t^{MX}}{N_i^{MX}} = \exp[-k_f (t - t_{MX})], \quad \text{Equation (5.40)}$$

where k_f is a rate constant and t_{MX} is the time beyond which appreciable change in the number density of MX precipitate occurs. The value of t_{MX} depends on Z phase kinetics which in turn depends on the material conditions such as composition and heat treatment. The time derivative of D_N^{MX} is expressed as

$$\begin{aligned} \dot{D}_N^{MX} &= 0 \text{ for } t < t_{MX} \text{ and} \\ \dot{D}_N^{MX} &= -k_f (1 + D_N^{MX}) \text{ for } t \geq t_{MX} \end{aligned}, \quad \text{Equation (5.41)}$$

The generalised form of σ_0 for T91 steel can be expressed as

$$\begin{aligned} \sigma_{0N} &= \chi_{0,i} \left[(1 + D_N^{MX})^{1/3} (N_i^{MX})^{1/3} + \left(\frac{6f^{M_{23}C_6}}{\pi} \right)^{1/3} \left(\frac{1 - D_p^{M_{23}C_6}}{d_i^{M_{23}C_6}} \right) \right] \\ &\times \ln \left[\frac{(1 + D_N^{MX}) N_i^{MX} d_i^{MX} + (1 + D_N^{M_{23}C_6}) N_i^{M_{23}C_6} \left(\frac{d_i^{M_{23}C_6}}{1 - D_p^{M_{23}C_6}} \right)}{2b \left\{ (1 + D_N^{MX}) N_i^{MX} + (1 + D_N^{M_{23}C_6}) N_i^{M_{23}C_6} \right\}} \right]. \end{aligned} \quad \text{Equation (5.42)}$$

The final set of coupled differential equations to describe the kinetics of creep strain, kinematic back stress, maximum achievable kinematic back stress, damage caused by dislocation substructure coarsening, $M_{23}C_6$ coarsening, solute depletion and cavitation, variations in the number density of MX and applied stress are given as

$$\begin{aligned}
\dot{\varepsilon} &= \dot{\varepsilon}_0 \frac{D_d}{1 - \left(1 - \frac{c_e}{c_0}\right) D_s} \sinh \left[\frac{\sigma(1-H)}{\sigma_{0N}(1-D_C)} \right] \\
\dot{H} &= \frac{h}{\sigma} \left[1 - \frac{H}{H_{\max}} \right] \dot{\varepsilon} \\
\dot{H}_{\max} &= \frac{(1-H_{\max})H_{\max}}{2} \left(\frac{\dot{D}_d}{D_d} \right) \\
\dot{D}_d &= K_d \left(\frac{D_d}{\rho_i} \right)^{0.5} \left(1 - \left(\frac{D_d \rho_0}{\rho_{sat}} \right)^{0.5} \right) \dot{\varepsilon} \\
\dot{D}_P &= \frac{K^{M_{23}C_6}}{3} (1-D_P)^4 \\
\dot{D}_s &= K_s D_s^{1/3} (1-D_s) \\
\dot{D}_C &= \frac{1}{3\varepsilon_f} \dot{\varepsilon} \\
\dot{D}_N^{MX} &= 0 \text{ for } t < t_{MX} \text{ and} \\
\dot{D}_N^{MX} &= -k_f (1 + D_N^{MX}) \text{ for } t \geq t_{MX} \\
\dot{\sigma} &= \sigma \dot{\varepsilon}
\end{aligned} \tag{5.43}$$

Two additional evolution relationships such as cavitation damage and the variations in the number density of MX with time have been incorporated in Equation (5.43) compared to the model for the description of creep behaviour of P9 steel. The distribution of micro-voids and their evolution during creep were reported for T91 steel [194]. This necessitates the incorporation of cavitation damage in the present formulations. Since precipitation strengthening is from the presence of finely distributed MX and $M_{23}C_6$ in T91 steel, the variations in the number density of MX along with the coarsening kinetics of $M_{23}C_6$ have

also been introduced in the present model. It is obvious that MX precipitates do not appear in P9 steel due to the absence of V, Nb and N in its chemical composition.

5.10 Material Constants Associated with the Developed Model

For the numerical simulation of creep curves, seven unknown material constant set i.e. $\{ \dot{\epsilon}_0, h, H_{\max,0}, K_d, K_p^{M_{23}C_6}, K_s \text{ and } k_f \}$ were considered for optimisation. Some of the constants involved in the numerical simulation have been fixed. The material constants with fixed value have been presented in Table 5.5. The values of initial (c_0) and equilibrium (c_e) Mo concentration in ferrite matrix, and volume fraction of $M_{23}C_6$ ($f^{M_{23}C_6}$) were computed using TCFE6 steels/Fe-alloys database for T91 steel at 873 K (Thermocalc, TCFE6). The constants associated with normalizing stress ($\chi_{0,i}$) was computed using C_0MkT/b^2 . The values of K_d , ρ_{sat} and ρ_i are obtained by fitting experimental dislocation density variation with strain following integral form of Equation (5.30) proposed by Kocks-Mecking-Estrin equation [82-84]. Dislocation density vs. strain data for the lowest stress of 70 MPa at 873 K [45] along with the fitted solid line is shown in Figure 5.18(a). The best fit values obtained for ρ_{sat} and ρ_i are fixed in the final material data. The variations in the number density of MX with time exhibiting insignificant variation up to 30000 h followed by drastic reduction at longer creep exposures for the MGC heat and test condition [45] is shown in Figure 5.18(b). Exponential relationship i.e. Equation (5.40) used to describe a decrease in the normalised number density of MX with time data. The fit has been superimposed in Figure 5.18(b). The value of t_{MX} is fixed as 30000 h for the present analysis. The value of ϵ_f is approximately fixed as 0.3 for all the stress conditions at 873 K for T91 steel.

Table 5.5- Material constants with fixed values for numerical integration.

Material Constant	c_0	c_e	$f^{M_{23}C_6}$	$\chi_{0,i}/10^{-7}$	$\rho_i/10^{14}$	$\rho_{sat}/10^{13}$	t_{MX}	ε_f
units	mol %	mol %	-	MPa.m	m^{-2}	m^{-2}	h	-
values	0.44	0.14	0.02	1.1	6.13	7.6	30000	0.3

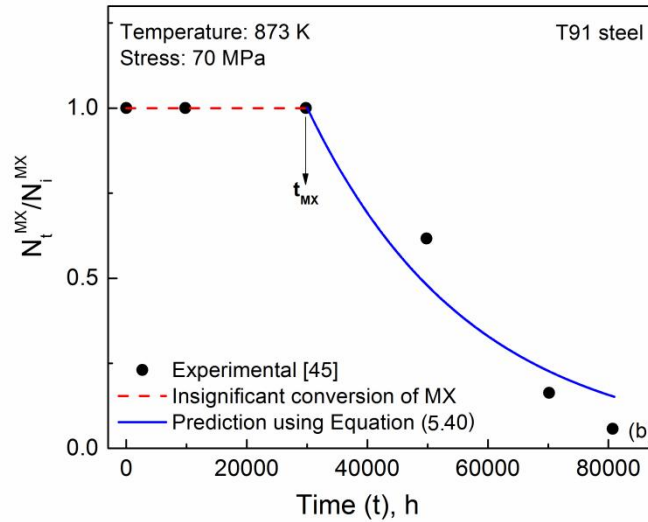
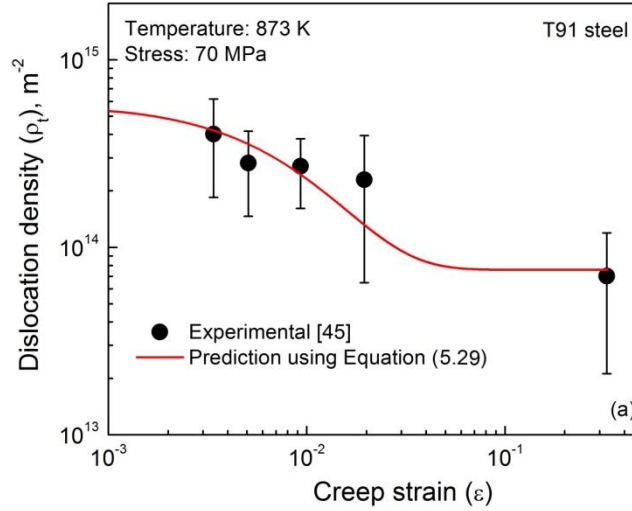


Figure 5.18 Variations of (a) dislocation density with strain fitted by the integral form of Kocks-Mecking-Estrin relationship given in Equation (5.29) and (b) normalised number density of MX with time described by exponential function i.e. Equation (5.40). Experimental data are extracted from the Ref. [45].

For optimisation, the initial guess values of $\dot{\varepsilon}_0$, h , $H_{max,0}$ and K_s are taken from Ref. [108] for the steel. The optimised coarsening rate value obtained for P9 steel in Q+T condition is

considered as an initial value of $K_p^{M_{23}C_6}$. Though dislocation accumulation parameter (K_d) has been found by fitting experimental dislocation density (ρ_t) vs. creep strain (ϵ) data, it has been considered as an unknown constant in order to fit the experimental creep strain-time data across different low stress levels. For optimisation, the fitted value of (K_d) has been used to fix the upper and lower bound values. Similarly, the obtained rate constant (k_f) associated with the evolution of the number density of MX with time has been considered as a guiding value to fix the upper and lower bounds. Following the parametric estimation using interior-point algorithm (Figure 5.12), the optimised material data is presented in Table 5.6 for T91 steel and the data set were used for the simulation of creep curves at different stress levels.

Table 5.6- Values of optimised material constants obtained for T91 steel in the framework of the modified Semba-Dyson-McLean approach.

Material or rate constants	Reference values for fixing bounds	Lower-Upper bounds	Optimised material constant obtained for T91 steel
$\dot{\epsilon}_0, h^{-1}$	6.0×10^{-11}	$1.0 \times 10^{-13} - 6.0 \times 10^{-9}$	4.575×10^{-11}
h, MPa	1×10^4	$1 \times 10^2 - 1 \times 10^6$	3.35×10^4
$H_{max,0}$	0.321	0 – 1	0.602
$K_p^{M_{23}C_6}, h^{-1}$	2.3×10^{-5}	$1 \times 10^{-3} - 1 \times 10^{-6}$	1×10^{-4}
K_s, h^{-1}	5.1×10^{-4}	$1 \times 10^{-6} - 1 \times 10^{-2}$	1.1×10^{-4}
K_d	1.56×10^9	$1 \times 10^7 - 1 \times 10^{11}$	1.15×10^9
k_f, h^{-1}	3.70389×10^{-5}	$1 \times 10^{-7} - 1 \times 10^{-3}$	1.72×10^{-5}

The comments related to the comparison between optimised data set obtained for T91 steel and P9 steel in quenched and tempered condition are noteworthy. For T91 steel, two orders of magnitude lower in characteristic strain rate ($\dot{\epsilon}_0$) and about one order of magnitude higher in rate constant associated with the evolution of dislocation density (K_d) have been obtained than for P9 steel. It clearly indicates that T91 steel exhibits higher characteristic creep resistance over P9 steel. Presence of fine distribution of MX precipitates in addition to $M_{23}C_6$

in T91 steel strongly resist the movement of dislocations as well as boundaries during creep which results in improved creep resistance of T91 steel. In P9 steel, reduced creep resistance is expected than T91 steel due to the absence of MX precipitates. This is in agreement with the observed lower creep rupture strength of P9 steel over T91 steel [1]. The observed constants such as h and $H_{\max,0}$ associated with the evolution of back stress show a marginal difference with respect to two different steels. T91 steel exhibits significantly higher rate constant values for the damage associated with the coarsening of $M_{23}C_6$ precipitates and solute depletion than those values observed for P9 steel. Higher nickel content in T91 steel (0.28 % Ni) could be the reason for high rate constant values. It was reported that increasing nickel content causes linear increase in precipitation coarsening rates in tempered martensitic steels [195]. On the contrary, creep data obtained on P9 steel having negligible nickel content had been used in the earlier analysis.

5.11 Applicability of the Modified Semba-Dyson-McLean Approach

The creep strain-time curves are computed using the developed model for the two different initial stress levels of 70 and 100 MPa as shown in Figure 5.19(a). The central difference formula has been used for obtaining creep rate vs. time curves from the calculated creep strain-time data. The predicted and experimental creep strain rate-time curves are shown in Figure 5.19(b) for 70 and 100 MPa. In the present analysis, based on the optimised material constants obtained for 70 and 100 MPa, the prediction of creep data has been performed for inside the identification range at 80 MPa and outside the range for different stress levels of 110-160 MPa. It can be seen that predicted creep curves follow closely experimental data in transient, secondary and tertiary creep stages for the low stress levels in the range 70-120 MPa (Figures 5.19 (a) and (b)). The considerable difference between predicted and experimental creep data at high stress levels of 140 and 160 MPa has been

noticed. Similarly, better agreement between experimental and predicted minimum creep rates and rupture lifetimes has been noticed for the stresses of 70-120 MPa than at high stress conditions as shown in Figure 5.20. It is expected for 9% Cr steels that the change in creep mechanisms from general climb at low stress regime to local climb at high stress regime could be the reason for the observed difference between experimental and prediction data at

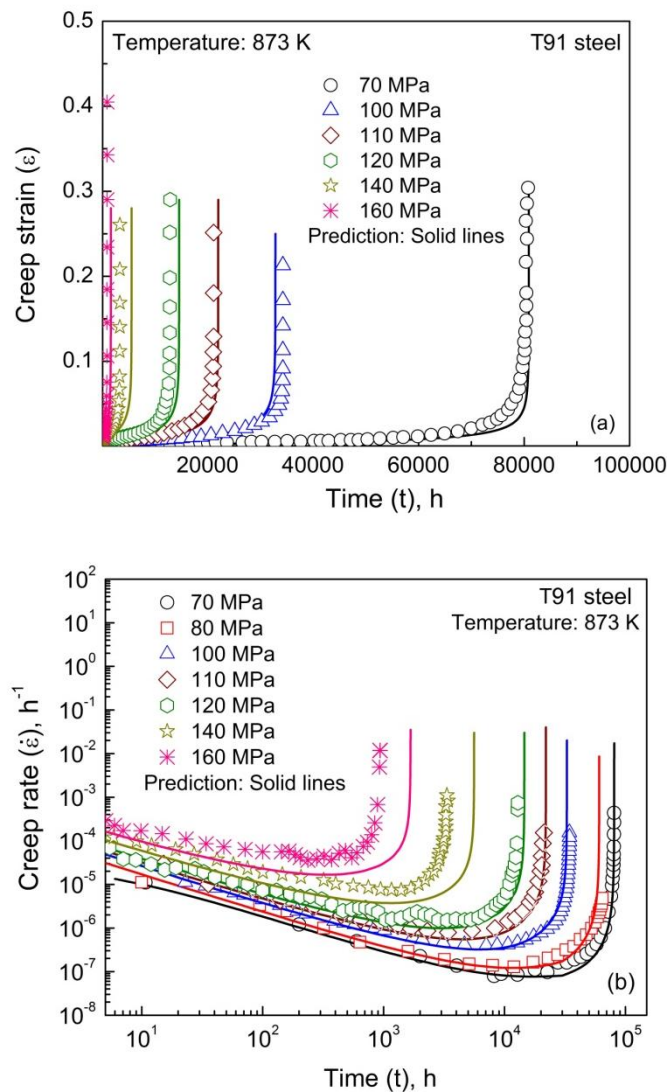


Figure 5.19 Comparison between predicted and experimental (a) creep strain-time and (b) creep rate-time data for different stress levels at 873 K. Experimental data are extracted from the Refs. [26, 45, 192].

high stresses above 120 MPa [196, 197]. However, the obtained creep lifetimes at high stresses falls within the scatter by considering factor of 2 in creep life extrapolations [198].

The present formulation does not deal with the influence of individual internal interfaces such

as prior austenitic grain, packet, block, sub-block and lath boundaries [199] on the creep deformation and damage behaviour of tempered martensitic steels. Since the evolution of these internal interfaces could differ with respect to the applied stress, the concept of kinematic back stress must be treated in terms of kinetics of individual internal interfaces for different applied stress levels. One of the major limitations of Dyson and McLean model is inapplicability at extremely low applied stresses where diffusional creep dominates. Since the origin of Dyson and McLean model is based on coupled glide/climb with dislocation-hard phase interaction mechanisms, it cannot predict the minimum creep rate vs. applied stress data obtained for diffusional creep regime [200] as shown in Figure 5.21.

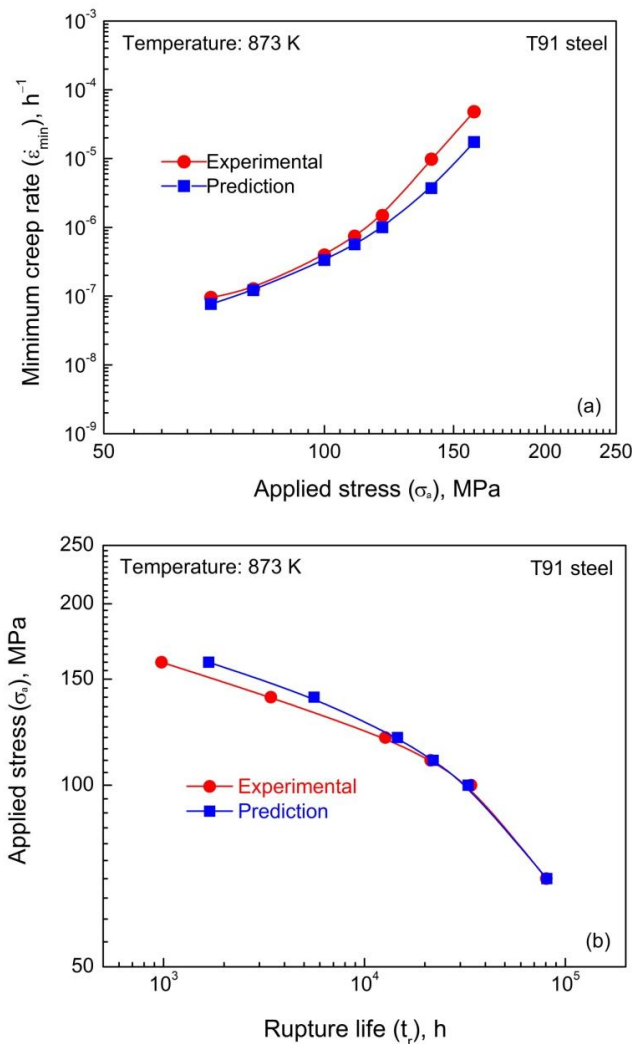


Figure 5.20 Comparison of predicted and experimental data for (a) minimum creep rate vs. applied stress and (b) applied stress vs. rupture life at 873 K for T91 steel. Experimental data are extracted from the Refs. [26, 45, 192].

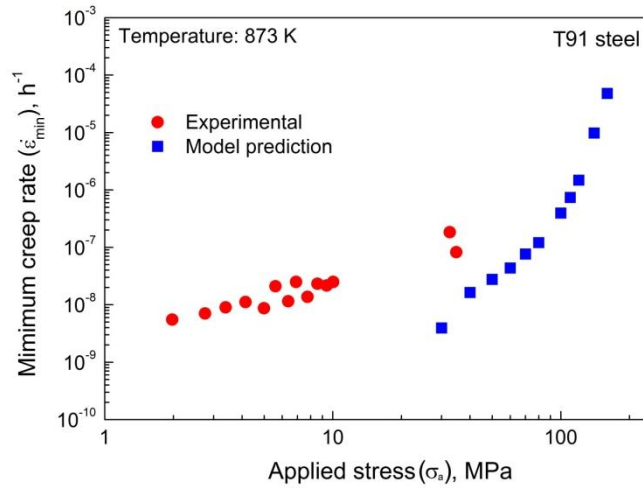


Figure 5.21 The variations in predicted minimum creep rate with the applied stress at 873 K for T91 steel. Experimental data obtained for very low stress levels depicting diffusion creep regime [200] are superimposed.

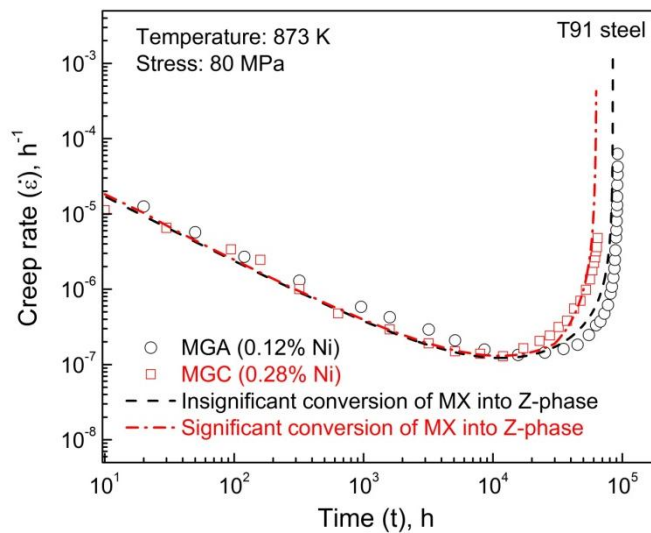


Figure 5.22 Comparison between predicted and experimental creep rate-time data for 80 MPa at 873 K for MGA and MGC heats of T91 steel containing 0.12 and 0.28% Ni [192], respectively. Dash and Dash-dotted lines represent predicted creep curves with the constant number density of MX precipitate and a significant decrease in the number density of MX precipitate, respectively.

The numerical simulations have also been performed for conditions with constant initial number density of MX. These simulations indicate that MX precipitates do not undergo any conversion to Z-phase. The simulated creep rate-time data at 80 MPa for two different conditions with constant initial number density of MX and varying number density of MX have been shown in Figure 5.22 as full and broken lines, respectively. The decrease in the

number density of MX precipitates and the formation and growth of Z-phase significantly affect tertiary creep behaviour of the steel. It has been reported that the increasing nickel content in the three heats, i.e. MGA (0.12% Ni), MGB (0.20% Ni) and MGC (0.28% Ni) greatly influences the long-term creep behaviour in terms of decrease in the creep-rupture strength of T91 steel [45]. Since heat MGA [45] containing 0.12% Ni with large number of MX precipitates and insignificant Z-phase were observed after creep exposure at 80 MPa, the creep rate vs. time for MGA heat has been used to represent the condition of constant number density of MX or the absence of conversion of MX to Z-phase in Figure 5.22. It can be seen that the simulated creep rate-time data (full line) for constant initial number density of MX closely follows the experimental data for MGA heat. In case of MGC heat with high Nickel exhibiting a significant decrease in the number density of MX at longer durations, a decrease in time to onset of rapid increase in creep rate and reduced rupture life has been observed.

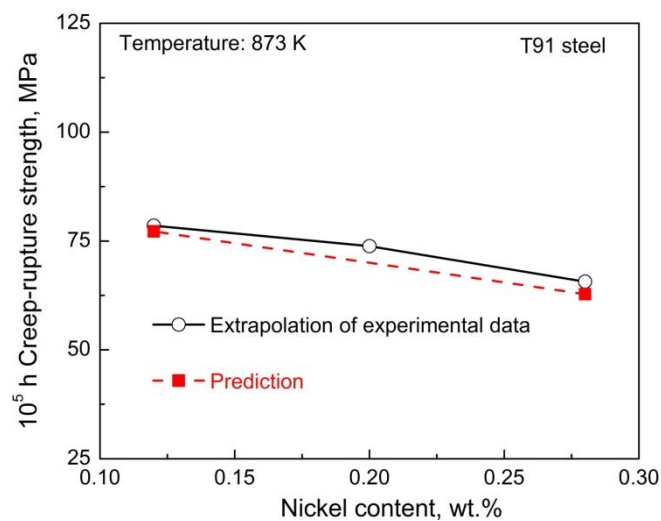


Figure 5.23 Comparison between predicted and extrapolated creep-rupture strength values for 10^5 h for the three heats MGA, MGB and MGC containing 0.12, 0.20 and 0.28% Ni [192], respectively.

Creep-rupture strength at 10^5 h at 873 K has been predicted with and without MX number density change using the modified approach. Figure 5.23 shows a good agreement between the 10^5 h strength values predicted using modified approach and those obtained by

extrapolation of experimental data for MGA, MGB and MGC heats with different Ni content in T91 steel [45]. The above findings clearly indicate that the developed model can be successfully used for prediction of long-term creep lifetimes. The present investigation also suggests that the computer simulation of creep curves is possible for T91 steel by coupling precipitation kinetics obtained from thermodynamic-kinetic data [201] and Dyson-McLean approach.

5.12 Conclusions

Additive creep rate model has been successfully developed by summing up sine hyperbolic rate relation interrelating primary and secondary creep, and modified MPC-Omega method for tertiary creep. The applicability of the model has been demonstrated for P9 steel for different applied stresses and microstructural conditions at 873 K. It has been shown that the coupling of sine hyperbolic relation with the evolution of internal stress accurately predicts primary as well as secondary creep strain contribution in the steel. A power law relation interrelating internal stresses with applied stress has been established using the parameters associated with the evolution law for internal stress. Modified MPC-Omega method has been observed to predict tertiary creep behaviour accurately at different stresses and microstructural conditions. Further, the tertiary creep damage has been successfully linked to $\beta\varepsilon_{tr}^{\eta}$ using tertiary creep constants β and η . At low stresses, higher damage accumulation $\beta\varepsilon_{tr}^{\eta}$ as a function of life fraction has been obtained compared to that at high stresses. The model has been further validated with experimental creep strain-data obtained for different microstructures at low stress level of 60 MPa. Good agreement between experimental and predicted rupture lives has been demonstrated for different stresses and microstructures in P9 steel.

Microstructure based Semba-Dyson-McLean model has been successfully used to predict the creep deformation behaviour of P9 steel at 873 K for two different heat treatment conditions. The material constants associated with the model has been successfully optimised for both Q+T and SPWHT conditions. The observed lower value of dislocation storage constant (K_d) and higher values of rate constants associated with the evolution of precipitation coarsening (K_p) and solute depletion (K_s) for SPWHT condition than those obtained for Q+T condition indicated that additional simulated post-weld heat treatment promotes enhanced recovery during creep deformation. This results in a noticeable difference in the primary, secondary and tertiary creep characteristics between Q+T and SPWHT conditions. In both the heat treatment conditions, good agreement between predicted and experimental creep strain/strain rate-time data at 873 K suggested the applicability of the improved microstructure based model for the description of creep deformation behaviour in P9 steel. In addition to above, good correlations obtained between the experimental and predicted steady state creep rates and time to reach the specified strain levels demonstrated further applicability of the model.

In the present research, the long-term creep behaviour of T91 steel has also been successfully predicted following necessary modifications in the kinetic creep law in the framework of microstructure based creep damage mechanics approach. The exponential rate relationship has been developed for accounting the evolution of number density of MX with time and it is successfully coupled with the kinetic creep law. The decrease in the number density of MX precipitates and the formation and growth of Z-phase greatly influence on the tertiary creep behaviour of the steel. Good agreement was observed between the predicted and experimental creep data in long-term creep regime using the modified version of Dyson-McLean approach.

Chapter 6: Internal-stress based sine hyperbolic creep rate model for stress-relaxation behaviour of 9% Cr steels

6.1 Introduction

Stress-relaxation technique offers considerable advantages for material testing in terms of economical evaluation of mechanical properties and kinetics of deformation useful to derive the constitutive laws in metals and alloys [202]. It has been demonstrated that the short-time stress-relaxation data can be conveniently employed for the evaluation of creep strength, life prediction and remnant life assessment of engineering materials [56, 203]. Further, stress-relaxation behaviour also finds application towards alloy design, development and optimisation of new alloys [203-205]. During stress-relaxation, the external constraint i.e., the total applied strain is kept constant. The total applied strain (ε_t), made up of elastic (ε_e) and inelastic (ε_{in}) strain components, is mathematically represented as

$$\dot{\varepsilon}_t = \dot{\varepsilon}_e + \dot{\varepsilon}_{in} = 0. \quad \text{Equation (6.1)}$$

The elastic strain rate ($\dot{\varepsilon}_e$) term in Equation (6.1) can be expressed as

$$\dot{\varepsilon}_e = \frac{\dot{\sigma}_r}{C_m} \quad \text{Equation (6.2)}$$

where C_m is the effective modulus of the sample-machine system and $\dot{\sigma}_r$ is the stress-relaxation rate. The relation between stress-relaxation rate and inelastic strain rate can be derived from Equation (6.1) and Equation (6.2) as

$$\dot{\varepsilon}_{in} = -\dot{\varepsilon}_e = -\frac{\dot{\sigma}_r}{C_m}. \quad \text{Equation (6.3)}$$

Equation (6.3) implies that the decrease in elastic strain is exactly balanced by an increase in inelastic strain during relaxation. This results in a decrease in stress values with hold time. All theoretical approaches [206-208] to the relaxation process are based on Equation (6.3) and therefore, Equation (6.3) represents a general differential equation describing stress-

relaxation behaviour. In general, relaxation models [206-208] mainly focus on the development of interrelationship between inelastic strain rate and relaxation stress. Among the existing models [206], the model proposed by Feltham [207] is widely used to describe the stress-relaxation behaviour of different metals and alloys [209-211].

Based on dislocation-local obstacle interaction theory, Feltham [207] proposed the inelastic strain rate relationship to describe the stress-relaxation behaviour as

$$\dot{\epsilon}_{in} = \dot{\epsilon}_0 \rho_m \exp\left(\frac{-(Q - (\sigma_r - \sigma_i)\Delta V)}{kT}\right), \quad \text{Equation (6.4)}$$

where σ_i is the internal stress and $\sigma_r - \sigma_i$ is equal to the effective stress (σ_e). $\dot{\epsilon}_0$ is a constant that includes a frequency factor, the area swept out by an activated dislocation and the Burgers vector (b). According to Feltham [207], the values of $\dot{\epsilon}_0$, ρ_m and ΔV are unchanged during stress-relaxation and the internal stress σ_i is assumed as a constant. Equation (6.4) is substituted in Equation (6.3) followed by the integration of Equation (6.3) with appropriate boundary conditions, which is represented as

$$\int_{\sigma_{r0}}^{\sigma_r} \exp\left(\frac{(Q - (\sigma_r - \sigma_i)\Delta V)}{kT}\right) d\sigma_r = \int_0^t -C \dot{\epsilon}_0 \rho_m dt, \quad \text{Equation (6.5)}$$

where σ_{r0} is the relaxation stress at $t = 0$. Equation (6.5) yields

$$\sigma_r = \sigma_{r0} - \frac{kT}{\Delta V} \ln\left(1 + \frac{t}{t_0}\right), \quad \text{Equation (6.6)}$$

where $\frac{1}{t_0} = \frac{C \dot{\epsilon}_0 \rho_m \Delta V}{kT} \exp\left(\frac{-(Q - (\sigma_{r0} - \sigma_i)\Delta V)}{kT}\right)$ with t_0 is treated as a constant. Equation

(6.6) is employed for the description of the relaxation behaviour of different materials. Further, Feltham relation [207] combined with Ramberg-Osgood [212] stress-strain formulation was used to describe the cyclic stress-strain and cyclic stress-relaxation behaviour of 1CrMoV rotor steel [213]. Based on kinetic rate theory, DiMelfi [208] derived a

similar relation applicable to stress-relaxation behaviour of engineering materials. However, predicted relaxation stress vs. hold time data derived by DiMelfi model [208] exhibited significant deviations from the experimental relaxation stress vs. hold time data at longer durations. In addition to this, the assumptions related to constancy in activation volume and internal stress in the stress-relaxation model directly implies constancy in the obstacle or inter-barrier spacing in the formulations [207, 208]. The reported increase in lath width or subgrain size accompanied with a decrease in dislocation density for P91 steel [57, 214] suggested that the substructural variations alter inter-barrier spacing which resulted in the variations in internal stress (σ_i) and activation volume (ΔV) during stress-relaxation. From the microstructural aspects, it is evident that Feltham relation [207] involving constancy in internal stress and activation volume is not applicable for describing the stress-relaxation behaviour of P91 steel. An alternative to the Feltham relationship [207], state variable based model has been developed in the present study.

6.2 Internal-Stress Based Model and its Numerical Implementation

In the present formulation, the proposed sine hyperbolic rate relation (Chapter 4) has been used to describe the inelastic strain rate during stress-relaxation. Equation (4.9) has been successfully used to evaluate the inelastic strain with time during stress-relaxation by incorporating relaxation stress in place of applied stress. The inelastic strain rate relation for describing stress-relaxation behaviour is represented by

$$\dot{\epsilon}_{in} = \frac{\rho_m b^2 v_D (\sigma_r - \sigma_i) (\sigma_i^2 (\sigma_r - \sigma_i))^{-1/3}}{M^2} \exp\left(\frac{-Q}{RT}\right) \sinh\left(\frac{(\sigma_r - \sigma_i)}{MkT} b^3 \left[\frac{\mu}{(\sigma_i^2 (\sigma_r - \sigma_i))^{1/3}}\right]\right).$$

Equation (6.7)

Further, the variation in internal stress as a function of relaxation stress is derived following reported interrelationships between internal stress vs. applied stress based on experimental observations and theoretical considerations for monotonic creep deformation. Argon and Takeuchi [215] proposed a relationship relating internal stress σ_i to applied stress σ_a as

$$\frac{\sigma_i}{\mu} = A_r \left(\frac{\sigma_a}{\mu} \right)^{2/3}, \quad \text{Equation (6.8)}$$

where A_r is the constant related to sub-boundary misorientation (θ). It can be seen that the internal stress (σ_i) increases with increase in applied stress with a power law exponent 0.67. The applied stress dependence of internal stress agrees well with the power law ($\sigma_i \sim \sigma^{0.87}$) experimentally observed for Al-Li solid solution alloy using stress-dip and stress increment tests during steady state creep conditions [157]. A similar power law dependence of internal stress on applied stress has been reported for many metals and alloys [156-159]. Based on these observations, the relationship between internal stress (σ_i) and relaxation stress (σ_r) has been treated as a power law in the present analysis and it is given as

$$\sigma_i = h_r \sigma_r^{m_r}, \quad \text{Equation (6.9)}$$

where h_r and m_r are the power law coefficient and exponent, respectively. Since the power law coefficient (A_r) in Equation (6.8) has definite physical interpretation as proposed by Argon and Takeuchi [215], the same symbol has not been used for the coefficient in Equation (6.9). The rate equation for the evolution of internal stress with time is derived from Equation (6.9) as

$$\dot{\sigma}_i = m_r \left(\frac{h_r \sigma_r^{m_r}}{\sigma_r} \right) \dot{\sigma}_r = m_r \left(\frac{\sigma_i}{\sigma_r} \right) \dot{\sigma}_r. \quad \text{Equation (6.10)}$$

In totality, two new equations have been employed for the description of stress-relaxation behaviour in the present investigation. The first is Equation (6.7) which is used to predict the evolution of inelastic strain rate during stress-relaxation. The second (Equation (6.10))

describes the evolution of internal stress with time based on power law dependence of internal stress on relaxation stress. Accordingly, the coupled differential equations, i.e., Equations (6.3), (6.7) and (6.10) defining the evolution of relaxation stress ($\dot{\sigma}_r = -C_m \dot{\epsilon}_{in}$), inelastic strain and internal stress with time have been used to represent the stress-relaxation behaviour of P91 steel. In the above formulation, there are three unknown constants such as initial relaxation stress (σ_{r0}), initial internal stress (σ_{i0}) and power law exponent (m_r) related to internal stress. In addition to the above, the power law coefficient (h_r) can be obtained as

$$h_r = \frac{\sigma_{i0}}{\sigma_{r0}^m}. \text{ In the present analysis, the mobile dislocation density of } 1 \times 10^{13} \text{ m}^{-2} \text{ is fixed as}$$

one order of magnitude lower than the total dislocation density value of $1 \times 10^{14} \text{ m}^{-2}$ reported for 9% Cr steels [40, 119]. The unknown parameters associated with the model such as initial relaxation stress (σ_{r0}), initial internal stress (σ_{i0}) and power law exponent (m_r) related to the internal stress were optimised using interior-point method. The upper and lower bounds along with optimised parameters for both 1.3 and 2.5% strain holds have been presented in Table 6.1. The derived optimised parameters as well as the estimated power law co-efficient (h_r) are included in the Table 6.1 for both the strain hold conditions.

Table 6.1- Optimised material constants for two different strain holds at 1.3 and 2.5% at 873 K.

Hold strain levels	σ_{r0} , MPa	σ_{i0} , MPa	m_r	h_r , MPa
Lower to upper bound limits	300 – 400	200 – 350	0 – 1	Estimated by $h_r = \frac{\sigma_{i0}}{\sigma_{r0}^m}$
1.3%	334.4	243.9	0.796	2.390
2.5%	339.2	246.0	0.785	2.546

6.3 Implications of the Internal-Stress Based Model

The experimental as well as predicted relaxation stress (σ_r)-time (t) plots for the strain holds of 1.3 and 2.5 % at 873 K have been presented in Figure 6.1. For both the strain holds, initial rapid decrease in relaxation stress with time followed by stress plateaus at longer durations has been observed. It can be clearly seen that the predicted σ_r -t data accurately describe the experimental σ_r -t behaviour for 1.3 and 2.5 % strain holds. Marginally higher relaxation stress values for 1.3% strain hold condition than those obtained for 2.5% strain hold can be seen in Figure 6.1. Relaxation stress (σ_r) dependence of strain rate ($\dot{\epsilon}_{in}$) evaluated from the predicted as well as experimental σ_r -t data for both the strain holds are shown in Figure 6.2. Like σ_r vs. t, inelastic strain rate vs. relaxation stress also displayed closer values for both the strain levels of 1.3 and 2.5 %. The stress dependence of inelastic strain rate obeyed power law with stress exponent $n = 10.1$ and 10.5 for the strain holds of 1.3 and 2.5 %, respectively. The stress exponent values obtained in the present study are in good agreement for those reported for monotonic creep deformation of P91 steel [24, 29]. Further, an excellent agreement between the predicted and experimental relaxation stress dependence of inelastic strain rate at two different strain holds is discernible in Figure 6.2. These observations clearly demonstrate that the proposed model adequately describes the stress-relaxation behaviour of P91 steel. The optimised initial relaxation stress values (Table 6.1) showed a good match with experimental initial relaxation stress values (Figure 6.1). The difference between the initial relaxation stress values of two different strain holds is 5 MPa. This marginal increase in flow stress value even with an additional strain of 1.2% from 1.3% implies the dominance of dynamic recovery over strain hardening at 873 K which is expected for P91 steel.

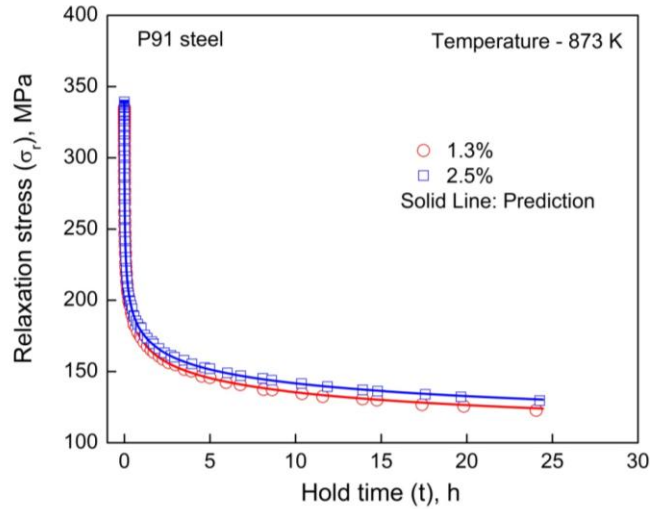


Figure 6.1 Variations of relaxation stress (σ_r) with hold time (t) for two different strain holds of 1.3 and 2.5% for P91 steel at 873 K. The best-fit σ_r - t is shown by solid lines for both the strain holds.

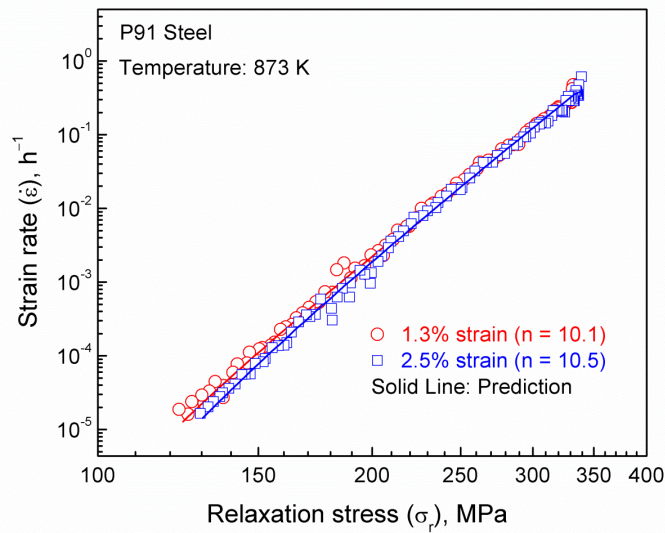


Figure 6.2 Variations of strain rates ($\dot{\epsilon}$) with relaxation stress (σ_r) for two different strain holds of 1.3 and 2.5% for P91 steel at 873 K. The best-fit $\dot{\epsilon}$ - σ_r is shown as solid lines for both the strain holds.

A comment on the evolution of internal stress (σ_i) and its dependence on relaxation stress (σ_r) following Equation (6.10) is important. It has been observed that the variations of internal stress (σ_i) with relaxation stress (σ_r) obey power law as $\sigma_i = h_r \sigma_r^{m_r}$. Based on the closer values of power law coefficient and exponent obtained for 1.3 and 2.5% strain hold (Table 6.1), an average value of $h_r = 2.47$ and $m_r = 0.79$ can be assigned for P91 steel. Based

on stress change experiments during steady state creep, it has been shown that the increase in internal stress with applied stress obey power law in several metals and alloys. The optimised power law exponent $m = 0.79$ for P91 steel is close to the exponent values in the range 0.7-1.0 reported for Cd, Mg, Al-Li and Al-Mg alloys [156-159]. Sine hyperbolic rate equation (Equation (6.7)) coupled with $\sigma_i = h_r \sigma_a^{m_r}$ has been used to fit the experimental minimum creep rate vs. applied stress data at 873 K for P91 steel as shown in Figure 6.3. The obtained

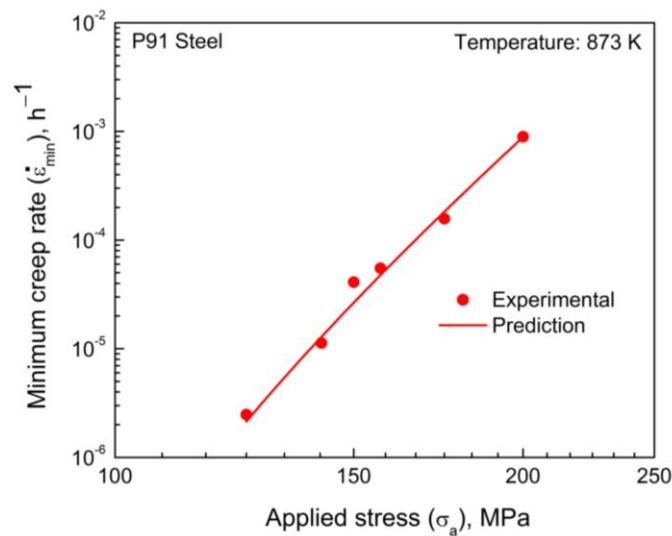


Figure 6.3 Variations of minimum creep rate ($\dot{\epsilon}_{min}$) with applied stress (σ_a) for P91 steel at 873 K. The prediction based on sine hyperbolic model is given by solid line.

values of power law coefficient (h_r) and exponent (m_r) are 2.88 and 0.77, respectively. These values are close to those obtained for stress relaxation behaviour of P91 steel. Based on internal-variable approach, the variations of the ratio of internal stress during secondary creep and applied stress (σ_i/σ_a) has been observed to decrease with applied stress (σ_a) for P9 steel at 873 K and this is presented in Figure 4.8. The observed variations in σ_i/σ_a with σ_a exhibited power law relation as $\sigma_{is}/\sigma_a \sim \sigma_a^{-0.21}$ or $\sigma_{is} = 2.22 \sigma_a^{0.79}$. This is in agreement with the observed power law interrelating internal stress and applied stress with exponent value 0.79 in P91 steel. These observations clearly indicate that the power law relation between

internal stress and applied stress observed for monotonic creep can be successfully implemented for stress-relaxation studies in 9% Cr steels.

The variations in relaxation stress, internal stress and effective stress with time predicted using present formulation are shown in Figure 6.4. Like relaxation stress vs. time, the variations in internal and effective stresses with hold time also displayed an initial rapid decrease followed by stress plateaus at longer durations. Further, for a given hold time, the predicted internal stress values have been observed to be significantly higher than the effective stress (Figure 6.4). The observed decrease in internal stress with time can be related to the instantaneous obstacle or inter-barrier spacing (L). Since inter-barrier spacing (L) is inversely related to internal stress i.e., $M\mu b/\sigma_i$, an increase in inter-barrier spacing with an increase in hold time has been observed as shown in Figure 6.5. The marginally higher values of internal stress are reflected in the relatively lower inter-barrier spacing for 2.5% strain than for 1.3% strain (Figure 6.5).

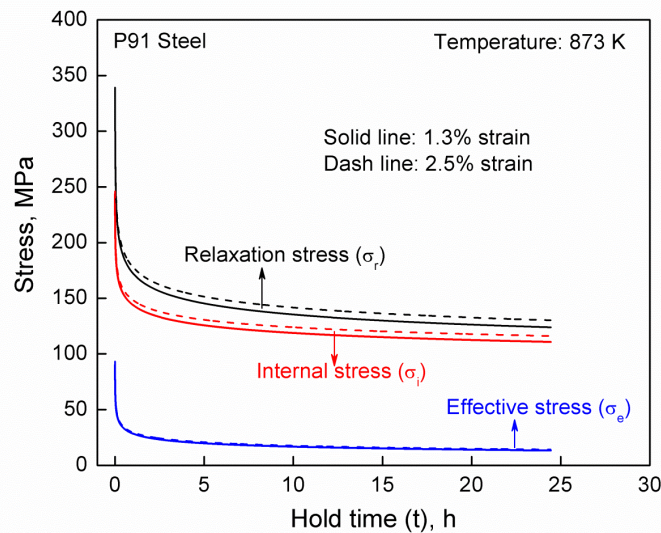


Figure 6.4 Variations in relaxation stress (σ_r), internal stress (σ_i) and effective stress (σ_e) with hold time (t) for two different strain holds of 1.3 and 2.5% for P91 steel at 873 K.

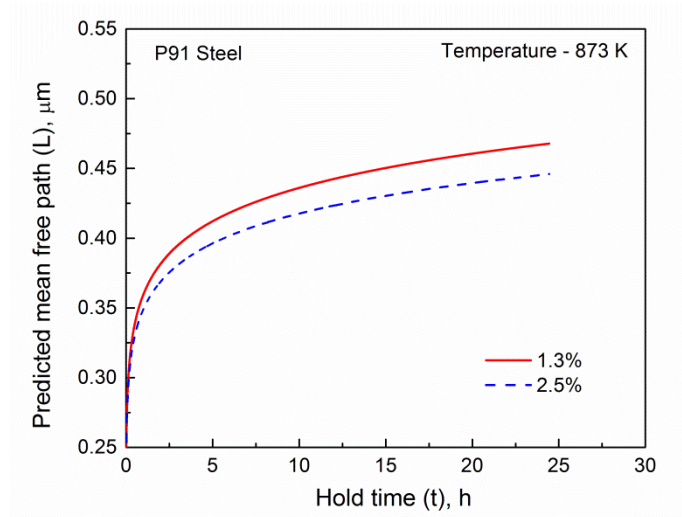


Figure 6.5 Variations of predicted mean free path (L) with hold time (t) for two different strain holds of 1.3 and 2.5% for P91 steel at 873 K.

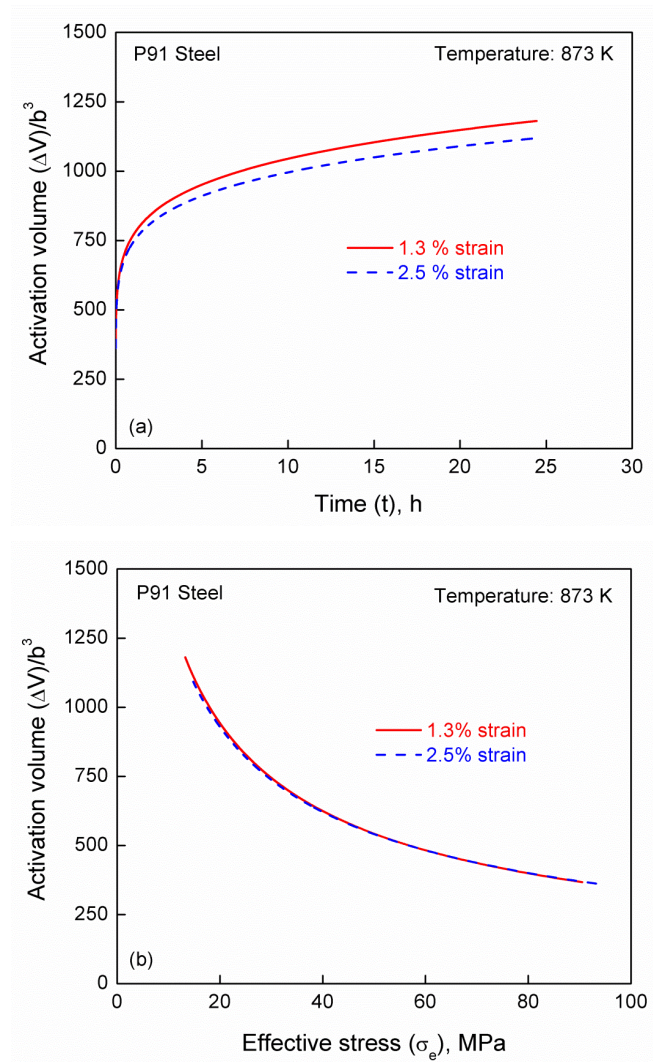


Figure 6.6 Variations of activation volume $(\Delta V)/b^3$ with (a) hold time (t) and (b) effective stress (σ_e) for two different strain holds of 1.3 and 2.5% for P91 steel at 873 K.

The variations in predicted activation volume with hold time and effective stress have been presented in Figures. 6.6 (a-b). For both the strain holds, the activation volume increases with an increase in hold time (Figure 6.6 (a)). Since effective stress decreases with an increase in hold time (Figure 6.4), the activation volume decreases with an increase in effective stress as shown in Figure 6.6 (b). Further, the values of activation volume (ΔV) in the range 400-1200 b^3 have been obtained for both the strain hold conditions in P91 steel. These observations are in consistent with those reported for monotonic creep deformation in P9 steel (Figure 4.15). It has been reported that the activation volume depends on the effective stress as $\Delta V \propto (\sigma_e)^{-k_r}$. Though the activation volume depends on internal stress and effective stress, the equation interrelating activation volume and effective stress has been derived from Figure 6.6 (b) as $\Delta V \propto (\sigma_e)^{-0.6}$. The value of $k_r = 0.6$ obtained in the present analysis is close to the k_r values in the range 0.5 to 1 reported for metals and alloys [216]. A comment on the values of activation volume (ΔV) in the range 400-1200 b^3 obtained in the present investigation is appropriate. It is well known that during diffusional creep such as Nabarro-Herring and Coble creep, the deformation process is characterised by activation volume of about atomic volume or b^3 .

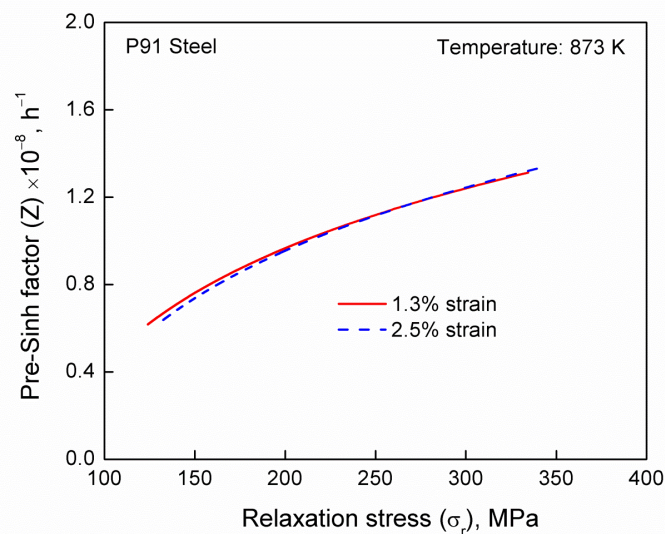


Figure 6.7 Variations of pre-sinh factor (Z) with relaxation stress (σ_r) for two different strain holds of 1.3 and 2.5% for P91 steel at 873 K.

Contrary to this, the observed higher activation volume in the range of 400-1200 b³ implies that the movement of dislocations with long segments is forwarded by a few Burgers vector to pass through forest dislocations [217]. Based on the proposed model, the observed increase in both activation volume and inter-barrier spacing with an increase in hold time implied that continual microstructural coarsening takes place during stress-relaxation in P91 steel [57, 214]. The pre-sine hyperbolic factor (Z) in Equation (6.7) can be given as

$$Z = \frac{\rho_m b^2 v_D (\sigma_r - \sigma_i) (\sigma_i^2 (\sigma_r - \sigma_i))^{-1/3}}{M^2} \exp\left(\frac{-Q}{RT}\right). \quad \text{Equation (6.11)}$$

The pre-sine hyperbolic factor increases with an increase in relaxation stress as shown in Figure 6.7. This is in agreement with those reported for monotonic creep deformation in several metals and alloys [91, 165]. These observations suggest that the pre-sinh hyperbolic factor (Z) contributes to increase in strain rate with increasing relaxation stress.

6.4 Conclusions

A constitutive model by coupling sine hyperbolic creep rate law with the evolution of internal and relaxation stresses with time has been successfully developed to describe the stress-relaxation behaviour of P91 steel for two different strain holds of 1.3 and 2.5% at 873 K. The power law relation between internal stress and relaxation stress, i.e., $\sigma_i = h_r \sigma_r^{m_r}$ has been successfully implemented for the description of stress-relaxation behaviour of P91 steel. The optimised power law exponent (m_r) of 0.79 is in agreement with the values reported in the literature. The predicted decrease in internal stress with time during stress-relaxation was interrelated to the increase in inter-barrier spacing (L) during relaxation. The predicted values of activation volume (ΔV) in the range 400-1200 b³ suggested that the stress-relaxation is governed by dislocation processes most importantly the dislocation-local obstacle interaction. Based on the outcome, the power law interrelationship between activation volume and

effective stress, i.e., $\Delta V \propto (\sigma_e)^{-0.6}$ for stress-relaxation has been established. The observed increase in both the activation volume and the inter-barrier spacing with an increase in hold time implies that continual microstructural coarsening takes place during stress-relaxation in P91 steel.

Chapter 7: General Conclusions and Future Directions

The general conclusions emanating from the investigations related to internal-state-variable based constitutive modelling of tensile, creep and stress-relaxation behaviour of 9% Cr tempered martensitic steels are as below:

7.1 Tensile Flow and Work Hardening Behaviour of 9% Cr Steels

Work hardening behaviour of P9 steel plate and tubeplate forging and P91 steel have been examined successfully in the framework of dislocation density based Kocks-Mecking-Estrin approaches for a wide range of temperatures. Detailed analysis towards work hardening behaviour of 9% Cr steels in the wide range of temperatures indicated that the hybrid model reduced to Estrin–Mecking one-internal-variable model. Parameter sensitivity analysis over optimisation results clearly suggested that the average mean free path arising from the dislocation dense lath/cell boundaries and precipitates act as effective barriers to glide of dislocations over total dislocation population inside the lath in P9 and P91 steels. The applicability of Estrin-Mecking one-internal-variable approach to 9% chromium steels is demonstrated in terms of good agreement between predicted and experimental true stress-true plastic strain with low least-square error values over the temperatures ranging from 300 to 873 K. The work hardening parameters associated with the Estrin-Mecking approach exhibited marginal variations in the values at room and intermediate temperatures, and rapid variations at high temperatures. The evaluation of activation energy based on Bergstrom and Hallen model using recovery parameter suggested that the dynamic recovery is controlled by cross-slip of dislocations at room and intermediate temperatures, and climb of dislocations at high temperatures. At room and intermediate temperatures, insignificant or, marginal variations in the evolution of dislocation density with plastic strain were noticed for P9 and P91 steels. At high temperatures, the dominance of dynamic recovery resulted in rapid

evolution of dislocation density towards saturation in all the steels. At all temperatures, a systematic influence of initial microstructure on the work hardening parameters associated with the Estrin-Mecking approach has been observed.

In general, P9 steel tubeplate forging exhibited higher work hardening due to its softened microstructure in terms of larger gains in the dislocation density and flow stress contribution from dislocations along with reduced dynamic recovery than the P9 plate and P91 steels in the temperature range 300-873 K. Contrary to this, relatively hardened microstructure in P91 steel displayed lower work hardening ability along with increased dynamic recovery than P9 plate and tubeplate forging. In addition, necking instability criterion proposed by Considère has been reexamined based on dislocation-density based Estrin-Mecking model for 9% Cr tempered martensitic steels in this study. It has been shown that instability sets-in as the evolution of dislocation density with the plastic strain approaches critical dislocation density which in turn is a function of the mean free path and dislocation annihilation parameter. Further, for 9% Cr steels, the interrelationship between true uniform plastic strain and dynamic recovery parameter has been established from the present formulation. The observed good agreement between experimental and predicted tensile properties showed better predictability of the model for 9% chromium containing steels.

7.2 Transient Creep Behaviour of 9% Cr Tempered Martensitic Steels

For the description of transient creep behaviour of 9% Cr steels, a constitutive description based on sine hyperbolic creep rate relation associated with the concept of stress dependent activation volume and average dislocation segment length related to the Friedel statistics has been developed. The sine hyperbolic creep rate relation coupled with the evolution of internal stress as a function of strain provides a better understanding of primary

and secondary creep behaviour of 9% Cr steels. Following Estrin-Mecking approach, the evolution of mean internal stress from the initial to saturation value during creep deformation has been considered. The model suggested that the increase in internal stress (or decrease in effective stress) with strain/time results in the observed decrease in creep rate during primary creep in 9% chromium containing tempered martensitic steels.

The applicability of the developed model has been demonstrated by comparing the predicted and experimental creep strain-time and creep rate-strain data in P9 steel in quenched and tempered (Q+T) and simulated post weld heat treatment (SPWHT) conditions at 793 and 873 K. The observed difference in the primary and secondary creep characteristics at 793 and 873 K between Q+T and SPWHT conditions has been ascribed to the variations in rate constant associated with the model. The lower rate constant values for SPWHT condition than for Q+T condition at both 793 and 873 K signifies the enhanced dynamic recovery effects in SPWHT condition due to the presence of relatively coarse initial microstructure. At all test conditions, good agreement observed between predicted and experimental steady state creep rates demonstrated further applicability of the model. The predicted variations in activation volume at steady state with applied stress are in accordance with the experimentally reported observations in metals and alloys.

7.3 Totality of Creep Deformation and Development of Damage in 9% Cr Tempered Martensitic Steels

In order to provide the constitutive description of the totality of creep deformation and development of damage in 9% Cr tempered martensitic steels, additive creep rate model by summing up sine hyperbolic rate relation interrelating primary and secondary creep, and modified MPC-Omega method for tertiary creep has been successfully developed. The applicability of the developed additive creep rate model has been demonstrated for P9 steel for different applied stresses and microstructural conditions at 873 K. It has been shown that

the coupling of sine hyperbolic relation with the evolution of internal stress accurately predicts primary as well as secondary creep strain contribution in the steel. Modified MPC-Omega method has been observed to predict tertiary creep behaviour accurately at different stresses and microstructural conditions. The model has been further validated with experimental creep strain-data obtained for different microstructures at a low stress level of 60 MPa. Further, the tertiary creep damage has been successfully linked to $\beta \varepsilon_r^\eta$ using tertiary creep constants β and η . At low stresses, higher damage accumulation $\beta \varepsilon_r^\eta$ as a function of life fraction has been obtained compared to that at high stresses. Good agreement between experimental and predicted rupture lives has been demonstrated for different stresses and microstructures in P9 steel.

For describing the totality of creep deformation and development of damage in 9% Cr tempered martensitic steels in the framework of microstructure based approach, Sembadyson-McLean model has been successfully employed. Predictability of the microstructure based approach has been demonstrated for the creep deformation behaviour of P9 steel at 873 K for two different heat treatment conditions. The material constants associated with the model has been successfully optimised for both Q+T and SPWHT conditions. The observed lower value of dislocation storage constant and higher values of rate constants associated with the evolution of precipitation coarsening and solute depletion for SPWHT condition than those obtained for Q+T condition indicated that additional simulated post-weld heat treatment promotes enhanced recovery during creep deformation. This results in a noticeable difference in the primary, secondary and tertiary creep characteristics between Q+T and SPWHT conditions. In both the heat treatment conditions, good agreement between predicted and experimental creep strain/strain rate-time data at 873 K suggested the applicability of the improved microstructure based model for the description of creep deformation behaviour in P9 steel. In addition to above, good correlations obtained between the experimental and

predicted steady state creep rates and time to reach the specified strain levels demonstrated further applicability of the model.

In the present study, the long-term creep behaviour of T91 steel has also been successfully predicted following necessary modifications in the kinetic creep law in the framework of microstructure based creep damage mechanics approach. The exponential rate relationship has been developed for accounting the evolution of number density of MX with time and it is successfully coupled with the kinetic creep law. The decrease in the number density of MX precipitates and the formation and growth of Z-phase greatly influence the tertiary creep behaviour of the steel. Good agreement was observed between the predicted and experimental creep data in long-term creep regime using the modified version of Dyson-McLean approach.

7.4 Stress-Relaxation Behaviour of 9% Cr Steels

Constitutive model by coupling sine hyperbolic rate law with the evolution of internal and relaxation stresses with time has been developed to describe the stress-relaxation behaviour of 9% Cr steels. The applicability of the model has been shown for the description of stress-relaxation behaviour of P91 steel for two different strain holds of 1.3 and 2.5% at 873 K. The power law relation between internal stress and relaxation stress, i.e., $\sigma_i = h_r \sigma_r^{m_r}$ has been successfully implemented for the description of stress-relaxation behaviour of P91 steel. The optimised exponent (m_r) of 0.79 is in agreement with the values reported in the literature. The predicted decrease in internal stress with time during stress-relaxation was interrelated to the increase in inter-barrier spacing (L) during relaxation. The predicted values of activation volume (ΔV) in the range 400-1200 b^3 suggested that the stress-relaxation is governed by dislocation processes most importantly the dislocation-local obstacle interaction. Based on the outcome, the power law interrelationship between activation volume and

effective stress, i.e., $\Delta V \propto (\sigma_e)^{-0.6}$ for stress-relaxation has been established. The observed increase in both the activation volume and the inter-barrier spacing with an increase in hold time implies that continual microstructural coarsening takes place during stress-relaxation in P91 steel.

7.5 Future Directions

Based on the understanding gained from the present work, it is suggested that there is a good scope for further investigations related to the modelling of inelastic deformation behaviour of 9% Cr steels. The following problems have been suggested for future perusal.

- In the present research, tensile work hardening behaviour of 9% Cr steels was modelled in the framework of strain-rate independent Estrin-Mecking approach. However, it becomes necessary to invoke the strain-rate and temperature dependency into the dynamic recovery parameter for the description of the tensile flow behaviour of materials for a wide range of test conditions. Therefore, there is a need to develop strain-rate and temperature dependent dislocation density based model. In addition, several strain rate/temperature jump tests will be required to validate the developed model.
- The developed internal-state-variable models need to be implemented into the finite element framework via user material (UMAT) subroutine. The validation of subroutines is required to be performed towards the deformation and damage behaviour of notch specimens. This method of implementation will be useful to integrate the model towards the finite element simulation of structural components for the damage tolerant analysis.
- In the present study, inelastic deformation behaviour of 9% Cr steels has been decoupled into time-independent (plastic) deformation and time-dependent (creep)

deformation. Accordingly, modelling aspects also treated them separately. However, for the complete description of inelastic deformation behaviour, unified internal-state-variable based model should be developed irrespective of tensile, creep and fatigue mode of loading conditions.

- In order to understand the long-term creep behaviour of 9% Cr steels, the coupling of thermodynamic and kinetic theories of precipitate evolution and microstructure based modified Semba-Dyson-McLean model needs to be performed for generating the simulated creep curves with rupture lives $> 10^5$ h.
- The models involved in the present investigation did not consider the kinetics of inelastic deformation of individual hierarchical (PAGB, packet, block, sub-block and lath) boundaries. In view of the above, several interrupted tests are required to be carried out to understand the kinetics of dislocation-pile up against these boundaries during tensile and creep deformation. This understanding can be integrated into mathematical formulations for the development of new and improved models for the description of deformation and damage behaviour of 9% Cr steels.

References

- [1] Klueh, R.L., 2005. Elevated temperature ferritic and martensitic steels and their application to future nuclear reactors. *International Materials Reviews*, 50, pp.287-310.
- [2] Parker, J. and Brett, S., 2013. Creep performance of a grade 91 header. *International Journal of Pressure Vessels and Piping*, 111, pp.82-88.
- [3] Abe, F., Tabuchi, M., Kondo, M. and Tsukamoto, S., 2007. Suppression of Type IV fracture and improvement of creep strength of 9Cr steel welded joints by boron addition. *International journal of pressure vessels and piping*, 84, pp.44-52.
- [4] Hald, J., 2004. Creep strength and ductility of 9 to 12% chromium steels. *Materials at High Temperatures*, 21, pp.41-46.
- [5] EN 10216-2: Seamless non-alloy and alloy steel tubes for pressure purposes with specified elevated temperature properties
- [6] Cerjak, H.H. and Mayr, P., 2008. Creep strength of welded joints of ferritic steels. In *Creep resistant steels*. Abe, F., Kern, T.U. and Viswanathan, R. (eds.) Woodhead Publishing Limited, Abington Cambridge CB21 6AH, England, pp.472-503.
- [7] Raj, B., 2009. Challenges to material scientists and technologists for robust and economical fast reactor technology. In: *Pressure Vessels and Piping: Codes, Standards, Design and Analysis*, Raj, B., Choudhary, B.K. and Velusamy. K., (eds.) Narosa Publishing House, New Delhi, India, pp.1-32.
- [8] Giroux, P.F., Dalle, F., Sauzay, M., Malaplate, J., Fournier, B. and Gourgues-Lorenzon, A.F., 2010. Mechanical and microstructural stability of P92 steel under uniaxial tension at high temperature. *Materials Science and Engineering: A*, 527, pp.3984-3993.
- [9] Harrelson, K.J., Rou, S.H. and Wilcox, R.C., 1986. Impurity element effects on the toughness of 9Cr-1Mo steel. *Journal of Nuclear Materials*, 141, pp.508-512.
- [10] Noble, F.W., Senior, B.A. and Eyre, B.L., 1990. The effect of phosphorus on the ductility of 9Cr-1Mo steels. *Acta Metallurgica et Materialia*, 38, pp.709-717.
- [11] Mathew, M.D., Vanaja, J., Laha, K., Reddy, G.V., Chandravathi, K.S. and Rao, K.B.S., 2011. Tensile and creep properties of reduced activation ferritic–martensitic steel for fusion energy application. *Journal of Nuclear Materials*, 417, pp.77-80.
- [12] Morito, S., Tanaka, H., Konishi, R., Furuhashi, T. and Maki, A.T., 2003. The morphology and crystallography of lath martensite in Fe-C alloys. *Acta materialia*, 51, pp.1789-1799.
- [13] Morito, S., Huang, X., Furuhashi, T., Maki, T. and Hansen, N., 2006. The morphology and crystallography of lath martensite in alloy steels. *Acta Materialia*, 54, pp.5323-5331.

- [14] Kitahara, H., Ueji, R., Tsuji, N. and Minamino, Y., 2006. Crystallographic features of lath martensite in low-carbon steel. *Acta Materialia*, 54, pp.1279-1288.
- [15] Yadav, S.D., Sonderegger, B., Stracey, M. and Poletti, C., 2016. Modelling the creep behaviour of tempered martensitic steel based on a hybrid approach. *Materials Science and Engineering: A*, 662, pp.330-341.
- [16] Roy, A.K., Kumar, P. and Maitra, D., 2009. Dynamic strain ageing of P91 grade steels of varied silicon content. *Materials Science and Engineering: A*, 499, pp.379-386.
- [17] Keller, C., Margulies, M.M., Hadjem-Hamouche, Z. and Guillot, I., 2010. Influence of the temperature on the tensile behaviour of a modified 9Cr–1Mo T91 martensitic steel. *Materials Science and Engineering: A*, 527, pp.6758-6764.
- [18] Choudhary, B.K., Srinivasan, V.S. and Mathew, M.D., 2011. Influence of strain rate and temperature on tensile properties of 9Cr–1Mo ferritic steel. *Materials at High Temperatures*, 28, pp.155-161.
- [19] Choudhary, B.K., Samuel, E.I., Sainath, G., Christopher, J. and Mathew, M.D., 2013. Influence of temperature and strain rate on tensile deformation and fracture behavior of P92 ferritic steel. *Metallurgical and Materials Transactions A*, 44, pp.4979-4992.
- [20] Choudhary, B.K., Mathew, M.D., Samuel, E.I., Christopher, J. and Jayakumar, T., 2013. Elevated temperature tensile properties of P9 steel towards ferritic steel wrapper development for sodium cooled fast reactors. *Journal of Nuclear Materials*, 443, pp.242-249.
- [21] Choudhary, B.K., 2013. Influence of strain rate and temperature on serrated flow in 9Cr–1Mo ferritic steel. *Materials Science and Engineering: A*, 564, pp.303-309.
- [22] Choudhary, B.K., 2013. Tertiary creep behaviour of 9Cr–1Mo ferritic steel. *Materials Science and Engineering: A*, 585, pp.1-9.
- [23] Choudhary, B.K., Phaniraj, C., Rao, K.B.S. and Mannan, S.L., 2001. Creep deformation behaviour and kinetic aspects of 9Cr-1Mo ferritic steel. *ISIJ international*, 41(Suppl), pp.S73-S80..
- [24] Choudhary, B.K. and Samuel, E.I., 2011. Creep behaviour of modified 9Cr–1Mo ferritic steel. *Journal of nuclear materials*, 412, pp.82-89.
- [25] Spigarelli, S. and Quadrini, E., 2002. Analysis of the creep behaviour of modified P91 (9Cr–1Mo–NbV) welds. *Materials & design*, 23, pp.547-552.
- [26] Kimura, K., Kushima, H. and Sawada, K., 2009. Long-term creep deformation property of modified 9Cr–1Mo steel. *Materials Science and Engineering: A*, 510, pp.58-63.

- [27] Ennis, P.J., Zielinska-Lipiec, A., Wachter, O. and Czyska-Filemonowicz, A., 1997. Microstructural stability and creep rupture strength of the martensitic steel P92 for advanced power plant. *Acta Materialia*, 45, pp.4901-4907.
- [28] Sklenička, V., Kuchařová, K., Svoboda, M., Kloc, L., Buršík, J. and Kroupa, A., 2003. Long-term creep behavior of 9–12% Cr power plant steels. *Materials characterization*, 51, pp.35-48.
- [29] Shrestha, T., Basirat, M., Charit, I., Potirniche, G.P., Rink, K.K. and Sahaym, U., 2012. Creep deformation mechanisms in modified 9Cr–1Mo steel. *Journal of Nuclear Materials*, 423, pp.110-119.
- [30] Choudhary, B.K., Rao, K.B.S. and Mannan, S.L., 1999. Steady state creep deformation behaviour of 9Cr-1Mo ferritic steel forging in quenched and tempered condition. *Transactions of Indian Institute of Metals*, 52, pp.327-336.
- [31] Samuel, E.I., Choudhary, B.K., Palaparti, D.R. and Mathew, M.D., 2013. Creep deformation and rupture behaviour of P92 steel at 923 K. *Procedia Engineering*, 55, pp.64-69.
- [32] Choudhary, B.K., 2016. Microstructural degradation and development of damage during creep in 9% chromium ferritic steels. *Transactions of the Indian Institute of Metals*, 69, pp.189-195.
- [33] Leckie, F.A. and Hayhurst, D.R., 1974. Creep rupture of structures. *Proceedings of the Royal Society A*, 340, pp.323-347.
- [34] Dyson, B.F. and Gibbons, T.B., 1987. Tertiary creep in nickel-base superalloys: analysis of experimental data and theoretical synthesis. *Acta Metallurgica*, 35, pp.2355-2369.
- [35] Monkman, F.C., and Grant, N.J., 1956. An empirical relationship between rupture life and minimum creep rate in creep-rupture tests. *Proceedings-American society for testing and materials*, 56, pp.593-620.
- [36] Leckie, F.A. and Hayhurst, D.R., 1977. Constitutive equations for creep rupture. *Acta Metallurgica*, 25, pp.1059-1070.
- [37] Ashby, M.F. and Dyson, B.F., 1984. Creep damage mechanics and micromechanisms. *In Fracture*, 84, pp.3-30.
- [38] Phaniraj, C., Choudhary, B.K., Rao, K.B.S. and Raj, B., 2003. Relationship between time to reach Monkman–Grant ductility and rupture life. *Scripta Materialia*, 48, pp.1313-1318.
- [39] Sakthivel, T., Selvi, S.P. and Laha, K., 2015. An assessment of creep deformation and rupture behaviour of 9Cr–1.8 W–0.5 Mo–VNb (ASME grade 92) steel. *Materials Science and Engineering: A*, 640, pp.61-71.

- [40] Maruyama, K., Sawada, K. and Koike, J.I., 2001. Strengthening mechanisms of creep resistant tempered martensitic steel. *ISIJ international*, 41, pp.641-653.
- [41] Maruyama, K. and Nakashima, H., 1997. *Materials Science for High Temperature Strength*. Uchida-Rokakuho, Tokyo, Japan.
- [42] Panait, C.G., Zielińska-Lipiec, A., Koziel, T., Czyrska-Filemonowicz, A., Gourgues-Lorenzon, A.F. and Bendick, W., 2010. Evolution of dislocation density, size of subgrains and MX-type precipitates in a P91 steel during creep and during thermal ageing at 600 C for more than 100,000 h. *Materials Science and Engineering: A*, 527, pp.4062-4069.
- [43] Baek, J.H., Kim, S.H., Lee, C.B. and Hahn, D.H., 2009. Mechanical properties and microstructural evolution of modified 9Cr-1Mo steel after long-term aging for 50,000 h. *Metals and Materials International*, 15, pp.565-573.
- [44] Armaki, H.G., Chen, R., Kano, S., Maruyama, K., Hasegawa, Y. and Igarashi, M., 2011. Microstructural degradation mechanisms during creep in strength enhanced high Cr ferritic steels and their evaluation by hardness measurement. *Journal of Nuclear Materials*, 416, pp.273-279.
- [45] Sawada, K., Kushima, H., Tabuchi, M. and Kimura, K., 2011. Microstructural degradation of Gr. 91 steel during creep under low stress. *Materials Science and Engineering: A*, 528, pp.5511-5518.
- [46] Golański, G., Kolan, C. and Jasak, J., 2018. Degradation of the Microstructure and Mechanical Properties of High-Chromium Steels Used in the Power Industry. In *Creep*. InTech.
- [47] Abe, F., 2004. Coarsening behavior of lath and its effect on creep rates in tempered martensitic 9Cr–W steels. *Materials Science and Engineering: A*, 387, pp.565-569.
- [48] Nes, E., Ryum, N. and Hunderi, O., 1985. On the Zener drag. *Acta Metallurgica*, 33, pp.11-22.
- [49] Cipolla, L., Danielsen, H.K., Venditti, D., Di Nunzio, P.E., Hald, J. and Somers, M.A., 2010. Conversion of MX nitrides to Z-phase in a martensitic 12% Cr steel. *Acta materialia*, 58, pp.669-679.
- [50] Hald, J., 2008. Microstructure and long-term creep properties of 9–12% Cr steels. *International Journal of Pressure Vessels and Piping*, 85, pp.30-37.
- [51] Yamamoto, K., Kimura, Y. and Mishima, Y., 2006. Effect of matrix microstructure on precipitation of Laves phase in Fe–10Cr–1.4 W (–Co) alloys. *Intermetallics*, 14, pp.515-520.

- [52] Lee, J.S., Armaki, H.G., Maruyama, K., Muraki, T. and Asahi, H., 2006. Causes of breakdown of creep strength in 9Cr–1.8 W–0.5 Mo–VNb steel. *Materials Science and Engineering: A*, 428, pp.270-275.
- [53] Dyson, B.E. and McLean, M., 1997. Microstructural evolution and its effects on the creep performance of high temperature alloys. In: *Microstructural Stability of Creep Resistant Alloys for High Temperature Plant Applications*, Strang, A. and Greenwood, G.W. (eds.), pp.371-393.
- [54] Oruganti, R., Karadge, M. and Swaminathan, S., 2011. Damage mechanics-based creep model for 9–10% Cr ferritic steels. *Acta Materialia*, 59, pp.2145-2155.
- [55] Praveen, C., Christopher, J. and Choudhary, B.K., 2017. Critical Assessment of Short-Term Stress-Relaxation Studies for the Prediction of Creep Properties of P91 Steel. *Transactions of the Indian Institute of Metals*, 70, pp.655-660.
- [56] Woodford, D.A., 2017. Comparison of creep strength and intrinsic ductility for serviced and reheat treated T91 steel based on stress relaxation testing. *Materials at High Temperatures*, 34, pp.140-148.
- [57] Guguloth, K., Swaminathan, J., Roy, N. and Ghosh, R.N., 2017. Uniaxial creep and stress relaxation behavior of modified 9Cr-1Mo steel. *Materials Science and Engineering: A*, 684, pp.683-696.
- [58] Hollomon, J.H., 1945. Tensile deformation. *AIME Transactions*, 12, pp.1-22.
- [59] Ludwik, P., 2013. *Elemente der technologischen Mechanik*. Springer-Verlag.
- [60] Swift, H., 1952. Plastic instability under plane stress. *Journal of the Mechanics and Physics of Solids*, 1, pp.1-18.
- [61] Ludwigson, D.C., 1971. Modified stress-strain relation for FCC metals and alloys. *Metallurgical Transactions*, 2, pp.2825-2828.
- [62] Voce, E., 1955. A practical strain hardening function. *Metallurgia*, 51, pp.219-226.
- [63] Palaparti, D.R., Choudhary, B.K., Samuel, E.I., Srinivasan, V.S. and Mathew, M.D., 2012. Influence of strain rate and temperature on tensile stress–strain and work hardening behaviour of 9Cr–1Mo ferritic steel. *Materials Science and Engineering: A*, 538, pp.110-117.
- [64] Christopher, J., Choudhary, B.K., Samuel, E.I., Srinivasan, V.S. and Mathew, M.D., 2011. Tensile flow and work hardening behaviour of 9Cr–1Mo ferritic steel in the frame work of Voce relationship. *Materials Science and Engineering: A*, 528, pp.6589-6595.

- [65] Klepaczko, J.R., 1987. A practical stress-strain-strain rate-temperature constitutive relation of the power form. *Journal of Mechanical Working Technology*, 15, pp.143-165.
- [66] Johnson, G.R. and Cook, W.H., 1985. Fracture characteristics of three metals subjected to various strains, strain rates, temperatures and pressures. *Engineering fracture mechanics*, 21, pp.31-48.
- [67] Larson, F.R. and Miller, J., 1952. A time-temperature relationship for rupture and creep stresses. *Trans. ASME*, 74, pp.765-775.
- [68] Orr, R.L., Sherby, O.D. and Dorn, J.E., 1953. Correlations of rupture data for metals at elevated temperatures (No. NP-4765; Technical Report 27). Institute of Engineering Research, University of California, Berkeley.
- [69] Manson, S.S. and Haferd, A.M., 1953. A linear time-temperature relation for extrapolation of creep and stress-rupture data, NASA Technical Notes.
- [70] Choudhary et al. yet to published.
- [71] Holdsworth, S.R., 2010. September. Advances in the assessment of creep data. In: *Proceedings of 9th Liege Conference, Materials for Advanced Power Engineering*, Lecomte-Beckers, J., Contrepolis, Q., Beck, T. and Kuhn, B. (eds.), pp. 946-947.
- [72] Andrade, E.N.D.C., 1910. On the viscous flow in metals, and allied phenomena. *Proceedings of the Royal Socioety A*, 84, pp.1-12.
- [73] McVetty, P.G., 1934. Working stresses for high temperature service. *Mech. Eng*, 56, p.149.
- [74] Garofalo, F., 1965. *Fundamentals of creep and creep-rupture in metals*. Macmillan.
- [75] Li, J.C.M., 1963. A dislocation mechansim of transient creep. *Acta Metallurgica*, 11, pp.1269-1270.
- [75] Kachanov, L. M., 1960. *The Theory of Creep*. Wetherby, Boston, MA.
- [77] Rabotnov, Y. N., 1969. *Creep Problems in Structural Members*. North-Holland, 419 Amsterdam, The Netherlands.
- [78] Evans, R.W., Parker, J.D. and Wilshire, B., 1992. The θ projection concept—A model-based approach to design and life extension of engineering plant. *International Journal of Pressure vessels and piping*, 50, pp.147-160.
- [79] Srinivasan, V.S., Choudhary, B.K., Mathew, M.D., and Jayakumar T., 2011. Creep behaviour of 9Cr-1Mo ferritic steel using theta-trojection approach and evolution of a damage criterion. Conference: Proc. 21st International Conference on Structural Mechanics in Reactor Technology, (SMIRT 21) 2011, 6-11 November, New Delhi, India, At New Delhi, India, Volume: Transactions, SMIRT 21, pp. 779:1-6

- [80] Domkin, K., 2005. Constitutive models based on dislocation density: Formulation and implementation into finite element codes (Doctoral dissertation, Luleå tekniska universitet).
- [81] Roters, F., Raabe, D. and Gottstein, G., 2000. Work hardening in heterogeneous alloys—a microstructural approach based on three internal state variables. *Acta materialia*, 48, pp.4181-4189.
- [82] Kocks, U.F., 1976. Laws for work-hardening and low-temperature creep. *Journal of engineering materials and technology*, 98, pp.76-85.
- [83] Kocks, U.F. and Mecking, H., 2003. Physics and phenomenology of strain hardening: the FCC case. *Progress in materials science*, 48, pp.171-273.
- [84] Estrin, Y. and Mecking, H., 1984. A unified phenomenological description of work hardening and creep based on one-parameter models. *Acta Metallurgica*, 32, pp.57-70.
- [85] Barlat, F., Glazov, M.V., Brem, J.C. and Lege, D.J., 2002. A simple model for dislocation behavior, strain and strain rate hardening evolution in deforming aluminum alloys. *International journal of Plasticity*, 18, pp.919-939.
- [86] Christopher, J. and Choudhary, B.K., 2015. Kinetics of Uniaxial Tensile Flow and Work Hardening Behavior of Type 316L (N) Austenitic Stainless Steel in the Framework of Two-Internal-Variable Approach. *Metallurgical and Materials Transactions A*, 46, pp.674-687.
- [87] Choudhary, B.K. and Christopher, J., 2015. Tensile flow and work hardening behaviour of type 316L (N) austenitic stainless steel in the framework of one-internal-variable and two-internal-variable approaches. *Materials Science and Engineering: A*, 636, pp.269-278.
- [88] Estrin, Y. and Kubin, L.P., 1986. Local strain hardening and nonuniformity of plastic deformation. *Acta metallurgica*, 34, pp.2455-2464.
- [89] Estrin, Y., 1996. Dislocation-density-related constitutive modelling. In: *Unified Constitutive Laws of Plastic Deformation*, Krausz, A.S. and Krausz, K., (eds.) Academic Press San Diego, CA. pp.69-1061.
- [90] Estrin, Y., Toth, L.S., Molinari, A. and Bréchet, Y., 1998. A dislocation-based model for all hardening stages in large strain deformation. *Acta materialia*, 46, pp.5509-5522.
- [91] Milicka, K., Dobes, F., Slamenikova, J. and Orlová, A., 1995. Constitutive description of creep curves based on internal stress evolution. *Acta metallurgica et materialia*, 43, pp.3947-3957.
- [92] Orlová, A. and Dobeš, F., 2003. Internal stress and heterogeneous dislocation structure in creep. *Philosophical Magazine*, 83, pp.2681-2691.

- [93] Saxl, I. and Kroupa, F., 1972. Relations between the experimental parameters describing the steady-state and transient creep. *Physica status solidi (a)*, 11, pp.167-173.
- [94] Dobeš, F., 1976. Stochastic approach to the interpretation of measured effective stress. *physica status solidi (a)*, 34, pp.K27-K29.
- [95] Ahlquist, C.N. and Nix, W.D., 1971. The measurement of internal stresses during creep of Al and Al-Mg alloys. *Acta metallurgica*, 19, pp.373-385.
- [96] Shaker, C. and El-Magd, E., (1990) Behaviour of high-temperature materials under time-dependent-creep conditions. In: *High Temperature Materials For Power Engineering, 1990, Part II*, Bachelet, E., Brunetaud, R., Coutsouradis, D., Esslinger, P., Ewald, J., Kvernes, I., Lindblom, Y., Meadowcroft, D.B., Regis, V., Scarlin, R.B., Schneider, K., and Singer, R., (eds.) Kulwer Academic Publishers, Dordrecht, pp. 1097–1106.
- [97] Esposito, L. and Bonora, N., 2011. A primary creep model for Class M materials. *Materials Science and Engineering: A*, 528, pp.5496-5501.
- [98] McLean, M. and Dyson, B.F., 2000. Modelling the effects of damage and microstructural evolution on the creep behavior of engineering alloys. *Journal of engineering Materials and Technology*, 122, pp.273-278.
- [99] Dyson, B., 2000. Use of CDM in materials modelling and component creep life prediction. *Journal of pressure vessel technology*, 122, pp.281-296.
- [100] Yin, Y.F. and Faulkner, R.G., 2006. Continuum damage mechanics modelling based on simulations of microstructural evolution kinetics. *Materials science and technology*, 22, pp.929-936.
- [101] Coakley, J., Dye, D. and Basoalto, H., 2011. Creep and creep modelling of a multimodal nickel-base superalloy. *Acta Materialia*, 59, pp.854-863.
- [102] Basirat, M., Shrestha, T., Potirniche, G.P., Charit, I. and Rink, K., 2012. A study of the creep behavior of modified 9Cr–1Mo steel using continuum-damage modelling. *International Journal of Plasticity*, 37, pp.95-107.
- [103] Yadav, S.D., El-Tahawy, M., Kalácska, S., Dománková, M., Yubero, D.C. and Poletti, C., 2017. Characterizing dislocation configurations and their evolution during creep of a new 12% Cr steel. *Materials characterization*, 134, pp.387-397.
- [104] Considère, A., 1885. *Ann. ponts et chaussées*. ser. 6, vol. 9, pp. 574-775.
- [105] Friedel, J., 1964. *Dislocations*. Pergamon Press, Oxford, 1964.
- [106] Orowan, E., 1940. Problems of plastic gliding. *Proceedings of the Physical Society*, 52, p.8.

- [107] Prager, M., 2000. The Omega Method—An Engineering Approach to Life Assessment. *ASME Journal of Pressure Vessel Technology* 122, pp. 273-280.
- [108] Semba, H., Dyson, B., and McLean, M., 2008. Microstructure-based creep modelling of a 9%Cr martensitic steel. *Materials at High Temperatures*, 25, pp. 131-137.
- [109] Senior, B.A., Noble, F.W. and Eyre, B.L., 1986. The nucleation and growth of voids at carbides in 9 Cr-1 Mo steel. *Acta Metallurgica*, 34, pp.1321-1327.
- [110] Hipsley, C.A. and Haworth, N.P., 1988. Hydrogen and temper embrittlement in 9Cr-1Mo steel. *Materials science and technology*, 4, pp.791-802.
- [111] Danielsen, H.K. and Hald, J., 2006. Behaviour of Z phase in 9–12% Cr steels. *Energy Materials*, 1, pp.49-57.
- [112] Thermo-Calc Software TCFE6 Steels/Fe-alloys database version 6.
- [113] Nosedal, J. and Wright, S.J., 2006. *Nonlinear Equations*, Springer, New York, pp. 270-302.
- [114] Nes, E., 1997. Modelling of work hardening and stress saturation in FCC metals. *Progress in Materials Science*, 41, pp.129-193.
- [115] Rollett, A.D. and Kocks, U.F., 1993. A review of the stages of work hardening. In *Solid State Phenomena*, Trans Tech Publications, 35, pp. 1-18.
- [116] Christopher, J. and Choudhary, B.K., 2016. On the assessment of tensile work hardening behaviour of type 316L (N) austenitic stainless steel in the framework of $\theta\sigma_d$ vs. σ_d using flow stress contribution from dislocations. *International Journal of Pressure Vessels and Piping*, 146, pp.151-160.
- [117] Bergström, Y. and Hallén, H., 1982. An improved dislocation model for the stress-strain behaviour of polycrystalline α -Fe. *Materials Science and Engineering*, 55, pp.49-61.
- [118] Hallén, H., 1985. A theory of dynamic recovery in FCC metals. *Materials Science and Engineering*, 72, pp.119-123.
- [119] Wang, L., Li, M. and Almer, J., 2014. Investigation of deformation and microstructural evolution in Grade 91 ferritic–martensitic steel by in situ high-energy X-rays. *Acta Materialia*, 62, pp.239-249.
- [120] Christopher, J. and Choudhary, B.K., 2014. Dislocation-density-based constitutive modelling of tensile flow and work-hardening behaviour of P92 steel. *Philosophical Magazine*, 94, pp.2992-3016.
- [121] Choudhary, B.K. and Christopher, J., 2016. Stage-II tensile work hardening behaviour of type 316L (N) austenitic stainless steel. *Materials Science and Engineering: A*, 651, pp.486-489.

- [122] Samuel, E.I., Choudhary, B.K. and Rao, K.B.S., 2007. Influence of post-weld heat treatment on tensile properties of modified 9Cr–1Mo ferritic steel base metal. *Materials Science and Technology*, 23, pp.992-999.
- [123] Rodriguez, P., 1984. Serrated plastic flow. *Bulletin of Materials Science*, 6, pp.653-663.
- [124] Design and Construction Rules for Mechanical Components of FBR Nuclear Islands, French Nuclear Design Code, 2007, RCC-MR, Section 1, Subsection Z, Appendix A3.18S.22.
- [125] Morooka, S., Tomota, Y. and Kamiyama, T., 2008. Heterogeneous deformation behavior studied by in situ neutron diffraction during tensile deformation for ferrite, martensite and pearlite steels. *ISIJ international*, 48, pp.525-530.
- [126] Fujita, M., Kaneko, Y., Nohara, A., Saka, H., Zauter, R. and Mughrabi, H., 1994. Temperature dependence of the dissociation width of dislocations in a commercial 304L stainless steel. *ISIJ international*, 34, pp.697-703.
- [127] Karlsen, W., Ivanchenko, M., Ehrnstén, U., Yagodzinsky, Y. and Hänninen, H., 2009. Microstructural manifestation of dynamic strain aging in AISI 316 stainless steel. *Journal of nuclear materials*, 395, pp.156-161.
- [128] Roy, A.K., Pal, J. and Mukhopadhyay, C., 2008. Dynamic strain ageing of an austenitic superalloy—Temperature and strain rate effects. *Materials Science and Engineering: A*, 474, pp.363-370.
- [129] Sauzay, M., 2009. Modelling of the evolution of micro-grain misorientations during creep of tempered martensite ferritic steels. *Materials Science and Engineering: A*, 510, pp.74-80.
- [130] Kubin, L., Hoc, T. and Devincre, B., 2009. Dynamic recovery and its orientation dependence in face-centered cubic crystals. *Acta Materialia*, 57, pp.2567-2575.
- [131] Morito, S., Saito, H., Ogawa, T., Furuhashi, T. and Maki, T., 2005. Effect of austenite grain size on the morphology and crystallography of lath martensite in low carbon steels. *ISIJ international*, 45, pp.91-94.
- [132] Prawoto, Y., Jasmawati, N. and Sumeru, K., 2012. Effect of prior austenite grain size on the morphology and mechanical properties of martensite in medium carbon steel. *Journal of Materials Science & Technology*, 28, pp.461-466.
- [133] Morito, S., Igarashi, R., Kamiya, K., Ohba, T. and Maki, T., 2010. Effect of cooling rate on morphology and crystallography of lath martensite in Fe-Ni alloys. In *Materials Science Forum*, Trans Tech Publications, 638, pp.1459-1463.

- [134] Parameswaran, P., Saroja, S., Vijavalakshmi, M. and Raghunathan, V.R., 1996. Decomposition modes of austenite in CrMo ferritic steels. *Journal of nuclear materials*, 232, pp.226-232.
- [135] Vitek, J.M. and Klueh, R.L., 1983. Precipitation reactions during the heat treatment of ferritic steels. *Metallurgical Transactions A*, 14, pp.1047-1055.
- [136] Shi, Z.M., Gong, W., Tomota, Y., Harjo, S., Li, J., Chi, B. and Pu, J., 2015. Study of tempering behavior of lath martensite using in-situ neutron diffraction. *Materials Characterization*, 107, pp.29-32.
- [137] Nes, E., Marthinsen, K. and Brechet, Y., 2002. On the mechanisms of dynamic recovery. *Scripta Materialia*, 47, pp.607-611.
- [138] Sainath, G., Choudhary, B.K., Christopher, J., Isaac Samuel, E. and Mathew, M.D., 2014. Effects of temperature and strain rate on tensile stress–strain and workhardening behaviour of P92 ferritic steel. *Materials Science and Technology*, 30, pp.911-920.
- [139] Malygin, G.A., 2005. Analysis of structural factors that control necking during tension of FCC metals and alloys. *Physics of the Solid State*, 47, pp.246-251.
- [140] Yasnikov, I.S., Vinogradov, A. and Estrin, Y., 2014. Revisiting the Considère criterion from the viewpoint of dislocation theory fundamentals. *Scripta Materialia*, 76, pp.37-40.
- [141] Hart, E.W., 1967. Theory of the tensile test. *Acta metallurgica*, 15, pp.351-355.
- [142] Vinogradov, A., Yasnikov, I.S., Matsuyama, H., Uchida, M., Kaneko, Y. and Estrin, Y., 2016. Controlling strength and ductility: dislocation-based model of necking instability and its verification for ultrafine grain 316L steel. *Acta Materialia*, 106, pp.295-303.
- [143] Yasnikov, I.S., Estrin, Y. and Vinogradov, A., 2017. What governs ductility of ultrafine-grained metals? A microstructure based approach to necking instability. *Acta Materialia*, 141, pp.18-28.
- [144] Li, Y.J., Mueller, J., Höppel, H.W., Göken, M. and Blum, W., 2007. Deformation kinetics of nanocrystalline nickel. *Acta Materialia*, 55, pp.5708-5717.
- [145] Holdsworth, S.R., Askins, M., Baker, A., Gariboldi, E., Holmström, S., Klenk, A., Ringel, M., Merckling, G., Sandstrom, R., Schwienheer, M. and Spigarelli, S., 2008. Factors influencing creep model equation selection. *International Journal of Pressure Vessels and Piping*, 85, pp.80-88.
- [146] Taylor, G.I., 1934. A theory of the plasticity of crystals. *Zeitschrift für Kristallographie-Crystalline Materials*, 89, pp.375-385.

- [147] Gibbs, G.B., 1969. Thermodynamic analysis of dislocation glide controlled by dispersed local obstacles. *Materials Science and Engineering*, 4, pp.313-328.
- [148] Lloyd, D.J., 1986. Precipitation hardening. In: *Strength of Metals and Alloys (ICSMA 7): Proceedings of the 7th International Conference on the Strength of Metals and Alloys*, McQueen, H.J., Bailon, J.P., Dickson, J.I., Jonas, J.J., and Akben, M.G., (eds.) Montreal, Canada, 12–16 August 1985 (Vol. 3). Elsevier. pp. 1745-1778.
- [149] McLean, D., 1966. The physics of high temperature creep in metals. *Reports on Progress in Physics*, 29, p.1.
- [150] Lagneborg, R. and Forsen, B.H., 1973. A model based on dislocation distributions for work-hardening and the density of mobile and immobile dislocations during plastic flow. *Acta Metallurgica*, 21, pp.781-790.
- [151] Lagneborg, R., 1972. Dislocation mechanisms in creep. *International Metallurgical Reviews*, 17, pp.130-146.
- [152] Shi, L. and Northwood, D.O., 1993. Creep of an AISI 310 type stainless steel and its numerical simulation using the Öström-Lagneborg creep model. *Acta metallurgica et materialia*, 41, pp.3393-3400.
- [153] Chen, H.S., Gilman, J.J. and Head, A.K., 1964. Dislocation Multipoles and Their Role in Strain-Hardening. *Journal of Applied Physics*, 35, pp.2502-2514.
- [154] Nix, W.D., Coghlan, W.A. and Barrett, C.R., 1969. Effect of internal stresses on the apparent stress dependence of dislocation velocities. *Materials Science and Engineering*, 4, pp.98-105.
- [155] Groisböck, F. and Jeglitsch, F., 1992. Internal and effective stresses in high-temperature creep evaluated from transient dip tests and dislocation bowing. *Journal of materials science*, 27, pp.4365-4372.
- [156] Northwood, D.O. and Smith, I.O., 1984. Steady-State Creep and Strain Transients for Stress-Dip Tests in Polycrystalline Magnesium at 300° C. *physica status solidi (a)*, 85, pp.149-158.
- [157] Northwood, D.O. and Smith, I.O., 1985. Steady-state creep and strain transients for stress change tests in an Al–0.4 wt% Li solid solution alloy. *physica status solidi (a)*, 88, pp.181-191.
- [158] Northwood, D.O. and Smith, I.O., 1986. Stress change tests during the steady state creep of aluminum alloy 3004 at 300 ° C. *Materials Science and Engineering*, 79, pp.175-182.
- [159] Northwood, D.O. and Smith, I.O., 1986. Internal and Effective Stresses in the Steady-State Creep of Polycrystalline Cadmium at 0.5 Tm. *physica status solidi (a)*, 98, pp.163-169.

- [160] Hayakawa, H., Nakashima, S., Kusumoto, J., Kanaya, A. and Nakashima, H., 2009. Creep deformation characterization of heat resistant steel by stress change test. *International Journal of Pressure Vessels and Piping*, 86, pp.556-562.
- [161] Magnusson, H. and Sandström, R., 2007. Creep strain modelling of 9 to 12 Pct Cr steels based on microstructure evolution. *Metallurgical and Materials Transactions A*, 38, pp.2033-2039.
- [162] Mikami, M., 2016. Effects of Dislocation Substructure on Creep Deformation Behavior in 0.2% C-9% Cr Steel. *ISIJ International*, 56, pp.1840-1846.
- [163] Orlova, A. and Čadek, J., 1973. Some substructural aspects of high-temperature creep in metals. *Philosophical Magazine*, 28, pp.891-899.
- [164] Fedoseeva, A., Dudova, N. and Kaibyshev, R., 2016. Creep strength breakdown and microstructure evolution in a 3% Co modified P92 steel. *Materials Science and Engineering: A*, 654, pp.1-12.
- [165] Milička, K., 1994. Constant structure experiments in high temperature primary creep of some metallic materials. *Acta metallurgica et materialia*, 42, pp.4189-4199.
- [166] Sueek, T., Luton, M.J. and Jonas, J.J., 1973. On the Pre-Exponential Factor in the Rate Equation for Plastic Flow. *physica status solidi (b)*, 57, pp.647-659.
- [167] Kauzmann, W., 1941. Flow of solid metals from the standpoint of the chemical-rate theory. *Trans. AIME*, 143, pp.57-83.
- [168] Tamura, M. and Abe, F., 2015. Changes in estimated dislocation density during creep in martensitic heat-resistant steel. *Journal of Materials Science Research*, 4, pp.48-69.
- [169] Evans, M., 2013. The Potential United Kingdom Energy Gap and Creep Life Prediction Methodologies. *Metallurgical and Materials Transactions A*, 44, pp.109-127.
- [170] Abe, F., 2011. Creep life estimation of Gr. 91 based on creep strain analysis. *Materials at High Temperatures*, 28, pp.75-84.
- [171] Sandström, R., 2012. Basic model for primary and secondary creep in copper. *Acta Materialia*, 60, pp.314-322.
- [172] Polcik, P., Straub, S., Henes, D., and Blum, W., 1998. Simulation of the Creep Behaviour of 9-12% CrMo-V Steels on the Basis of Microstructural Data. In: *Microstructural Stability of Creep Resistant Alloys for High Temperature Plant Application*. Strang, A., Cawley, J., and Greenwood, G. W. (eds.) Institute of Materials, London, pp. 405-429.
- [173] Stouffer, D. C., and Dame, L. T., 1996. *Inelastic Deformation of Metals: Models, Mechanical Properties, and Metallurgy*, Wiley Interscience, New York.

- [174] Sasikala, G., Ray, S.K. and Mannan, S.L., 2004. Evolution of damage in tertiary creep of type 316 (N) SS weld metal. *Acta materialia*, 52, pp.5677-5686.
- [175] Ion, J.C., 1986. The modelling of creep for engineering design. Teddington, Middx, U.K: The National Physical Laboratory; 1986. (NPL Report DMA A115).
- [176] Dyson, B.F. and McLean, M., 2001. Micromechanism-quantification for creep constitutive equations. In: IUTAM symposium on Creep in Structures, Murakami, S., and Ohno, N., (eds.) Springer, Dordrecht, pp.3-16.
- [177] Roy, N., Das, A. and Ray, A.K., 2015. Simulation and quantification of creep damage. *International Journal of Damage Mechanics*, 24, pp.1086-1106.
- [178] Lin, J., Liu, Y. and Dean, T.A., 2005. A review on damage mechanisms, models and calibration methods under various deformation conditions. *International Journal of damage mechanics*, 14(4), pp.299-319.
- [179] Sawada, K., Takeda, M., Maruyama, K., Ishii, R., Yamada, M., Nagae, Y., and Komine, R., 1999. Effect of W on recovery of lath structure during creep of high chromium martensitic steels. *Materials Science and Engineering: A*, 267, pp.19-25.
- [180] Kadoya, Y., Nshimura, N., Dyson, B.F., and McLean, M., 1997. Origins of tertiary creep in high chromium steels. In: *Proceeding of Creep and Fracture of Engineering Materials and Structures*. Eathman, J.C. and Mohamed, F.A., (eds), TMS, Warrendale, PA, United States, pp.343–352.
- [181] Choudhary, B.K., Saroja, S., Rao, K.B.S. and Mannan, S.L., 1999. Creep-rupture behavior of forged, thick section 9Cr-1Mo ferritic steel. *Metallurgical and Materials Transactions A*, 30, pp.2825-2834.
- [182] Blum, W. and Chilukuru, H., 2009. Tertiary creep of tempered martensite 9-12% Cr-steels-on the microstructural origin of creep life limitation. *Press Vessels Piping*, 2, pp.125-136.
- [183] Perrin, I.J. and Hayhurst, D.R., 1996. Creep constitutive equations for a 0.5 Cr–0.5 Mo–0.25 V ferritic steel in the temperature range 600–675 °C. *The Journal of Strain Analysis for Engineering Design*, 31, pp.299-314.
- [184] Mustata, R. and Hayhurst, D.R., 2005. Creep constitutive equations for a 0.5 Cr 0.5 Mo 0.25 V ferritic steel in the temperature range 565 °C–675 °C. *International Journal of pressure vessels and piping*, 82, pp.363-372.
- [185] Hayhurst, R.J., Vakili-Tahami, F. and Hayhurst, D.R., 2009. Verification of 3-D parallel CDM software for the analysis of creep failure in the HAZ region of Cr–Mo–V crosswelds. *International Journal of Pressure Vessels and Piping*, 86, pp.475-485.
- [186] Igual, J.Z. and Xu, Q., 2015, September. Determination of the material constants of creep damage constitutive equations using Matlab optimization procedure. In

- Automation and Computing (ICAC), 2015 21st International Conference, IEEE, pp. 1-6.
- [187] Zhou, Y., Chen, X.D., Fan, Z.C. and Rao, S.X., 2015. Finite Element Modelling of Welding Residual Stress and Its Influence on Creep Behavior of a 2.25 Cr-1Mo-0.25 V Steel Cylinder. *Procedia Engineering*, 130, pp.552-559.
- [188] Hyde, T.H., Becker, A.A., Sun, W. and Williams, J.A., 2006. Finite-element creep damage analyses of P91 pipes. *International journal of pressure vessels and piping*, 83(11-12), pp.853-863.
- [189] Christopher, J., Sainath, G., Srinivasan, V.S., Samuel, E.I., Choudhary, B.K., Mathew, M.D. and Jayakumar, T., 2013. Continuum damage mechanics approach to predict creep behaviour of modified 9Cr-1Mo ferritic steel at 873 K. *Procedia Engineering*, 55, pp.798-804.
- [190] Ashby, M.F., 1968. The theory of the critical shear stress and work hardening of dispersion-hardened crystals. In: *Metallurgical Society Conference*, Ansell, G.S., Cooper, T.D. and Lenel, F.V., (eds), Gordon and Breach New York, pp.143-205.
- [191] Holzer, I., Kozeschnik, E. and Cerjak, H., 2010. New approach to predict the long-term creep behaviour and evolution of precipitate back-stress of 9–12% chromium steels. *Transactions of the Indian Institute of Metals*, 63(2-3), pp.137-143.
- [192] Kimura, K., Sawada, K., Kushima, H. and Toda, Y., 2013. Influence of chemical composition and heat treatment on long-term creep strength of grade 91 steel. *Procedia Engineering*, 55, pp.2-9.
- [193] Hald, J. and Korcakova, L., 2003. Precipitate stability in creep resistant ferritic steels-experimental investigations and modelling. *ISIJ international*, 43(3), pp.420-427.
- [194] Kobayashi, S., Sawada, K., Hara, T., Kushima, H., and Kimura, K., (2014). Heat-to-Heat variation in creep rupture ductility of ASME Gr.91 steels in the long-term investigation into recovery of microstructure and void formation. In: *Advances in Materials Technology for Fossil Power plants: Proceedings from the Seventh International Conference*, Gandy, D., and Shingledecker, J., (eds), Ohio: ASM International, pp.637-647.
- [195] Strang, A., and Vodarek, V., 1997. Microstructural stability of creep resistant martensitic 12% Cr steels. In: *Microstructural Stability of Creep Resistant Alloys for High Temperature Plant Applications*, Strang, A., Cawley, J., and Greenwood, G.W., (eds). London: Institute of Materials, pp.117-133.
- [196] Masuyama, F., 2007. Creep rupture life and design factors for high-strength ferritic steels. *International journal of pressure vessels and piping*, 84(1-2), pp.53-61.

- [197] Zhao, J., Gong, J., Saboo, A., Dunand, D.C. and Olson, G.B., 2018. Dislocation-based modelling of long-term creep behaviors of Grade 91 steels. *Acta Materialia*, 149, pp.19-28.
- [198] Srinivasan, V.S., Choudhary, B.K., Mathew, M.D. and Jayakumar, T., 2012. Long-term creep-rupture strength prediction for modified 9Cr–1Mo ferritic steel and type 316L (N) austenitic stainless steel. *Materials at High Temperatures*, 29(1), pp.41-48.
- [199] Dronhofer, A., Pešicka, J., Dlouhý, A. and Eggeler, G., 2003. On the nature of internal interfaces in tempered martensite ferritic steels: Dedicated to Professor Dr. Otmar Vöhringer on the occasion of his 65th birthday. *Zeitschrift für Metallkunde*, 94(5), pp.511-520.
- [200] Kloc, L. and Sklenička, V., 1997. Transition from power-law to viscous creep behaviour of P-91 type heat-resistant steel. *Materials Science and Engineering: A*, 234, pp.962-965.
- [201] Prasad, S., Rajkumar, V.B. and KC, H.K., 2012. Numerical simulation of precipitate evolution in ferritic–martensitic power plant steels. *Calphad*, 36, pp.1-7.
- [202] Krausz, A.S. and Krausz, K., 1996. The constitutive law of deformation kinetics. In: *Unified Constitutive Laws of Plastic Deformation*, Krausz, A.S. and Krausz, K., (eds.) Academic Press San Diego, CA. pp. 229-279.
- [203] Woodford, D.A., 1993. Test methods for development, design, and life assessment of high temperature materials, *Materials and Design*, 14, pp.231-242.
- [204] Woodford, D.A., 1997. Creep Analysis of Directionally Solidified GTD111 based on Stress Relaxation Testing. *Materials at High Temperatures*, 14, pp.413-420.
- [205] Woodford, D.A., 2002. Advances in the use of stress relaxation data for design and life assessment in combustion turbines. *JSME International* 45, pp.98-103.
- [206] Dotseneo, V.I., 1979. Stress relaxation in crystals. *Physica status solidi (b)*, 93, pp.11-43.
- [207] Feltham, P., 1963. Stress relaxation in magnesium at low temperatures. *Physica status solidi (b)*, 3, pp.1340-1346.
- [208] Dimelfi, R.J., 1983. Application of a unified deformation rate law to stress-relaxation of AISI type 316 stainless steel. *Transactions of the American Nuclear Society*, 45, pp.282-283.
- [209] McCarthy, P.R., Robertson, D.G., Orr, J. and Strang, A., 2000. Recent development in stress relaxation methodologies within Europe. *Key Engineering Materials*, 171–174, pp.9-16.

- [210] Humphries, S.R., Snowden, K.U. and Yeung, W., 2010. The effect of repeated loadings on the stress relaxation properties of 2.25Cr-1Mo steel at 550 °C and the influence on the Feltham ‘a’ and ‘b’ parameters, *Materials Science Engineering A*, 527, pp.3240-3244.
- [211] Trojanová, Z., Máthis, K., Lukác, P., Németh, G. and Chmelík, F., 2011. Internal stress and thermally activated dislocation motion in an AZ63 magnesium alloy. *Materials Chemistry and Physics* 130, pp.1146-1150.
- [212] Ramberg, W. and Osgood, W.R., 1946. Description of stress strain curves by three parameters, *NACA Tech. Note No.902*.
- [213] Holdsworth, S.R., 1999. A knowledge based system for creep–fatigue assessment. *Nuclear Engineering and Design*, 188, pp.289-301.
- [214] Bose, S.C., Singh, K., Swaminathan, J. and Sarma, D.S., 2004. Prediction of creep life of X10CrMoVNbN-91 (P-91) steel through short term stress relaxation test methodology. *Materials Science Technology*, 20, pp.1290-1296.
- [215] Argon, A.S. and Takeuchi, S., 1981. Internal stresses in power-law creep. *Acta Metallurgica*, 29, pp.1877-1884.
- [216] Kocks, U.F., Argon, A.S. and Ashby, M.F., 1975. Thermodynamics and kinetics of slip, *Progress in Materials Science*, 19, pp.1-271.
- [217] Morris, D.G., 2011. Strengthening mechanisms in nanocrystalline metals. in: *Nanostructured Metals and Alloys*, Whang, S.H. (ed.), Woodhead Publishing Limited, New Delhi, pp.299-328.